

STAVEBNÍ OBZOR

číslo 4/2019



Obsah:

39	EXPERIMENTAL RESEARCH INTO THE RESPONSE OF A MONUMENTAL HISTORIC STRUCTURE TO TRAFFIC-INDUCED EFFECTS OF TECHNICAL SEISMICITY <i>Jiří Witzany¹, Radek Zigler, Shota Urushadze</i>
40	TRUSS STRUCTURE OPTIMIZATION BASED ON IMPROVED WOLF PACK ALGORITHM <i>Yan-cang LI, Zong-jin YANG, Cheng-hua Dang</i>
41	EVALUATION OF MASONRY GROUTING EFFECTIVENESS USING THERMOGRAPHY AND ULTRASONIC METHODS <i>Radek Zigler</i>
42	THE MEASUREMENT OF HIGH-SPEED RAILWAY (HSR)-PRECISION ENGINEERING <i>Alhossein Mohamed, Qiyuan Peng, Malik Muneeb Abid</i>
43	STATISTICAL STUDY OF MODIS ALGORITHMS IN ESTIMATING AEROSOL OPTICAL DEPTH OVER THE CZECH REPUBLIC <i>Saleem Ibrahim and Lena Halounova</i>
44	INFLUENCE OF PANEL ZONE SIZES ON ULTIMATE BEARING CAPACITY OF H-SHAPED STEEL FRAMES <i>Yan Zhang, Huijuan Liu, Yuhong Yang, Enhe Bao</i>
45	PHYSICAL AND MECHANICAL PROPERTIES OF RECYCLED PET COMPOSITES <i>Yurani García Quintero, Daniel Ruíz Figueroa, Harveth Gil, and Alejandro Alberto Zuleta</i>
46	A STUDY ON THE ULTIMATE LOAD BEARING CAPACITY OF CARBON FIBRE REINFORCED POLYMER TENSEGRITY SYSTEM IN A SUSPEN DOME <i>IfeOlorun Olofin, Ronggui Liu</i>
47	EFFECT OF MOISTURE ON THE INTERFACE OF TIMBER AND EXTERNALLY BONDED FIBRE REINFORCED POLYMERS: A REVIEW PAPER <i>Nayan Das and Rijun Shrestha</i>
48	GEOMETRY CONSTRUCTION METHOD OF HEX-TRI RECIPROCAL FRAME <i>Lin Qi, Wenbo Zhang, Zifei Li, Ronglai Sun and Xin Huang</i>
49	SELECTED POSSIBILITIES OF DATA EXCERPTION FROM THE DATABASE OF HISTORICAL ATLASES <i>Petra Jílková and Tomáš Janata</i>
50	MECHANISM OF EFFICIENCY OF SELECTED NANOSYSTEMS INTENDED FOR CONSOLIDATION OF POROUS MATERIALS <i>Klára Kroftová and David Škoda</i>

51	<p>FINITE ELEMENT ANALYSIS OF THE SEISMIC BEHAVIOR OF THE ASSEMBLED LIGHT STEEL FRAME-LIGHT WALL STRUCTURES <i>Liu Wenchao, Chen Zheng, Wang Cheng, Dong Hongying, Wang Ruwei</i></p>
52	<p>PARAMETRIC MODELLING FOR HBIM: DESIGN OF WINDOW LIBRARY FOR RURAL BUILDING <i>Zdeněk Poloprutský</i></p>
53	<p>A COMPARISON OF THE EFFECTIVENESS OF GROUTING METHODS, PENETRATION AND SURFACE APPLICATION OF GELS IN INCREASING THE STRENGTH OF HISTORIC MASONRY <i>Tomáš Čejka, Jiří Karas and Jan Kubát</i></p>
54	<p>STUDY ON THE INFLUENCE OF SAFETY EDUCATION ON THE WILLINGNESS OF CONSTRUCTION WORKERS TO HABITUAL SAFETY BEHAVIOUR <i>Mei Shang and Wei Zhang</i></p>
55	<p>VERTICAL WALL STRUCTURES IN TENEMENT HOUSES AT THE TURN OF 20TH CENTURY <i>Martin Ebel</i></p>

EXPERIMENTAL RESEARCH INTO THE RESPONSE OF A MONUMENTAL HISTORIC STRUCTURE TO TRAFFIC-INDUCED EFFECTS OF TECHNICAL SEISMICITY

Jiří Witzany¹, Radek Zigler¹, Shota Urushadze²

1. CTU in Prague, Faculty of Civil Engineering, Department of Building Structures, Prague, Thákurova 7, Czech Republic; wizany@fsv.cvut.cz, zigler@fsv.cvut.cz,
2. The Institute of Theoretical and Applied Mechanics AS CR, v. v. i, Prague, Prosecká 809/76, Czech Republic; urushadze@itam.cas.cz

ABSTRACT

The growing volumes of particularly heavy truck traffic with high road pavement loading values and, in many cases, poor quality and uneven road pavement surfaces intensify the effects technical seismicity on buildings situated in the vicinity of traffic routes.

KEYWORDS

Monitoring, Technical seismicity, Structure response, Traffic, Historic masonry

INTRODUCTION

The term technical seismicity denotes dynamic effects caused by traffic. Traffic-induced technical seismicity principally differs from natural seismicity in frequencies higher by an order of magnitude, which propagates into the surroundings, and in frequent repetitions where the material fatigue limit may be exceeded. The frequencies of traffic-induced shocks range from 10 to 200 cycles/sec, being most often in the 30 to 150 cycles/sec range, while the amplitudes of vibrations are very small reaching several tens of micrometres at the most. Natural seismicity has oscillation frequencies approximately 100 times lower and vibration amplitudes, on the contrary, by several orders higher [1]. The acceleration of traffic-induced shocks corresponds to the values of catastrophic earthquakes with a magnitude of 10 to 12 on the Richter scale. Vibrations due to road traffic propagating through the surrounding environment into the nearby development usually range in an interval of 5 – 25 Hz. By their amplitudes, the vibrations are in the 0.005 to 2 ms² range in accelerations, and the 0.05 – 25 mm/s range in velocities. The oscillation intensity criterion is usually the **oscillation velocity**, related to the relative dynamic deformation causing damage to buildings. The dominant frequencies and vibration amplitudes of the excitation of a building depend on numerous factors: the road type and condition, vehicle mass and construction, its speed and riding manner, the composition, compactness and moisture of the subsoil, and the distance from the building. The severity of traffic-induced technical seismicity largely depends on the condition and type of the building structure. Buildings damaged by cracks with insufficient stiffness of the floor and foundation structure are more vulnerable to failure due to dynamic effects. Oscillation velocities in the 1-2mm/s range should be the criterion for the assessment of the resistance of the building structure to the effects of technical seismicity. Masonry buildings without bond beams or beam and wall anchors, buildings with yielding (e.g. beam) floors, with vaults without bowstrings and with insufficiently deep and stiff, unbonded foundations are exceptionally sensitive to seismicity-induced dynamic effects.

BASILICA OF THE ASSUMPTION OF OUR LADY IN STARÁ BOLESLAV

The Basilica of the Assumption of Our Lady in Stará Boleslav is a Roman Catholic Parish Church from the beginning of the 17th century, the oldest Marian pilgrimage site in Bohemia (Figure 1). Today's church, built in the style of Early Baroque Roman churches according to the design by the Italian architect, Giovanni Maria Filippi, in 1613 to 1625, replaced an older Gothic structure. The northern tower was completed by Abraham Leuthner in 1675, while the southern tower and the new western façade were built according to the design by Kilian Ignaz Dientzenhofer in 1748–1749. In 1728–1732, the cloister behind the eastern chevet was added, the space in front of the Basilica was landscaped and a terrace built.



Fig. 1 - Basilica of the Assumption of Our Lady

Spatial, structural and material layout

The Basilica is a single-nave, rectangular-shaped structure with side chapels with a semi-circular apse along the longitudinal axis on the east side. The church dimensions are – 22.0 m in width, 48.0 m in length including the apse, the main nave height is 22.0 m, and the nave width 13.8 m.

The main nave is covered by a brickwork barrel vault 6.9 m high with a span of 13.8 m, with reinforcing arches 1.3 m wide in a 7.9 m spacing. The vault thickness, including plaster, is approx. 0.2 m, and the interior curve of the reinforcing arches reaches 0.3 m below the interior curve of the barrel vault. The barrel vault impostes lean against perimeter masonry 1 m thick. Below the level of pilaster heads (the upper edge of the heads is 15.15 m above the church floor), the masonry extends to 1.6 m in width and is founded on the barrel vaults of side chapels, which form the cloister on both sides of the main church nave. The crown of these vaults is 12.4 m above the church floor, their depth from the interior face of the main church nave perimeter masonry to the side façade is 3.1 m, and they are supported by pillars 1.35 m in width situated in the places of reinforcing arches. The dimension of the pillars in the direction perpendicular to the longitudinal axis of the church is 4.3 m, including the 1.2 m exterior perimeter wall forming the back wall of the side chapels. There is a gallery above the level of the side chapel vaults approx. 1.5 m wide covered by a barrel vault.

The church has two towers on both sides of the presbytery, which is situated on the east side of the church nave. The presbytery is also barrel-vaulted with a smaller span (Figure 2).



Fig. 2 - Vaulted structures in the interior of Basilica

The masonry of the Basilica is made of bricks with lime mortar, foundations of the Basilica are estimated to be under the crypt floor level, which is approx. 3 m below the church floor level. The church foundations are probably situated on terrace deposits with a significant proportion of sandy fraction. The vaults are made up of brick masonry with lime mortar and the Basilica is roofed by gable roof with king post roof truss.

The Basilica is located in the city center close to the 2nd class road II/610 at a distance of 5 – 12 m (Figure 3). This former state road no. 10 was, in the past, replaced by the D10 motorway, to which it forms an accompanying road and, in the case of motorway closure, forms a bypass. At the 2016 national traffic census [2], the total traffic intensity was set at 10948 vehicles / 24 hours, of which heavy motor vehicles (trucks, buses, etc.) amounted to 1655 vehicles / 24 hours, passenger vehicles 9188 vehicles / 24 hours and two-wheeled vehicles (motorcycles) 105 vehicles / 24 hours. Compared to the previous traffic census in 2010, the increase in total traffic intensity was 132% (with 185% for heavy motor vehicles, 122% for passenger cars and 89% for two-wheelers).

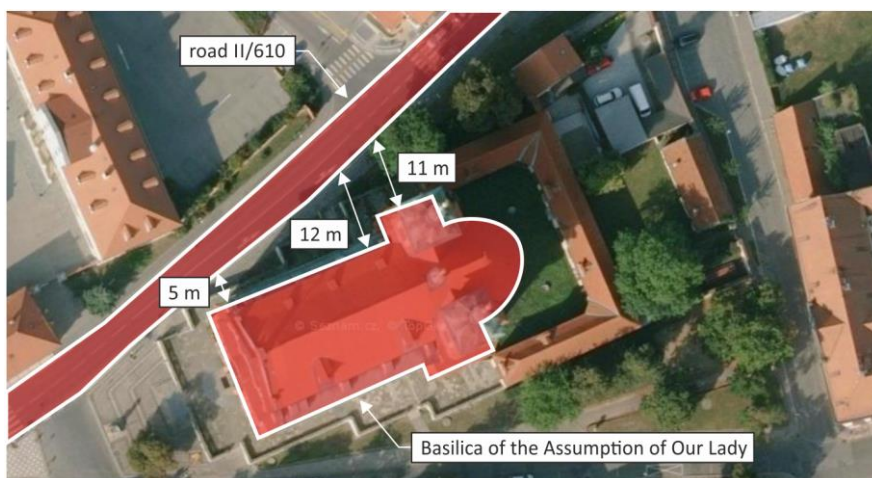


Fig. 3 - Location of the basilica by the 2nd class road No. 610

Results of a visual inspection

A preliminary (visual) survey was conducted in the Basilica aimed at the identification of the mechanical failures manifested on the surface of the load-bearing masonry, both in the interior and the exterior.

No visually observable cracks were detected in the vertical bearing walls of the perimeter and interior masonry, the masonry of the towers and the pillars. The barrel vault of the main nave and the presbytery is damaged by a longitudinal crack at the vault crown running along the entire length. It is a tensile crack up to 5 mm in width visible in the plaster on the vault face. The vault of the main nave is also damaged by cracks in the springers of barrel vault bay windows running in the same direction. The vaults of longitudinal galleries above the vaults of the main nave side chapels are damaged by cracks perpendicular to the longitudinal axis of the church and located near the main nave lunettes. The barrel vaults of the side chapels are also damaged by cracks at the crowns running in the direction perpendicular to the longitudinal axis of the church (Figure 4).

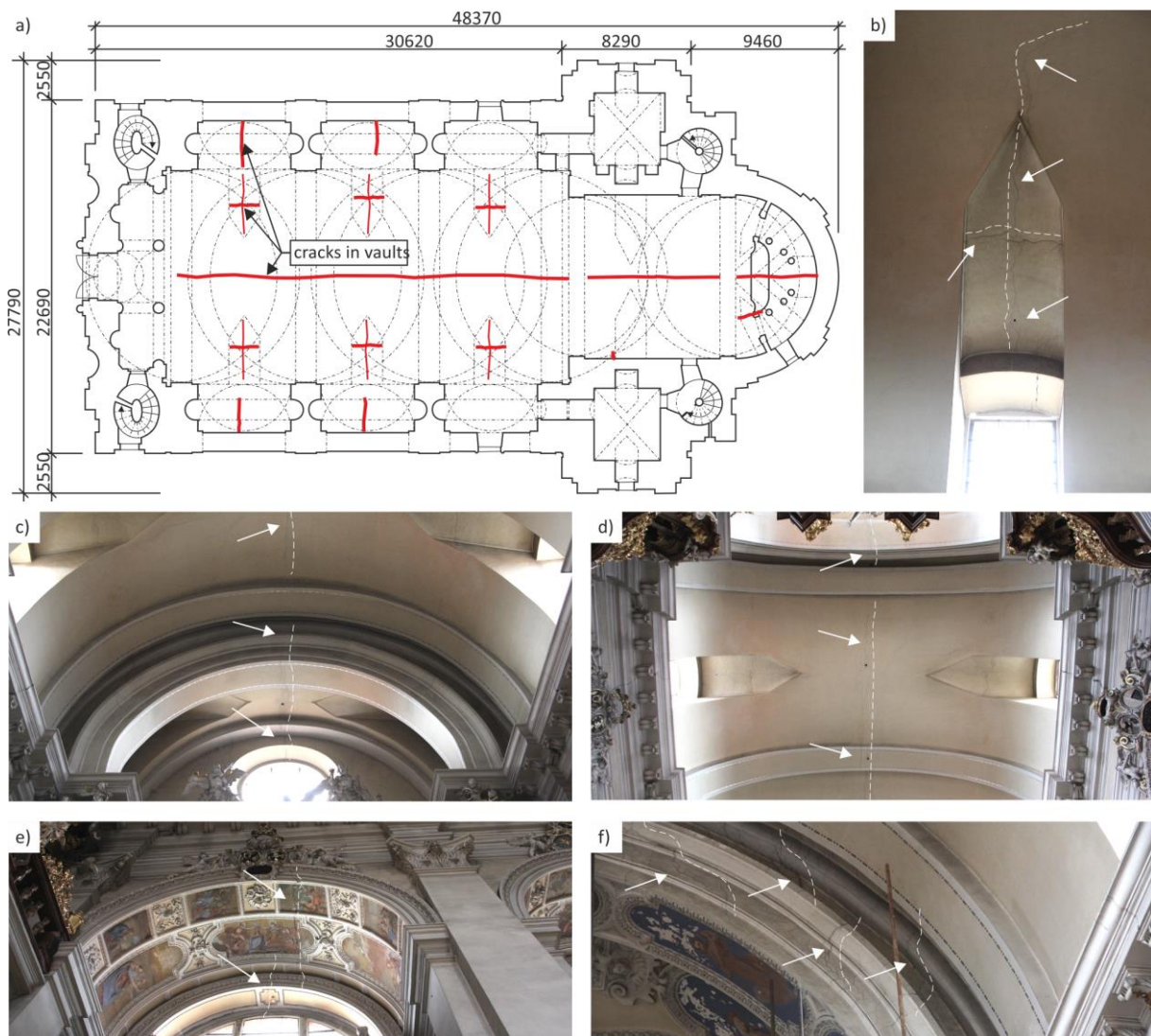


Fig. 4 - a) Scheme of the church structures' failure, b) Detail of the lunettes' failure, c) Failure of barrel vault and the arch ring at the western façade, d) Longitudinal crack in the main nave's barrel vault, e) Failure of the barrel vault of the side chapels, f) Detail of failure in arch ring footing

ANALYSIS OF THE RESULTS OF EXPERIMENTAL RESEARCH INTO A TRAFFIC-INDUCED DYNAMIC RESPONSE

The experimental measurement of the dynamic response was performed by the Institute of Theoretical and Applied Mechanics of the Czech Academy of Sciences [3]. The Wilcoxon Research accelerometers, Model 731A, with a high sensitivity of 10 V/g and a noise performance of 0.5 µg RMS were used for the measurement. The dynamic response was measured at a reference point (marked by letter R) and at another three points (Figure 5) in the X, Y, Z directions. Hourly records provided 5 to 12 second sections, which were computer-processed into the final effective oscillation velocities.

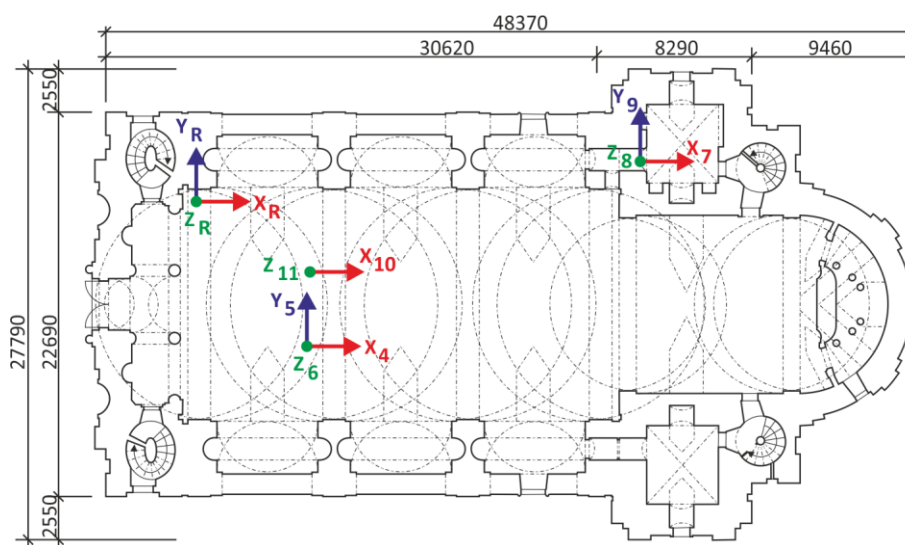


Fig. 5- Diagram of measuring points (accelerometers)

The identification of traffic-induced seismic loading is based on the analysis of the road response induced by a vehicle passing on the uneven surface of a road pavement. The response to loading by technical seismicity is usually assessed as the value of the effective oscillation velocity on the lowest storey, or in the foundation of a building – at reference points. In other parts of the structure, oscillation velocities greater than those measured at the reference point may be identified. In evaluating the propagation of technical shocks, deflections in the vertical direction w and deflections in the horizontal direction, in u and v components, are assessed. The deflection w_x decreases with the horizontal distance x from the source of seismic waves following approximately the formula valid for $x > l$:

$$w_x = w_l \left(\frac{l}{x}\right)^{1/2} \times \exp[-a - l] \quad (1)$$

where:

- w_l deflection at a distance l from the source measured on the surface of the territory;
- w_x deflection at a distance x from the source measured on the surface of the territory;
- l horizontal distance from the source in metres at the point where the deflection w_l was detected
- a absorption constant

Formula (1) was derived for Rayleigh waves and for a distance $l > 10$ m, but its indicative application for other types of waves is also possible.

The dynamic response caused by technical seismicity, except for the response to blasting operations, does not need to be further analysed in terms of the ultimate bearing capacity, unless the effective velocity of movement at the reference point exceeds the limit values for the respective resistance class (pursuant to ČSN 73 0040 [4]) and significance of a building (pursuant to ČSN EN 1991-1-7 [5]).

The analysis and evaluation of the results of the measurement of the response of the structure of the Basilica of the Assumption of Our Lady [3] are in compliance with ČSN 730040 (resistance classes of buildings) [4] and ČSN EN 1991-1-7 (classes of significance of buildings and effective velocity limits) [5].

The measured values of the effective velocity of the dynamic response (mm/s) for cases of bidirectional lorry, heavy truck, bus and tractor traffic range as follows:

vault ... (0.1199 to 0.5013) mm/s, at points ACC 6 and ACC 11

tower ... (0.3135 to 1.1947) mm/s, at points ACC 8 and ACC 9

reference point ... (0.0400 max. ref. X, 0.0481 max. ref. Y, 0.0413 max. ref. Z).

To evaluate the detected velocities of movement at the selected points the building was classified in Class CC3 in the category of significance (ČSN EN 1991-1 [5]) and in Class A in the category of resistance (ČSN 730040 [4]).

The main criterion for the evaluation of movements (shocks) under ČSN 730040 [4] is the response to loading by vibrations assessed by the effective velocity value. Pursuant to ČSN EN 1991-1-7 [5], the Basilica building can be classified in the highest class according to significance, "Class CC3", and if we choose the resistance of the building in "Class A" (ČSN 730040 [4]), the effective velocity limit value will be 0.2 mm/s.

The velocity of movement (oscillation shocks) values at the reference point do not exceed the limit values specified by ČSN 730040. However, at points ACC6, ACC11, ACC4 (on the vault) and at points in the tower, they exceed the limit values, which complies with the note under ČSN 730040 [4]: at points other than the reference point, the oscillation velocity is usually greater. In the case of the response in the tower, where the velocity is by 100% greater than the velocity at the reference point REF, it is necessary to verify the loading by a dynamic calculation using the computational model under ČSN 730040, Art. 5 [4].

The analysis of the effect of velocity on the damage rate of a building is significantly affected by the oscillation frequency. It was manifested that frequencies higher than 100 Hz (characteristic frequencies of technical seismicity), as a rule, do not cause such failures as frequencies lower than 10 Hz (characteristic frequencies of natural seismicity). This is caused by the lag of deformations behind the stresses.

SUMMARY OF THE RESULTS OF EXPERIMENTAL RESEARCH INTO A TRAFFIC-INDUCED DYNAMIC RESPONSE

In monitoring the response of a structure to loading by technical seismicity, the value of the effective oscillation velocity (RMS) on the lowest storey, or in the foundation of a building, at the so-called reference point, is usually assessed. The effective velocity values at the reference point measured in two horizontal directions X, Y and in the vertical direction Z are rather small, the traffic passages were evident, but their manifestation was insignificant. The standard also admits that in

other places of the structure, the oscillation velocities may be higher. This is the case of monitored structure, as in some places the measured values are above the limit. Based on the results of oscillation velocity measurements at selected points and the monitoring of a potential movement of the crack on the vault, we may conclude that the load-bearing structure of the church is not at risk due to traffic-induced technical seismicity on the adjacent road. After reaching a certain number of cycles in the order of magnitude larger than 10^5 , very high frequencies may cause material fatigue with a subsequent growth in deformations and permanent strain preceding major failures of the vaulted structure.

STABILISATION OF THE EXISTING STATE OF DAMAGE TO THE BASILICA STRUCTURE IN TERMS OF STATIC AND DYNAMIC LOADING

Although the experimental measurements of the effect of traffic-induced technical seismicity show that the load-bearing structure of the Basilica is not at risk due to traffic-induced technical seismicity on the adjacent road, it is recommended to take preventive measures to protect the load-bearing structure of the Basilica. It is evident from the type and pattern of cracks on the vaulted system, considering the results of the experimental measurement of the dynamic response [3], that the most likely and the main cause of the existing damage to the barrel vault and arches over the Basilica main nave, the damage to the barrel vault in the springers of bay windows and the vaults of longitudinal galleries above the vaulted spaces of chapels is insufficient absorption of horizontal forces exerted by the barrel vaults. The barrel vaults over the main nave and the adjoining vaults lack visible bowstrings, and horizontal forces – particularly the forces exerted by the effects of the barrel vault with a span of 13.8 m over the main nave – are mostly transferred by the massive structures of the supporting system. The relatively very small horizontal deformations of the supporting system in the order of magnitude of 10^{-3} of the vault span may be the cause of the appearance of tensile stresses at the vault crown, which exceed the vault masonry strength in tension and are the cause of tensile cracks. In the case that a solution with a visible bowstring system cannot be used, the following solution is recommended as the main rehabilitation measure of the existing damage to the vaults:

- execution of vault beam ties at a level above the vaults;
- execution of inclined bowstrings suspended on an additionally mounted stiff girder;
- execution of a prestressed steel strip on the outer curve of the vault made up of prestressed partial segments prestressed by a composite strip (for example according to patent application no. 2018-608 [6]).

To increase the overall efficiency of the proposed solution, it is desirable to prestress the supporting walls of the vaults in the horizontal and vertical direction by prestressed carbon lamellas, or by carbon composite strips fitted in thin horizontal grooves in the area of vault imposts on the outer side of the supporting walls and in thin vertical grooves with anchoring zones at the crown and near the footing bottom of the supporting walls.

Based on an additional survey, a modification enhancing the stiffness of the footing should be designed and executed. An inseparable part of enhancing the stability of the Basilica and preventing further crack propagation is continuous monitoring, the application of simple methods of measuring changes in crack widths and, last but not least, monitoring the quality of the road pavement surface on the adjoining road.

ACKNOWLEDGEMENTS

The article was written with support from the NAKI DG16P02M055 project “Development and Research into Materials, Procedures and Technologies for Restoration, Conservation and

Strengthening of Historic Masonry Structures and Surfaces and Systems of Preventive Care of Historic and Heritage Buildings Threatened by Anthropogenic and Natural Risks”.

REFERENCES

- [1] Witzany, J. a kol., Experimental research into dynamic characteristics of masonry segment barrel vaults, In: Proceedings of SMAR 2015, The Third Conference on Smart Monitoring, Assessment and Rehabilitation of Structures. Istanbul: ITU, 2015, pp. 1-8. ISBN 978-3-905594-65-2
- [2] National Census of Transport on the Motorway and Road Network of the Czech Republic 2016, Ředitelství silnic a dálnic ČR, 2017, available online: <http://scitani2016.rsd.cz>, cited 23-08-2019
- [3] Research report on measuring of the dynamic response in the Basilica of the Assumption of Our Lady in Stará Boleslav, Insitute of Theoretical and Applied Mechanics, CAS ČR, v. v. i., Praha, 2018
- [4] ČSN 730040 Loads on structures by technical seismicity and their response, UNMZ, 2019
- [5] ČSN EN 1991-1-7 Eurocode 1: Actions on structures - Part 1-7: General actions - Accidental actions, UNMZ, 2007
- [6] Witzany, J., Zigler, R., Equipment for securing brick barrel vaults against the effects of natural and technical seismicity, patent application no. 2018-608, Praha, 2018.

TRUSS STRUCTURE OPTIMIZATION BASED ON IMPROVED WOLF PACK ALGORITHM

Yan-cang LI¹, Zong-jin YANG², Cheng-hua Dang^{3}*

- 1. Hebei University of Engineering, College of Water Conservancy and Hydroelectric Power, No. 199 Guangmin South Street, Handan, China; liyancang@hebeu.edu.cn*
- 2. Hebei University of engineering, College of Civil Engineering, No. 199 Guangmin South Street, Handan, China; yangzongjin6781@sina.com*
- 3. * Corresponding author, Hebei University of engineering, No. 199 Guangmin South Street, Handan, China; rebecca77@163.com*

ABSTRACT

Aiming at the optimization of truss structure, a wolf pack algorithm based on chaos and improved search strategy was proposed. The mathematical model of truss optimization was constructed, and the classical truss structure was optimized. The results were compared with those of other optimization algorithms. When selecting and updating the initial position of wolves, chaos idea was used to distribute the initial value evenly in the solution space; phase factor was introduced to optimize the formula of wolf detection; information interaction between wolves is increased and the number of runs is reduced. The numerical results show that the improved wolf pack algorithm has the characteristics of fewer parameters, simple programming, easy implementation, fast convergence speed, and can quickly find the optimal solution. It is suitable for the optimization design of the section size of space truss structures.

KEYWORDS

Wolf pack algorithm, Improved wolf pack algorithm, Truss optimization, Chaos thought

INTRODUCTION

Structural optimization design is an important research direction in structural engineering. Engineers can achieve energy saving and material reduction through reasonable optimization[1]. Truss structures are widely used in engineering applications, such as transmission towers, long-span bridges, large space roofs and other structural systems. Therefore, in engineering design, it is an important research direction how to optimize the design of the structure to minimize the structural consumables on the premise of satisfying the safety, economy and reliability of the structure. In recent years, bionic intelligent algorithms have been emerging in the field of engineering structure design, such as genetic algorithm, ant colony algorithm, particle swarm optimization, cuckoo algorithm and so on[2-5]. These algorithms have effectively promoted the development of structural optimization in the research of truss structure optimization. However, there is still room for research on the convergence speed and stability of the algorithm. Wolf pack algorithm was first proposed by Yang in 2007 as a swarm intelligence optimization algorithm to simulate the characteristics of wolf hunting. After that, many scholars had studied and improved the wolf swarm algorithm[6-9]. The algorithm has good global convergence and is especially suitable for solving high-dimensional and multi-peak complex functions. Because of its strong

robustness, wolf pack algorithm has been applied in many fields, such as multi-area power generation control, job shop scheduling, disease treatment, TSP problem, etc. [10-15]. But the algorithm also has some shortcomings such as easy to fall into local optimum.

On the basis of previous studies, wolf pack algorithm is improved by introducing chaos strategy and reverse learning strategy into initialization and wolf swarm updating, so that prey can be distributed as evenly as possible in solution space. And the search flexibility of wolf-hunting is enhanced by changing the formula of wolf-hunting. The information exchange between the wolves is increased through the method that the wolves understand the overall information in the course of the attack, so as to avoid falling into local extremes. The improved algorithm was applied to the truss simulation experiment and compared with other algorithms, which verifies the effectiveness of the improved wolf pack algorithm.

IMPROVED WOLF PACK ALGORITHM

It is found that wolves are tightly organized in hunting, with a clear division of labour and concerted efforts to catch prey. Wolves first sent a small number of strong wolves to search for odour within a certain range, and the strong-smelling wolves called their companions to attack and surround their prey by howling. Finally, they distributed food through the principle of survival of the fittest. Wolf swarm algorithm is proposed based on the predatory behaviour of wolves mentioned above. It is intended to simulate the optimization of processing function of wolves' predatory behaviour. However, there are also some shortcomings in the basic wolf pack algorithm, such as precocity, incomplete migration mode of detective wolves, and lack of information exchange in the running process, which may lead to the embarrassing situation of local optimization.

Initialization and update selection of wolves

In the basic wolf pack algorithm, the generation criterion is to find the wolf with the best fitness value as the wolf in the search space. The basic wolf pack algorithm does not initialize the location of the wolf swarm, which will lead to the uneven individual wolf swarm. We combines reverse learning and chaos optimization idea to design reverse chaos update strategy[16].

(1) Two one-dimensional chaotic mapping equations, Sinusoidal iterator and Gauss map, are used to generate D chaotic sequences of length H with equal probability. $AX=(ax_1, ax_2, \dots, ax_D)$, $ax_d=(ax_{1d}, ax_{2d}, \dots, ax_{Hd})^T$, $d=1, 2, \dots, D$. H is defined as the number of artificial wolves that need to be updated or initialized. The following expressions are one-dimensional mapping expressions of Sinusoidal iterator and Gauss map, respectively.

$$x_{k+1} = b \cdot x_k \sin(\pi x_k), x_k \in (0, 1) \quad (1)$$

$$x_{k+1} = \begin{cases} 0, & x_k = 0 \\ 1/x_k - [1 - x_k], & x_k \in (0, 1) \end{cases} \quad (2)$$

(2) According to the following formula, chaotic sequences are mapped into solution space to initialize or update wolves: $X=\{x_1, x_2, \dots, x_H\}^T$

$$x_{id} = \lambda ax_{id}(1 - x_{id}) \quad \lambda = 3 \quad (3)$$

(3) According to the following formula, the reverse wolf pack of wolves is obtained: $OX=\{ox_1, ox_2, \dots, ox_H\}^T$

$$ox_{id} = s \cdot (\min_d + \max_d) - x_{id} \quad (4)$$

Where: \min_d is the lower limit of the d-dimensional solution space; \max_d is the upper limit of the d-dimensional solution space; s is a random number between 0 and 1.

(4) The objective function values of X and OX were calculated, and H artificial wolf with the largest objective function value was selected as the initialization or update artificial wolf.

Improvement of Walking Behaviour

Choose the best m wolves besides the head wolf as the head wolf, search in the predefined direction, and retain the better prey. Once the better prey than the current head wolf is found, the head wolf with the prey becomes the head wolf. This process is called the head wolf wandering behaviour. The purpose of roaming behaviour is to explore the solution space comprehensively and search for new candidate solutions. However, the basic roaming behaviour lacks guidance. Once the number of search directions is determined, the roaming direction will be determined, and the solution space cannot be searched comprehensively, which easily leads to the algorithm falling into local optimization[14]. For this reason, the new formula is obtained by introducing the phase factor as follows:

$$x_{id}^p = x_{id} + (1/z_{max}) \cdot \sin(2\pi \cdot p/h + \theta) \cdot step_a^d \quad (5)$$

Where z is the number of iterations, $z=1,2,\dots,z_{max}$; $\theta \in (0, p/h)$; $h=6$. The design of $(1/z_{max})$ embodies the asymptotic idea of "from coarse to fine" of wolf searching, and the introduction of phase factor improves the flexibility, randomness and ergodicity of wolf searching. In addition, the introduction of wolf detection update rules and the design of "from coarse to fine" wandering mechanism. The basic idea is as follows: if the function value of H direction is less than the objective function value of wolf i , there will probably be a maximum value around wolf i . At this time, shorten the search distance (walking step) and search the surrounding h direction again. If the function value of H direction is still less than the objective function value of wolf i , the search distance will continue to be shortened. After several times of shortening the search distance, the function values of H directions around the wolf are still smaller than the objective function values of the wolf i . It can be considered that the wolf i falls into the local optimal position. At this time, the wolf i needs to restart its initial position and then perform the walking behaviour. The design idea further embodies the asymptotic idea of wolf swarm algorithm from coarse to fine.

Improvement of Running Behaviour

The wolf howls to inform the surrounding fierce wolves to quickly approach the wolf and search for high-quality prey. If the wolf finds better prey than the wolf, the wolf howls again instead of the wolf until the wolf stops at a certain distance from the prey. This process is called rush behaviour. In the $k+1$ iteration of the wolf i , the position in the d -dimensional variable space is:

$$x_{id}^{k+1} = x_{id}^k + step_b^d \cdot (g_d^k - x_{id}^k) \div |g_d^k - x_{id}^k| \quad (6)$$

where, g_d^k is the position of the K generation group of wolves in the d -dimensional space. In the course of the attack, the lack of necessary information exchange between the wolves and the lack of timely understanding of the "companion" information limit the search ability in the attack. Interaction among individuals in intelligent algorithms helps to enhance the optimization ability and the ability to jump out of local extremum. In order to increase the interaction between wolves, this paper uses the following search methods, as shown in Formula (7).

$$x_{id} = x_{id} + v_{id}(x_{best,d} - x_{id}) + \tau_{id}(x_{jd} - x_{kd}) \quad (7)$$

Where, v_{id} is the random number in $[0,1]$; τ_{id} is the random number in $[-1,1]$; $k \neq j$; $x_{best,d}$ is the dimension coordinate of the current optimal solution. The first half of Formula (7) enhances the local search ability of the algorithm, and the second half of it enhances the global search ability of the algorithm. It balances the exploiting ability and exploring ability of the roaming behavior well. It

not only embodies the leadership ability of the wolf, but also maintains the exchange of information between wolves and improves the diversity of the population.

In swarm algorithm, no matter what stage of search, the communication between groups is an important link. Therefore, after each round (6) is executed, the one-time (7) interactive search process is carried out to select the most odorous prey which is larger than the current position odour concentration Y_i , and to move forward a step, update the position X of the wolf. Wolves with the highest odour concentration in wolves are currently selected as the first wolf.

The specific rules of interactive attack are as follows:

- (1) The head wolf initiates the summoning behaviour and calls the surrounding fierce wolves to approach the head wolf position quickly. According to formula (6), the wolf carries out a rush once to get the position of the new prey after the rush.
- (2) Random selection of fierce wolves k, j , according to formula (7) for an interaction, get new prey after interaction, so far, fierce wolf i rushed to search for a total of two prey;
- (3) By comparing the odour concentration of the two new prey and the original location of the fierce wolf, fierce wolf i made a step towards the direction with the strongest smell of the three.
- (4) A comparison was made between the fierce wolf with the maximum concentration of prey odour and the lead of the wolf. If $Y_i > Y_{lead}$, fierce wolf i replaced the lead wolf as the new lead wolf and initiated the summoning behaviour again. Otherwise, the head wolf remained in the same position and entered the wolf siege behaviour.

By increasing fierce wolf information interaction between, better let the fierce wolf on the impact on the way to understand the global information, avoid falling into local extremum, reduce the number of attacks, simplify the complexity of the algorithm. Through the analysis, the basic behaviour fired fine search, but easy to fall into local optimization, algorithm premature convergence, and constantly tumbling makes the algorithm complexity, robustness is not stable, and the running time is too long, unfavourable to better solve the problem of real-time. It appear that that primary attacking behaviour is not finis, but after the interaction has been added, the algorithm has global direction, the local optimal is better, and the global convergence speed is accelerate.

The standard wolf pack algorithm is an algorithm proposed to solve the continuity problem. Considering that the truss structure is optimized as a discrete problem, a binary wolf pack algorithm is introduced[17]. The position X_i of artificial wolf i is represented as binary encoding $(x_{i1}, x_{i2}, \dots, x_{ij}, \dots, x_{im}) (i = 1, 2, \dots, N, j = 1, 2, \dots, m)$; N is the total number of artificial wolves; M is the encoding length. x_{ij} is the value of the number j for position X_i and can only be 0 or 1. The distance between p and q of two artificial wolves is defined as the binary encoded Manhattan distance between them, as shown below:

$$L(p, q) = \sum_{j=1}^m |x_{pj} - x_{qj}|, p, q \in \{1, 2, \dots, N\} \quad (8)$$

$\Gamma(X_i, M, r)$ is defined as the motion operator, which represents the moving position of the artificial wolf. M is the set of inverted coding bits and is not empty, which can be understood as the range of activity of the artificial wolf. r represents the number of coding bits to invert, which can be understood as the walking step of the artificial wolf. For example: $X_i = \{0, 0, 1, 0, 0, 1\}$, $M = 3$, $r = 1$, so, $\Gamma(X_i, M, r) = \{1, 0, 1, 1, 0, 0\}$. The modified Wolf pack algorithm formula is replaced by the corresponding binary formula, which can be used in truss structure optimization.

Improve the basic flow chart and flow chart of the Wolf pack algorithm

The basic flow of the improved Wolf pack algorithm is as follows (taking solving the maximum value as an example) :

Step1: initialize. Initialise that number N of artificial wolf, the maximum number of iterations k_{max} , the maximum number of walk T_{max} , the distance determination factor ω , the step factor S , updating the scale factor β , and initializing the spatial position X of the wolf by the inverse double chaos updating strategy;

Step2: walk behaviour. The artificial wolf with the largest value of the objective function was selected as the head wolf, and the other artificial wolves were regarded as the detective wolves and walked away according to equation (5) (During the exploration of wolf i wandering, if the function values of h directions around exploration of wolf i are all smaller than the target function values of exploration of wolf i , $step_a$, the wandering step length, is halved. If the exploration of wolf i is still unable to move forward after repeated halving of the wandering step length, it is considered that exploration of wolf i is trapped in local optimum, and the spatial location of exploration of wolf should be updated with the reverse double-chaos updating strategy), until the target function value Y_i of detective wolf i , which is greater than the target function value Y_{lead} or the wandering number of detective wolf, reaches the maximum wandering number T_{max} , and is transferred to **step3**

Step3: summon behaviour. The first wolf calls upon the surrounding fierce wolves to quickly approach the position of the first wolf. According to formula (6), the fierce wolf runs once to obtain the position of the new prey after the attack. The fierce wolves k, j were randomly selected, and an interaction was conducted according to equation (7) to obtain the new prey V_i after interaction. Thus, fierce wolf i ran and found two prey in total. Comparing the odour concentration of the two new prey and the original location of the fierce wolf, fierce wolf i made a step towards the direction with the strongest smell of the three. Compare the fierce wolf i , which has the maximum concentration of prey odour, with the concentration of head wolf. If $Y_i > Y_{lead}$, fierce wolf i becomes the new head wolf instead of head wolf and starts the summoning behaviour again.

Step4: act of siege. The head of the wolf position as the moving position of the prey, the fierce wolves involved in the siege by the formula of the prey siege;

$$x_{id}^{k+1} = x_{id}^k + \lambda \cdot step_b^d \cdot |g_d^k - x_{id}^k| \quad (9)$$

Where, λ is the random number with uniform distribution between $[-1, 1]$; $Step_c$ is the attack step size of wolf i during siege.

Step5: wolf pack update. The objective function of the optimal wolf generated in this iteration is compared with the objective function value of the head wolf in the last iteration. If it is larger, the position of the head Wolf is updated. Otherwise, the first wolf is recorded with no update times t . Determine the number of artificial wolves with smaller values of the elimination objective function R , $R \in (N/2 \cdot \beta, N/\beta)$ based on the updated proportional factor. If t is less than the limit value t_{max} , then the wolf pack is updated according to equation (10) and combined with reverse learning. On the contrary, the wolves will be updated according to the reverse double-chaos strategy.

$$x_{id} = g_d \cdot [2 - \cos(\psi)] \quad \psi \in (-0.1, 0.1) \quad (10)$$

Step6: judge termination. Judge whether the target function value of head wolf meets the calculation accuracy requirement, or whether the algorithm reaches the maximum iteration number k_{max} . If so, output the location of head wolf and the target function value, otherwise turn to **Step2**.

The flow chart of the improved wolf pack algorithm is shown in Figure 1.

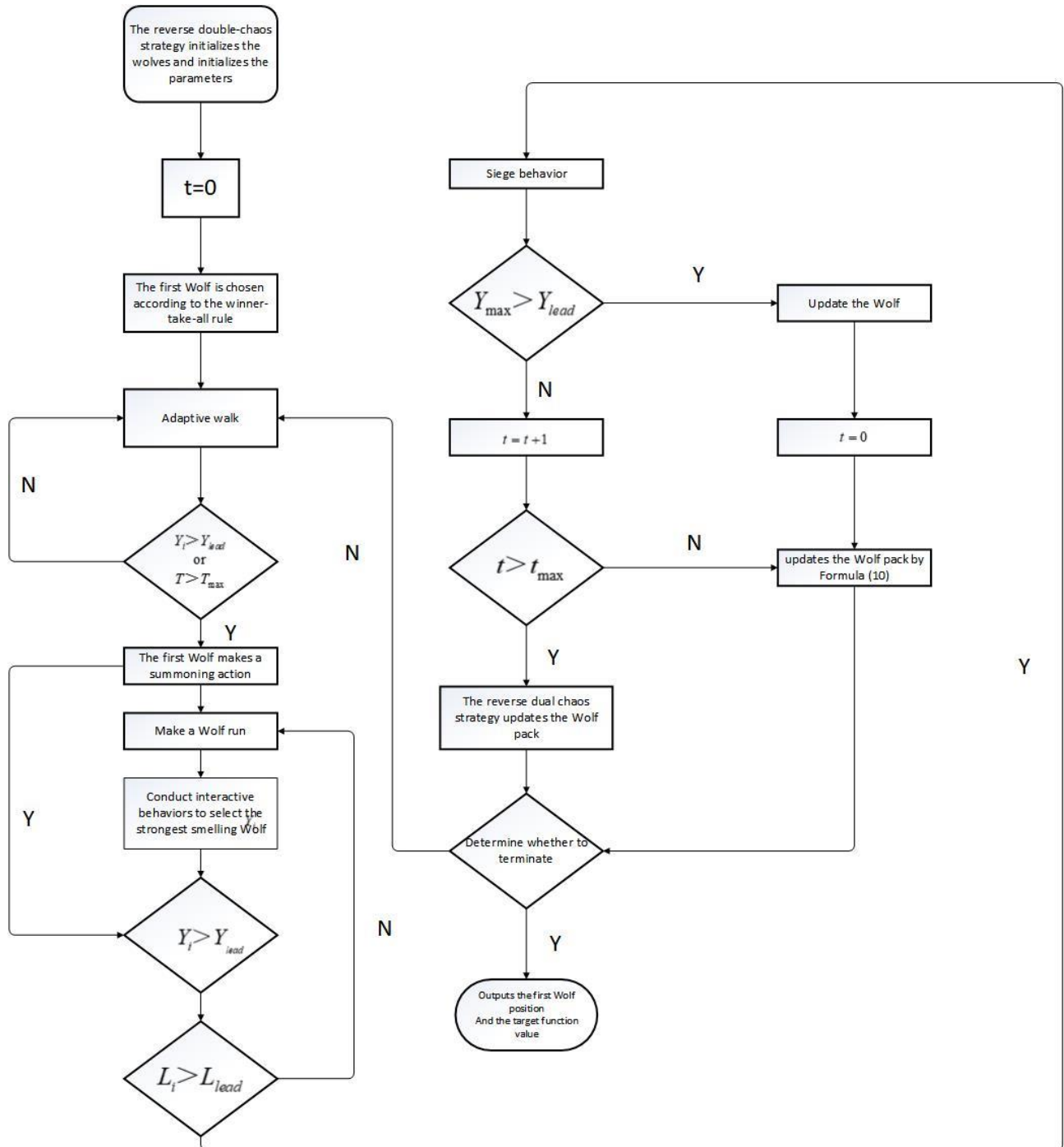


Fig.1 – Flow chart of improved WPA

EXAMPLE ANALYSIS

In industrial production, the cross-sectional area of truss structure members is generally standardized, that is, the cross-sectional area is selected from a given set of discrete real Numbers. Due to different conditions and different requirements, truss structure optimization can have multiple optimization objectives, such as minimum total mass of the structure, minimum displacement of designated nodes, maximum natural frequency, etc. [18]. In this paper, the optimal

cross sectional area of the truss and the minimum mass of the truss and the minimum joint displacement are found under the stress constraint condition of the truss. Taking the n-bar truss structure system as the research object, the basic parameters of the system are known (Including elastic modulus, material density, maximum allowable stress, maximum allowable displacement, etc) . Under the given load conditions, the optimal section area of the n - bar truss is found to minimize the mass.

10-bar plane truss

Figure 2 shows the 10-bar spatial truss structure model with the known material density $\rho = 2768 \text{ kg/m}^3$, the elastic modulus $E = 68950 \text{ MPa}$, the stress constraint is $[-172.4, 172.4] \text{ MPa}$, $L = 9144 \text{ mm}$, the downward load $p = 444.5 \text{ KN}$ concentrated force at nos. 2 and 4, and the downward displacement constraint of movable nodes is 50.8 mm . The truss has 6 joints and 10 design variables and is made of aluminium. The control parameters of the algorithm are set as: the maximum number of iterations is 500; Search space dimension 10. The node loads are shown in Table 1.

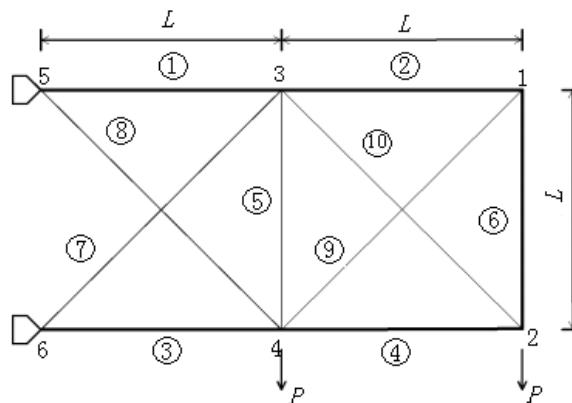


Fig.2 – Schematic diagram of the 10-bar space truss structure

Tab.1 - Design area of cross section of ten bar trusses

number	1	2	3	4	5
area	0.645	3.225	6.450	12.90	19.35
number	6	7	8	9	10
area	25.80	32.25	38.70	41.93	45.15
number	11	12	13	14	15
area	48.38	51.60	54.83	58.05	61.28
number	16	17	18	19	20
area	64.50	70.95	77.40	83.85	90.30
number	21	22	23	24	25
area	96.75	103.2	109.7	116.1	122.6
number	26	27	28	29	30
area	129.0	135.5	141.9	148.4	154.8
number	31	32	33	34	35
area	161.3	167.7	173.1	183.2	190.5
number	36	37	38	39	40
area	195.8	202.0	207.6	211.2	216.8

The optimized results are shown in Table 2.

Tab. 2 - The results of truss optimization of ten pole

Serial number	Section area of member (cm ²)		
	IACO [19]	IPSO[20]	IWPA
1	210.76	196.92	198.25
2	0.64	0.64	0.66
3	147.97	149.79	146.85
4	98.47	97.91	97.03
5	0.64	0.64	0.62
6	3.39	3.55	3.01
7	128.91	135.58	135.69
8	49.70	48.07	48.37
9	0.65	0.64	0.63
10	138.41	139.18	136.94
The total weight of the structure (kg)	2299.69	2295.50	2283.68

From the above Table 2, we can conclude that, in the same conditions of constraints, the algorithm with the improved wolves of the 10 bar truss structure has been optimized design, the optimized the structure of the total mass of 2283.68 kg, compared with the improved particle swarm algorithm quality reduced 0.70%, the quality reduced 0.52% compared with the improved genetic algorithm, the optimization results better improved. The optimal iteration curves of the three algorithms are shown in Figure 3.

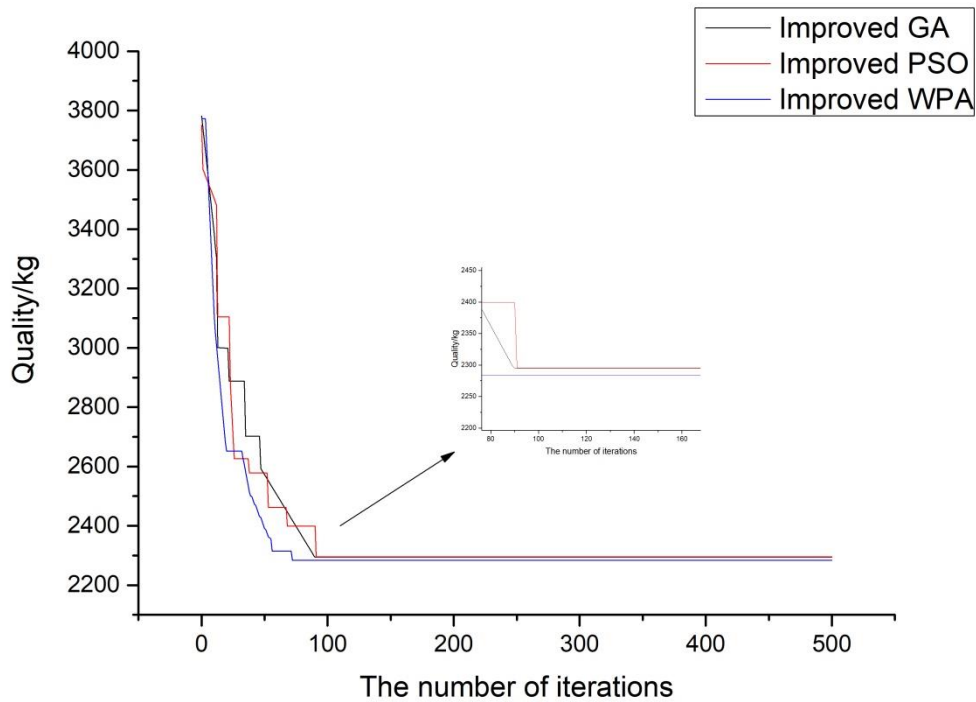


Fig.3 – Three algorithms optimization iteration curve

As can be seen from Figure 3, the improved wolf pack algorithm can search for the global optimal solution, which has higher convergence accuracy and speed than the improved genetic algorithm and the improved particle swarm optimization algorithm, with obvious effect. This is due to the use of chaos during the initialization so that the wolves as much as possible to traverse the solution space in all states, to avoid early into early maturity. By introducing the phase factor, the hunting wolf walk formula is optimized and the hunting flexibility is improved. The interactive behaviour is added to make the algorithm have global guidance, better jump out of the local optimal, accelerate the global convergence speed, and improve the global optimization ability.

72 bar space truss

Figure 4 shows the 72 bar space truss structure, which takes into account two load conditions, as shown in Table 3. The 72 bars in the structure are divided into 16 groups according to the stress of the bars, and the specific groups of the bars are shown in Table 4. Bar all use the same materials, the material density of $\rho = 2678 \text{ kg/m}^3$, the elastic modulus $E = 68950 \text{ MPa}$, bar in every direction of each connection point of the maximal displacement change interval for $\pm 6.35 \text{ mm}$, limit allowable stress range is $[-172.375, 172.375]$, the optimized results as shown in Table 5.

Tab.3 - Load cases of the 72-bar spatial truss structure

node	Condition 1			condition 2		
	F_x	F_y	F_z	F_x	F_y	F_z
1	22250	22250	-22250	0	0	-22250
2				0	0	-22250
3				0	0	-22250
4				0	0	-22250

Note: the data unit in the table is (kN).

Tab.4 - The grouping of the 72-bar spatial truss structure

Group number	Bar code	Group number	Bar code
A_1	1,2,3,4	A_9	37,38,39,40
A_2	5,6,7,8,9,10,11,12	A_{10}	41,42,43,44,45,46,47,48
A_3	13,14,15,16	A_{11}	49,50,51,52
A_4	17,18	A_{12}	53,54
A_5	19,20,21,22	A_{13}	55,56,57,58
A_6	23,24,25,26,27,28,29,30	A_{14}	59,60,61,62,63,64,65,66
A_7	31,32,33,34	A_{15}	67,68,69,70
A_8	35,36	A_{16}	71,72

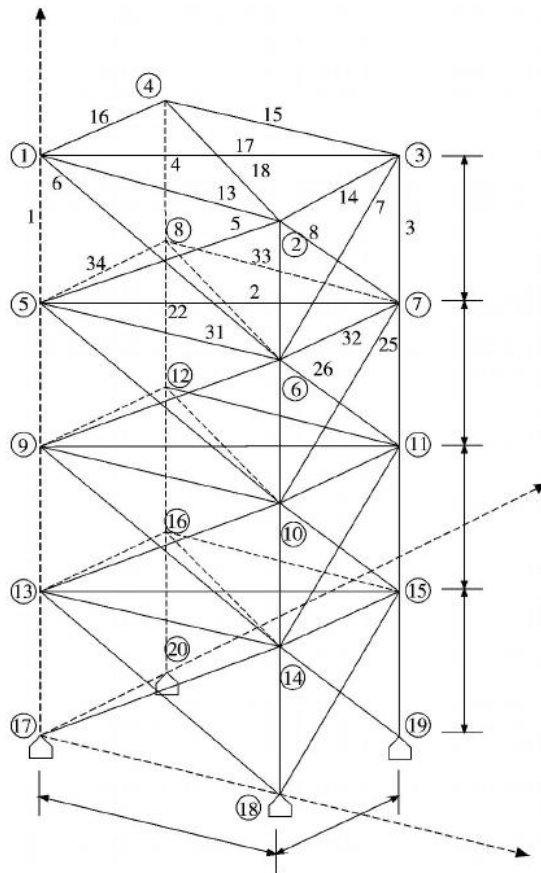


Fig.4 – structure diagram of the 72-bar spatial truss

Tab.5 - Comparison of optimal designs for the 72-bar spatial truss structure

Bar grouping number	IPSO [20]	IGA[21]	IWPA
1	100.74	102.257	101.334
2	360.28	372.965	345.552
3	269.20	220.268	264.254
4	367.69	391.997	367.293
5	342.92	170.513	326.915
6	336.70	353.458	335.484
7	64.516	64.516	64.514
8	64.516	64.516	64.517
9	870.23	713.977	825.875
10	318.26	373.811	332.126
11	64.516	64.516	64.536
12	64.516	64.516	64.514
13	1188.0	1330.019	1224.055
14	325.44	324.878	332.776
15	64.516	64.516	64.518
16	64.516	64.516	64.513
The total weight of the structure (kg)	172.44	173.26	172.20

Note: the weight unit of the data in the table is (kg), and the cross-sectional area unit of the bar is (mm²).

According to Table 5 of the optimization results, the total weight of the 72 bar truss structure was changed to 172.36kg after the improvement of the Wolf pack algorithm. IWPA algorithm further reduced the self-weight of the truss structure by 0.14% compared with IPSO algorithm. Compared with IGA, the mass is reduced by 0.62%, so the improved drosophila optimization algorithm has certain advantages in the final optimization results.

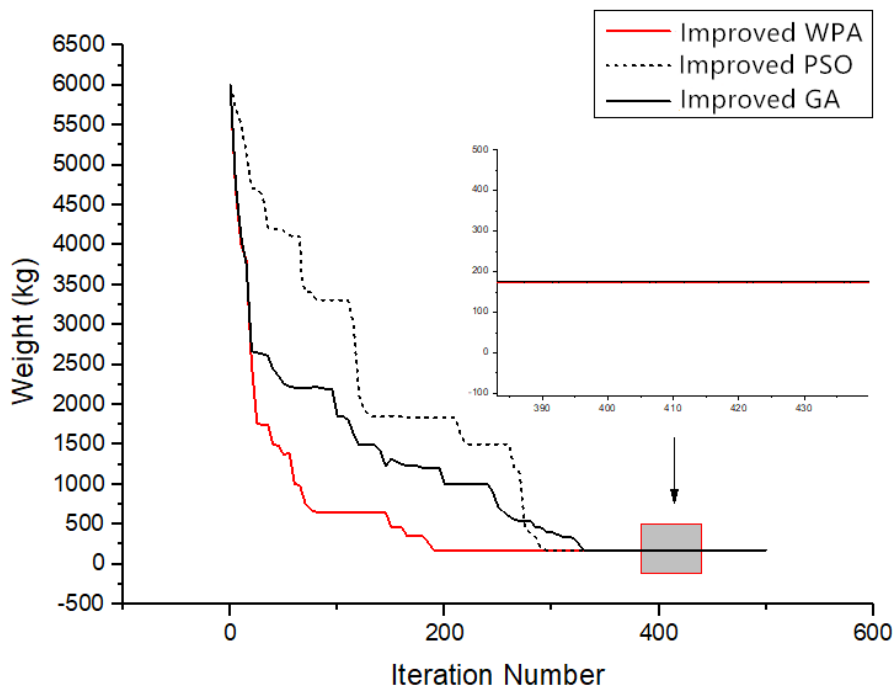


Fig.5 - Iterative curve diagram of improved WPA

It can be seen from the iterative graph 5 that the improved WPA we proposed is superior to the comparison algorithm in both the convergence speed and the final global optimal solution. The global optimal solution can be found after about 200 iterations, and the optimization efficiency is also superior to the comparison algorithm, and the optimization process is relatively stable.

CONCLUSION

- (1) Structural optimization design is very important for the truss structural engineering. In recent years, with the concerted efforts of many scholars, the artificial intelligent algorithms have been successfully applied in the field of engineering structure design. But, for the efficiency of the algorithms, we still have a long way to go.
- (2) Aiming at providing a new method for the optimization of truss structure, an improved wolf pack algorithm based on chaos and improved search strategy was proposed. The improved wolf pack algorithm is applied to the optimization design of truss structure. The example verifies that the improved wolf pack algorithm has good stability, high optimization efficiency and fast convergence speed. The example of truss optimization shows that the improved algorithm can be successfully applied to the section optimization of truss structure.
- (3) Only the initialization of the wolf algorithm, the exploring wolf walk formula and the running way are improved, and the values of the wolf algorithm's wolf pack size, the siege algorithm threshold and other parameters need to be further studied. Future work will apply the improved algorithm to other fields, such as radar imaging.
- (4) The results on the example cases show that reducing of weight is not so large (less than 1 %). Companies are looking for ways to save costs of course, but design of the truss structures

from many different cross-sections are not the best solution. This should be taken into account in the future work.

ACKNOWLEDGEMENTS

This work was supported by the Project of Scientific Research Program of Colleges and Universities in Hebei Province (No. ZD 2019114) and the Fund of Hebei Engineering Technology Research Centre for Water Resources High Efficiency Utilization.

REFERENCES

- [1] Mathias S. Jørgensen, Uffe F. Larsen, Karsten W. Jacobsen, et al., 2018. Exploration Versus Exploitation in Global Atomistic Structure Optimization. *Journal of Physical Chemistry A*, vol. 122, no. 5: 1504-1509.
- [2] Pirmohammad S, Marzdashti S E., 2018. Crashworthiness Optimization of Combined Straight-tapered Tubes Using Genetic Algorithm and Neural Networks. *Thin-Walled Structures*, vol. 127: 318-332.
- [3] Imran M M, Mazhar F, Ahmad R., 2016. Multivariate Optimization of Fiber Reinforced Laminate Using Ant Colony Optimization Algorithm. *Materials Science Forum*, vol. 867: 116-120.
- [4] El-Shorbagy, M.A, Hassanien A E., 2018. Particle Swarm Optimization from Theory to Applications. *International Journal of Rough Sets and Data Analysis*, vol. 5, no. 2: 1-24.
- [5] Nguyen T T , Vo D N ., 2018. The Application of an Effective Cuckoo Search Algorithm for Optimal Scheduling of Hydrothermal System Considering Transmission Constraints. *Neural Computing & Applications*, vol. 9: 1-22.
- [6] Yang Chenguang, Tu Xuyan, Chen Jie., 2007. Algorithm of Marriage in Honey Bees Optimization Based on the Wolf Pack Search. *International Conference of the International Conference on Intelligent Pervasive Computing*, 462-467.
- [7] Rui Tang, Simon Fong, Xin She Yang, et al., 2012. Wolf Search Algorithm With Ephemeral Memory. *Seventh International Conference on Digital Information Management*, 165-172.
- [8] Simon Fong, Suash Deb, XinShe Yang, et al., 2015 A Heuristic Optimization Method Inspired by Wolf Preying Behavior. *Neural Computing & Applications*, vol. 26, no. 7: 1725-1738.
- [9] Wu Husheng, Zhang Fengming, Wu Lushan., 2013. New Swarm Intelligence Algorithm-wolf Pack Algorithm. *Systems Engineering and Electronics.*, vol. 35, no. 11: 2430-2438.
- [10] Komaki G M, Kayvanfar V., 2015. Grey Wolf Optimizer Algorithm for the Two-stage Assembly Flow Shop Scheduling Problem with Release Time. *Journal of Computational Science*, vol. 8: 109-120.
- [11] Mirjalili S, Saremi S, Mirjalili S M, et al., 2016. Multi-objective Grey Wolf Optimizer: A novel Algorithm for Multi-criterion Optimization. *Expert Systems with Applications*, vol. 47: 106-119.
- [12] Sharma Y, Saikia L C., 2015. Automatic Generation Control of a Multi-area ST – Thermal Power System Using Grey Wolf Optimizer Algorithm Based Classical Controllers. *International Journal of Electrical Power and Energy Systems*, vol. 73: 853-862.
- [13] Radu Emil Precup, Radu Codrut David, Emil M Petriu., 2016. Grey Wolf Optimizer Algorithm-Based Tuning of Fuzzy Control Systems With Reduced Parametric Sensitivity. *IEEE Transactions on Industrial Electronics*, vol. 64, no.1: 527-534.
- [14] Shubham G, Kusum D., 2018. Cauchy Grey Wolf Optimiser for Continuous Optimisation Problems. *Journal of Experimental and Theoretical Artificial Intelligence*, vol. 30, no. 6: 1051-1075.
- [15] Shankar Chakraborty, Ankan Mitra., 2018 Parametric Optimization of Abrasive Water-jet Machining Processes Using Grey Wolf Optimizer. *Materials and Manufacturing Processes*, vol. 33, no.13: 1-12.

- [16] Goulianas K, Margaritis A, Refanidis I, et al., 2018. Solving Polynomial Systems Using a Fast Adaptive Back Propagation-type Neural Network Algorithm. *European Journal of Applied Mathematics*, vol.29, no. 2: 301-337.
- [17] Wu Husheng, Zhang Fengming, Li Hao, et al., 2015. Discrete Wolf Pack Algorithm for Traveling Salesman Problem. *Control and Decision*, 30(10): 136-142.
- [18] Lu Dai, Fuling Guan, James K.Guest., 2014. Structural Optimization and Model Fabrication of a Double-Ring Deployable Antenna Truss. *Acta Astronautica*, vol. 94, no. 2: 843-851.
- [19] Kaveh A, Azar B F, Hadidi A, et al., 2010. Performance-based Seismic Design of Steel Frames Using Ant Colony Optimization. *Steel Construction*, vol. 66, no. 4: 566-574.
- [20] Teke T, Pekcan O., 2013. A Bat-inspired Algorithm for Structural Optimization. *Computers & Structures*, vol. 128, no. 128:77-90.
- [21] Assimi H, Jamali A, Nariman-Zadeh N., 2018. Multi-objective Sizing and Topology Optimization of Truss Structures Using Genetic Programming Based on a New Adaptive Mutant Operator. *Neural Computing & Applications*, vol. 23–24: 1-21.

EVALUATION OF MASONRY GROUTING EFFECTIVENESS USING THERMOGRAPHY AND ULTRASONIC METHODS

Radek Zigler

*Czech Technical University of Prague, Faculty of Civil Engineering,
Department of Building Structures, Prague, Thákurova 7, Czech Republic;
zigler@fsv.cvut.cz*

ABSTRACT

One of the frequently used methods of stabilization and reinforcement of historic masonry is grouting, especially grouting of cracks and voids in masonry structures. Determination of the properties of the injected structure, both in terms of physico-mechanical properties (with regard to the subsequent compatibility of the grouting mixture) and in terms of its condition and failures (cracks, voids, cavities), is a prerequisite for correct design and realization of reinforcement grouting. Minimization of interventions into the historic structure while performing surveys and the associated use of non-destructive diagnostic methods is one of the requirements for the remediation of listed buildings. Within the experimental research of reinforcement of historic masonry structures, the possibility of using thermography and ultrasound methods was evaluated and conditions and limitations for the use of these non-destructive methods were formulated.

KEYWORDS

Masonry grouting, Non-destructive testing, Ultrasound, Thermography

INTRODUCTION

Grouting of historic masonry structures is one of the frequently used methods of stabilization of damaged masonry. Reliable penetration of the grouting material into the masonry structure is a prerequisite for ensuring the desired reinforcement (stabilization) effect. However, it is very difficult to verify the rate of penetration of the grouting mixture into the masonry. Use of core samples and subsequent laboratory determination of chemical composition or total porosity to prove the presence of the grouting mixture is time-consuming and costly, but above all it is an intervention (albeit limited) into the historic structure. As such, it may not be, especially in case of buildings with heritage protection, possible.

The analysis of results of experimental research carried out within the project DG16P02M055 [1] showed the need for verification of the penetration of the grouting mixture into the masonry structures. Within this research, the possibilities of using two selected non-destructive diagnostic methods (NDT) for determination of the rate of injection of masonry structures were evaluated. Namely the method based on the infrared thermographic analysis of the temperature field on the surface of the injected structure (IRT) and the method based on the measurement of the velocity of the ultrasonic signal passing through the grouted structure (UST) were verified.

Among the various non-destructive diagnostic methods, acoustic methods (both ultrasonic - UST and sonic - ST) are often used to determine the internal layout of building structures, including structures being grouted [2]. Knowledge of the individual masonry components, the state of their failure by cracks and the percentage, size and distribution of voids or cavities are essential for the proper design and execution of reinforcing grouting [3-7]. Ultrasonic methods are also often used in

laboratory verification of penetration of grouting mixtures into masonry structures (especially in the research of stabilization of multi-leaf masonry) [3, 7-10].

EXPERIMENTAL RESEARCH

Experimental research was carried out on test specimens consisting of stone blocks of approx. 250 x 250 x 250 mm of two types of sandstone (coarse-grained - Hořice quarry and fine-grained - Božanov quarry), marlstones and limestone, and mortar blocks of approx. 250 x 250 x 250 mm made of mortar 1: 3 and mortar 1: 5 (ratio of 5 years of slaked lime and sand fraction 0-4 mm). Nine test specimens were prepared from each material. One specimen was a reference (ungROUTED), the other specimens were grouted in pairs (Figure 1, Table 1). In the middle of the upper wall, a grouting borehole \varnothing 18 mm ending 50 mm in front of the opposite side (borehole length 200 mm) was made. Grouting boreholes in experimental specimens designed for pressure grouting were equipped with grouting packers.

Grouting mixtures used for the experimental verification of the injectability can be divided into two groups according to the main base:

- **BV3** - mixture based on hydraulic lime and mineral admixtures without cement, resistant to sulphates, with very low modulus of elasticity, low viscosity and good fluidity, mechanical characteristics at 28 days: bending strength of ca 3.3 N/mm², compressive strength of ca 16 N/mm², dynamic modulus of elasticity of 9.6 kN/mm².
- **BV7** - mixture based on hydraulic lime and nanosuspension of calcium acetate $\text{Ca}(\text{OCOCH}_3)_2 \cdot \text{H}_2\text{O}$ and magnesium acetate $\text{Mg}(\text{OCOCH}_3)_2 \cdot 4\text{H}_2\text{O}$, which were dissolved in distilled water (this mixture was developed within the NAKI II DG16P02M055 [1] research project in cooperation with The Centre of Polymer Systems, Tomas Bata University in Zlín).
- **BP** - two-component epoxy resin with low viscosity of 100 mPa*s, mechanical characteristics at 7 days – tensile strength of 51 N/mm², bond strength of 7.4 N/mm², friction of 16.8 N/mm².
- **BK** – mixture based on silicic acid ethyl ester with no content of solvents with gel separated amounts greater than 40%, with deep penetration and high resistance to weathering and UV radiation, colourless to slightly yellowish.

A total of 4 grouting mixtures were used, of which 2 were based on hydraulic lime, 1 based on resins and 1 based on organosilicates. Hydraulic lime grouting mixtures were applied by low pressure grouting (LP) using a screw grouting pump (2-10 bar) and the grouting compositions based on resin and organosilicate were applied by non-pressure grouting (NP) by hydrostatic pressure (about 0.5 bar).

The total porosity and pore distribution were determined on test specimens. Laboratory research of porosity was carried out in cooperation with the Institute of Rock Structure and Mechanics of the Czech Academy of Sciences using the high-pressure mercury porosimetry method on samples (fragments) of 5 mm of materials used in test specimens. The measurement was carried out on a set of Pascal 140 + 240 fir thermo Electon - porotec.

Samples of the masonry for determining the porosity before and after grouting were, after the grouting mixture had cured, taken from the test specimens using a \varnothing 35 mm core borehole perpendicular to the grouting boreholes about 80 mm above the lower edge of the test specimen (Figure 2). Samples were taken from each core borehole at a distance of 5 mm from the grouting borehole (grouted sample) and at a distance of 100 mm from the injection well (ungROUTED sample).

Tab. 1 - Overview of test specimens

Label	Material	Dimension [mm]	Grouting mixture
O1a	Marlstone	257x257x250	Hydraulic lime mixture BV3
O1b		253x251x250	
O2a		255x255x250	Hydraulic lime mixture BV7
O2b		254x254x250	
O3a		252x252x250	Epoxy resin BP
O3b		247x254x250	
O4a		252x255x250	Organosilicate BK
O4b		260x257x250	
OR		250x250x250	Reference sample (ungrouted)
B1a		Fine-grained sandstone (Božanov)	252x252x250
B1b	252x252x250		
B2a	251x252x250		Vápenná směs BV7
B2b	251x251x250		
B3a	252x252x250		Epoxy resin BP
B3b	252x252x250		
B4a	252x252x250		Organosilicate BK
B4b	252x252x250		
BR	252x252x250		Reference sample (ungrouted)
H1a	Coarse-grained sandstone (Hořice)		249x249x250
H1b		250x250x250	
H2a		251x253x250	Hydraulic lime mixture BV7
H2b		251x252x250	
H3a		252x251x250	Epoxy resin BP
H3b		252x252x250	
H4a		250x251x250	Organosilicate BK
H4b		251x252x250	
HR		248x248x250	Reference sample (ungrouted)
L1a		Limestone	254x255x250
L1b	254x254x250		
L2a	253x253x250		Hydraulic lime mixture BV7
L2b	253x254x250		
L3a	253x251x250		Epoxy resin BP
L3b	254x253x250		
L4a	253x253x250		Organosilicate BK
L4b	253x259x250		
LR	252x252x250		Reference sample (ungrouted)
M3_1a	Mortar 1:3		248x250x250
M3_1b		248x245x250	
M3_2a		250x245x250	Hydraulic lime mixture BV7
M3_2b		248x249x250	
M3_3a		250x245x250	Epoxy resin BP
M3_3b		249x250x250	
M3_3c		245x250x250	Organosilicate BK
M3_4a		250x250x250	
M3_R		250x248x250	Reference sample (ungrouted)
M5_1a		Mortar 1:5	251x248x250
M5_1b	249x250x250		
M5_2a	251x248x250		Hydraulic lime mixture BV7
M5_2b	248x245x250		
M5_3a	248x252x250		Epoxy resin BP
M5_4a	246x252x250		
M5_4b	250x248x250		Organosilicate BK
M5_4c	248x245x250		
M5_R	245x250x250		Reference sample (ungrouted)

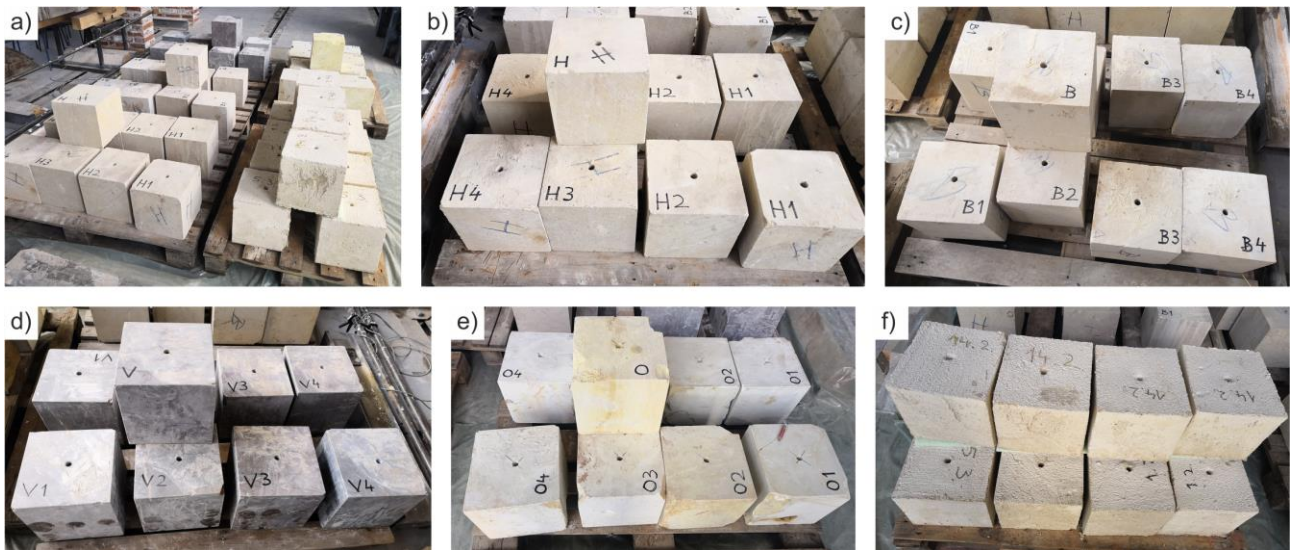


Fig. 1 – a) Stone a mortar test specimens, b) Coarse-grained sandstone test specimens (Hořice), c) Fine-grained sandstone (Božanov), d) Limestone test specimens, e) Marlstone test specimens, f) Mortar test specimens

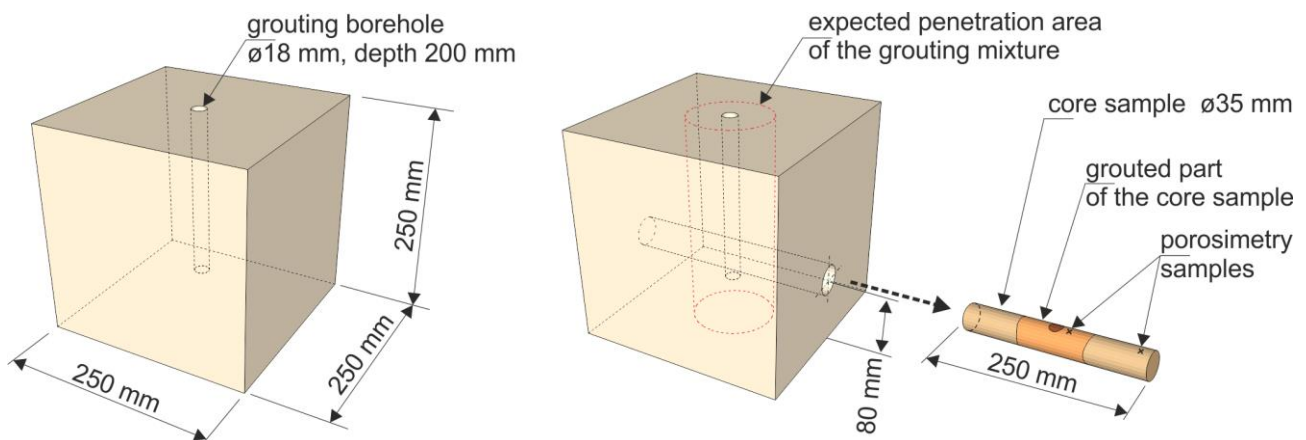


Fig. – 2 Test specimens' scheme

Based on the analysis of the total porosity (Figure 3), it can be concluded that the total porosity of the samples taken at a distance of 5 mm from the grouting borehole was in most cases lower than the total porosity of the samples taken at a distance of 100 mm from the grouting borehole.

In case of marlstone samples, the change in total porosity ranged from 2 to 15%, in case of coarse-grained sandstone samples between 8 and 20%, in case of fine-grained sandstone between 17 and 38% and in case of limestone between 1 and 35%. Thus, it is possible to assume that the test specimens are sufficiently grouted in their central part. On the other hand, extreme (or side) part of the test specimens can be labeled as grouted, because there was no decrease in the total porosity or a significant change in the distribution of individual pore groups.

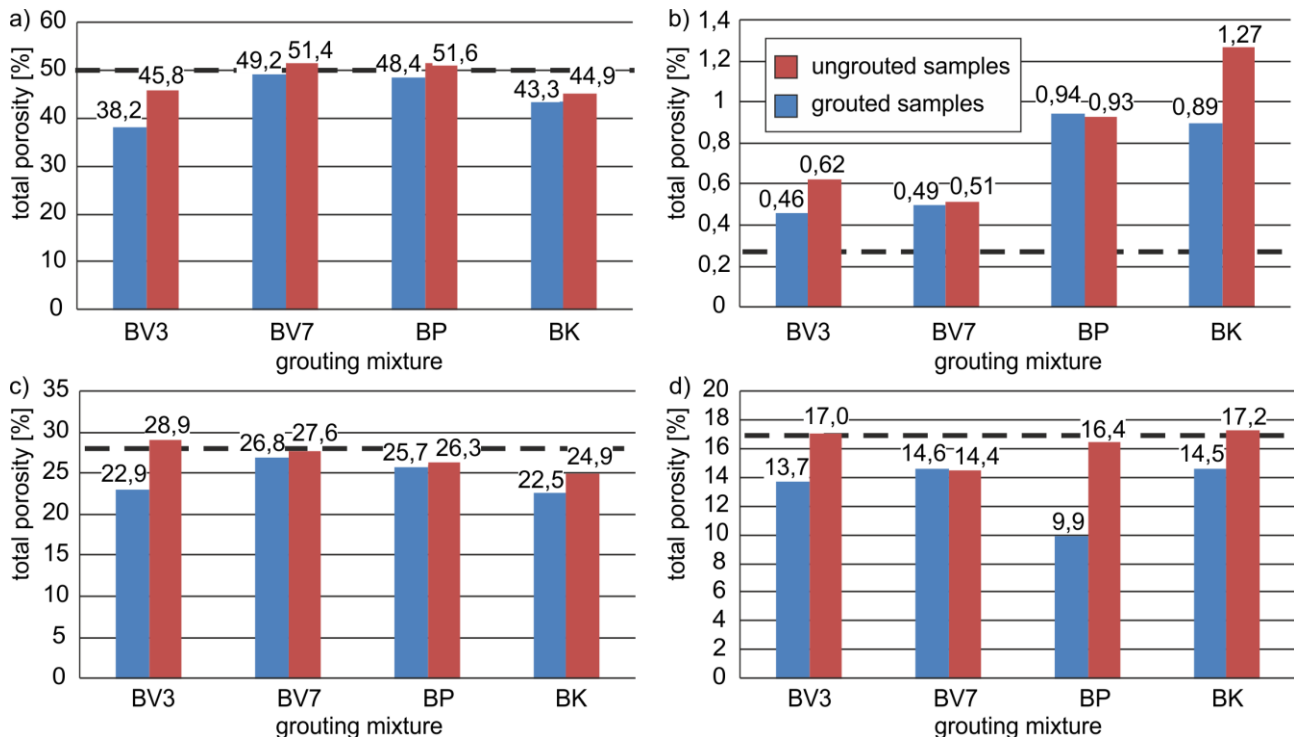


Fig. 3 – Comparison of total porosity of selected materials before and after grouting, a) Marlstone, b) Limestone, c) Coarse-grained sandstone (Hořice), d) Fine-grained sandstone (Božanov)

INFRARED THERMOGRAPHY

Thermal imaging (infrared thermography – IRT) is based on scanning and subsequent analysis of the distribution of the temperature field on the surface of the investigated body (structure). This temperature field is the result of the infrared radiation that each body emits. The accuracy of the measurement (resulting temperature field) is dependent on a number of parameters, in particular the emissivity of the surface and the apparent reflected temperature. Emissivity is a property of a material related to its ability to emit radiation and describes how much energy is emitted from a material relative to the amount emitted from an absolutely black body at the same temperature. The highest emissivity ($\epsilon_T = 1$) therefore has an absolutely black body (it is an ideal absorber and at the same time an ideal emitter). Real material always has lower emissivity ($\epsilon_T < 1$). Emissivity of a body depends on a number of material properties, such as type of materials (metal, plastic, masonry, glass, etc.), chemical composition, structure and condition of its surface (roughness, degree of oxidation, soiling). The apparent reflected temperature is ambient thermal radiation, which is reflected by the surrounding (especially shiny) surfaces and is detected by a thermal imaging device (thermographic camera).

Evaluation of grouting mixture penetration into masonry specimens by thermal imaging was performed using the Flir One Pro thermovision set (sensor resolution 160 x 120 px, visual sensor resolution 1440 x 1080 px, temperature range -20 ° C to +400 ° C, spectral range 8 to 14 μ m, temperature sensitivity 70 mK). Thermal imaging (static thermal imaging, thermal imaging videos) was performed during grouting of test specimens (Figure 4). The monitored parameter was the change of the surface temperature in the vicinity of the grouting borehole due to the penetration of the grouting mixture. Thermal imaging was performed for low-pressure (NT) and non-pressure (BT) grouting.

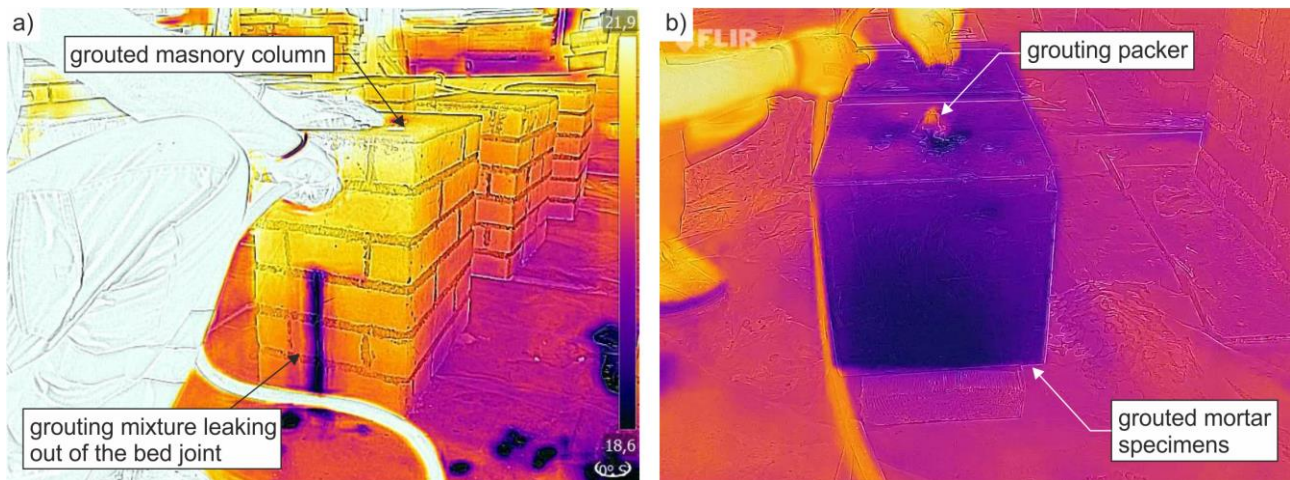


Fig. 4 – a) Thermovision image captured during grouting brick masonry test specimen with hydraulic lime based grouting mixture with nanosuspension labelled BV7, b) Thermovision image captured during grouting mortar test specimen with hydraulic lime based grouting mixture labelled BV3

Performed evaluation of the use of thermal imaging can be summarized as follows:

- monitoring of grouting mixture penetration is limited only to the surface of the grouted structure,
- grouting of the internal structure is manifested on the surface of the test specimens in a very limited extent,
- different properties of grouted masonry within the grouted structure (different emissivity and surface roughness of individual masonry elements and mortar) make it difficult to determine the appropriate parameters needed for thermal imaging,
- small temperature difference between the grouting mixture and the grouted masonry does not allow reliable monitoring of the penetration of the grouting mixture into the masonry,
- in the case of grouting of bodies damaged by a crack that extends to the masonry surface, it is possible, in some cases, to detect the grouting of the body (crack) by thermal imaging before it is visually observable.

ULTRASONIC MEASUREMENT

Ultrasonic testing methods (UST) are based on the determination of the speed of the acoustic signal passing through the investigated body (structure). The principle is based on sending repeated ultrasonic pulses into the material, their sensing and measuring the time of the front of the transmitted ultrasonic pulse through the material. From the known exciter – sensor distance (measuring base) and the measured pulse transit time, we can determine the ultrasonic propagation speed in the measured environment, which is the basic acoustic characteristic according to ČSN EN 12504-4 [11]. The value of the dynamic modulus of elasticity can be directly calculated from the measured speed and based on the statistically derived calibration relationships according to ČSN 73 1371 [12] some indicative properties of investigated material can be determined (e.g. compressive strength, modulus of elasticity, density etc.). The results can be refined by the methodology recommended by ČSN EN 13791 [13] for particular examined material. This method can also be used to detect various anomalies in the teste structure or material (cracks, voids, cavities etc.). Digital inspection ultrasonic flaw detectors operating at frequencies of 30 - 250 kHz are used for structural testing.

Evaluation of grouting mixture penetration into masonry specimens using ultrasonic testing was performed using a Proceq Tico ultrasonic instrument (measuring range 15 to 6550 μ s, resolution 0.1 μ s, transmit and receive probe frequencies 54 kHz). The ultrasonic measurement of the acoustic signal velocity was performed by direct measurement on the specimens after curing of the grouting mixtures in 9 locations in the longitudinal direction and 9 locations in the transverse direction of the specimen (Figure 5 and Figure 6). The measurement locations included both theoretically grouted and ungrouted parts of the test specimens. In total 810 measurements on 45 test specimens was performed.

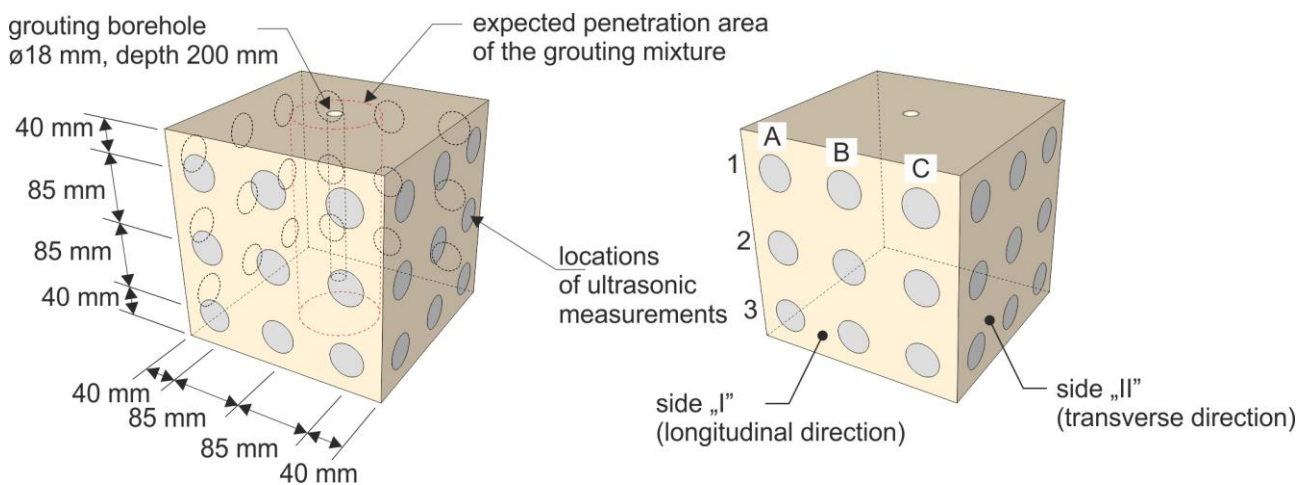


Fig. 5 – Ultrasonic testing scheme

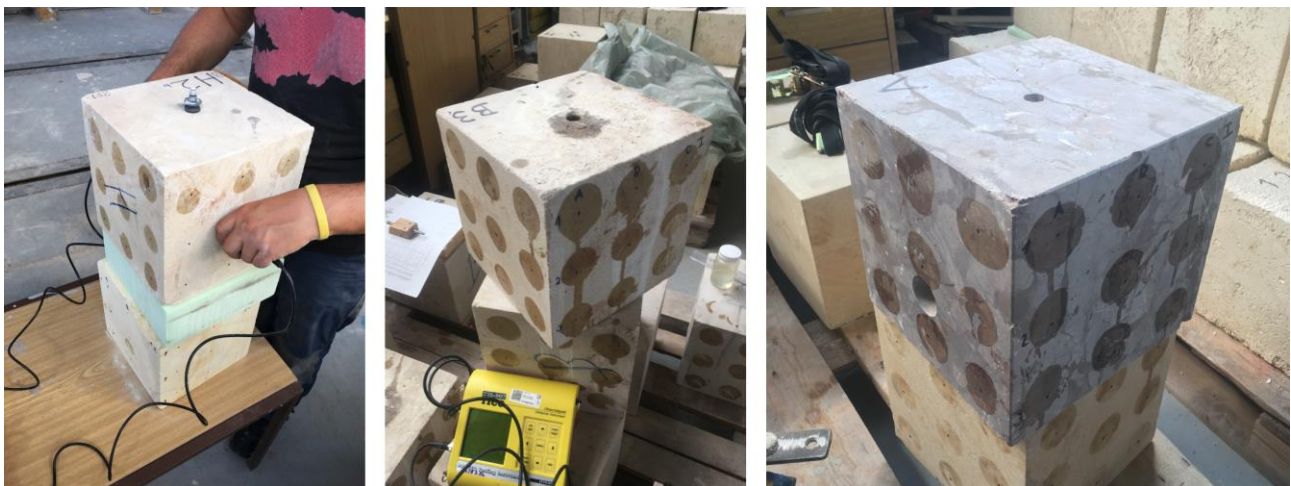


Fig. 6 – Ultrasonic testing

The recorded measurement results (ultrasonic signal velocity) were subsequently analyzed and statistically evaluated (Table 2 to Table 6). Due to the dispersion of the measured values of ungrouted samples of the same material, the grouting mixture penetration analysis was always performed within one or two test specimens.

Tab. 2 - Results of ultrasonic measurements (ultrasonic signal velocity) of reference (ungROUTED) test specimens

Material	Average velocity [m/s]	Standard deviation [m/s]	Coefficient of variation
Fine-grained sandstone	3276,6	80,1	2,4%
Coarse-grained sandstone	2663,4	83,5	3,1%
Marlstone	1969,6	245,3	12,5%
Limestone	6137,3	338,4	5,5%
Mortar 1:5	1198,4	162,3	13,5%
Mortar 1:3	1247,8	131,0	10,5%

Tab. 3 - Results of ultrasonic measurements (ultrasonic signal velocity) of test specimens grouted with hydraulic lime based mixture labelled BV3

Material	Velocity in grouted part [m/s]	Velocity in ungrouted part [m/s]	Standard deviation in ungrouted part [m/s]	Velocity difference in grouted and ungrouted parts [m/s]
Fine-grained sandstone	3349,3	3331,5	44,1	17,8
Coarse-grained sandstone	3080,2	3121,0	105,9	40,7
Marlstone	1861,4	1928,5	191,4	67,2
Limestone	6511,9	6475,6	48,0	36,3
Mortar 1:5	1111,4	1236,0	31,1	124,6
Mortar 1:3	1229,8	1351,2	66,5	121,4

Tab. 4 - Results of ultrasonic measurements (ultrasonic signal velocity) of test specimens grouted with hydraulic lime based mixture with nanosuspension labelled BV7

Material	Velocity in grouted part [m/s]	Velocity in ungrouted part [m/s]	Standard deviation in ungrouted part [m/s]	Velocity difference in grouted and ungrouted parts [m/s]
Fine-grained sandstone	3197,1	3193,2	38,8	3,9
Coarse-grained sandstone	2557,7	2570,1	85,8	12,4
Marlstone	1737,7	1673,4	38,9	64,3
Limestone	6365,8	6387,6	153,3	21,8
Mortar 1:5	1093,4	1256,0	56,9	162,6
Mortar 1:3	1083,4	1188,1	67,7	104,8

Tab. 5 - Results of ultrasonic measurements (ultrasonic signal velocity) of test specimens grouted with epoxy resin based mixture labelled BP

Material	Velocity in grouted part [m/s]	Velocity in ungrouted part [m/s]	Standard deviation in ungrouted part [m/s]	Velocity difference in grouted and ungrouted parts [m/s]
Fine-grained sandstone	3436,0	3271,1	39,5	164,9
Coarse-grained sandstone	3094,6	3053,8	128,3	40,8
Marlstone	1819,7	1825,1	143,6	5,4
Limestone	6337,6	6349,8	143,6	12,2
Mortar 1:5	1184,1	1289,2	45,5	105,1
Mortar 1:3	1212,6	1248,3	100,3	35,7

Tab. 6 - Results of ultrasonic measurements (ultrasonic signal velocity) of test specimens grouted with organosilicate based mixture labelled BK

Material	Velocity in grouted part [m/s]	Velocity in ungrouted part [m/s]	Standard deviation in ungrouted part [m/s]	Velocity difference in grouted and ungrouted parts [m/s]
Fine-grained sandstone	3282,9	3120,5	166,1	162,3
Coarse-grained sandstone	2728,5	2675,2	42,7	53,3
Marlstone	2025,2	2016,5	175,4	8,7
Limestone	6377,0	6391,2	48,3	14,3
Mortar 1:5	863,3	1061,9	109,5	198,7
Mortar 1:3	1036,0	1086,8	115,1	50,8

Experimental evaluation of the use of ultrasonic methods based on comparison of ultrasonic signal transmission velocity in grouted and ungrouted test specimens showed:

- the penetration of lime-based grouting mixtures could be monitored especially in mortar test specimens and in the case of a mixture with nanosuspension also in the marl test specimens,
- the penetration of the epoxy-based grout can be monitored in fine-grained sandstone test specimens and mortar test specimens with a mixing ratio 1:5,
- the penetration of the grouting mixture based on organosilicate could be monitored in the test specimens of fine-grained and coarse-grained sandstone (however, in both cases the influence of the grouting on the velocity of the ultrasonic signal transmission was small) and further in the mortar test specimen with mixing ratio 1:3,
- there was a significant difference in the velocity of the ultrasonic signal passing through the monitored masonry materials and mortar mixtures. This difference is directly related to the material properties of the individual masonry components and can therefore be used to detect individual materials in a heterogeneous masonry structure. However, it also points out other possible obstacles in the use of ultrasound diagnostic methods.

Performed evaluation of the use of ultrasonic methods can be summarized as follows:

- the main prerequisite for the application of ultrasonic methods is to ensure perfect contact of the transducer with the investigated structure. In case of partial contact between the transducers and the masonry structure, the results may be subject to significant error,
- results may also be affected by the heterogeneity of the structure under investigation. Even specimens of the same material used in the experimental evaluation showed differences in measured values,
- differences in the measured values were observed even within one specimen due to internal inhomogeneities (especially cracks and microcavities).
- small differences in physico-mechanical properties of the grouting mixtures and the grouted structure (especially when using hydraulic lime based grouting mixtures) limits the possibility of reliable determination of the penetration of grouting mixture into the masonry structure.

CONCLUSION

Based on the experimental verification of the possibility of using non-destructive diagnostic thermovision and ultrasonic methods and subsequent evaluation of the obtained results, these methods cannot be unambiguously recommended as a reliable way of determining the penetration of the grouting mixtures into the masonry structure. In the case of infrared (thermal) imaging, apart

from other parameters (surface properties of the injected structure, ambient temperature, etc.), the relatively small (difficult to measure) temperature difference of the grouting mixture and the grouted body appears to be the main obstacle. Ensuring bigger temperature difference is possible by heating the grouting mixture just prior to grouting. In such a case, penetration of the grouting mixture into the grouted masonry is detectable better. However, it is necessary to carefully consider the heating of the grouting mixture with regard to its composition so as not to affect its properties (especially in the case of epoxy resins and organosilicates). In case of ultrasonic methods it is necessary to ensure perfect contact of measuring probes (sending and receiving) with the surface of the measured structure. This can be rather complicated and sometimes even impossible, especially in case of historic masonry. The resulting measurements can be significantly influenced by this fact. The small difference in material properties of grout mixtures and grouted masonry structures, especially when taking into account the requirement to ensure their maximum compatibility in terms of heritage preservation (physico-mechanical and chemical compliance), also significantly limits the possibility of reliable detection of grouting penetration into masonry.

ACKNOWLEDGEMENTS

The article was written with support from the NAKI DG16P02M055 project “Development and Research into Materials, Procedures and Technologies for Restoration, Conservation and Strengthening of Historic Masonry Structures and Surfaces and Systems of Preventive Care of Historic and Heritage Buildings Threatened by Anthropogenic and Natural Risks”.

REFERENCES

- [1] NAKI DG16P02M055 Development and Research into Materials, Procedures and Technologies for Restoration, Conservation and Strengthening of Historic Masonry Structures and Surfaces and Systems of Preventive Care of Historic and Heritage Buildings Threatened by Anthropogenic and Natural Risks, 2015-2020, lead researcher prof. Ing. Jiří Witzany. DrSc.
- [2] Uranjek M, Bosiljkov V, Zarnic R, Bokan-Bosiljkov V., 2012. In situ tests and seismic assessment of a stone-masonry building. *Materials and Structures*, vol. 45: 861–79
- [3] Binda L., Modena C., Baronio G., Abbaneo S., 1997, Repair and investigation techniques for stone masonry walls. *Construction and Building Materials*, vol. 11: 133–142
- [4] Binda L., Baronio G., Tiraboschi C., Tedeschi C., 2003. Experimental research for the choice of adequate materials for the reconstruction of the Cathedral of Noto. *Construction and Building Materials*, vol. 17: 629–639
- [5] Valluzzi M.R., 2005. Requirements for the choice of mortar and grouts for consolidation of three-leaf stone masonry walls, Pap. Present. Work. Repair Mortars Hist. Masonry. Delft Univ. Technol. Fac. Civ. Eng. Geosci. Delft; 26–28 January 2005
- [6] Bosiljkov V., Uranjek M., Zarnic R., Bokan-Bosiljkov V., 2010. An integrated diagnostic approach for the assessment of historic masonry structures. *Journal of Cultural Heritage*, vol. 11: 239–249
- [7] Da Porto F., Valluzzi M.R., Modena C., 2003. Use of sonic tomography for the diagnosis and the control of intervention in historic masonry buildings, Int. Symp.
- [8] Jorne, F., Henriques, F.M.A., Baltazar, L.G., 2014. Evaluation of consolidation of grout injection with ultrasonic tomography. *Construction and Building Materials*, vol. 66: 494-506
- [9] Jorne, F., Henriques, F.M.A., Baltazar, L.G., 2015. Evaluation of consolidation of different porous media with hydraulic lime grout injection. *Journal of Cultural Heritage*, vol. 16: 438-451
- [10] Almeida C., Guedes J.P., Arêde A., Costa C.Q., Costa A., 2012. Physical characterization and compression tests of one leaf stone masonry walls. *Construction and Building Materials*, vol. 30: 188–197
- [11] ČSN EN 12504-4 Testing concrete - Part 4: Determination of ultrasonic pulse velocity, UNMZ 2005, Prague
- [12] ČSN 73 1371 Non-destructive testing of concrete - Method of ultrasonic pulse testing of concrete, UNMZ 2011, Prague



- [13] ČSN EN 13791 Assessment of in-situ compressive strength in structures and precast concrete components, UNMZ 2007, Prague

THE MEASUREMENT OF HIGH-SPEED RAILWAY (HSR)- PRECISION ENGINEERING

Alhossein Mohamed¹, Qiyuan Peng¹, Malik Muneeb Abid²

1. *School of Transportation and Logistics, Southwest Jiaotong University, Chengdu 610031, China; mxhx83@163.com, qiyuan-peng@swjtu.edu.cn*
2. *Department of Civil Engineering, College of Engineering and Technology, University of Sargodha; muneeb.abid@uos.edu.pk, malik.muneeb.abid@hotmail.com*

ABSTRACT

The paper proposed the optimization of the network construction timing of the control network according to the specific conditions of the survey route. Moreover, presented here are the adjustments according to the layout requirements of the control network layout process, strengthening the control of the line level base point during the construction process. Several optimization solutions are discussed for the special design of the level control before the construction of the long tunnel. It has been explained the methodology to introduce new Continuously Operating Reference Station (CORS) technology in railway survey and design with appropriately adjustment of the position requirements of the control network according to the specification. In order to carry out the special design of the levelling route with precision, it is advisable to set a certain stable reference point in the level control of the long line. The proposed methodology can effectively solve some problems existing in the current high-speed railway construction process, and make the precision measurement control network better for survey, design, construction, supervision and operation.

KEY WORDS

High-speed railway, Precision engineering survey, Network construction timing, Levelling network

INTRODUCTION

In 2018, the Taiqing high-speed railway was completed and opened to traffic, which means that the construction of the China Railway Framework Network is about to be completed, and it entered the final stage. Since the commencement of construction in Beijing and Tianjin in 2005, China's high-speed railway technology development has steadily entered a mature stage. Under the guidance of the strategy of "introduction-evaluation-re-innovation", the localization of high-speed rail technology has been carried out. The result is a series of independent intellectual property rights, creating a unique Chinese high-speed rail brand. On March 20, 2017, the National Development and Reform Commission officially released the "eight vertical and eight horizontal" road network plan: It is planned that by 2020, with the completion and commissioning of a number of major landmark projects, the scale of the railway network will reach 150,000 km. Out of which the high-speed railway covers 30,000 km and covers more than 80% of the big cities. Under the circumstances of China's high-speed railway's sustained and steady development, further

evaluation and absorbing the previous construction experience is of great significance for improving the standardized management of technology, production and operation at all stages.

In 2009, the Ministry of Railways issued the "High-speed Railway Engineering Measurement Specification" (TB10601-2009). Through the practice of several high-speed rails such as Beijing-Shanghai, Harbin and Beijing-Shiwu, the standard system adopted has withstood the test of design, construction and operation, verifying its scientific, advanced, applicability and reliability. But in some details, there are still some areas for improvement. For example, the timing of the control network construction network is out of line with the previous design, and the design of the control network simply considers its own mesh shape without considering the actual construction conditions.

PARTICULAR TIME OF NETWORK CONSTRUCTION

The traditional railway engineering control network establishes a low-level control network at the initial stage of measurement. After the scheme is stabilized, the precision engineering measurement is carried out separately. There is a situation in which the design documents generated by the initial measurement control benchmark are inconsistent with the construction reference documents. This deviation is often huge for the earthwork volume. There are hidden dangers such as insufficient clearance in the upper cross. There are many comparison schemes for new railways, and it is uneconomical to directly establish a complete set of precision measurement and control systems when the scheme is unstable. Therefore, on the basis of referring to the traditional measurement control process, the following rules are set for the network construction timing at each stage:

1. The CP0 control network should be established by global navigation satellite system (GNSS) measurement method before the initial measurement, and the whole line should be laid at one time, unified measurement, and overall adjustment [1].
2. The CPI control network should be established in the initial test stage. When it is difficult, it should be completed before the test. The whole line should be deployed once, and the measurement should be unified, and the overall adjustment [1].
3. The CP II control network should be completed in the calibration stage and measured by GNSS measurement or traverse measurement method [1].

Selection of CP0 network construction time: In the early stage of China's high-speed railway construction, the national control network is imperfect and the accuracy is insufficient. Therefore, the specification requires the establishment of CP0 in the initial stage. After the official launch of the 2000 National Geodetic Coordinate System on July 1, 2008, the poor accuracy of the national network has ceased to exist in most areas, so the provisions of this article may not be entirely appropriate today. At this stage, China's high-speed railway and trunk railway network has begun to take shape. It is more effective and reasonable to adopt the control standard of railways at both ends and directly realize the smooth connection of road network control.

"CPI control network should be established in the initial stage of testing" is to prevent the initial survey and design data from being inconsistent with the construction network control network data. There are many options in the initial test phase. At this time, the implementation of precision measurement will result in a large cost waste. In addition, from the initial test to the opening of the trade union for a long time, the control network established at this stage often has a large segment. The control pile is destroyed, and even the local loss of the control network function may occur. With the gradual improvement of the construction of the national Continuously Operating Reference Station (CORS) base station, there are fundamental solutions to this contradiction. At present, 27 provinces and municipalities in China have built provincial-level CORS networks with

an average station spacing of 40 to 70 km, and the remaining provinces have also been included in the planning. The application of CORS technology carried out by various railway design institutes in the process of multiple railway survey and design proves that the accuracy of CORS technology is sufficient to ensure the application of survey and design and the production. Moreover, efficiency will be greatly improved during the initial stage of railway survey.

Therefore, a reasonable recommendation should be that analyse the line data before the initial test, and clarify the frame control network reference adopted by the line; Establish the CP0 control network using GNSS measurement method in areas where the national control is insufficient or the CORS base station cannot cover it. And combined with national A and B GNSS control points; the initial test can be completed with CORS. After the program is basically stable, the CPI is established and the test is completed (see Table 1).

Tab. 1 - Comparison of advantages and disadvantages of different processes in precision measurement control network

Process	Pattern	Advantages and disadvantages
Traditional measurement control	Establish an initial test control network in the initial test phase, and establish a fine test network once the line is stable.	The design and construction are out of line, and it is easy to produce problems such as large deviation of earth and stone volume and insufficient clearance of upper and lower crosses.
Specification recommendation process	Initially establish CP0, CPI, establish CPII after calibration	Affected by the instability of the program, a large number of CPI supplementary network construction work is required.
Suggest further adjustments	The initial control stage determines the framework control benchmark, and the initial measurement can be completed by CORS; after the scheme is basically stable, the CPI is established for the final measurement.	Economic and operational efficiency is more reasonable and feasible under the condition of precision guarantee

With the increasing accuracy of the national surveying and mapping geographic information, the density is getting larger and larger. Especially the construction of the continuous operation reference station system CORS is more and more mature, which brings great convenience and precision guarantee for the measurement work. In the precision measurement and control of high-speed railways, the traditional process system has already had certain defects, and some adjustments should be made during the implementation process.

CONTROL NETWORK

The current specification stipulates that the CPI Control Network will deploy one GNSS control point every 4 km. After the construction period and operation period, the loss of control piles may occur, which directly affects the retest stability judgment of the line control network CPII and the track reference network CPIII. This will further affect the long-wave irregularity maintenance of the track structure. Therefore, it is recommended that the CPI be buried in the area where the construction interference is small.

With the introduction of GNSS- Real-time kinematic (RTK) technology, offline construction with low precision requirements no longer relies on total station construction stakeout. The change of operation mode makes the requirement of communication between railway control outlets in local areas no longer a hard condition (Except for mountain tunnel sections). Similarly, the

requirements for control points from the center line of the line should also be changed, and should focus on point maintenance and GNSS operations. Therefore, the network requirements of the GNSS control network should be optimized and adjusted in the specification limit: The CPI basic control network recommends that 1 pair be placed every 4 km (the vertical line direction should be laid as far as possible), and the spacing should be 50 to 1 000 m.; CPII line control network is recommended to be adjusted from the current 50 ~ 200 m to 200 ~ 400 m; CPII line encryption control points should be placed within the railway construction limit. When the control network is laid, the position of the surrounding control points should be fully considered, so that the distribution and control of the entire railway control network is more reasonable [2,3,4].

LEVELING NETWORK STABILITY CONTROL

The control network plane observation uses GNSS operations with less manual intervention and strong stability, and the results are more reliable. In the process of elevation measurement, there are many problems caused by national control standards, regional settlement, crossing tunnels, crossing rivers, etc. In the precision measurement and control of high-speed railways, the quality assurance of levelling and the reasonableness of data processing methods are essential. The analysis of the operational retest data of the completed high-speed rail shows that there are serious settlements in many sections, and even led to the railway speed limit. In these areas, if there is no stable control point, the control network retest will often fail to determine the stability of the control base. In order to perform deformation monitoring in these sections, it must be taken from a reliable stable control point (national bedrock point), which is often time consuming and labour intensive [5, 6].

There are no requirements for deep burial and bedrock points in the railway elevation control network in the Interim Provisions on the Measurement of the Passenger Dedicated Railway. During the implementation of the Beijing-Tianjin Intercity and Beijing-Shanghai high-speed railways, due to the complexity of the geological conditions along the line, there are number of uneven settlement areas. In some places, the surface settlement is very critical. Therefore, the control method of deep buried level base points is adopted. Repeated retests have proved that the deep burial point has significant anti-settling properties compared to the ground control standard, which provides long-term elevation reference support for railway operation, maintenance and monitoring. Therefore, the "High-speed Railway Engineering Measurement Specification" has the following requirements for deep-buried stone: In areas with uneven surface subsidence and geological conditions, it is advisable to set a deep burial level every 10 km and set a bedrock every 50 km. The bedrock levelling point and the deep-buried levelling point should use the stable bedrock levelling point and deep-buried levelling point buried by the state or other surveying and mapping units as far as possible [1].

Therefore, in areas with uneven surface subsidence and geological conditions, the bedrock standard point should be used as a high-level control point of the line level base point, one for every 50 km. The deep burial level is the same level control point of the line level base point, but it is better than the general level point anti-sedimentation. The retesting process of the control network can be used as an important basis for judging the stability of the section. The deep buried level can be replaced by a stable old building foundation and a large abutment foundation. The bedrock and benchmarks buried by the state or other surveying and mapping units can also be selected as deep buried control piles [7,8,9].

TREATMENT OF LEVEL CONTROL NETWORK AFTER LONG TUNNEL

The high-speed railway precision measurement control network is usually established during the survey and design stage. When crossing large rivers and long tunnels, the level is measured by means of bypass observation or cross-river observation. After the construction of the bridge pavement is completed or the tunnel is penetrated, for the levelling measurement, new conditions are generated. Take the elevation control of a mountain railway tunnel as an example: the designed tunnel length is about 10km, which is affected by the ground shape and traffic conditions, and the standard bypass route reaches 100 km. According to the second-class observation method, the difference of the line closure difference before the tunnel penetration is 40.0 mm; after the penetration is limited to 12.6 mm, the height of the fine measurement network may be broken after the tunnel is penetrated [10, 11, 12 and 13]. If no additional considerations are made in the previous period, even then the precise measurement of the tunnel section before the tunnel penetration measurement will have a greater impact on the later construction. Therefore, under such special construction conditions, special design of the precision measurement of the work site must be carried out as follows [14]:

(1) According to the standard bypass design observation results, the closure difference between the elevation control points at both ends of the tunnel is calculated.

(2) Estimate the closure difference between the elevation control points of the two ends after the penetration of the inclined well, the penetration route and the level tolerance; the total error of the level measurement per km is calculated by the following formula:

$$M_w = \sqrt{\frac{1}{N} \left[\frac{W^2}{L} \right]} \quad (1)$$

Where W is the correction of the level ring after various corrections/mm;

L is the level ring circumference /km;

N is the number of levels.

According to formula (1), take $MW = 2$, $N = 1$, $L = 10$, then calculate the level closure difference $W = 6.3$ mm;

(3) Calculate the maximum breaking height value generated under the most unfavourable conditions:

$$H_{closure} = H_{bypass} + H_{Through} \quad (2)$$

The high-level adjustment section should be reserved for the construction of the loft and the construction of the ballastless track.

(4) After the completion measurement is conducted, the construction cut height is set according to the closed measurement level closure condition. In addition, it is coordinated with the two ends of the fine measurement net in the local range. In the as-built measurement, the entire line of precision measurement control network unified adjustment, eliminate the height, and re-measure and evaluate the line condition according to the latest fine measurement network results, and if necessary, carry out the secondary design of the vertical curve.

Similar situations include: Measurement of the construction level of large rivers and rivers across rivers; construction of ballastless (without ballast) transition sections (fine adjustment of ballast plate construction, front and rear alignment after installation of turnouts); elevation measurement of subway sections.

CONCLUSIONS

The "High-speed Railway Engineering Measurement Specification" has been promulgated and implemented for nearly 10 years. With the development of surveying and mapping science and technology and the transition of the trunk line project from the construction period to the operation period, it should be further improved to establish a complete mapping basis for system authority. It is still necessary to further study how the results of the testing and re-testing of the control network can be more effectively and safely applied to the fine adjustment of railway engineering and improvement of the level of smoothing and optimization of the line. In summary, it is necessary to carry out further systematic research on China's high-speed iron precision measurement and control technology, which helps to ensure the measurement accuracy of high-speed railway, improve measurement efficiency and quality during construction and operation. Moreover save costs, and have obvious social economy benefit.

ACKNOWLEDGEMENT

Authors are thankful to the anonymous reviewers for their valuable comments.

REFERENCES

- [1] China Railway Second Construction Engineering Group Co., Ltd. TB10601—2009 High-speed railway engineering measurement Specification [S]. Beijing: China Railway Publishing House, 2009
- [2] Min Minyi. Discussion on the measurement system of high-speed railway engineering[C]||High-speed railway precision measurement theory Proceedings of the International Symposium on the Application of New Techniques in Surveying and Mapping. Chengdu: Southwest Jiaotong University Publisher, 2010: 11-15
- [3] Su Quanli. On the high-speed railway measurement network layout technology [J]. Railway Survey, 2010 (6): 1-4
- [4] An Guodong. Research and application of high-speed railway precision engineering measurement technology standards [J]. railway Journal, 2010(2) : 98-104
- [5] Chen Xinhuan. Research on precision of high-speed railway control measurement [J]. Railway Survey, 2004 (1):29-31
- [6] Zhu Ying, Min Minyi, Lu Jiankang. Passenger Dedicated Line, Ballastless Track and Railway Engineering Measurement and Control NetworkDegree standard research [Z]. Chengdu: Railway Second Survey and Design Institute, Southwest Jiaotong University, 2006: 30
- [7] He Huawu. On the precision engineering measurement technology of railways with a speed of more than 200 km [J]. Chinese ironRoad, 2007 (3): 1-5
- [8] Liu Cheng, Liu Hongdong, Xu Dazhi. The quasi-point and deep burial of the ballastless track of the passenger dedicated railway, the establishment of benchmarks [J]. Railway Survey, 2007 (6): 26-27
- [9] Lu Jiankang, Liu Hua. The establishment and characteristics of high-speed railway precision engineering measurement technology system [J]. Railway Standard Design, 2010(S1): 70-73
- [10] Lu Jiankang. On China's high-speed railway precision engineering measurement technology system and characteristics [J]. high speed Railway Technology, 2010(1): 31-35
- [11] Lu Jiankang. Discussion on measurement method of railway passenger dedicated line [J]. Railway Survey, 2005 (6): 1-4
- [12] Luo Lin. High-speed railway tracks must have high ride comfort [J]. China Railway, 2000 (10):8-11
- [13] Mei Xi. Discussion on Several Problems of Establishing Plane Control Network for Railway Passenger Dedicated Line by GPS Technology [J].Railway Investigation, 2005(5): 3-7
- [14] Luo Yan, Zheng Zitian, Cao Titao. Research on high-speed railway free station elevation calculation method [J]. Railway Survey, 2017(3): 21-23.

STATISTICAL STUDY OF MODIS ALGORITHMS IN ESTIMATING AEROSOL OPTICAL DEPTH OVER THE CZECH REPUBLIC

Saleem Ibrahim and Lena Halounova

Czech Technical University, Faculty of Civil Engineering, Department of Geomatics, Prague, Thákurova 7, 166 29 Praha 6, Czech Republic; saleem.ibrahim@fsv.cvut.cz, lena.halounova@fsv.cvut.cz.

ABSTRACT

As a result of the rapid development of remote sensing techniques and accurate satellite observations, it has become customary to use these technologies in ecological and aerosols studies on a regional and global level. In this paper, we analyse the performance of three Moderate Resolution Imaging Spectroradiometer (MODIS) algorithms in estimating Aerosol Optical Depth (AOD) in the Czech Republic to gain knowledge about their accuracy and uncertainty. The Dark Target (DT), the Deep Blue (DB), and the merged algorithm (DTB) of the MODIS latest collection 6.1 Level 2 aerosol products (MOD04_L2) were tested by comparing its results with the measurements of Aerosol Robotic Network (AERONET) Level 3 Version 2.0 ground station at Brno airport. The DT algorithm is compatible the best with AERONET observations with a correlation coefficient ($R = 0.823$), retrievals falling within the EE envelope ($EE\% = 82.67\%$), root mean square error ($RMSE = 0.059$), and mean absolute error ($MAE = 0.044$). The DTB algorithm provided close results of the DT algorithm but with less accuracy, on the other hand the DB algorithm has the lowest accuracy between all, but this algorithm was able to provide a bigger sample size than the other two algorithms.

KEYWORDS

AERONET, AOD, DB, DT, DTB, MODIS, Remote sensing

INTRODUCTION

Aerosol Optical Depth (AOD) is a measure of the columnar atmospheric aerosol content, these particles could absorb or scatter the sunlight and prevent it reaching the ground [1]. These small solid or liquid particles are suspended in the atmosphere and they differ in the size, shape, and chemical adaption [2]. Studying of AOD is obtaining more interest day by day, due to its negative impact on all living things by affecting the respiratory system beside reducing naked eye visibility [3]. Humans are not the main cause of aerosols. Aerosols come from many resources like fires, volcanoes, burning of fossil fuels, dust storms and sea drizzles. AOD causes both direct and indirect effects on climate systems according to the lightness or darkness of these particles, in addition to affect the atmospheric radiation energy balance [4]. Deeper and better understanding of aerosol distribution and characteristics is essential for climate change studies [5].

It is not possible to solely rely only on ground observations in estimating AOD, since this process requires a great number of such stations in order to cover all areas, which requires high costs and efforts. For this reason, researches focused on climate changes had to find alternative methods to measure AOD. One of these effective techniques is the Moderate Resolution Imaging Spectroradiometer (MODIS), which is considered the first satellite plan that can provide an accurate information of aerosol optical characteristics. Both the Terra and Aqua satellite platforms have been

carrying MODIS instrumentations in a sun-synchronous polar orbits, since the year 1999 and 2002, respectively [6]. They are able to record earth's surface with 2330 km viewing swath width every 1 to 2 days [7]. MODIS measures 36 spectral bands between 0.4 and 14.4 μm wavelengths at many different spatial resolutions that provides a great opportunity to study aerosols thickness and parameters characterizing aerosol size from space with good accuracy and on a world-wide scale [8,9], this information helps researchers to estimate AOD loads caused by human-being activities and distinguish it from natural causes [10]. MODIS data has been used to provide useful information on climate changes. Yet, there are many limitations facing satellite aerosol retrieval, including the radiometric calibration, cloud screening, surface reflectance estimation, and aerosol model presumption [11,12]. To get better results from MODIS, several algorithms were designed and developed to use the observed radiances for deriving many important aerosol products. The main purpose of modifying these algorithms is to comply better with the observing instrument specification, properties of aerosols, and nature of clouds [6]. Updated versions of operational aerosol products have been made available over the years, and because of the improvements of these products, we have new datasets collections continuously, starting with collection 4 (C4) to C5, C6, and the latest collection (C6.1) which was released in July 2017.

MODIS Characterization Support Team (MCST) has produced the C6.1 aerosol products, based on the new updated Level 1B calibrated radiance products [13]. Additionally, NASA Ocean Biology Processing Group (OBPG) developed more calibration corrections and these improvements were applied to the MCST top of atmosphere (TOA) products starting with C5 [14,15]. MODIS C6.1 aerosol products have major improvements in both radiometric calibration and all aerosol retrieval algorithms.

MODIS products include many scientific data sets (SDS). In recent updated products, Quality Assurance (QA) dataset is added, which serves as a check point for certain conditions that are to be met during the retrieval process [16]. At the end of the process, QA dataset will provide confidence level; 0 = no retrieval, 1 = poor quality, 2 = moderate quality and 3 = good quality [17]. Since the launch of Terra and Aqua satellites, the Dark Target (DT) algorithm which was proposed by [2] has been applied to the MODIS data. There are two distinct DT algorithms for retrieving AOD, one for retrieving AOD over ocean and the second for retrieving AOD over land. Many improvements were applied to the latest algorithm especially of estimating the model for main urban surfaces [18]. The most common used SDS for the DT algorithm is "Optical-Depth-Land-And-Ocean" it contains only filtered values of AOD retrievals which meet the quality assurance ($QA \geq 1$ over ocean and $QA = 3$ over land) to provide beneficial retrievals over dark areas [19]. By contrast, this algorithm has disadvantages over bright surfaces. For this reason, another algorithm called the Deep Blue (DB) was developed in order to retrieve AOD over bright surfaces like deserts and arid areas [20,21]. Since the releasing of C6, DB has been improved to work affectively over vegetated land surfaces, brighter deserts and urban areas [15]. In the latest C 6.1 DB algorithm was developed from collection 6. It has the following advantages over land, the ability to detect thick smoke, efficient modelling for terrains, and many bug fixes, among others mentioned elsewhere [13]. Beside DB and DT products, there is a merged dataset consists of both DT and DB algorithms (DTB). This merged algorithm works based on the Normalized Difference Vegetation Index (NDVI). According to this methodology, if $NDVI > 0.3$ then the DT algorithm will be applied on the retrievals, if $NDVI < 0.2$ then the DB algorithm will be applied, and if NDVI value is between 0.2 and 0.3 then the combined algorithm of both DT and DB will be applied. DTB dataset offers a better spatial coverage especially for low vegetated areas [19].

To validate the results obtained from MODIS or other satellite sensors, data is usually compared with the measured aerosol parameters of ground-AERONET. A similar regional study by Zawadzka and Markowicz compared the Spinning Enhanced Visible Infrared Radiometer (SEVIRI) data with AERONET observations in Poland and their study showed a good correlation with a root mean square error (RMSE) equals to 0.05 [22]. Based on such comparison, MODIS retrieving algorithms could be further improved to reach a satisfactory outcome [23,24].

DATA DESCRIPTION

MODIS Data

Tow worldwide products are included in the MODIS level-2 daily swath, MxD04-L2 at 10 km resolution and MxD04-3k at 3 km resolution, whereas: $x = O$ for Terra, and $x = Y$ for Aqua. In this study we use the level-2 daily product at 10 km resolution MOD04_L2 of the TERRA satellite, during the period of 18 months (Jun 2017- Dec 2018) over the Czech Republic. Three AOD subset products; DT, DB, and the merged DTB at 550 μm , are generated from the MODIS latest collection C 6.1. All data is publicly available and was downloaded from <https://ladsweb.modaps.eosdis.nasa.gov/>.

Tab. 1 - Scientific dataset of MODIS used in this study

Product	(SDS) name	Contents	Spatial resolution
MOD04-L2 C6.1	Optical-Depth-Land-And-Ocean	DT over land (QA=3)	10 Km
	Deep-Blue-Aerosol-Optical-Depth-Land-Best-Estimate	DB over land (QA \geq 2)	
	AOD-550-Dark-Target-Deep-Blue-Combined	DTB over land and ocean	

AERONET Data

NASA co-sponsors a global network of ground sensors called the Aerosols Robotic Network (AERONET), which is considered as one of the most common and reliable aerosol networks [25]. It is a multi-channel instrument that takes automatic measurements for both direct solar irradiance and sky radiance at the Earth's surface. AERONET takes observations of the solar radiation at seven wavelengths (380, 440, 500, 675, 870, 936 and 1020 nm) around every 15 minutes with low uncertainty ranging between (0.01-0.02) under cloud-free conditions [26]. The AOD is retrieved from these channels to provide high accuracy and quick results. The latest version of AERONET is version three (V3) level two (L2.0) which is computed for three data quality levels: Level 1.0 (unscreened), Level 1.5 (cloud-screened and quality controlled), and Level 2.0 (quality-assured). Inversions, precipitable water, and other AOD-dependent products are derived from these levels [27]. In the Czech Republic there is only one AERONET station. This AERONET CIMEL instrument has approximately 1.2° full angle field of view (FOV) and it is installed on the roof of the administrative

building in Brno Airport (Figure 1) at the following coordinates: latitude 49.15647° N, longitude 16.68333° E, and with an elevation of 238 m above sea level, this station can observe and process the data automatically, and it is calibrated yearly to provide the best results, and to avoid offsets occurrence in the radiance measurements [28].

In this study, we present data from level 2.0 of the data quality assurance. AERONET AOD measurements at 440 μm and 675 μm from Brno Airport station during the period (June 2017 – December 2018). These observations were interpolated to 550 nm, in order to compare it with MODIS retrievals, using the Angstrom exponents (440 – 675 μm) provided in the AERONET datasets according to the Angstrom’s turbidity equation [29] represented in Equation (1).

$$\tau_a(\lambda) = \beta\lambda^{-\alpha} \tag{1}$$

The AOD values at two different wavelength values λ_1, λ_2 are related by Equation (2).

$$\tau_a(\lambda_1) = \tau_a(\lambda_2) * \left(\frac{\lambda_1}{\lambda_2}\right)^{-\alpha} \tag{2}$$

where $\tau_a(\lambda)$ is the AOD at a wavelength λ in microns, α is the Angstrom wavelength exponent, and β is the Angstrom’s turbidity coefficient.

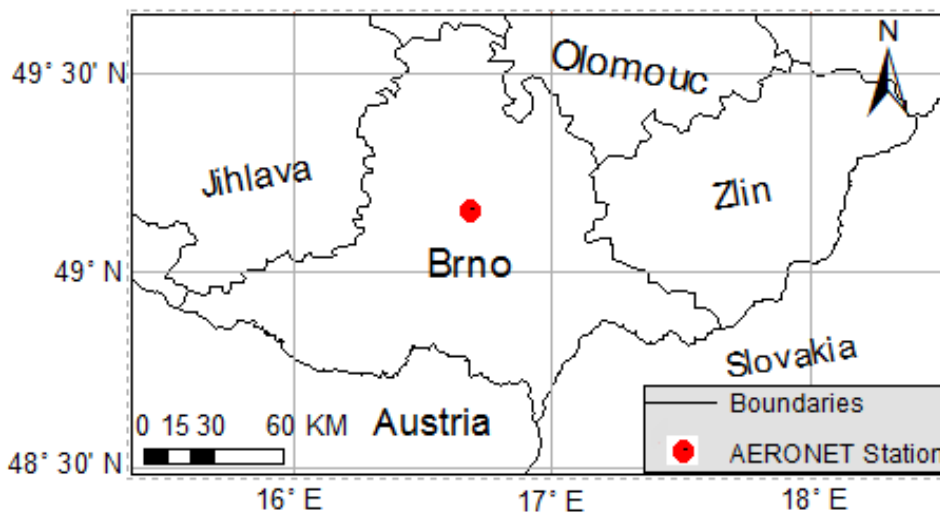


Fig. 1 – Geographical boundaries of the area of study. The red dot represents the location of the AERONET station.

METHODOLOGY

The comparison takes place between the average of Brno AERONET observations in the period (± 30 minutes) of the Terra satellite passing over this station (approximately 10:30 am), and the mean value of AOD retrievals at 550 μm of nine-pixel sample centered on this AERONET station, at least three pixels should be available and have the required quality assurance, QA=2,3 for DB, and QA=3 for DT and DTB. Considering that AODAERONET represents the true value [30]. To determine the uncertainty of retrieving algorithms with a sample size (N) versus AERONET measurements, we calculate the Pearson product-moment correlation coefficient (R), RMSE, shown in Equation (3), and the Mean Absolute Error (MAE) as presented in Equation (4), to find which algorithm is compatible the best with the ground observations. Moreover, we will use the Expected Error (EE) equation for retrieving AOD over land at the 10 km spatial resolution [31] to determine the

quality of retrievals, the EE equation is represented in Equation (5). Retrievals falling within the EE envelopes must meet Equation (6).

$$RMSE = \sqrt{\frac{1}{N} \sum (AOD_{AERONET} - AOD_{MODIS})^2} \quad (3)$$

$$MAE = \frac{1}{N} \sum |AOD_{AERONET} - AOD_{MODIS}| \quad (4)$$

$$EE = \pm (0.05 + 0.15 \times AOD_{AERONET}) \quad (5)$$

$$AOD_{AERONET} - |EE| \leq AOD_{MODIS} \leq AOD_{AERONET} + |EE| \quad (6)$$

RESULTS AND DISCUSSION OF VALIDATION AND COMPARISON WITH AERONET OBSERVATIONS

After downloading and processing MODIS data, only data satisfying QA requirements corresponding to each algorithm in question were used during the study analysis.

Figure 2 shows the validations of Terra C6.1 DB, DT, and DTB retrievals compared to AERONET AOD measurements at the Brno Airport site from June 2017 to December 2018 (18 months). During the retrieval process, we noticed that the least number of retrievals were obtained from winter months due to thick cloud and snow coverage. According to data analysis, the C6.1 DT AOD retrievals agrees the best with AERONET AOD measurements ($R = 0.823$), and the percentage of retrievals falling within the EE envelope is remarkably high (82.67%), with an average Mean Absolute Error ($MAE = 0.044$) and the smallest root mean square error compared to the other algorithms ($RMSE = 0.059$). DB has the lowest correlation coefficient ($R = 0.765$), also the error was noticeably high with ($RMSE = 0.069$ and $MAE = 0.052$). On the other hand, the DB has a slightly better percentage of data samples that fell within the EE envelope than the DTB retrievals with EE (80.85%) and (80%) respectively. Moreover, DTB retrievals show better results than DB retrievals ($R = 0.819$), and the error is slightly higher than that of DT retrievals ($MAE = 0.047$ and $RMSE = 0.063$). Figure 3 shows the linear regression between each MODIS algorithm retrievals and AERONET observations, it also shows the real error ($\tau_{MODIS} - \tau_{AERONET}$) for each pair of AOD. According to Figure 3, we found that the errors of all three algorithms have normal distribution on both sides of the 1:1 line with close proportions. Besides that, almost all retrievals of the three algorithms with low values of AOD ($AOD < 0.1$) have small errors. Based on obtained results, we found that the DTB (Figure 3c) was more influenced by the DT (Figure 3b) than DB (Figure 3a). Besides, the sample size for both algorithms was the same ($N = 75$) since the required QA value for both the DT and DTB algorithms is 3. DT algorithm alone gave good results. This is of no surprise, as the DT algorithm is known to be suitable for highly vegetated areas, such as the Czech Republic. According to Wie et al, the DT is more suitable for highly vegetated and low AOD loading areas in all Europe, which is consistent with our findings [13]. However, one drawback for this algorithm might be the sample size as larger sample size and probably larger coverage area can be obtained by the DB algorithm due to lower QA requirement ($QA = 2$ or 3). One challenge that faced us during this study is the fact that there is only one AERONET station in the Czech Republic located in Brno. Even this station was under calibration and data from three months (June – August, 2018) was missing. However, by merging the data from the years 2017 and 2018 we were able to have MODIS AOD retrievals from the four seasons and increase the reliability of the validation.

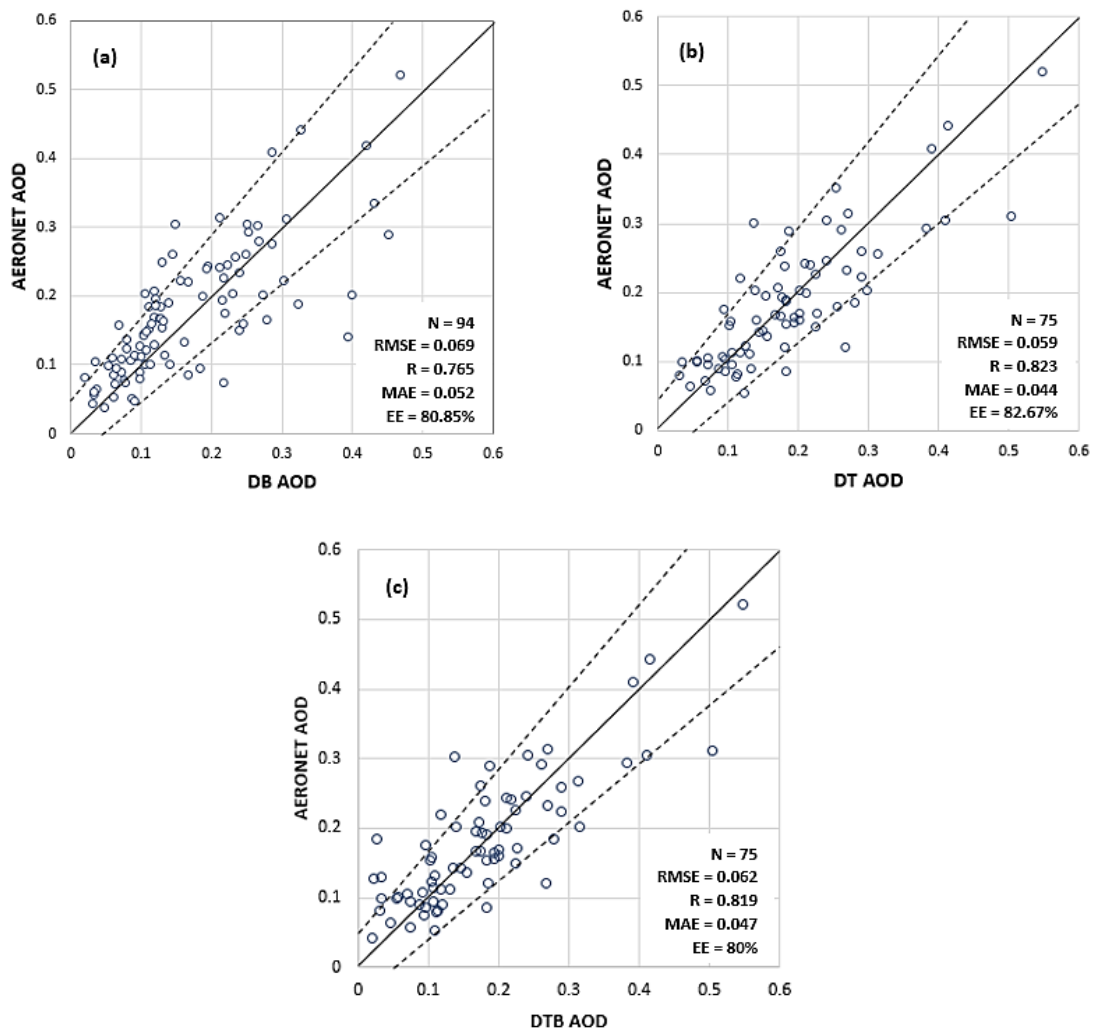


Fig. 2 – Scatter plots of Terra MODIS C6.1 DB (a), DT (b) and DTB (c) AOD retrievals against AERONET AOD observations from June 2017 to December 2018. The solid line indicates the 1:1 line, and the dashed lines indicates the envelopes of the expected error (EE). The sample size (N), correlation coefficient (R), mean absolute error (MAE), and root-mean-square error (RMSE) are also given. EE represent the percentages (%) of retrievals falling within the EE envelopes.

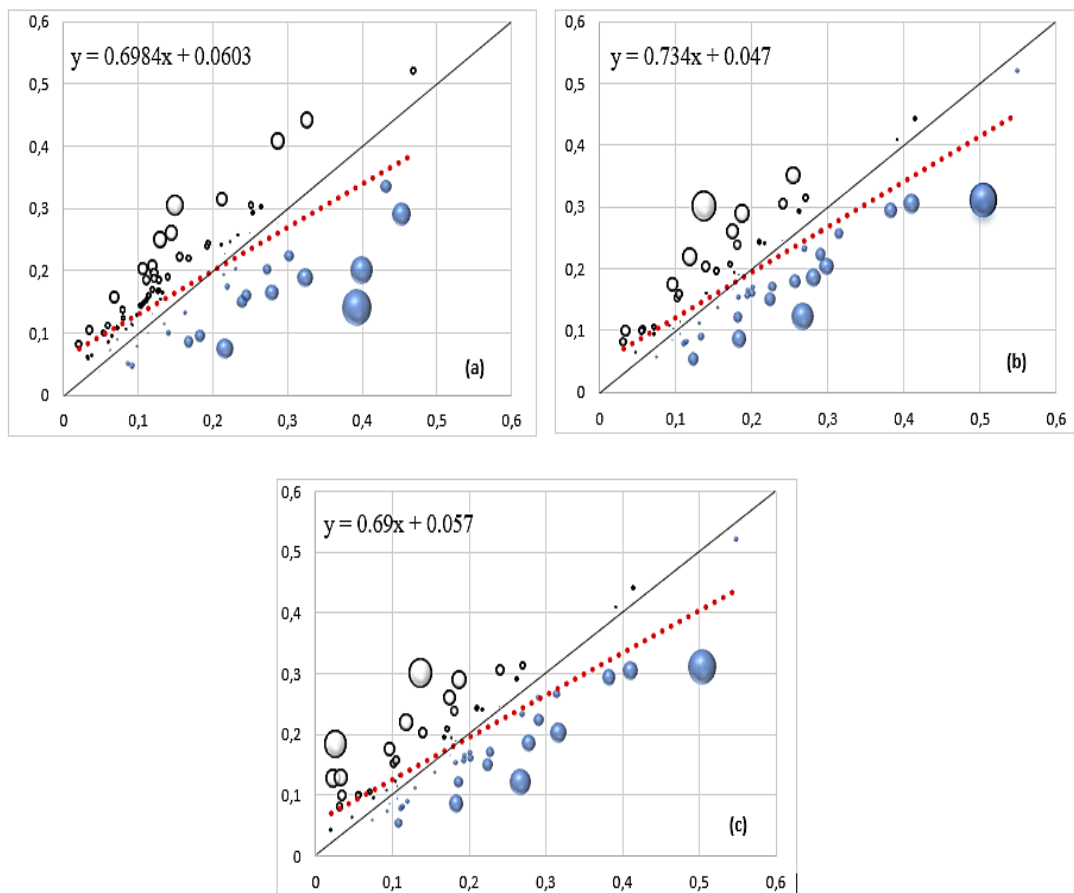


Fig. 3 – The linear regression between MODIS C6.1 DB (a), DT (b), and DTB (c) AOD retrievals against AERONET AOD observations. The X axis represents MODIS retrievals and the Y axis represents AERONET observations. The solid line indicates the 1:1 line. Each circle represents one pair of MODIS/AERONET AOD, and its size is based on the value of the real error. The blue circles represent the pairs of AOD when ($\tau_{MODIS} > \tau_{AERONET}$) and white circles represent the pairs when ($\tau_{AERONET} > \tau_{MODIS}$).

SUMMARY AND CONCLUSION

Three AOD products; DB, DT, and DTB, generated from MODIS C6.1, were compared and validated over land at Brno AERONET station (version 3 Level 2) in the Czech Republic during the period (June 2017 till the end of 2018). We investigated the accuracy and uncertainty of the three algorithms in order to draw recommendations. Based on our results, the DT algorithm gave the closest estimations to the real AOD values observed at Brno AERONET station, with a correlation coefficient ($R = 0.823$), root mean square error ($RMSE = 0.059$), and with a high percentage of retrievals falling within the EE envelope ($EE = 82.67\%$). The combined algorithm, DTB, failed to bring better estimations than the DT algorithm alone, yet it was found to be more suitable than the use of the DB algorithm solely. The accuracy of the DB was lower than the other two algorithms, yet still acceptable for estimating AOD as 80.85% of retrievals fell within the expected error envelope. We also found that the MODIS coverage is highly effected by NDVI, among other factors like snow surfaces and cloud density, and thus we recommend testing the coverage of the three MODIS

algorithms above all the Czech Republic first and then use the results of the current study to reach an optimal methodology to estimate the AOD over the whole country. Another recommendation would be using the AERONET data of 2019 when it is fully available to investigate whether a longer period influences the results of the current statistics study.

ACKNOWLEDGMENTS

Authors would like to thank NASA for making the MODIS and AERONET data public available, we also thank the principle investigator of AERONET CIMEL sunphotometer in Brno airport Mr. Jan Hanuš and his staff for establishing and maintaining Brno airport site. All data used in this study are available at the Level-1 and Atmosphere Archive and Distribution System Distributed Active Archive Center (<http://ladsweb.nascom.nasa.gov>), and AERONET data is available at (<https://aeronet.gsfc.nasa.gov>). Finally, we would like to thank Prof. Čepek from the Department of Geomatics and Prof. Štroner from the Department of Geodesy, Czech Technical University (CTU), for proofreading this manuscript. This work was funded by Project: 2018-EU-IA-0095 INEA entitled "Geo-harmonizer : building an EU-wide automated mapping system".

REFERENCES

- [1] Zhang, L., M. Zhang, and Y.B. Yao., 2019. Multi-Time Scale Analysis of Regional Aerosol Optical Depth Changes in National-Level Urban Agglomerations in China Using Modis Collection 6.1 Datasets from 2001 to 2017. *Remote Sensing*, 11(2).
- [2] Kaufman, Y.J., et al., 1997. Passive remote sensing of tropospheric aerosol and atmospheric correction for the aerosol effect. *Journal of Geophysical Research-Atmospheres*, 102(D14): 16815-16830.
- [3] Cheng, A.Y.S., M.H. Chan, and X. Yang., 2006. Study of aerosol optical thickness in Hong Kong, validation, results, and dependence on meteorological parameters. *Atmospheric Environment*, 40(24): 4469-4477.
- [4] IPCC (2007), *Climate Change 2007: The Physical Science Basis*, Contribution of Working Group I to the Fourth Assessment Report of the Intergovernmental Panel on Climate Change, edited by S. Solomon et al., Cambridge University Press, Cambridge, United Kingdom and New York, NY, USA.
- [5] Poschl, U., 2005. *Atmospheric aerosols: Composition, transformation, climate and health effects*. *Angewandte Chemie-International Edition*, 44(46): 7520-7540.
- [6] Remer, L.A., et al., 2005. The MODIS aerosol algorithm, products, and validation. *Journal of the Atmospheric Sciences*, 62(4): 947-973.
- [7] Sun, L., et al., 2016. A Universal Dynamic Threshold Cloud Detection Algorithm (UDTCDA) supported by a prior surface reflectance database. *Journal of Geophysical Research-Atmospheres*, 121(12): 7172-7196.
- [8] Tanre, D., M. Herman, and Y.J. Kaufman., 1996. Information on aerosol size distribution contained in solar reflected spectral radiances. *Journal of Geophysical Research-Atmospheres*, 101(D14): 19043-19060.
- [9] Tanre, D., et al., 1997. Remote sensing of aerosol properties over oceans using the MODIS/EOS spectral radiances. *Journal of Geophysical Research-Atmospheres*, 102(D14): 16971-16988.
- [10] Kaufman, Y.J., D. Tanre, and O. Boucher., 2002. A satellite view of aerosols in the climate system. *Nature*, 419(6903): 215-223.
- [11] Li, Z., et al., 2009. Uncertainties in satellite remote sensing of aerosols and impact on monitoring its long-term trend: a review and perspective. *Annales Geophysicae*, 27(7): 2755-2770.
- [12] Bilal, M., et al., 2013. A Simplified high resolution MODIS Aerosol Retrieval Algorithm (SARA) for use over mixed surfaces. *Remote Sensing of Environment*, 136: 135-145.
- [13] Wei, J., et al., 2019. MODIS Collection 6.1 aerosol optical depth products over land and ocean: validation and comparison. *Atmospheric Environment*, 201: 428-440.
- [14] Jeong, M.J., et al., 2011. Impacts of Cross-Platform Vicarious Calibration on the Deep Blue Aerosol Retrievals for Moderate Resolution Imaging Spectroradiometer Aboard Terra. *Ieee Transactions on Geoscience and Remote Sensing*, 49(12): 4877-4888.
- [15] Sayer, A.M., et al., 2014. MODIS Collection 6 aerosol products: Comparison between Aqua's e-Deep Blue, Dark Target, and "merged" data sets, and usage recommendations. *Journal of Geophysical Research-Atmospheres*, 119(24): 13965-13989.

- [16] Levy, R.C., et al., 2010. Global evaluation of the Collection 5 MODIS dark-target aerosol products over land. *Atmospheric Chemistry and Physics*, 10(21): 10399-10420.
- [17] King, M.D., et al., 2013. Spatial and Temporal Distribution of Clouds Observed by MODIS Onboard the Terra and Aqua Satellites. *Ieee Transactions on Geoscience and Remote Sensing*, 51(7): 3826-3852.
- [18] Gupta, P., et al., 2016. A surface reflectance scheme for retrieving aerosol optical depth over urban surfaces in MODIS Dark Target retrieval algorithm. *Atmospheric Measurement Techniques*, 9(7): 3293-3308.
- [19] Levy, R.C., et al., 2013. The Collection 6 MODIS aerosol products over land and ocean. *Atmospheric Measurement Techniques*, 6(11): 2989-3034.
- [20] Hsu, N.C., et al., 2006. Deep blue retrievals of Asian aerosol properties during ACE-Asia. *Ieee Transactions on Geoscience and Remote Sensing*, 44(11): 3180-3195.
- [21] Hsu, N.C., et al., 2004. Aerosol properties over bright-reflecting source regions. *Ieee Transactions on Geoscience and Remote Sensing*, 42(3): 557-569.
- [22] Zawadzka, O. and Markowicz, K., 2014. Retrieval of aerosol optical depth from optimal interpolation approach applied to SEVIRI data. *Remote Sensing*, 6, 7182-7211; doi:10.3390/rs6087182
- [23] Chu, D.A., et al., 2002. Validation of MODIS aerosol optical depth retrieval over land. *Geophysical Research Letters*, 29(12).
- [24] Remer, L.A., et al., 2002. Validation of MODIS aerosol retrieval over ocean. *Geophysical Research Letters*, 29(12).
- [25] Holben, B.N., et al., 1998. AERONET - A federated instrument network and data archive for aerosol characterization. *Remote Sensing of Environment*, 66(1): 1-16.
- [26] Holben, B.N., et al., 2001. An emerging ground-based aerosol climatology: Aerosol optical depth from AERONET. *Journal of Geophysical Research-Atmospheres*, 106(D11): 12067-12097.
- [27] Goddard Space Flight Center. Aerosol Robotic Network 2019. Available online at <https://aeronet.gsfc.nasa.gov/> (accessed on 10th of May, 2019).
- [28] Dubovik, O., et al., 2000. Accuracy assessments of aerosol optical properties retrieved from Aerosol Robotic Network (AERONET) Sun and sky radiance measurements. *Journal of Geophysical Research-Atmospheres*, 105(D8): 9791-9806.
- [29] Liu, Y., et al., 2004. Validation of multiangle imaging spectroradiometer (MISR) aerosol optical thickness measurements using aerosol robotic network (AERONET) observations over the contiguous United States. *Journal of Geophysical Research-Atmospheres*, 109(D6).
- [30] Wei, J. and L. Sun, 2017. Comparison and Evaluation of Different MODIS Aerosol Optical Depth Products Over the Beijing-Tianjin-Hebei Region in China. *Ieee Journal of Selected Topics in Applied Earth Observations and Remote Sensing*, 10(3): 835-844.
- [31] Remer, L.A., et al., 2013. MODIS 3 km aerosol product: algorithm and global perspective. *Atmospheric Measurement Techniques*, 6(7): 1829-1844.

INFLUENCE OF PANEL ZONE SIZES ON ULTIMATE BEARING CAPACITY OF H-SHAPED STEEL FRAMES

Yan Zhang, Huijuan Liu, Yuhong Yang, Enhe Bao

College of Civil Engineering and Architecture, Guilin University of Technology, Guilin 541004, China; 864476103@qq.com

ABSTRACT

In order to explore the influence of panel zone sizes on the ultimate bearing capacity of H-shaped steel frames, this study examines a steel frame structure with cross-shaped sections consisting of beams, columns and panel zones based on mechanical equilibrium principles. The area ratio of either side of the flange to the web is taken as the main parameter.

The results show that the ultimate bearing capacity ratio curves can be grouped into three types. For the first type, the plastic hinge is formed in the panel zone. For the second type, when R_{pcb} , the strong column factor, is greater than 1.2, the plastic hinge is formed at the beam end; otherwise the plastic hinge is formed in the panel zone. For the third type, when $R_{pcb} \leq 0.8$, the plastic hinge is formed in the panel zone; otherwise the plastic hinge is formed at the beam end. The ultimate bearing capacity ratio curves of the local section of H-shaped steel largely fall in the first curve type, and the ultimate bearing capacity is larger when the panel zone size is excluded from the calculation than otherwise with the former being one to five times as large as the latter.

KEYWORDS

H-shaped steel frame, Panel zone, Strong column factor, Ultimate bearing capacity

INTRODUCTION

According to the current Chinese seismic code, panel zones are usually excluded from the calculation of the bearing capacity of steel frames. Generally, a panel zone is considered as either a "strong panel zone" or "rigid panel zone" in the overall steel framework structure calculation. Studies [1, 2] show that, according to the results from the common local cyclic loading test, the panel zone yields early and features better performance in terms of elastic-plastic deformation and energy dissipation. A new conformation form to connect the H-beam with the box-shaped panel zone of the I-beam weak axis is proposed in research [3] and, according to the results of the Finite Element Analysis, the panel zone of the box-shaped joint of the I-beam weak axis is discovered to be a "strong panel zone" whose mechanical property is superior to the traditional box-section columns structure. In the research of [4], numerical results have revealed that designs according to AISC360 and Eurocode 3 resulted in significant amounts of yielding of the panel zone while the designs according to FEMA 355D resulted in minimal amount of yielding. The panel zone deformation demands were quantified and an equation used to estimate the deformation levels. Weak panel zones are designed for the two specimens to drive plastic deformation in the panel zones, the plastic deformation will mainly develop in the panel zones without apparent plastic straining at the beam ends [5]. Studies [6-8] examine rectangular columns filled with concrete and the hysteresis loop model of the panel zone of H-shaped beams. Meanwhile, the experiments also focus on the mechanical properties of rectangular steel columns with outer ring stiffeners and irregular joint zones of H-shaped steel

beams. Moreover, with the assumption of the “rigid panel zone”, the damage mechanism of the whole steel frame structure has been explored. For example, Ref. [9] has studied the dynamic response of multi-levelled steel frame structure when the maximum speed of seismic waves is 0.5m/s, however, the factor of column base should be almost equal to strong column factor but more than 1.5; Ref. [10, 11] study American steel frame structure using the model of the sheared mass and the flexure bar system to comprehensively evaluate the anti-seismic effect while columns beams and column bases are articulated in the frame; Ref. [12] examines the elasto-plasticity dynamic performance of a super high-rise structure. Previous studies are mainly focused on the elastic-plastic performance of different plane zones in steel frames and the elastic-plastic performance of high-rise steel structures. Consequently, little light has been shed on the effect of the sizes of panel zones on the ultimate bearing capacity of H-shaped steel frames, especially of Chinese-manufactured H-shaped steel.

To unveil general patterns regarding the ultimate bearing capacity of Chinese H-shaped steel frames, this study examines cruciform steel frames consisting of beams, columns and panel zones for analysis purposes. Also, based on the principles of equilibrium mechanics, this study takes into account the flange-to-web area ratio as the main parameter while also considering other factors such as the axial compression ratio of columns, the span-depth ratio of structures, the depth-to-width ratio of panel zones and the ratio of panel zone width to floor height.

Research model

Panel zones are commonly designed strong enough to avoid premature buckling due to the shear load transferred by the adjacent beams. This design concept has been accepted by most of the countries, such as the US and China [13]. As shown in Figure 1(a), exemplifying a regular H-shaped steel frame where its storey height equals span, a cruciform steel frame consisting of common beams columns and panel zones is taken for analysis purposes. The size of the analytical model is also shown in Figure 1(a). In this model, the connections of beams, columns and panel zones are rigid, but supports are hinged. The calculation diagram with external force is shown in Figure 1 (b).

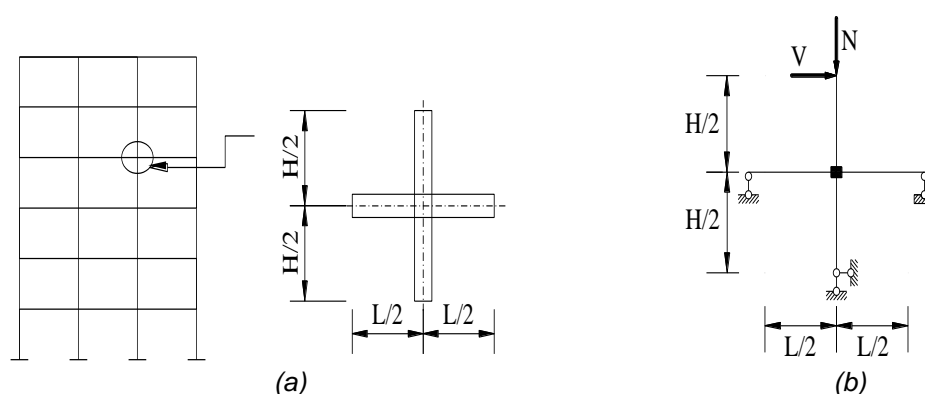


Fig. 1 - Local cruciform steel frame model

When the axial compression ratio (μ) is taken into consideration, Equation 1 is used to calculate the plastic section modulus in the direction of the major axis, and Equation 2 is used to calculate the plastic section modulus of the H-shaped steel beam [14].

$$W_{pc} = \begin{cases} \frac{\beta(4+\beta_c) - \mu^2(2+\beta_c)^2}{4\beta_c(2+\beta_c)} Ah & (\mu < \frac{A_w}{A}) \\ \frac{1}{2} Ah(1 - \mu) & (\mu \geq \frac{A_w}{A}) \end{cases} \quad (1)$$

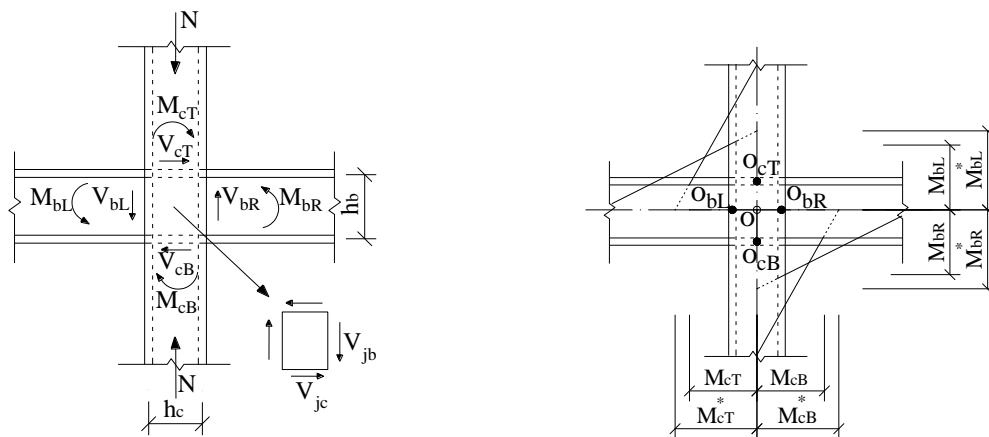
$$W_{pb} = Ah \left(\frac{4\beta_b + 1}{8\beta_b + 4} \right) \quad (2)$$

In the equations, β is the area ratio of either side of the flange (A_f) to the web (A_w) (the flange-to-web area ratios of beam and column are β_b and β_c , respectively); h is the section height of the H-shaped steel; A is the section area of the component.

Model analysis

Stress analysis

When the horizontal load (V) and the axial load (N) are applied to the local steel frame model, as shown in Figure 1(b), the pattern of force distribution in the beam, the column and the panel zone is shown in Figure 2(a). The bending moments in steel moment resisting frames are transferred between the beams and columns in the frame through either rigid or semi-rigid connections or joints [15]. The moment distribution in the column, the beam-end and the center node are shown in Figure 2(b).



(a) Force distribution in beam, column and panel (b) Moment distribution in column, beam-end and node center

Fig. 2 - Stress analysis of the model

In this model, h_b and h_c stand for the heights of the flange center in the beam and the column, respectively and the same calculation method is used both for the panel zone and for the column. So according to Figure 2(a), the equilibrium equations of the force in the panel zone are listed as follows:

$$M_j = V_{jb}h_c = V_{jc}h_b \quad (3)$$

$$V_{jc} = \frac{M_{bL} + M_{bR}}{h_b} - \frac{V_{cT} + V_{cB}}{2} \quad (4)$$

$$V_{jb} = \frac{M_{cT} + M_{cB}}{h_c} - \frac{V_{bL} + V_{bR}}{2} \quad (5)$$

where $M_{cT} = M_{cB} = 0.5V(H - h_b)$, $V_{cT} = V_{cB} = V$, $M_{bL} = M_{bR} = 0.5VH(L - h_c)/L$ and $V_{bL} = V_{bR} = VH/L$.

M_j is the bending moments of panel zone; M_{bL} and M_{bR} are the bending moments at both beam ends; V_{bL} and V_{bR} are the shear forces at both beam ends. M_{cT} and M_{cB} are the bending moments at both the upper end and the lower end of the column; V_{cT} and V_{cB} are the shear forces of the beam; V_{jc} and V_{jb} are the shear forces of the panel zone for column and beam.

According to Figure 2(b), the bending moment equations of the beam, the column and the center node are shown below:

$$M_{bL}^* + M_{bR}^* = M_{cT}^* + M_{cB}^* = M_j^* \quad (6)$$

$$M_{bL}^* + M_{bL}^* = M_{pbL} + M_{pbR} + (V_{bL} + V_{bR}) \times h_c/2 \quad (7)$$

$$M_{cT}^* + M_{cB}^* = M_{pcT} + M_{pcB} + (V_{cT} + V_{cB}) \times h_b/2 \quad (8)$$

$$M_j^* = M_j + (V_{cT} + V_{cB}) \times h_b/2 + (V_{bL} + V_{bR}) \times h_c/2 \quad (9)$$

Assuming that the whole section plastic moments at column ends, beam ends and in the panel zone are M_{pc} (the top and bottom end moments of the column consequently being M_{pcT} and M_{pcB}), M_{pb} (the left and right end moments of the beam being M_{pbL} and M_{pbR}) and M_{pj} , respectively, then correspondingly, the moments of the column, beam and panel zone in the node center O are M_{pcT}^* , M_{pcB}^* , M_{pbL}^* , M_{pbR}^* and M_{pj}^* , respectively. The equations concerning these variables are:

$$M_{pbL}^* + M_{pbR}^* = M_{pbL} + M_{pbR} + (V_{bL} + V_{bR}) \times h_c/2 \quad (10)$$

$$M_{pcT}^* + M_{pcB}^* = M_{pcT} + M_{pcB} + (V_{cT} + V_{cB}) \times h_b/2 \quad (11)$$

$$M_{pj}^* = M_{pj} + (V_{cT} + V_{cB}) \times h_b/2 + (V_{bL} + V_{bR}) \times h_c/2 \quad (12)$$

where, when the whole section plastic moment is reached, the following equations are true:

$$V_{cT} = V_{cB} = 2M_{pc}/(L - h_b) \quad (13)$$

$$V_{bL} = V_{bR} = 2M_{pb}/(L - h_c) \quad (14)$$

$$V_{cT} = V_{cB} = M_{pj}^*/H \quad (15)$$

$$V_{bL} = V_{bR} = M_{pj}^*/L \quad (16)$$

When Equation 13 – 16 are substituted into 10 – 12, the following equations can be obtained:

$$M_{pcT}^* = M_{pcB}^* = M_{pc}^* = M_{pc}/(1 - h_b/H) \quad (17)$$

$$M_{pbL}^* = M_{pbR}^* = M_{pb}^* = M_{pb}/(1 - h_c/L) \quad (18)$$

$$M_{pj}^* = M_{pj}/(1 - (h_c/L + h_b/H)) \quad (19)$$

Also the two equations below are taken into account :

$$M_{pc} = W_{pc} \times f_y \quad (20)$$

$$M_{pb} = W_{pb} \times f_y \tag{21}$$

The equation of the plastic moment in the whole section of the H-shaped steel column panel zone is written as [16]:

$$M_{pj} = (Ah_b\sqrt{1-u^2}) \times f_v/\sqrt{3}(2\beta_c + 1) \tag{22}$$

When the panel zone size is taken into consideration, V_u^* the ultimate horizontal bearing capacity of the cross-shaped steel frame section, is expressed as:

$$V_u^{J*} = \text{Min}\{2M_{pc}^*, 2M_{pb}^*, M_{pj}^*\} \times \frac{1}{H} \tag{23}$$

Accordingly, when the panel zone size is excluded, V_u^j , the ultimate horizontal bearing capacity of the cross-shaped steel frame section, is expressed as:

$$V_u^j = \text{Min}\{2M_{pc}, 2M_{pb}\} \times \frac{1}{H} \tag{24}$$

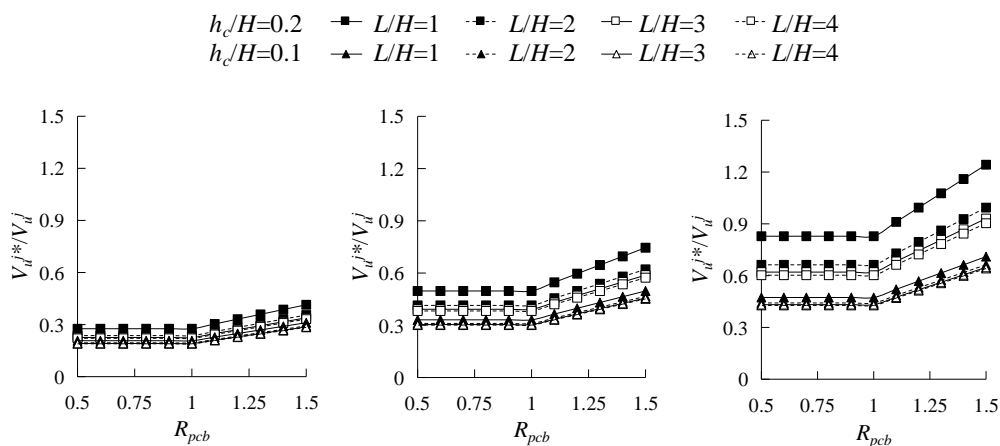
And the strong column factor is calculated as:

$$R_{pcb} = M_{pc}/M_{pb} \tag{25}$$

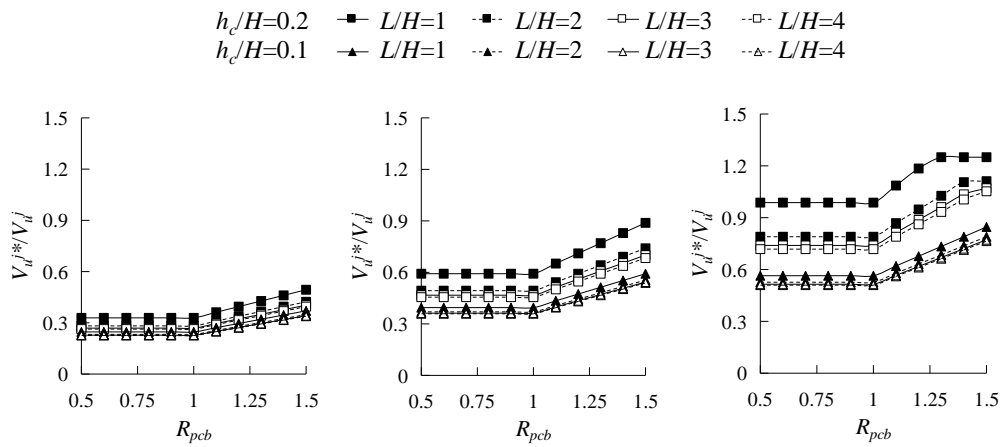
Influence of panel zone size on ultimate bearing capacity of H-shaped steel analysis model

Based on Equation 23 and 24, β is taken as the main parameter under study (given the fact that there is no significant difference in the β values of a certain section with the same specification, an average β value is assigned to each specific section. Therefore, β_b in narrow flange beam of Chinese-made H-shaped steel is 0.7, in middle flange beam is 1.06, and β_c in wide flange column of Chinese-made H-shaped steel is 1.49). Additionally, μ , L/H (span-to-depth ratio of structure), h_b/h_c (depth-to-width ratio of panel zone) and h_c/H (ratio of panel zone width to floor height) are taken into consideration as well for the study to examine the difference between the results from when the panel zone size is included in and excluded from the model. In both cases, the panel zone which is defined as the portion of the column contained within the beam-to-column joint can be subjected to high shear stresses arising from the unbalanced moments at interior joints that are produced by lateral loads such as wind and earthquake forces [17].

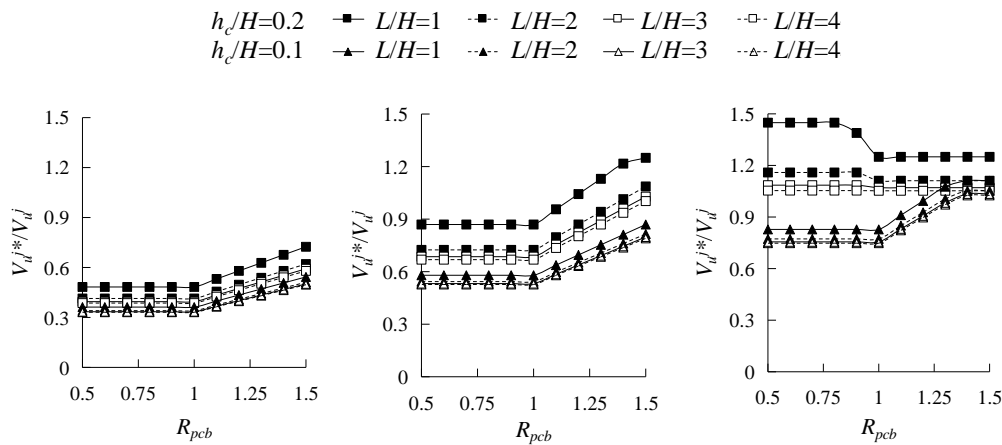
In Figure 3, the vertical axis shows the ultimate bearing capacity ratio (V_u^*/V_u^j), while the horizontal axis indicates strong column factor (R_{pcb}).



(a) Axial compression ratio of column $\mu=0$



(b) Axial compression ratio of column $\mu=0.3$



(c) Axial compression ratio of column $\mu=0.6$

Fig. 3 - Narrow flange beam of H-shaped steel ($\beta_b=0.70$)

$h_c/H=0.2$ \blacksquare $L/H=1$ \blacksquare $L/H=2$ \square $L/H=3$ \square $L/H=4$
 $h_c/H=0.1$ \blacktriangle $L/H=1$ \blacktriangle $L/H=2$ \triangle $L/H=3$ \triangle $L/H=4$

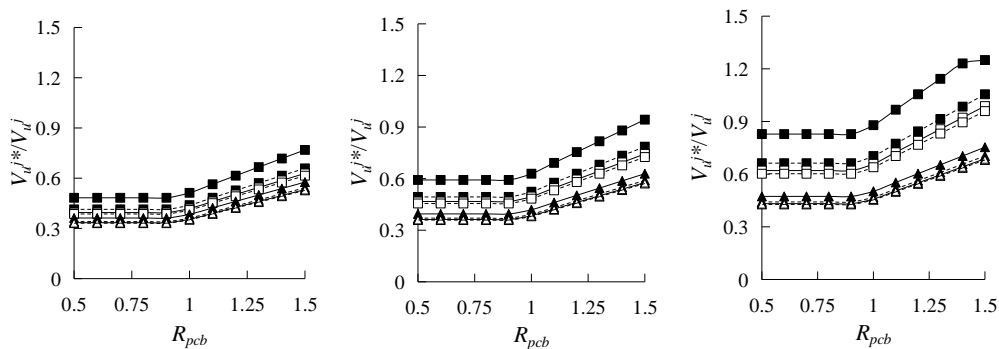
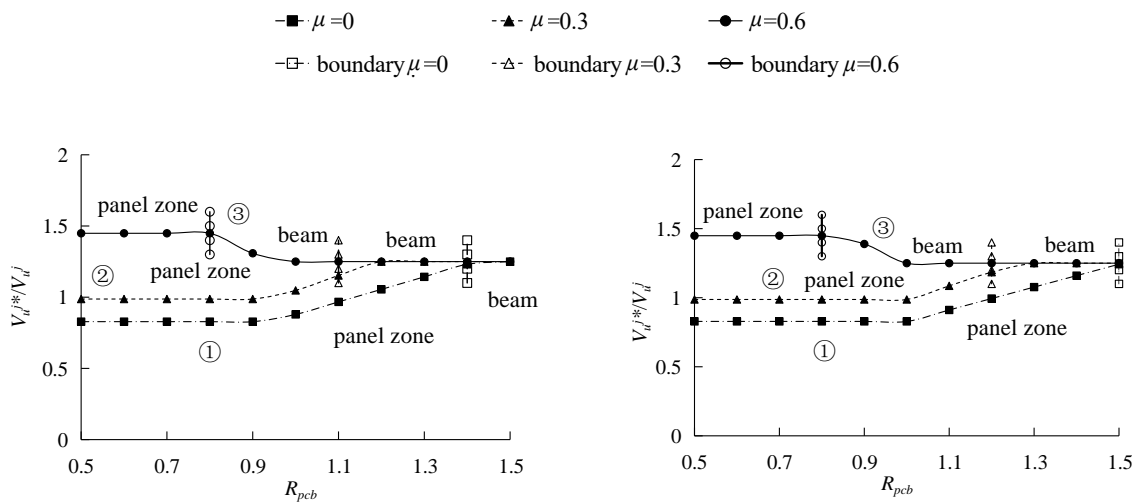


Fig. 4 - Ultimate bearing capacity ratio patterns of middle flange beam analysis model



(a) Narrow flange beam of H-shaped steel ($\beta_b = 0.70$) (b) Middle flange beam of H-shaped steel ($\beta_b = 1.06$)
 Fig. 5 - Plastic damage change boundary of analysis model

As shown in Figure 3(a) and Figure 3(b), when the panel zone size is not taken into consideration, the ultimate bearing capacity is dependent either on the column end moment (when $R_{pcb} < 1$) or on the beam end moment (when $R_{pcb} \geq 1$). On the other hand, when the panel zone size is taken into consideration, there are three types of curves regarding the ultimate bearing capacity. For the first type, when $R_{pcb} \leq 1$, the curve stays a horizontal line; when $R_{pcb} > 1$, the curve turns into an oblique line going upwards as R_{pcb} increases indicating plastic damage in the panel zone, as is shown in Figure 5(a) ①. For the second type, when $R_{pcb} \leq 1$, the curve stays a horizontal line indicating plastic damage in the panel zone; when $R_{pcb} > 1$, the curve first becomes an oblique line going upwards as R_{pcb} increases also indicating plastic damage in the panel zone, and then (as R_{pcb} grows larger) turns into a horizontal line indicating plastic damage at the beam end (see Figure 5(a) ②). For the third type, when $R_{pcb} \leq 0.8$, the curve stays a horizontal line with a relatively large vertical value indicating plastic damage in the panel zone; when $R_{pcb} > 0.8$, the curve first becomes an oblique line going downwards as R_{pcb} increases, and then turns into a horizontal line as R_{pcb} grows larger indicating plastic damage at the beam end (see Figure 5(a) ③).

Figure 3 illustrates the $V_u^*/V_u^j \sim R_{pcb}$ correlation of the narrow flange beam of H-shaped steel. In the case where $\mu=0$, the curve where $h_c/H=0.2$, $L/H=1$ and $h_b/h_c=2$ grows over 1 (i.e., $V_u^*/V_u^j > 1$) when $R_{pcb} > 1.1$; the ultimate bearing capacity is larger when the panel zone size is incorporated than otherwise. In any other cases, $V_u^*/V_u^j < 1$, specifically ranging from 0.2 to 1.0 (i.e., V_u^* is one to five times of V_u^j); the ultimate bearing capacity is larger when the panel zone size is excluded. It can thus be concluded that when $\mu=0$, V_u^j is most likely to be larger than V_u^* with V_u^j being five times as large as V_u^* in the most extreme case scenario. In addition, the shape of the $V_u^*/V_u^j - R_{pcb}$ curve shows great resemblance with that of Figure 5(a) ① when $\mu=0$, and yielding all occurs in the panel zone when the panel zone size is taken into consideration.

In the case where $\mu=0.3$, the curve where $h_c/H=0.2$ and $h_b/h_c=2$ largely grows over 1 (i.e., $V_u^*/V_u^j > 1$) when $R_{pcb} > 1.2$; the ultimate bearing capacity is larger when the panel zone size is incorporated than otherwise. The shape of the curve shows great resemblance with that of Figure 5(a) ②. When the panel zone size is taken into consideration, yielding occurs in the panel zone (in the case where $R_{pcb} < 1.2$) or in the beam (in the case where $R_{pcb} \geq 1.2$). In any other cases, $V_u^*/V_u^j < 1$, specifically ranging from 0.2 to 1.0 (i.e., V_u^* is one to five times of V_u^j); the ultimate bearing capacity is larger when the panel zone size is excluded. It can be concluded that when $\mu=0.3$, V_u^j is most likely to be larger than V_u^* with V_u^j being five times as large as V_u^* in the most extreme case scenario. In addition, the shapes of all the $V_u^*/V_u^j - R_{pcb}$ curves (except the one where $h_c/H=0.2$ and $h_b/h_c=2$) show great resemblance with that of Figure 5(a) ① when $\mu=0.3$, and yielding all occurs in the panel zone when the panel zone size is taken into consideration.

In the case where $\mu=0.6$, $V_u^*/V_u^j > 1$ always stands true for the curves where $h_c/H=0.2$ and $h_b/h_c=2$, and mostly stands true, when $R_{pcb} > 1.2$, for the curves either where $h_c/H=0.2$ and $h_b/h_c=1.5$ or where $h_c/H=0.1$ and $h_b/h_c=2$; the ultimate bearing capacity is larger when the panel zone size is incorporated than otherwise. In any other cases, $V_u^*/V_u^j < 1$, specifically ranging from 0.3 to 1.0 (i.e., V_u^* is one to three times of V_u^j); the ultimate bearing capacity is larger when the panel zone size is excluded. The shape of the $V_u^*/V_u^j - R_{pcb}$ curve where $h_c/H=0.2$ and $h_b/h_c=2$ shows great resemblance with that of Figure 5(a) ③. When the panel zone size is taken into consideration, yielding occurs in the panel zone (in the case where $R_{pcb} \leq 0.8$) or in the beam (in the case where $R_{pcb} > 0.8$). The shapes of the $V_u^*/V_u^j - R_{pcb}$ curves either where $h_c/H=0.2$ and $h_b/h_c=1.5$ or where $h_c/H=0.1$ and $h_b/h_c=2$ show great resemblance with that of Figure 5(a) ②. When the panel zone size is taken into consideration, yielding occurs in the panel zone (in the case where $R_{pcb} \leq 1.2$) or in the beam (in the case where $R_{pcb} > 1.2$). In any other cases, the shape of the $V_u^*/V_u^j - R_{pcb}$ curves shows great resemblance with that of Figure 5(a) ①. When the panel zone size is taken into consideration, yielding all occurs in the panel zone.

Figure 4 illustrates the $V_u^*/V_u^j \sim R_{pcb}$ relationship of the middle flange beam analysis model ($h_b/h_c=1.5$, $\mu=0, 0.3$ and 0.6). In the case where $\mu=0.6$, the curve where $h_c/H=0.2$ largely grows over 1 (i.e., $V_u^*/V_u^j > 1$) when $R_{pcb} > 1.1$; the ultimate bearing capacity is larger when the panel zone size is incorporated than otherwise. The curve has the same shape as Figure 5(a) ② does. When the panel zone size is taken into consideration, yielding occurs in the panel zone (in the case where $R_{pcb} < 1.2$) or in the beam (in the case where $R_{pcb} \geq 1.2$). In any other cases, $V_u^*/V_u^j < 1$, specifically ranging from 0.3 to 1.0 (i.e., V_u^* is one to three times of V_u^j) and showing a curve shape similar to Figure 5(a) ①; the ultimate bearing capacity is larger when the panel zone size is excluded; and yielding all occurs in the panel zone when the panel zone size is taken into consideration. According to the model analysis, the ultimate bearing capacity ratio of the middle flange beam of H-shaped steel is larger than that of the narrow flange beam.

Figure 5(a) illustrates the three curves with the largest ultimate bearing capacity ratios, each chosen from each of the three types of curves in Figure 3 (regarding narrow flange beam of H-shaped steel). Figure 5(b), in contrast, shows the ultimate bearing capacity ratio curves of middle flange beam of H-shaped steel. As is shown in Figure 5(b), in the case where $\mu=0$, the shape of the

curve matches not the first but the second type of curve in Figure 5(a), and yielding occurs in the beam when $R_{pcb}=1.5$.

As is shown in Figure 3 to Figure 5, when and only when $h_b/h_c=2.0$, $\mu=0.6$ and $h_c/H=0.2$, the shape of the ultimate bearing capacity ratio curve matches that of the third curve type, and yielding occurs in the panel zone (in the case where $R_{pcb}<0.8$) or in the beam (in the case where $R_{pcb}\geq 0.8$); the ultimate bearing capacity is larger when the panel zone size is incorporated than otherwise. When $h_b/h_c=2.0$, $\mu=0.3$ and $h_c/H=0.2$ or when $h_b/h_c=2.0$, $\mu=0.6$ and $h_c/H=0.1$, the shape of the ultimate bearing capacity ratio curve matches that of the second curve type; yielding occurs in the panel zone when $R_{pcb}<1.2$ or in the beam if $R_{pcb}\geq 1.2$. When yielding occurs in the beam, the ultimate bearing capacity is larger with the panel zone size incorporated than otherwise. In any other cases, the shape of the ultimate bearing capacity ratio curve matches that of the first curve type. The shape of the ultimate bearing capacity ratio curve of the local section of H-shaped steel largely matches that of the first type of curve, and a plastic hinge forms in the panel zone of the analysis model. The ultimate bearing capacity is smaller when the panel zone size is incorporated than otherwise with V_u^j being one to five times as large as V_u^{j*} . The behaviour of the panel zone plays a significant role in determining the overall stiffness and capacity of the frame [18]. Therefore, if the panel zone size is not incorporated in the calculation, the ultimate bearing capacity of an H-shaped steel frame may be overestimated, leading to unsafe structure design.

CONCLUSION

In order to examine the influence of the panel zone size on the ultimate bearing capacity of Chinese H-shaped steel frames, β , the area ratio of either side of the flange (A_f) to the web (A_w), is taken as the main research parameter and the study is based on mechanical equilibrium principles with findings shown below:

- (a) The ultimate bearing capacity ratio curves can be grouped into three types. For the first type, the plastic hinge is formed in the panel zone. For the second type, when R_{pcb} , the strong column factor, is greater than 1.2, the plastic hinge is formed at the beam end, otherwise the plastic hinge is formed in the panel zone. For the third type, when $R_{pcb}\leq 0.8$, the plastic hinge is formed in the panel zone, otherwise the plastic hinge is formed at the beam end.
- (b) When the height-to-width ratio of the panel zone (h_b/h_c) equals 2.0, the axial compression ratio (μ) equals 0.6 and $h_c/H=0.2$, the shape of the ultimate bearing capacity ratio curve matches that of the third type of curve, and the ultimate bearing capacity is larger when the panel zone size is incorporated than otherwise. In the case where $h_b/h_c=2.0$, $\mu=0.3$ and $h_c/H=0.2$, or where $h_b/h_c=2.0$, $\mu=0.6$ and $h_c/H=0.1$, the shape of the ultimate bearing capacity ratio curve matches that of the second type of curve. In the case where $R_{pcb}\geq 1.2$, the ultimate bearing capacity is larger when the panel zone size is incorporated than otherwise. In any other conditions, the shape of the ultimate bearing capacity ratio matches that of the first curve type.
- (c) The ultimate bearing capacity ratio curves of the local section of H-shaped steel largely fall in the first curve type, which means that the plastic hinge is formed in the panel zone. The ultimate bearing capacity is smaller when the panel zone size is incorporated than otherwise with V_u^j being one to five times as large as V_u^{j*} . Therefore, if the panel zone size is not incorporated in the calculation, the ultimate bearing capacity of an H-shaped steel frame may be overestimated, leading to unsafe structure design.
- (d) In the case where the panel zone size is not taken into account, the ultimate bearing capacity is dependent on the moment of the column end when $R_{pcb}\leq 1$, or on the moment of the beam end when $R_{pcb}>1$.

REFERENCES

- [1] Pan L.L., Chen Y.Y., 2012. Experimental study on H-shaped beam-to-column connections with vertical Stiffener. *Journal of Building Structures*, 33(12): 1-9. DOI: 10.14006/j.jzjgxb.2012.12.004
- [2] Pan L.L., Chen Y.Y., Jiao W.F., Chuan G.H., 2015. Experimental study on panel zone in spatial H-shaped beam-column connections under cyclic loading. *Journal of Building Structures*, 36(10): 11-19.
- [3] Lu L.F., Xu Y.L., Zhou T.H., Zheng H., 2016. Experimental research on box strengthened Joint connection for weak axis of I-section column-H-shaped beam under Monotonic Loading. *Journal of Building Structures*, 37(2): 73-80. DOI: 10.14006/j.jzjgxb.2016.02.010
- [4] Mehmet T., Cem T., 2015. Panel zone deformation demands in steel moment resisting frames. *Journal of Constructional Steel Research*, 110:65–75. DOI: 10.1016/j.jcsr.2015.02.017
- [5] Chen Y.Y., Pan L.L., Jia L.J., 2017. Post-buckling ductile fracture analysis of panel zones in welded steel beam-to-column connections. *Journal of Constructional Steel Research*, 132: 117-129. DOI: 10.1016/j.jcsr.2017.01.015
- [6] Toshiyuki F., 2007. Local elasto-plastic behavior of steel beam to concrete-filled square steel tube column moment connections—Simple model of load-deformation relations for connection details using internal diaphragms or internal diaphragms with extended flanges. *Journal of Structural and Construction Engineering*, 617: 177-184.
- [7] Toshiyuki F., 2015. Local elasto-plastic behavior of steel beam to concrete-filled square steel tube column moment connections—Model of load-deformation relations for eccentric details using internal diaphragms or internal diaphragms with extended flanges. *Journal of Structural and Construction Engineering*, 714(80): 1337-1345.
- [8] Shintaro M., Takuro O., Ryusuke I., Tsuyoshi T., 2013. Elasto-plastic behavior of offset beam-to-column connection panels with exterior diaphragms. *Journal of Structural and Construction Engineering*, 692(10):1823-1830. DOI: 10.3130/aijs.78.1823
- [9] Iathong C., Yuji K., Keiichiro S., 2015. Effects of input direction of ground motion and column overdesign factor on seismic response of 3D steel moment frames with square tube columns. *Journal of Structural and Construction Engineering*, 717(80): 1773-1783.
- [10] Hiroyuki T., Gregory M., Laura L., 2007. Evaluation of seismic response of multi-story structures using dynamic stability coefficients. *Journal of Structural and Construction Engineering*, 618(8): 65-72.
- [11] Hiroyuki T., Gregory M., Laura L., 2010. Continuous Column Effects of Gravity Columns in U.S. Steel Moment-resisting Frame Structures—Continuous columns effects in steel moment frames in perspective of dynamic stability Part 2. *Journal of Structural and Construction Engineering*, 650(75): 761-770.
- [12] Zhang H.D., Wang Y.F., 2012. Energy-based study on the dynamic elastic plasticity seismic capacity of a high-rise steel structure. *China Civil Engineering Journal*, 45(6): 65-73. DOI: 10.15951/j.tmgcxb.2012.06.015
- [13] AISC (American Institute of Steel Construction), 2016. AISC 314-16: Specification for Structural Steel Buildings. AISC, Chicago, Illinois, USA.
- [14] BRI (Building Research Institution of Japan), 2006. Design specifications of steel structure joint 3: 206. BRI, Tokyo, Japan.
- [15] Trahair N.S., Bradford M.A., Nethercot D.A., 2001. The behaviour and design of steel structures to BS5950. 3rd British ed. Spon press, London, UK. 356-390.
- [16] Inoue K., 2003. The theory and design of the building steel structure. The Kyoto University Publishing House, Kyoto, Japan.
- [17] Heidarpour A., Bradford M.A., 2009. Elastic behaviour of panel zone in steel moment resisting frames at elevated temperatures. *Journal of Constructional Steel Research*, 65(2): 489-496. DOI: 10.1016/j.jcsr.2008.02.010
- [18] Castro J.M., Elghazouli A.Y., Izzuddin B.A., 2005. Modelling of the panel zone in steel and composite moment frames. *Engineering Structures*, 27(1): 129-144. DOI: 10.1016/j.engstruct.2004.09.008

PHYSICAL AND MECHANICAL PROPERTIES OF RECYCLED PET COMPOSITES

Yurani García Quintero¹, Daniel Ruíz Figueroa¹, Harveth Gil¹, and Alejandro Alberto Zuleta²

- 1. Grupo de Investigación Innovación y Sostenibilidad Aplicadas a las Infraestructuras en Ingeniería - ISAI, Facultad de Ingenierías, Politécnico Colombiano Jaime Isaza Cadavid PCJIC, CO 050022, Medellín, Colombia, email: hhgil@elpoli.edu.co*
- 2. Grupo de Investigación de Estudios en Diseño - GED, Facultad de Diseño Industrial, Universidad Pontificia Bolivariana- Sede Medellín, CO 050031, Medellín, Colombia*

ABSTRACT

Virgin and recycled polyethylene terephthalate (PET) has been examined for the production of composites with additions of 5-20% by weight of sand particles. Density and compressive strength were estimated using virgin (V-PET) and recycled PET (R-PET). Scanning electron microscope (SEM) equipped with energy dispersive X-ray (EDX) spectroscopy was used to characterize the morphology and elemental composition of the composites. Also, thermogravimetric analysis (TGA) was used to find degradation temperature on both types of polymer. On the other hand, a streamlined life cycle assessment (SLCA) was made for the different composites to get environmental impacts. The results indicated that a maximum of 52.94 MPa and 52.03 MPa on compressive strength were obtained for virgin and recycled PET without sand, respectively. With the addition of sand, compressive strength decreases in both cases. The best performance was found at 5% sand addition, which causes a reduction of 9.07% and 16.68% for V-PET and R-PET composites, respectively. Environmental results show that resource extraction is the dominant life stage; meanwhile, gas residues are the dominant environmental impact in both types of composites. R-PET composites are the best environmentally friendly option because they used recycled material, which in return recovers part of the embodied energy used to make the primary production. The results show it could be explored the potential to be used the composites in pavement blocks or architectonic elements.

KEYWORDS

Polymer-matrix composites (PMCs), Mechanical properties, Compressive strength, Life cycle assessment

INTRODUCTION

One of the significant problems of our society is the increasingly growing demand for non-renewable materials such as plastics. The impact of plastics is higher due to its low degradation rates causing considerable environmental damage. In that sense, polyethylene terephthalate (PET) is a kind of thermoplastic material which has ample use in dairy activities as well in the industry. PET is a material cheap to produce and have the mayor recycled percentage between all polymers

(~ 22%). In Colombia, a pollution problem exists due to the production of about 1500 million PET bottles by year, which reaches rivers, fields, and beaches or directly to landfill [1]. It is known that to degrade PET bottles is necessarily more than a hundred years [2]. For such reason, the use of recycled PET in different composites has been investigated for some time.

Tavares et al. [3] developed polymer concrete with silica sand bound to epoxy resin. Also, waste PET bottles have been used as fibres to produce such types of concretes [2,4]. However, the cost of producing concrete from such waste is still high [5]. Miranda et al. [6] produced mortar polymers using recycled PET and unsaturated polyester resin (UPER), showing that the best mechanical and physical properties of the composite were to mortars with ratio 78/20/2 sand/UPER/PET particles. Most studies regarding fracture toughness improving are focused on the melt mixing of virgin and recycle PET with rubber [7].

On the other hand, there are some studies on polymer matrix and sand particles. Kumi-Larbi Jnr et al. [8] use recycled LDPE water sachets to form sand blocks, and they found that the density and compressive strength of composites increases as the particle size of the sand decreases. Composite materials produced by PET wasted, and rigid sand has been studied concerning tensile properties. Zahran [9] found a decreasing linear function of tensile strength with the sand content and depending on the sand particle size. More studies have been performed on polymer composites with particles such as silica. The addition of silica particles to a polymer matrix has a positive effect on the elastic modulus of the composites [10,11]. Mohandesi et al. [12] investigated molten PET with silica sand particles in a 5-40% weight ratio at different composite temperatures. They found that the highest mechanical strength was obtained at 25°C and 10% sand above which composite strength decreases.

From the literature review is clear that limited research has been carried out on using waste PET and sand particles. The main aim of this study is to investigate the incorporation of sand particles on a PET matrix concerning mechanical properties and sustainability aspects, such as a rationalized life cycle assessment. Morphology was studied by scanning electron microscopy (SEM), thermal behaviour by thermogravimetric analysis (TGA), and compressive strength and density were determined for the composites. The use of these particles in the polymer has environmental advantages and also strength and friction enhancement that could lead to future applications on paving stones.

METHODS

Materials and composite preparation

PET produced by Codesarrollo corporation was used. The material was obtained from transparent bottles that had a pelletization process. Two types of composites samples were prepared, virgin PET (V-PET) of 1330 kg/m³ and recycled PET (R-PET) of 1339 kg/m³ reinforced with sand particles. PET was heated up to 260°C, and after 5 minutes of homogenization with continuous stirring, sand was added slowly to the molten polymer. Samples with 0%, 5%, 10%, 15%, and 20% by weight were obtained, and they were poured into cubic steel forms of 2 inches. Sand particles (2590 kg/m³) were sieving, and the range material was selected between sieve # 30 (0.6mm) and #16 (1.18 mm) for all mixtures. Thermogravimetric analysis (TGA) was carried out in TGA Q500, V20.3 Build 39 for PET (10-20 mg) using a TGA Q500 in a nitrogen atmosphere at a flow rate of 90 mL/min from 20° to 900 °C.

Testing of specimens

Compressive strength was determined using a universal testing machine Instron 5582 equipped with a load cell of 100 KN, according to ASTM C109. The test was performed at 2 mm/min. A scanning electron microscope (SEM) with a JEOL model JSM2490 CV device equipped

with energy dispersive X-ray (EDX) spectroscopy (OXFORD INCA PentaFET-x3) was used to perform morphological observations on selected composites samples. The accelerating voltage used was 20 kV.

Streamlined life-cycle assessment (SLCA)

An SLCA method developed by Graedel and Allenby [13,14] was followed to find out the environmental burden regarding life stages and environmental stressors. In practice, An SLCA measures the relative environmental impacts when searching for issues that occur during the life stages of a product [15]. The central feature of the assessment is a 5 x 5 matrix, with life-cycle stages in the rows and environmental stressors in the columns. According to Graedel, the assessor studies the product design, manufacture, packaging, use, and disposal scenario and assign to each element of the matrix an integer rating from 0 (highest impact, a very negative evaluation) to 4 (lowest impact, an exemplary evaluation) [13]. Because the approach is not quantitative, the results are not strictly a measure of environmental performance, but rather an estimate for improvement and comparison between products. The assignments of the numbers were made with a protocol exposed by Graedel [13].

RESULTS

Visual appearance

Figure 1a-b shows the visual appearance of the composite with and without sand particles. In the absence of sand particles, the composites exhibit defects indicating solidification problems during the process. In contrast, composites modified with sand particles exhibit fewer defects, although the distribution of the sand is not even. As the sand content increases, the location of the material seems to go to the bottom of the molds.

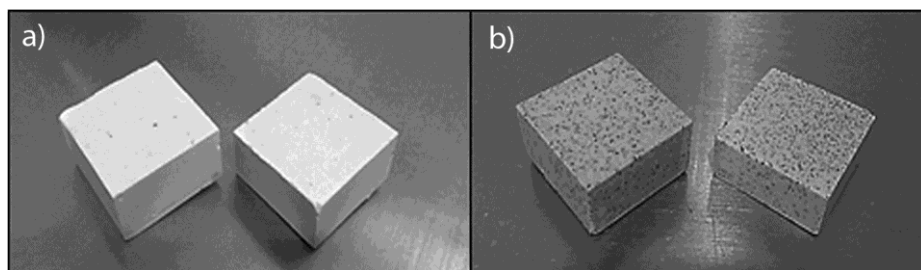


Fig. 1 – Visual appearance of R-PET samples without a) and with sand particles b)

Density

Figure 2 shows the variation of composite's density against sand percentage. Composite density for both, V-PET and R-PET, increases with sand content as is expected. Density ranges from 1280 kg/m³ to 1530 kg/m³ and from 1310 kg/m³ to 1580 kg/m³ for V-PET and R-PET composites, respectively. Polymer density without sand addition is within the range of values reported by the literature [16]. From the deviation of the experimental results, no statistical difference was found for the two different composites.

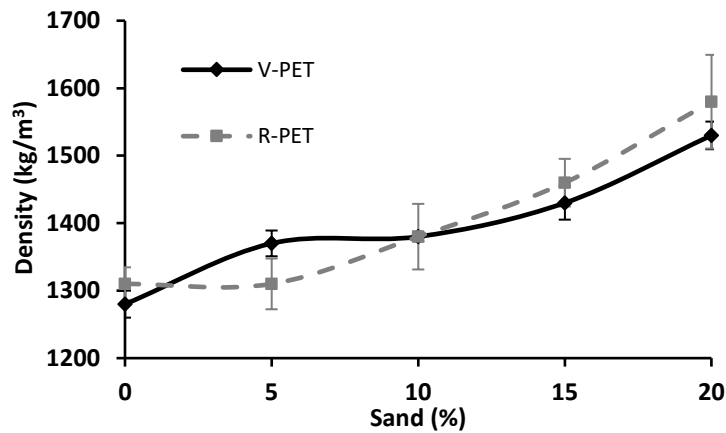


Fig. 2 – Composite density as a function of the sand content for V-PET and R-PET

Compressive strength

Figure 3a-b shows the average compressive strength of V-PET and R-PET for the different sand percentages. PET samples without sand exhibit an average compressive strength of 52.94 ± 2.54 MPa and 52.03 ± 10.1 MPa for virgin and recycled, respectively. The values are close to the reported in the literature [16,17]. The 5% of sand obtained the best performance in both cases, which result in decreasing compressive strength in 9.07% and 16.68% for V-PET and R-PET composites, respectively.

Both composites samples exhibit similar stress-strain curves, showing an initial linear behaviour, and further loading causes yield until it reaches the maximum compressive values. As can be seen, ductility decreases with the addition of sand reaching lower values in the case of R-PET composites. The data exhibits visco-elastic behaviour for higher sand content, as was observed on LDPE/sand composites [8]. Sand changes plastic flow under load, clearly reducing its ductility.

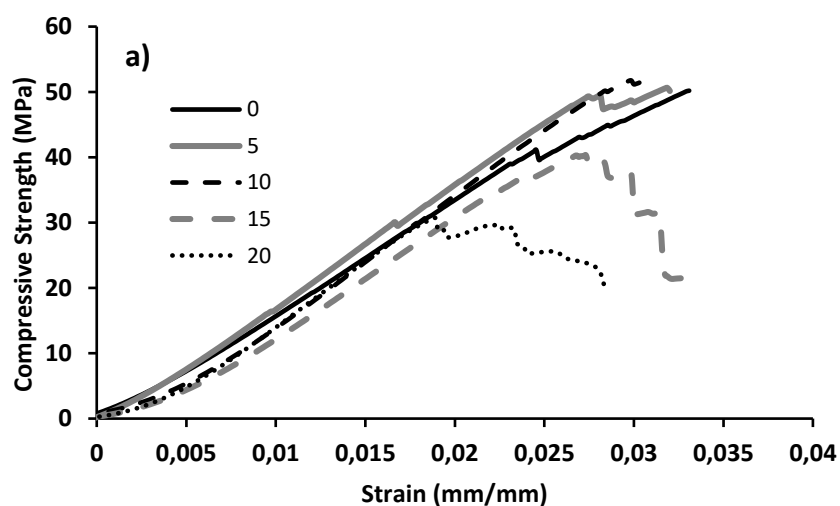


Fig. 3a – Stress-strain curves for V-PET

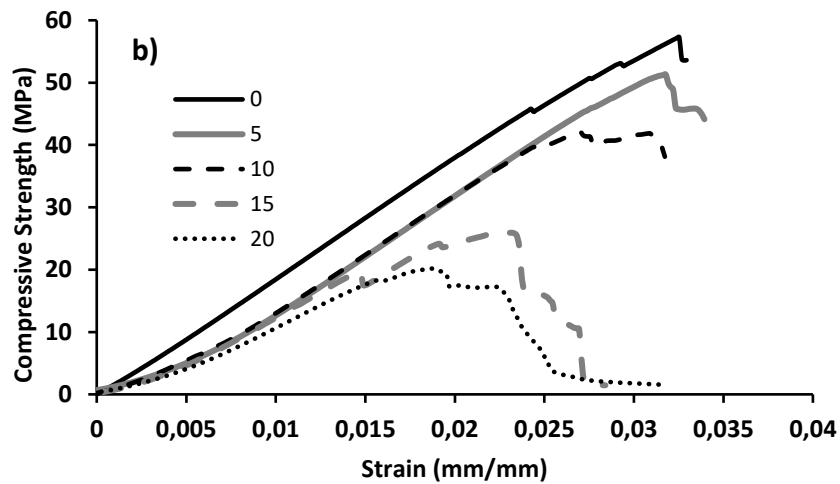


Fig. 3b – Stress-strain curves for R-PET for the different sand percentages

The average results of compressive strength for all sand percentages are presented in Figure 4. Due to the high variability of R-PET results, the values are pretty much the same compared to V-PET for percentage below 10%. At higher sand addition, the values decrease considerably. In both cases, composite's resistance decreases as increase sand content. These could be explained to the overpopulation of sand particles, which causes a weak interaction between sand and PET matrix and inefficiencies for stress transfer. The reduce in compressive strength has been seen on LDPE/sand composites for larger sand-size particles (> 1mm) [8]. Sand size has an influence on the mechanical properties of the composites due to an increase in porosity, reducing the encapsulating area by the binder. In this research, larger air voids were found in both types of PET. SEM results corroborate these (see below). Sand addition results in a slight reduction of elastic modulus for sand percentage above 10%, although the results give no statistically differences.

The fact that R-PET exhibits relatively excellent resistance, especially for sand content of 5% and 10%, is highlighted because of the presence of semicrystalline phases. Polymers with high crystallinity usually exhibit higher modulus, toughness, and tensile strength values [18]. On the other hand, the results present larger standard deviation values, especially for R-PET composites, probably due to some adhesion problems between sand particles and the polymer matrix coupling with difficulties with the manufacturing process, as can be seen in the SEM images shown below (Figure 8).

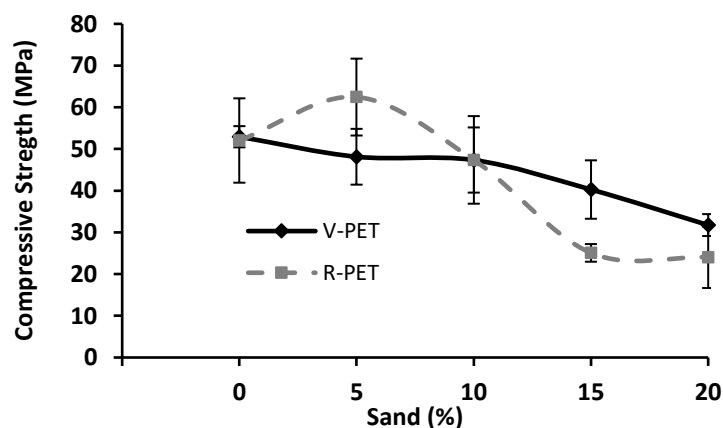


Fig. 4 – Compressive strength as a function of the sand content for V-PET and R-PET

Figure 5 exhibits the thermograms for V-PET and R-PET, respectively. V-PET maintains its properties until 400°C approximately, meanwhile R-PET starts to degrade a little bit earlier. Dimitrov et al. [19] reported 435°C and 434°C as temperatures of maximum decomposition rate for V-PET and R-PET, respectively; such values are above reported in this study. As can be seen in Figure 5, derivative mass loss indicates that the decomposition temperatures for V-PET and R-PET are 431.45 °C and 420.15 °C, respectively. As expected, R-PET starts to decompose at a lower temperature than V-PET due to the thermal history of the material and possible residual impurities present in the samples. The mass loss of PET is attributed to a polymer degradation process involving a random scission of ester links in the main chain resulting in the formation of different oligomers [20]. The curve shows 85 wt.% loss in the case of V-PET and 88 wt.% loss in the case of R-PET at their respective end set temperatures.

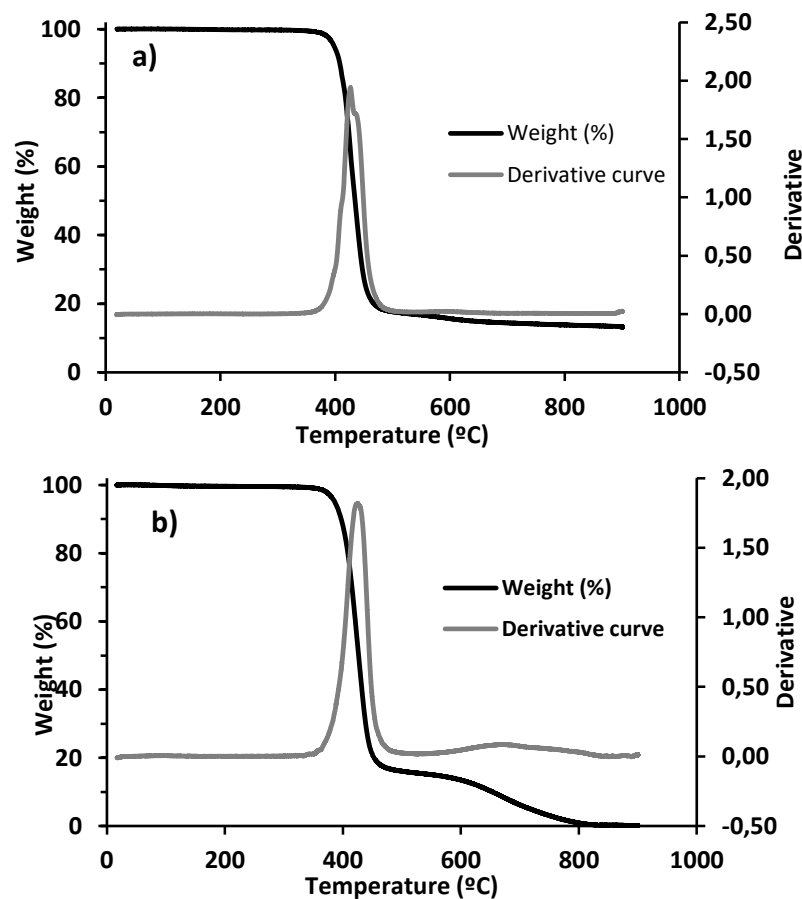


Fig. 5 – TGA thermograms of a) V-PET and b) R-PET

After a comparison of the two TGA curves, it is observed the apparition of a second plateau in the case of R-PET. This plateau is related to a second decomposition due to a reorganization of the crystals during the test. The effect has seen before, and the first plateau has been related to the melting of imperfect crystals and the second one to the fusion of the original crystals that suffer reorganizations, and they melt at higher temperatures [21].

Figure 6a and 7a show an SEM image of the V-PET and R-Pet composites, respectively. It can be observed that sand particles are mechanically bonded into the polymeric matrix. The adhesion mechanism could be related to a molecular bonding interaction due to sand surface irregularities [22,23]. However, as sand percentage increases, the adhesion is less effective. According to the energy-dispersive X-ray spectroscopy (EDX) (see Figure 6b and Figure 7b), carbon and oxygen were detected on the PET matrix for both virgin and recycled. On the other hand, magnesium, aluminium, silicon, potassium, and iron were detected on the sand particles (see Figure 6c and Figure 7c). The presence of potassium and magnesium could be due to contamination on the sand particles. Traces of iron and aluminium oxides are typical in this type of sand. According to EDX results, no impurities were found on the R-PET matrix.

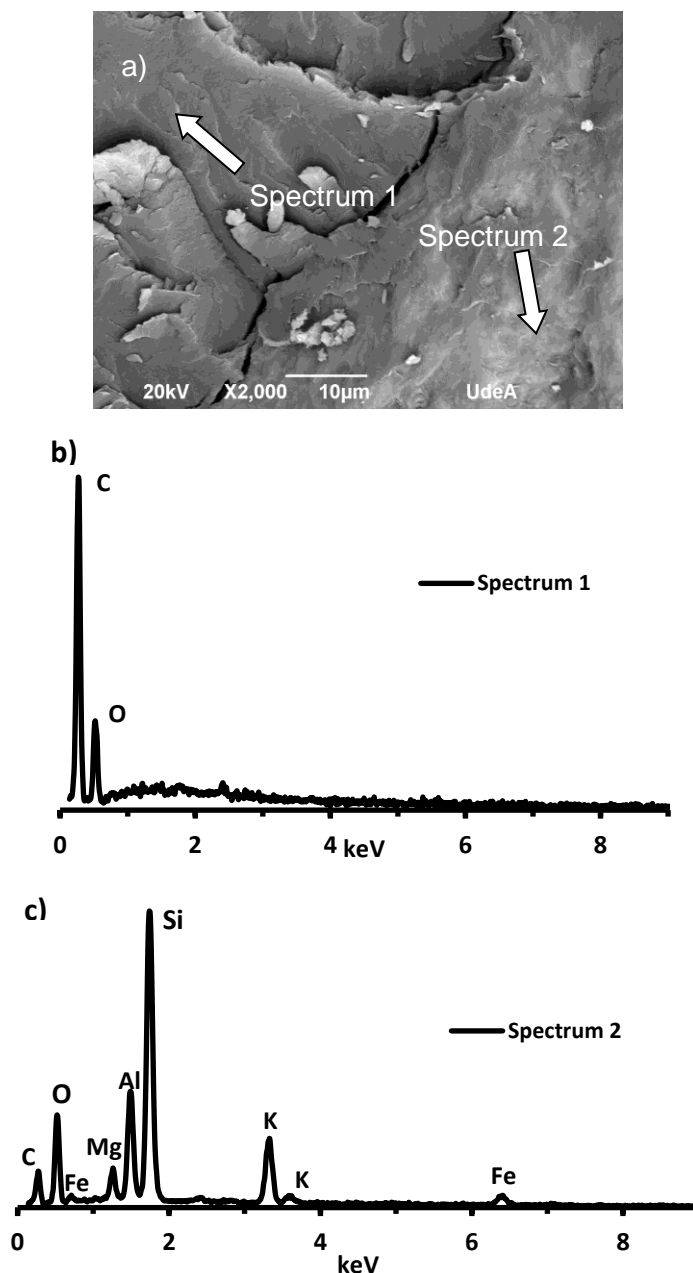


Fig. 6 – a) SEM micrograph of V-PET with 10% of sand particles and EDX results of two different local points within b) matrix and c) particles

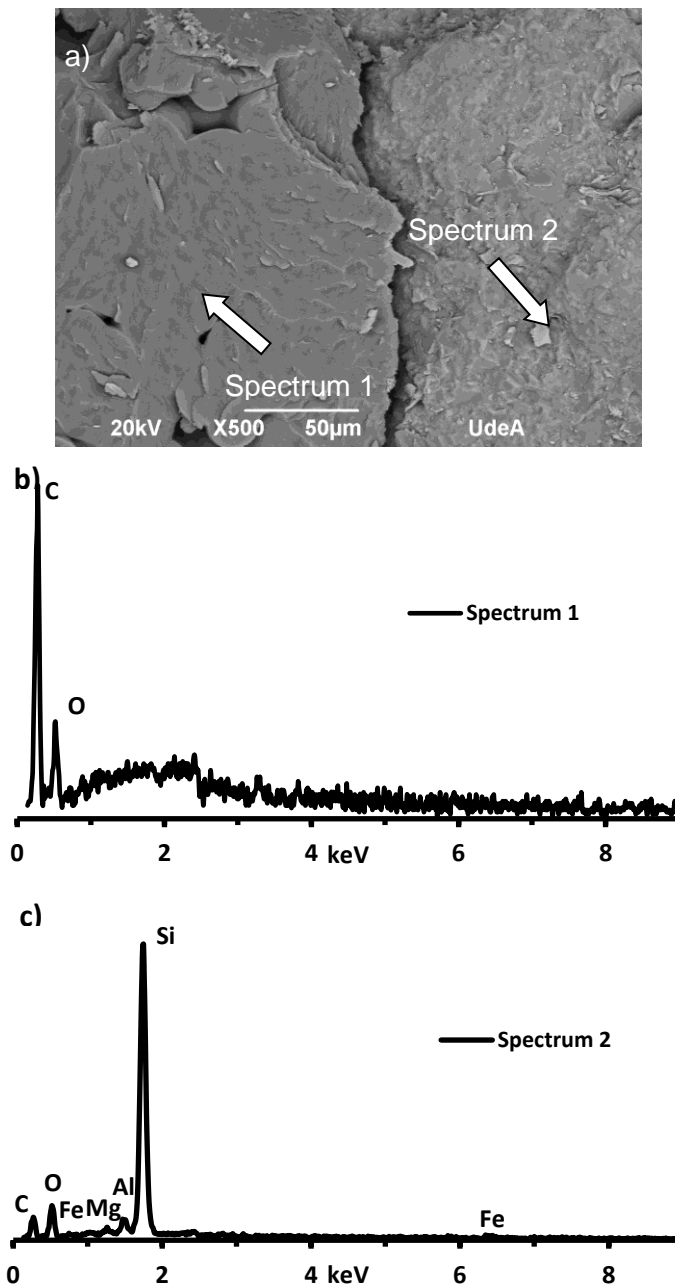


Fig. 7 – a) SEM micrograph of R-PET with 20% of sand particles and EDX results of two different local points within b) matrix and c) particles

Figure 8 shows SEM micrographs for V-PET and R-PET composites without sand. The morphology of the samples is very similar, exhibiting reproducible solidification process. Also, in both cases, porosity was present after the solidification. Those voids lead to more substantial variation in density and resistance. As can be seen in the figure, as the sand percentage increases, the cracking routes rise because of the poor adhesion between particles and the matrix. Samples without sand were free of porosity.

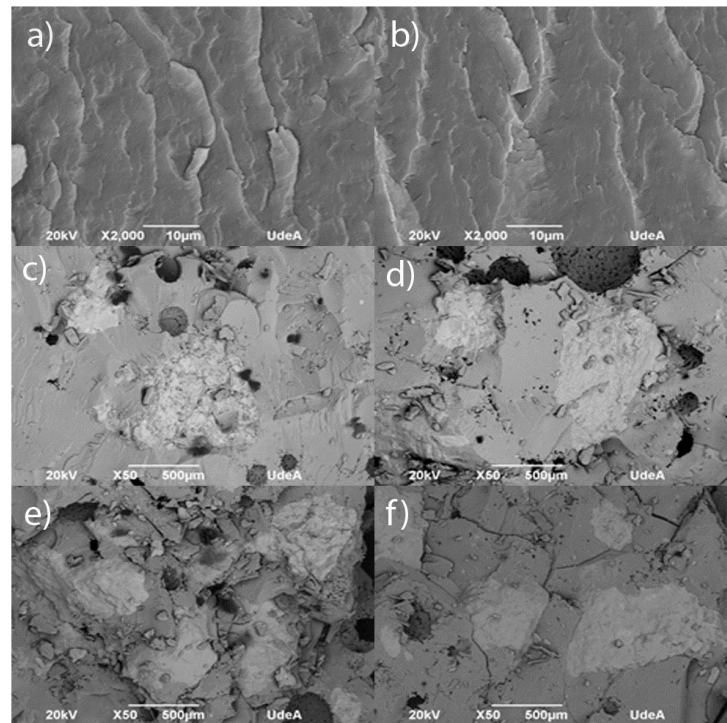


Fig. 8 – SEM micrographs for 0, 10, and 20% sand corresponding to a), c) and e) V-PET and b), d), and f) R-Pet respectively

Streamlined life cycle analysis (SLCA)

An SLCA of composites was performed to determine which scenario is present less environmental issues. The problem with PET is that in spite of its recycling possibilities, the actual amount of recovering of the material is still low. The usual disposal of the material is in a high deal landfill, which causes pollution by introducing solid wastes into the soil that are not easily degradable. PET is usually employed to manufacture water bottles and containers, but virgin or recycled pellets of PET can be used to obtain composites such as this study.

For the resource extraction life stage, it is considered virgin PET and recycled PET depending on the type of sample, so for virgin material, it produces more residues compared to the second scenario. Since PET is a petroleum-based material, the primary resource is non-renewable energy; also, the number of residues is the highest compared to the other life stages. The processing of PET is relatively easy to accomplish, allowing high speed with low temperatures. The main concern in this stage is due to the gaseous residues produced from the production plant, but the solid and liquid residues are minimal. For the delivery of the product, it is considered the low density of PET, which allows flexible and easy transportation. However, carbon dioxide (CO₂) emission has to be accounted for due to the use of fossil fuel during this stage.

The application of this type of composite could be related to the fabrication of polymer composites for pavement blocks. In that case, the blocks could be easy to carry and install. During its life, the product will produce no solid, liquid, and gas residues. The end of life of these composites could be recycling instead of the landfill, which causes solid and not degradable residues. For the separation process between the polymer matrix and sand particles, it will be used energy, and together with the transportation to the recycling facility, it will produce gas residues.

In Table 1 and 2, is presented the SCLA analysis for composited made of V-PET and R-PET, respectively. The analysis was conducted through five life stages: resource extraction (RE), product manufacturing (PM), product delivery (PDe), product use (PU), and product disposal (PDi). For each stage, it was evaluated material choice (MC), energy use (EU), solid residue (SR), liquid residue (LR), and gas residue (GR) as the environmental stressors.

Tab. 1 - Streamlined LCA for V-PET

	MS	EU	SR	LR	GR	Σ
RE	3	3	2	2	2	12
PM	3	2	3	3	2	13
PDe	4	3	3	3	2	15
PU	4	4	4	4	4	20
PDi	3	2	3	4	2	14
Σ	17	14	15	16	12	74

Tab. 2 - Streamlined LCA for R-PET

	MS	EU	SR	LR	GR	Σ
RE	4	4	3	3	3	14
PM	3	2	3	3	2	13
PDe	4	3	3	3	2	15
PU	4	4	4	4	4	20
PDi	3	2	3	4	2	14
Σ	18	15	16	17	13	79

After the evaluation, the overall environmentally responsible product rating (R_{erp}) is calculated as the sum of the matrix element values as is depicted in Equation 1 [13]:

$$R_{erp} = \sum_{i=1}^n \sum_{j=1}^n M_{i,j} \quad (1)$$

where $M_{i,j}$ corresponds to each element of the matrix.

R-PET has a R_{erp} value of 79, which is better compared to the V-PET with a R_{erp} value of 72. However, both scenarios are excellent choices in terms of environmental impact [24].

A more succinct display of the SLCA results could be made using target plots using each element of the matrix. Figure 9 shows the target plots corresponding to V-PET and R-PET. As can be seen, values for R-PET composite have more dots closed to the center, indicating a better product compared to V-PET.

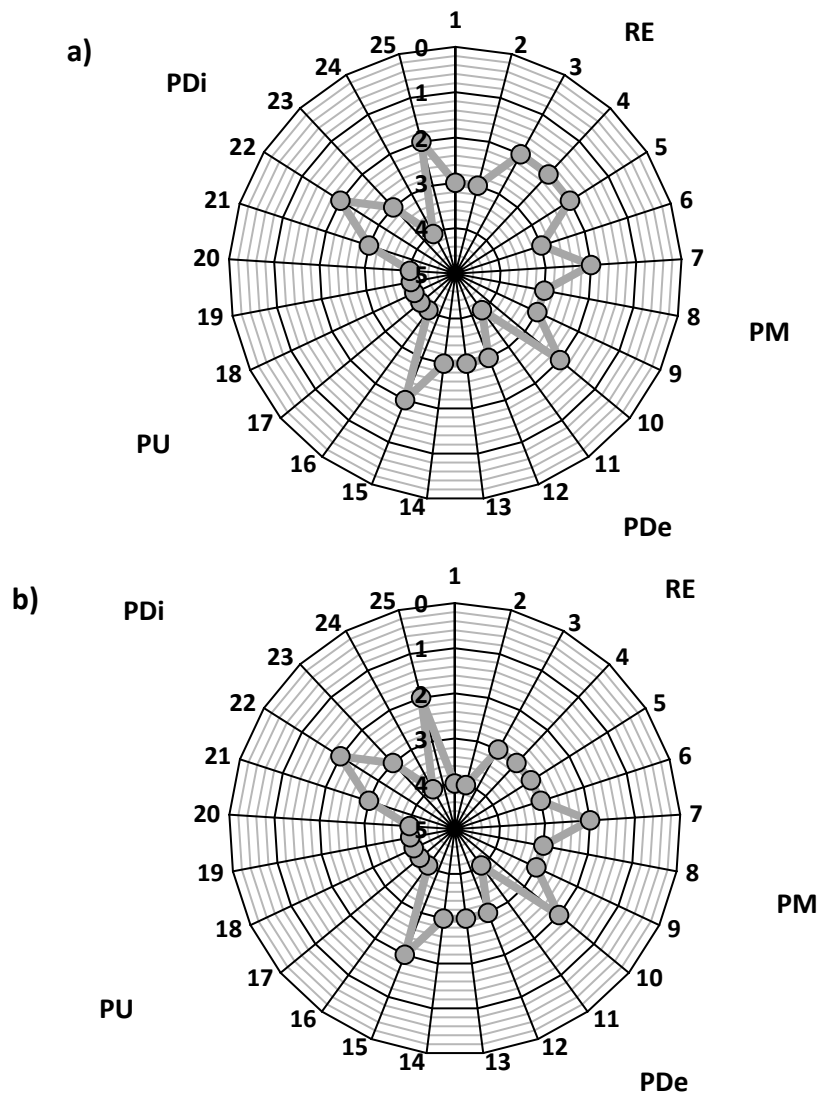


Fig. 9 – Target plots corresponding to a) V-PET and b) R-PET

Both composites exhibit gas residues as the dominant environmental impact. These are because of the manufacturing, transport, and separation process at the end of life. The separation of PET and sand requires the melting of the polymer and then using non-renewable energy.

Resource extraction is the dominant life stage in the case of V-PET, due to the high impact of the petroleum base material as the primary resource, which becomes an impact depleting the non-renewable fossil energy. Besides, during this stage, the amount of solid, liquid, and gaseous residues are highest compared to the other phases. Product manufacturing has a definite impact concerning gaseous residues produced as well as energy use for the polymer processing. Product manufacturing is the dominant life stage in the case of R-PET, due to the energy and generation of residues during the fabrication of the elements. Resource extraction for R-PET is reduced in the benefit of the recycled material.

Product delivery has a low impact due to the low density of the material, which results in a reduction of lightweight energy consumption. However, it has to take into account the release of gaseous pollutants during transport. Use stage in both types of materials have a low impact due to the low cleaning services, and it is expected to produce a meager amount of solid residues in any chosen application. The disposal phase has a moderate impact in both cases considering its mechanical recycling route. A recycling strategy can significantly reduce environmental burden in terms of solid waste and hydrocarbons emissions [25]. However, when the product has an incineration route, it will yield heavy metals to the environment [24].

CONCLUSION

Based on the results obtained, the following conclusions can be drawn:

1. Compressive strength decreases with sand content. These are associated with poor adhesion between particles and polymeric matrix and porosity generated within the composites, as was observed in SEM micrographs, causing a low transfer of stresses. Sand addition achieves better performance at 5%, causing a reduction of 9.07% and 16.68% for V-PET and R-PET composites, respectively.
2. According to TGA results, decomposition temperatures for V-PET and R-PET are 431.45 °C and 420.15 °C, respectively. However, during this study, this limit was not reached in any case, indicating the viability to fabricate these composites.
3. Recycled and virgin PET as a matrix is good choice in terms of environmental impact. R-PET has a R_{erp} of 79 and V-PET a R_{erp} of 72. R-PET composite has a less harmful environmental evaluation because it used recycled material, which recovers part of the embodied energy used to make the primary production. However, both cases require the use of non-renewable energy to separate composite materials.
4. According to physical and mechanical properties obtained, it could be explored the used of the R-PET in pavement blocks or architectonic elements.

ACKNOWLEDGEMENTS

This work was supported by “Centro de Investigación para el Desarrollo y la Innovación (CIDI)” from the Universidad Pontificia Bolivariana through UPB-Innova grant 597B-05/16-35.

REFERENCES

- [1] Amariz, A.D.M., Jiménez, M.L.C., 2014. Diseño y fabricación de ladrillo reutilizando materiales a base de PET, INGE CUC, vol. 10: 76–80.
- [2] da Silva, D.A., Betioli, A.M., Gleize, P., Roman, H.R., Gomez, L., Ribeiro, J, 2005. Degradation of recycled PET fibers in Portland cement-based materials. Cement and Concrete Research, vol. 35: 1741–1746. <https://doi.org/10.1016/j.cemconres.2004.10.040>.
- [3] Tavares, C., Ribeiro, M., Ferreira, A., Guedes, R., 2002. Creep behaviour of FRP-reinforced polymer concrete. Composite Structures, vol. 57: 47–51. [https://doi.org/10.1016/S0263-8223\(02\)00061-2](https://doi.org/10.1016/S0263-8223(02)00061-2).
- [4] Ochi, T., Okubo, S., Fukui, K., 2007. Development of recycled PET fiber and its application as concrete-reinforcing fiber. Cement and Concrete Composites, vol. 29: 448–455. <https://doi.org/10.1016/j.cemconcomp.2007.02.002>.
- [5] Akçaözoglu, S., Atiş, C.D., Akçaözoglu, K., 2010. An investigation on the use of shredded waste PET bottles as aggregate in lightweight concrete. Waste Management, vol. 30: 285–290. <https://doi.org/10.1016/j.wasman.2009.09.033>.

- [6] Vidales, J.M.M., Hernández, L.N., López, J.I.T., Flores, E.M.M., Hernández, L.S., 2014. Polymer mortars prepared using a polymeric resin and particles obtained from waste pet bottle. *Construction and Building Materials*, vol. 65: 376–383. <https://doi.org/10.1016/j.conbuildmat.2014.04.114>.
- [7] Tanrattanakul, V., Hiltner, A., Baer, E., Perkins, W., Massey, F., Moet, A., 1997. Effect of elastomer functionality on toughened PET. *Polymer*, vol. 38: 4117–4125. [https://doi.org/10.1016/S0032-3861\(96\)00991-3](https://doi.org/10.1016/S0032-3861(96)00991-3).
- [8] Jnr, A.K-L., Yunana, D., Kamsouloum, P., Webster, M., Wilson, D.C., Cheeseman, C., 2018. Recycling waste plastics in developing countries: Use of low-density polyethylene water sachets to form plastic bonded sand blocks. *Waste Management*, vol. 80: 112–118. <https://doi.org/10.1016/j.wasman.2018.09.003>
- [9] Zahran, R., 1998. Effect of sand addition on the tensile properties of compression moulded sand/polyethylene composite system. *Materials Letters*, vol. 34: 161–167. [https://doi.org/10.1016/S0167-577X\(97\)00154-7](https://doi.org/10.1016/S0167-577X(97)00154-7).
- [10] Zhang, Q., Tian, M., Wu, Y., Lin, G., Zhang, L., 2004. Effect of particle size on the properties of Mg (OH) 2-filled rubber composites. *Journal of Applied Polymer Science*, vol. 94: 2341–2346. <https://doi.org/10.1002/app.21037>.
- [11] Reynaud, E., Jouen, T., Gauthier, C., Vigier, G., Varlet, J., 2001. Nanofillers in polymeric matrix: a study on silica reinforced PA6. *Polymer*, vol. 42: 8759–8768. [https://doi.org/10.1016/S0032-3861\(01\)00446-3](https://doi.org/10.1016/S0032-3861(01)00446-3).
- [12] Mohandes, J.A., Refahi, A., Meresht, E.S., Berenji, S., 2011. Effect of temperature and particle weight fraction on mechanical and micromechanical properties of sand-polyethylene terephthalate composites: A laboratory and discrete element method study. *Composites Part B: Engineering*, vol. 42: 1461–1467. <https://doi.org/10.1016/j.compositesb.2011.04.048>.
- [13] Graedel, T.E., 1998. *Streamlined life-cycle assessment*. (Prentice Hall Upper Saddle River, NJ) 99-110.
- [14] Graedel, T.E., Allenby, B.R., 2010. *Industrial ecology and sustainable engineering*. (Prentice Hall Upper Saddle River, NJ).
- [15] Lee, S., Xu, X., 2005. Design for the environment: life cycle assessment and sustainable packaging issues. *International Journal of Environmental Technology and Management*, vol. 5: 14–41.
- [16] Ashby, M.F., 2012. *Materials and the environment: eco-informed material choice*. (Elsevier) 616 pp.
- [17] Li, Y., White, D.J., Peyton, R.L., 1998. Composite material from fly ash and post-consumer PET. *Resources, Conservation and Recycling*, vol. 24: 87–93. [https://doi.org/10.1016/S0921-3449\(98\)00041-X](https://doi.org/10.1016/S0921-3449(98)00041-X).
- [18] Demirel, B., Yaraş, A., Elçiçek, H., 2016. Crystallization behavior of PET materials. *Balikesir Üniversitesi Fen Bilimleri Enstitüsü Dergisi*, vol. 13: 26–35.
- [19] Dimitrov, N., Krehula, L.K., Siročić, A.P., Hrnjak-Murđić, Z., 2013. Analysis of recycled PET bottles products by pyrolysis-gas chromatography. *Polymer Degradation and Stability*, vol. 98: 972–979. <https://doi.org/10.1016/j.polymdegradstab.2013.02.013>.
- [20] Lecomte, H.A., Liggat, J.J., 2006. Degradation mechanism of diethylene glycol units in a terephthalate polymer. *Polymer Degradation and Stability*, vol. 91: 681–689. <https://doi.org/10.1016/j.polymdegradstab.2005.05.028>.
- [21] Elmari, A., Abid, K., Harzallah, O., Lallam, A., 2015. Characterization of recycled/virgin PET polymers and their composites. *Nano* vol. 3: 11–16. doi: 10.11648/j.nano.s.2015030401.13.
- [22] Awaja, F., Gilbert, M., Kelly, G., Fox, B., Pigram, P.J., 2009. Adhesion of polymers. *Progress in Polymer Science*, vol. 34: 948–968. <https://doi.org/10.1016/j.progpolymsci.2009.04.007>.
- [23] Pukánszky, B., Fekete, E., 1999. Adhesion and surface modification, 109-153 (in: *Mineral Fillers in Thermoplastics I*, Springer).
- [24] Huang, C.-C., Ma, H.-W., 2004. A multidimensional environmental evaluation of packaging materials. *Science of the Total Environment*, vol. 324: 161–172. <https://doi.org/10.1016/j.scitotenv.2003.10.039>.
- [25] Γεωργακέλλος, Δ.Α., 2005. The use of streamlined LCA for the environmental assessment of plastics recycling: the case of a PVC container. *SPOUDAI-Journal of Economics and Business*, vol. 55: 31–46. waters (ČVUT v Praze) 415 pp.

A STUDY ON THE ULTIMATE LOAD BEARING CAPACITY OF CARBON FIBRE REINFORCED POLYMER TENSEGRITY SYSTEM IN A SUSPEN DOME

IfeOlorun Olofin, Ronggui Liu

Jiangsu University, Faculty of Civil Engineering and Solid Mechanics, No 301 Xuefu Road, Zhenjiang, China; epher2002@yahoo.com, liurg@ujs.edu.cn

ABSTRACT

Structural stability is one of the major factors considered for structural design. The integrity of carbon fiber reinforced polymer as a tensegrity system in a suspen dome is investigated by employing a computational model with a span of 93m. ANSYS software was employed for the investigation. The load-displacement curve of the structure was studied to understand the ultimate load bearing capacity in comparison with steel cable using Newton-Raphson and arc length methods. Parameters such as nodal displacement, stresses on the single reticulated layer and internal forces of the tension members that influence the structures integrity were considered. Results show that despite the antistrophic nature of carbon fiber reinforced polymer it possesses similar characteristics as steel cables.

KEYWORDS

Suspen dome, Tensegrity system, Carbon fibre reinforced polymer cables, Steel cables, Ultimate load bearing capacity

INTRODUCTION

Carbon fiber reinforced polymer cables have obviously become the best alternative choice in the design of bridgeworks for Civil Engineering structures as reviewed by Olofin and Liu [1]. Exploring the material in other cable structures has been limited. A suspen dome which is a composite structure made up of a single reticulated layer and a tensegrity system which is a cable structure has become popular in the present world [2]. The need to explore more properties of the structure is required in order to make conclusive findings for researchers and designers. In order to explore such excellent mechanical properties for a suspen dome, a study is performed, first and foremost to comprehend the ultimate load bearing capacity of carbon fiber reinforced polymer cable due to its anisotropic nature in order to compare the result with the corresponding behavior of steel cables. Carbon fiber reinforced polymer cables may experience severe damage when subjected to certain load conditions. Under such conditions, the load imposed area deforms and alters the material behavior resulting in a decrease in residual strength and subsequently a risk of total failure.

The purpose of the study is to determine the extent to which carbon fiber reinforced polymer cables as a tensegrity system in a suspen dome structure can sustain their capacities under high impact load bearing condition with a finite element model; namely, the Beijing Olympics Stadium using ANSYS software for its simulation and comparing results with that of its counterpart steel.

Newton-Raphson method was used for the initial loading and when the load was close to ultimate load. Then arc length method was employed to cross pass the critical point. The methods are restricted to static analyses with proportional loads for deflections based on the actual member sizes which were performed with as much accuracy as possible for the constructed model to predict structural response under various loading conditions in order to put forward some design recommendations.

LITERATURE REVIEW

In today's world long span structures are becoming trendy, the need to explore lightweight, high stiffness and low cost material are required to fulfil such requirement. Steel cables have been known for centuries to be the best choice of material for cable structures. Of recent, carbon fibre reinforced polymer cables have taken a toll in competing with steel cables with its exceptional mechanical properties. To explore such properties in other cable structures apart from bridgework, Yue *et al.* [3] investigated the application of carbon fibre reinforced polymer cables on roof cables; namely, the wheel spoked and roof façade and concluded it was more economical and material usage was limited as compared to steel. Similarly Olofin and Liu [4-6] investigated the application of carbon fibre reinforced polymer cables as a tensegrity system in a suspen dome and concluded that applying the material increases the stiffness and stability just as steel.

An overview on buckling load

Local buckling is greatly affected by the stiffness, loads on the adjacent elements and the flexural strength of the joint in most cases it is likely to occur in single-layered space frames [7] which leads to global buckling. An approximate formula for local buckling load was proposed by Lind, applicable to triangular network with all elements of same cross-section [8]. The formulas are expressed in Equations 1-3.

For a uniform load, the critical load is given as:

$$Q_{cr} = \frac{E_t}{1 + \alpha^2 / (8\pi^2)} \left(0.47 \frac{Al^3}{R^3} + 3 \frac{BI}{Rl} \right) \quad (1)$$

where $\alpha = l^2 / (rR)$, r is the radius of gyration, A is the area of an element, B is the non-dimensional bending stiffness of the grid near a joint, I is the moment of inertia, R is the radius of curvature of the mid-surface of the framework, l is the length of the element, h is the rise and E_t is the tangent modulus.

For concentrated load, the critical load is given as:

$$W_{cr} = \frac{3EAh^3}{l^3} \left\{ \frac{8B}{\alpha^2} + 0.241 \left(1 - 1.595 \frac{8B}{\alpha^2} \right) \right\} \quad (2)$$

Valid if α is greater than 9 (approximately), and

$$W_{cr} = 0.0905 EAl^3 / R^3 \quad (3)$$

Valid for a regular pin-jointed structure.

METHODS

This section describes in details the study material, procedures and methods used for the analysis.

Principle of comparison and design

In this case study, the following properties were compared:

- i) The ultimate load bearing capacity of the models,
- ii) The hoop and radical cables in tension.

During the comparison the following were used as guidelines:

- i) Initial geometry loads and boundary condition of steel and carbon fiber reinforced polymer tensegrity systems are same,
- ii) The external load conditions of steel and carbon fiber reinforced polymer suspen dome are kept the same,
- iii) Each cable reached its ultimate tensile strength,
- iv) The deflection limits of steel and carbon fiber reinforced tensegrity systems are reached.

Numerical technique

The purpose of finite element analysis is to create mathematically the behavior of an actual system. The analysis is an accurate mathematical model for the physical prototype. Figure 1 illustrates the flowchart of the occurrence of a progressive collapse in a suspen dome.

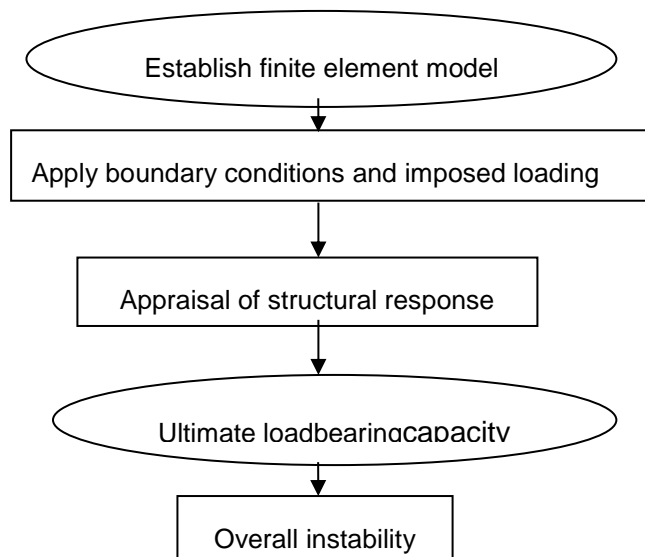


Fig.1-Identification flowchart for occurrence of a progressive collapse in a suspen dome

Description of investigated structure

Based on appropriate simplification, the physical dimensions of Beijing Olympic Badminton Gymnasium suspen dome are given as follows [9-11]: the span of the model is 93m and 8m high, fixed and hinged as shown in Figure 2.

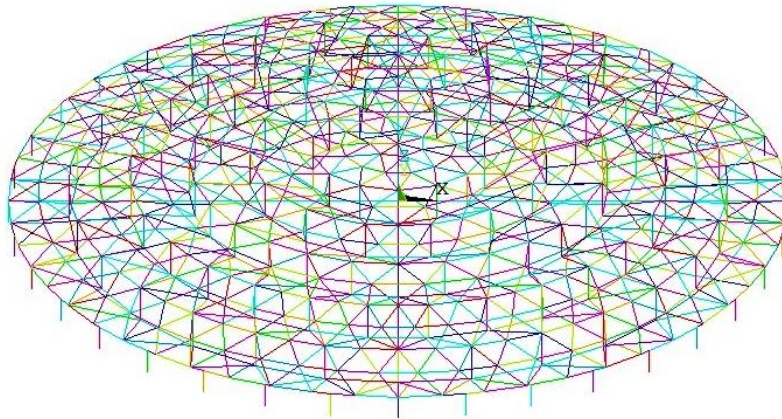


Fig. 2 - Model design of Beijing Olympic Badminton stadium

The single layer reticulated shell is a $\phi 219 \times 10$ circular steel pipe with Q345 steel circular tube of $\phi 168 \times 8$ for strut and a yielding strength of 345 N/mm^2 . The permanent and live loads of the roof are 0.85 kN/m^2 and 0.5 kN/m^2 respectively for initial simulation. Based on static equivalent principle, the uniformly distributed load is equivalent to a vertical concentrated load on each node of the upper single layer of the reticulated shell. According to Wenjiang et al. [12], in general, for a suspen-dome with N_r rings, the suggested pre-stress force ratio is given as $N_r: N_{r-1}: N_{r-2}: \dots : 1$. For the model, $1.8 \times 10^5 \text{ N/mm}^2$ was adopted for the pre-stressed cable with distribution ratio of 5:4:3:2:1 from the outer to the inner hoop. The area and material properties are illustrated in Tables 1 and 2 respectively.

Tab. 1 - Details of hoop cables and radial cables

		Hoopcable			Cable diameter	
		HS1	HS2~3	HS4	JS1	JS2~4
Cable						
	Cross-section area (mm²)	7658	2730	1179	1179	726
	The equivalent axial stiffness (MPa)	9898	3258	1524	1524	938
	Strength (MPa)	6950	2478	1070	1070	659

Tab.2 - Material Properties

	Modulus of elasticity (E)/GPa	Density /kg/m ³	Tensile strength /MPa	Design strength (f) /MPa	Poisson ratio	The temperature coefficient of expansion (α)/K ⁻¹
Section steel	206	7850	550	315	0.3	12×10 ⁻⁶
Steel Cable	180	7850	1670	835	0.3	12×10 ⁻⁶

Material type proposed

Aside from the geometric configuration and stiffness of the tensegrity system, the static performance of the suspen dome is essentially governed by axial mechanical properties of the cables. As hinted earlier, carbon fiber reinforced polymer cables is proposed to replace steel ones. Based on the structural dimensions of Beijing Olympic Badminton stadium suspen dome, the structural scheme of the tensegrity system made up of carbon fiber reinforced polymer cables would involve material properties illustrated in Table 3.

Tab.3 - Material Properties Proposed for carbon fibre reinforced polymer cables

	Modulus of elasticity (E)/GPa	Density /kg/m ³	Tensile strength /MPa	Design strength (f)/MPa	Poisson ratio	The temperature coefficient of expansion (α) /K ⁻¹
Radical and hoop cables	160	1600	2300	920	0.3	6.8×10 ⁻⁷
Strut	390	1600	2740	920	0.3	6.8×10 ⁻⁷

Exploiting the relative high tensile strength of carbon fiber reinforced polymer cables and avoiding the unfavorable influence of their relatively low elastic modulus can improve the structural mechanical property of the system.

Element and mesh selection

A suspen dome structure is made up of series of beams and truss elements. Two types of elements were selected for the analyses of the structure, namely: LINK 10 and BEAM188.

LINK 10 element is a uniaxial 3-D elastic truss element with tension only (or compression only) capability. The element has three degrees of freedom at each node: translation in x, y and z directions of the nodal, translation in node x, y and z directions [13]. BEAM 188 is an element to

analyze slender to moderately thick structures. It is a quadratic 3-node beam element in 3-D, having a six to seven degree of freedom at each node [13].

The single reticulated layer is meshed using BEAM188 and the tensegrity system is meshed using LINK10 (Bar element). A reasonable mesh of element size 1mm x 1mm was implemented for both cases. The model consists of 1785 elements and 621 nodes. Carbon fiber reinforced polymer cables were modeled as an anisotropic linear-elastic material and an isotropic elastic-plastic material was assumed for the mechanical behavior of steel cables.

Loading and Boundary conditions

The joints of the upper single layer are rigid joints. The degrees of freedom for the supporting joints are restricted as the boundary conditions. The upper single reticulated shells are under uniform loads. The dead, live, seismic, temperature values were considered alongside with all pertinent load combinations as specified in Chinese standard codes [14-16].

RESULTS

Firstly, results obtained from carbon fiber reinforced polymer model were compared with steel model to see the influence of the advantages of carbon fiber reinforced polymer. Carbon fiber reinforced polymer and steel models were analyzed at different imposed load for the whole system. In addition, the reactions of the radial and hoop cables were considered due to the snap effect.

Load bearing capacity of the models

Elastic design is based on full calculated loads. The minimum load causing buckling depends on the mechanical and geometrical characteristics which include section, length, young modulus and end support conditions. The load displacement curves for loading conditions on the models to achieve their ultimate bearing capacities are illustrated in Figure 3.

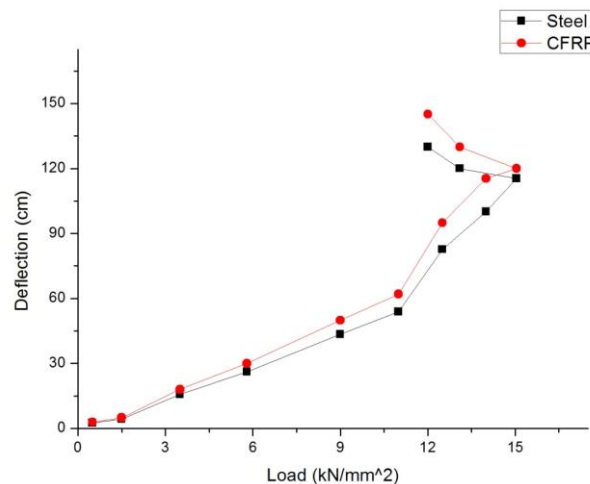


Fig. 3 - Load-displacement curve of the suspen dome at maximum load

In the elastic phase, the two curves are consistent. The suspen dome showed a linear nature in the initial loading period for both carbon fiber reinforced polymer and steel cables due to the pre-stressed nature of the tensegrity system. When carbon fiber reinforced polymer reaches its

maximum elastic phase it fails whereas steel cables can still withstand additional load due to its strain hardening effect. The elastic ultimate load bearing capacity for steel was 15.0kN/m^2 and that of carbon fiber reinforced polymer was 18kN/m^2 . Pre-stressed carbon fiber reinforced polymer increased the stiffness of the structure with an ultimate capacity a little bit closer to steel. This is advantageous when improving the serviceability of the structure is desired.

The performance of carbon fiber reinforced polymer also increased as a result of its high ultimate strength. Any additional load on carbon fiber reinforced polymer cable model would yield to elastic-plastic which means instability of the structure and a progressive collapse will occur. In reality, non-linearity and imperfections prevent real structure from achieving its theoretical capacity.

Stress behavior of the suspen dome members

Figure 4 illustrates the typical nodes and elements of the structure. Due to the symmetrical nature of the structure any node or element can be represented by one of the typical nodes or elements.

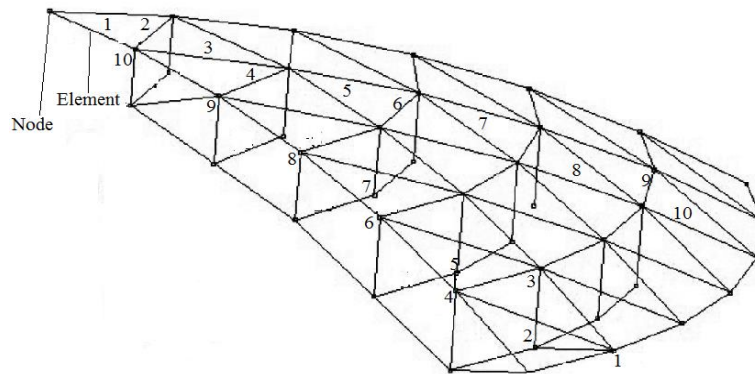


Fig. 4 - Typical numbering of nodes and element

Buckling always occur at members near the support point of the suspen dome. It is necessary to strength the members near the support to avoid buckling which can lead to the instability of the whole structure. At maximum load bearing capacity of steel cables, as shown in Figure 5, stresses are generated at a quarter part of the outermost ring whereas the maximum stresses for carbon fiber reinforced cable just occurred at a point.

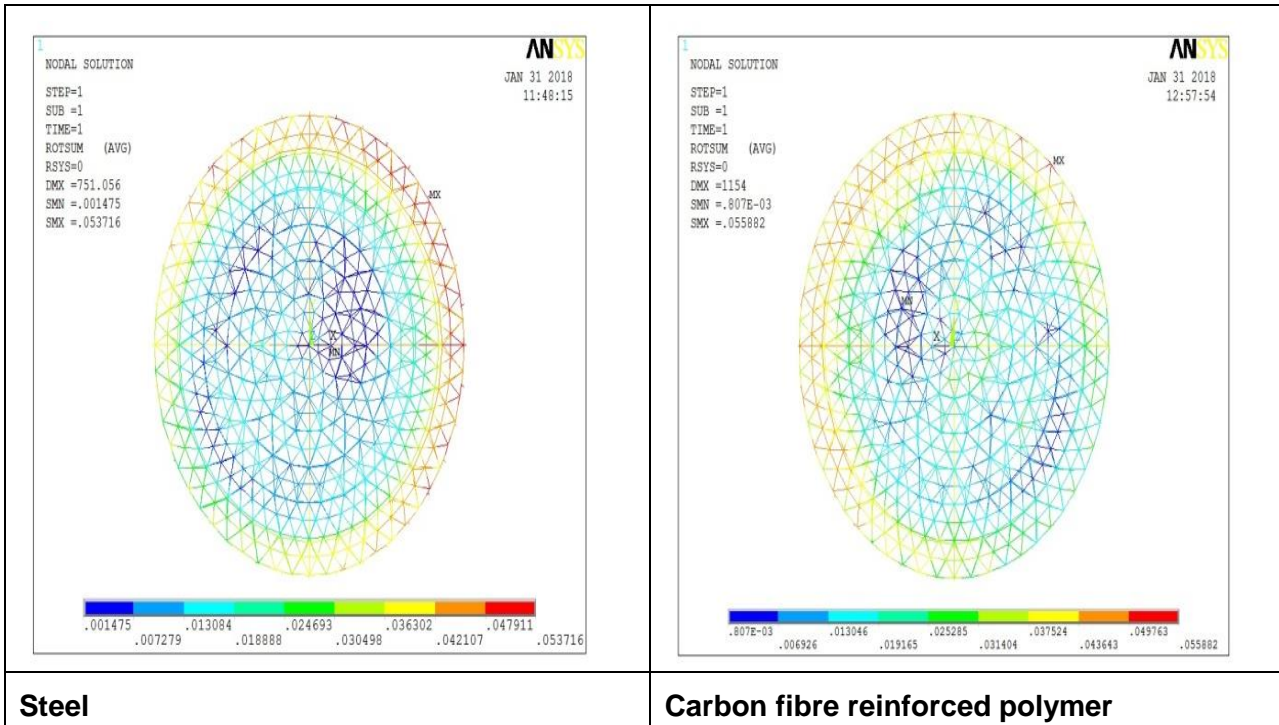


Fig.5 - Comparison of maximum load bearing capacity contour

In Figure 6, it is observed that the force experienced in carbon fiber reinforced polymer cables in relation to element is similar to that of steel cables; they both had a linear form showing that carbon fiber reinforced cables had the tendency to withstand force transfer better than steel based on applied load.

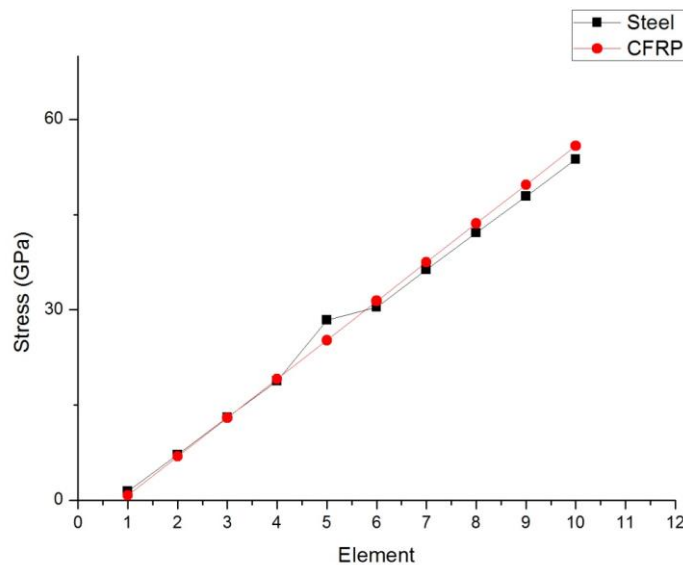


Fig.6 - Comparison of stresses at maximum load bearing capacity in element

Comparison of deflection in nodes

The maximum deflection occurs at the midpoint of the system within the perimeter axis of node 10. The deflection values for carbon fiber reinforced polymer are higher than those of steel cables with a percentage difference of 10% as illustrated in Figure 7. This is as a result of relatively small ultimate strain and low elastic modulus of carbon fiber reinforced polymer applied. A high stiffness could have been incorporated to reduce the effect of deformation sensitivity. However, this did not have much impact on the overall behavior pattern of carbon fiber reinforced polymer tensegrity system in the suspen dome as shown in Figure 3 and Figure 6. Relatively, a high pre-stressed carbon fiber reinforced polymer cable does not increase the elastic stiffness, bringing about the issue of exploiting the relatively high tensile strength of carbon fibre reinforced polymer cable and effectively avoiding the unfavorable conditions of its relatively low elastic modulus.

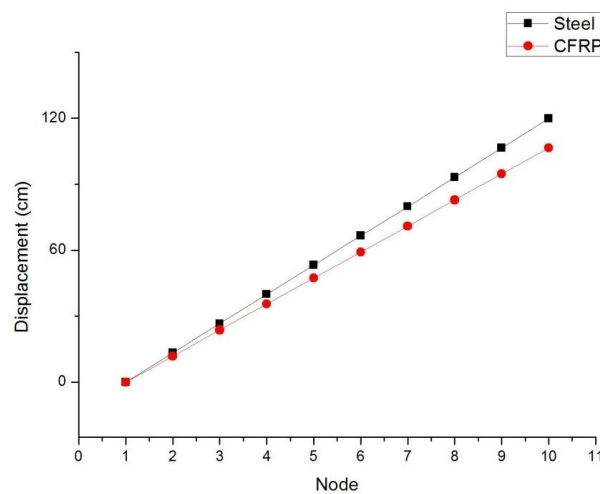


Fig. 7 - Comparison of displacement in at maximum load bearing capacity in nodes

Influence of internal forces on hoop cables

Internal forces of the cable segment are considered. The pretension of the initial hoop cable would have great influence on the next cable. The internal forces at different locations in the cable differ due to the friction between the cable and joints. The outermost hoop cable (hoop1) is considered because it has the most significant influence on the mechanical properties of the suspen dome. Based on the findings of Zhu et al. [17], the hoop cable rupture would result in the failure of the whole tensegrity strut assemble; meaning that the hoop cable has more influence on the displacement and internal force of the structure than the ridge cable.

Figure 8 illustrates the position of the hoop cables within the suspen dome. Results based on the internal generated force in the hoop cables are illustrated in Table 4.

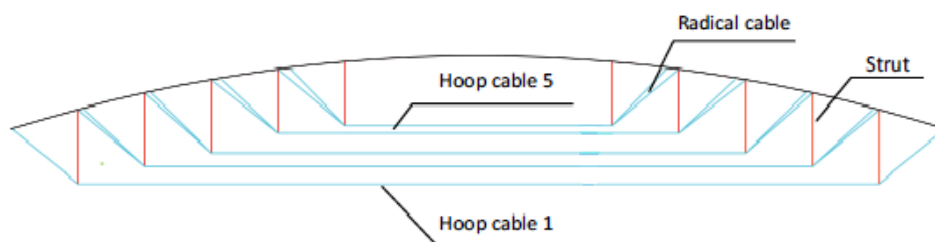


Fig. 8- Position of hoop cables

From the results obtained as illustrated in Table 4, carbon fiber reinforced polymer cable has proven its capability when compared with steel. The outer most hoop for the steel has more effect on the suspen dome structure and the inner hoops have relatively low effect on the structure which is similar to that of carbon fiber reinforced polymer tensegrity system. In addition to this, carbon fiber reinforced polymer hoop cables had similar internal generated force and stresses as compared to steel when the ultimate bearing capacity was reached.

Tab 4 - Internal Forces of Hoop Cables at maximum load bearing capacity (kN)

	Steel	CFRP
Hoop 1	21280	21460
Hoop2	11704	11916
Hoop3	11218	11370
Hoop4	7134	8126
Hoop5	2148	2180

Influence of internal forces on the radical cable

The internal forces of the radical tension member obtained had small values for all the hoops except for hoop1. Only the internal force of hoop1 in relation to radical tension member was considered because the change of internal forces of the radical tension member is similar to the change of the internal force of the hoop cable which affects the internal forces of the radical member directly since internal forces of the radical member are generated due to pretension in the hoop cable [18-19]. Table 5 shows that the generated internal force of the radical cable carbon fiber reinforced polymer is in agreement with that of steel with only a very minimal difference.

Tab.5 - Internal force of radical cable at maximum load bearing capacity (kN)

Steel	5129.3
CFRP	5131.7

CONCLUSION

This study examines the most likely cause of structural failure of a suspen dome with carbon fiber reinforced polymer as the tensegrity system by observing the node point which is the weakest component in the structure that is expected to yield when loads are imposed on it. However, from the analysis, carbon fiber reinforced polymer cable improved the ultimate bearing capacity of the system at the support end due to its high tensile strength which has similar values with steel despite a little difference in their load bearing capacity.

Given the results obtained from carbon fiber reinforced polymer tensegrity system, one can conclude that it gives rigidity and stiffness to the single reticulated layer. Hence a super stability of the system is guaranteed when the tensegrity system is designed with carbon fiber reinforced polymer cables.

ACKNOWLEDGEMENTS

The authors acknowledge the support of the National Science Foundation of China (Grant no: 51608234; 51478209) and Province Science of Jiangsu BK20160534

REFERENCES

- [1] Olofin I., Liu R., 2015. The Application of Carbon Fibre Reinforced Polymer (CFRP) Cables in Civil Engineering Structures. SSRG International Journal of Civil Engineering, vol. 2:1-5.
- [2] Olofin I. Liu R., 2017. Suspen-dome System: A Fascinating space Structure. The Open Journal of Civil Engineering, vol.11: 131-142.
- [3] Yue L., Bernd Z., Schlaich M., 2016. Advantages of using CFRP cables in orthogonally loaded cable structures. AIMS Material Science, vol. 3: 862-880.
- [4] Olofin I & Liu R., 2016. Numerical modal analysis of a suspen-dome with carbon fibre reinforced polymer tensegrity system. ASME Journals: Series Modelling A, vol. 8:13-24.
- [5] Olofin I., Liu R., 2017. Structural Optimization of Beijing Gymnasium Suspen-dome with carbon fibre reinforced polymer (CFRP) cable. Scientific Herald of the Voronezh State University of Architecture and Civil Engineering, vol. 36:106-115.
- [6] Olofin I., Liu R., 2017. Transient behavior of CFRP tensegrity system in a Suspen- dome. Civil Engineering Journal, vol. 8: 547-555.
- [7] Subramanian N., 2006. Space Structures: Principles and Practice, Multi-Science Publishing Co Ltd, Brentwood, Essex, UK.
- [8] Tsuboi Y., 1984. Analysis, design and realization of space frames: A state –of-the –art Report, Bulletin of International Association of Shell and Spatial Structures, No 84/85, vol. XXV-1/2.
- [9] Ge J., Zhang G., Wang S., 2007. The overall stability analysis of the suspend-dome structure system of the badminton gymnasium for 2008 Olympic Games. Journal of Building Structures, vol. 44: 22-30(in Chinese).
- [10] Ge J., Wang S., Liang H., 2007. Design and research of the large-span steel structure of the badminton gymnasium for 2008 Olympic Games. Journal of Building Structures, vol. 51: pp10-21 (in Chinese).
- [11] Liu X., 2010. Innovation of New-type Large-span Prestressing suspend-dome Structure System and Application of Project for Beijing Olympic Games. The College of Architecture and Civil Engineering of Beijing University of Technology, (in Chinese).
- [12] Kang W, Chen Z, Lam H., Zuo C., 2003. Analysis and design of the general and outmost ring stiffened suspen-dome structure. Engineering structures, vol. 25: 1685-1695.
- [13] ANSYS., 2008. Release 10.0 Documentation for Ansys, USA.
- [14] GB50009-2012. Load code for the design of building structures. Chinese planning press, Beijing (In Chinese).
- [15] GB50017-2003. Code for design of steel structures. Chinese planning press, Beijing (In Chinese).
- [16] GBJGJ7-2012. Technical specification for space frame structure, Chinese planning press, Beijing (In Chinese).
- [17] Zhu ML., Dong S., 2012. Failure analysis of suspen dome by vector form intrinsic. Journal of Zhejiang University, vol. 46: 9-15.
- [18] Chen Z., Renzhang Y., Xiaodun W., Hongbo L., Xiao X., 2015. Experimental researches on suspen-dome structure with rolling cable-strut joint. Advanced Steel Construction, vol.11: 15-38.
- [19] Shekastehband B., Abedi K., Dianat N., 2014. Experimental and numerical studies on the progressive collapse behavior of tensegrity systems, International journal of space structures, vol. 29: 9-24.

EFFECT OF MOISTURE ON THE INTERFACE OF TIMBER AND EXTERNALLY BONDED FIBRE REINFORCED POLYMERS: A REVIEW PAPER

Nayan Das and Rijun Shrestha

University of Technology Sydney, Faculty of Engineering and IT, School of Civil and Environmental, Ultimo, NSW-2007, Australia; nayan.das@student.uts.edu.au

ABSTRACT

Timber as a structural material has been in use since the medieval period. Even today, there are many residential houses being built with timber frame in Australia. Wooden wharfs and bridges are common examples of timber structures in coastal regions of Australia. Humidity in such coastal regions is often high causing an increase in moisture level in the timber structures. Besides, over-loading, rot and decay, termites and borers, etc. cause damage to timber and presence of moisture either aggravates this or favours such causes. Hence, there has been an increased demand for repair and rehabilitation of heritage and important timber structures. Strengthening wooden structures with fibre reinforced polymers (FRPs) is becoming popular in the construction industry. The objective of this paper is to demonstrate the effect of moisture on the durability of the timber-FRP interface. After reviewing previous studies in the durability of the timber-FRP composite, it has been found that prolonged moisture exposure leads to premature debonding in the timber-FRP interface. A graphical representation of the effect of moisture on bond failure has been established through this research work after investigating the previous work of scholars. This paper also highlights the significance of applying adhesion promoter in enhancing the performance of timber-FRP interface.

KEYWORDS

Rehabilitation, Timber/FRP interface, Adhesive, Moisture

INTRODUCTION

Australia has most of its cities established around the coastal belt with over 40,000 timber wharfs and bridges which are vital for public transportation. However, most of these structures are old and approaching their end of design life. Hence, rehabilitation of these timber structures is gaining popularity to meet the rapidly increasing traffic-load demands. Another reason for the growing need for rehabilitation is to mitigate the financial risk of losing the vast amount of infrastructural resources [1].

In Australia, many residential buildings are made up of Engineering Wood Products (EWPs). Solid woods go through reconstitution and densification to produce EWPs which exhibit superior mechanical features than the original unprocessed timber. Some of the common EWPs are laminated veneer lumber (LVL), glued laminated (Glulam) and oriented strand lumber (OSL). There are some other benefits of using timber products as structural materials. They have low embodied energy and pleasant aesthetics. They are cost-effective alternatives to concrete and steel [2]. Another research carried by Wang et al. indicated that timber structures typically present

good seismic performance [3]. The application of timber in the construction industry is not only popular in Australia but also all around the world. In fact, the European Union has identified the need to adopt renewable sources of energy and rebuild old structures as its important strategy to combat the global crisis of climate change [4]. The push for green energy has led to an increase in demand for timber materials as well as the rehabilitation of existing timber structures.

Factors such as damage due to over-loading, decay, etc. can lead to the need for repair. Changes to functionality, loads or changes to code can require structural retrofitting [5]. Repair and rehabilitation are two distinct terminologies. Repair can be defined as a process of restoring the original strength of an element or a section of an existing structure. It is done to a structure either as a part of maintenance activities or to correct damaged sections due to faulty construction practices. On the contrary, rehabilitation is a much broader term. It encompasses the repair process to regain the original capacity as well as the strengthening of an existing structure to accommodate the changes in the current standards and design guidelines [6]. Traditional methods of strengthening timber structures include increasing the flexural strength of an existing timber section by adding new wood elements or by using metallic cover plates tied with the help of mechanical fasteners [7]. However, there are disadvantages of the conventional strengthening techniques of timber elements. The use of mechanical fasteners creates a region of stress concentration which is vulnerable to deterioration with time. Moreover, the addition of new materials increases the labour costs as well as the dead load of the structure [8]. These problems associated with the traditional rehabilitation methods paved the way for the modern age strengthening techniques with fibre reinforced polymers (FRPs). The ease of conducting rehabilitation works in selected patches of the structures and the high strength as well as durability of FRPs have made them popular rehabilitation materials for timber structures. The most commonly used FRPs as strengthening material for timber structures are carbon fibre, glass fibre and high-strength glass fibre [9].

The motivation of strengthening timber elements with FRPs was drawn from the success of concrete-FRP composites in the construction industry. Gilfillan, Gilbert & Patrick in their research work indicated that FRP materials can easily help attain a full strength of timber elements [10]. This idea was reinforced by another scholarly work by Svecova & Eden which showed an application of glass fibre reinforced polymers as a strengthening material in timber member enhanced both the flexural and shear strength of the element by 50% [11]. Similar studies are found in the field of concrete-FRP composites where externally bonded FRPs are installed to enhance the performance of concrete structures [12]. Researchers were successful with their experiments in increasing the flexural and tensile strength of concrete sections using externally bonded FRPs [13]. Despite the remarkable achievements of scholars in the past 30 years in the domain of strengthening timber structures using FRP yet, the effect of environmental stresses on the long-term performance of the timber-FRP composites has not been properly investigated. There are many quality literature review works which highlighted the fact that there is a lack of knowledge in the bond durability of timber-FRP composites compared to concrete-FRP composites [14].

This paper presents the effect of moisture on the interface of timber and externally bonded FRP by demonstrating state-of-the-art review of previous studies in the field of rehabilitation of timber using FRP composites. The paper is divided into 4 major sections comprising of the materials involved in the timber-FRP interface, factors affecting the bond durability, effect of moisture on individual components and finally, the conclusion highlighting the key outcomes of the paper and issues that can be addressed in the future research work.

TIMBER-FRP INTERFACE

The materials involved in the timber-FRP joint are timber, structural adhesives, and the FRP composites. FRPs are manufactured through a polymeric process where the fibres are fused within a matrix. The fibres impart the strength to the FRP composites. They have a low weight to density ratio, high strength, high stiffness and are resistant to corrosion. However, FRPs are anisotropic (sensitive to directions) in nature and hence, special care is required to install them in proper orientations for strengthening purposes. Moreover, FRP composites are susceptible to dimensional changes under varying moisture and temperature conditions [15]. Carbon, glass, and aramid are the common commercially available fibres. Nonetheless, carbon and glass fibres are mostly used in civil engineering projects [16]. The adhesive in the timber-FRP acts as the medium of stress transfer between the timber substrate and the externally bonded FRPs [17]. The application of adhesive in fabricating a bond is an efficient method as compared to using mechanical fasteners since it does not yield any region of stress concentration. Epoxies are the common structural adhesives used at the timber-FRP interface during the rehabilitation work of timber structures [7]. The contemporary construction industry prefers using epoxy adhesives to conventional structural adhesives. It is because epoxies are thermosetting resins which cure at ambient temperature and have superior gap-filling properties [18]. The chemical properties of epoxy adhesives make them suitable for civil engineering applications. These adhesives can cure over a wide range of outdoor temperatures and have limited shrinkage during the curing process [19]. However, previous research strongly indicated that the presence of moisture is detrimental to the durability of the timber-FRP interface [18,19]. Hence, the behaviour of individual components of the timber-FRP interface under varied service conditions is required to be studied and examined for durable rehabilitation works. Among various service conditions, moisture plays a dominant role in affecting the durability of the timber-FRP composite system. Figure 1 portrays a section of the timber-FRP interface in moisture conditions.



Fig. 1 – Shows Timber-FRP interface under moisture conditions

FACTORS AFFECTING THE BOND DURABILITY

The timber-FRP interface is composed of three dissimilar materials. Several factors affect the integrity of the interface. Environmental factors such as ultraviolet (UV) radiations, temperature variations, and moisture conditions play key roles in defining the durability of the bond. Researchers have established that the performance of the interface also depends on the surface preparation of the timber substrate. Vanerek et al. in the year 2014 highlighted the significance of the surface preparation to the long-term performance of the timber-FRP interface. The timber surface is to be suitably prepared to avoid any air bubble formations during the application of the adhesive. Air bubbles are detrimental to the durability of the bond. The adhesive should be applied within a short time interval after the surface preparation to prevent air bubble formations as well as surface contamination [18]. This philosophy is further consolidated by research work carried by Vahedian, Shrestha & Crews in the year 2017 and Cabral-Fonseca et al. in the year 2018 by outlining the requirement of surface preparation to produce a rough surface for better adhesion. Researchers recommended sanding as a cheap and efficient surface preparation method.

Cleaning the timber surface with acetone and air blasting are few other methods of surface preparation [8,20].

The main constituent of wood is cellulose. It is responsible for the wood growth and performance of the wood products. On the other hand, epoxies are made up of two components, namely hardener and base mixed at a specific ratio to produce thermosetting resins. The cellulose-epoxy bond in the timber-FRP interface is a van-der Waal's bond which is the weakest bond in nature [21]. However, a thicker adhesive bond does not circumvent the weak bonds of the interface. This essentially means the thickness of the interface needs to be carefully determined while enhancing the bond performance. This is due to the fact that thicker bond at the interface may cause increased porosity leading to failure. Hence, it is essential to reinforce the adhesion with mechanical fasteners or adhesion promoters. Commonly available classes of adhesion promoters in the market are zircoaluminate, organotitanate, organosilane, alkyl phosphate ester and metal organics. But, silane-based adhesive promoters are considered suitable for epoxies due to their high degree of chemical resistance and the ability to transfer stresses between two composite materials. This is evident from the scholarly work conducted at the National University of Ireland in 2009. A team of researchers investigated the effect of adhesion promoter on the performance of timber-FRP interface in a series of experiments. A silane-based compound in aqueous solution was used as an adhesion promoter in the experiments to evaluate the performance of the timber-FRP interface. It was found that the adhesion promoter prevented the premature failure of most of the timber-GFRP (glass fibre reinforced polymer) specimens. However, dissimilarities in moduli of elasticities in materials and coefficients of expansion raise some concerns for the dimensional stability of the bonded system [18,22].

UV rays, changes in temperature and moisture exposure can cause deterioration to the timber-FRP bonded system. It was found that UV rays caused photo-degradation of the top surface of the FRP strips. This led to the decolorisation of the FRP strips and eventually a reduction in shear and tensile strengths of the FRP material [20]. Temperature also plays an important role when it comes to the long-term performance of the timber-FRP interface. The epoxies are tolerant to a wide range of operating temperature and do not show many deteriorating mechanical properties under the effect of temperature. On the contrary, FRPs are susceptible to heat and temperature changes. The matrix holding the fibres tend to crack under high temperature [23]. Another environmental factor that plays an important role in influencing the durability of the timber-FRP interface is the moisture condition. Researchers agree to the fact that the effect of moisture is unavoidable. It affects the mechanical properties of all the individual components involved in the timber-FRP. Timber composites are susceptible to changes in the moisture content. Any change in moisture content can cause a drastic effect on the dimension and strength of timber products. Moreover, researchers claim that the adhesive strength also reduces under continuous wet and dry cycles throughout the design life of the structure [8,18,20,21,24].

Overall, this section summarizes the critical factors that can affect the success of the rehabilitation work of timber structures using externally bonded FRPs. Further, a tabular matrix has been developed showing both the positive and negative relationships between the effect of environmental, cost, mechanical and visual factors respectively on the individual components of the timber-FRP interface. The matrix has been represented in a tabular format as shown in Table 1.

Tab. 1 - Shows the analysis of material properties

TIMBER - FRP INTERFACE: ANALYSIS OF MATERIAL PROPERTIES				
Categories	Wood / Timber		Epoxy Adhesives	
	Positive features	Negative features	Positive features	Negative Features
Environmental factor	Renewable	Degrades	No gaseous emission	Dimensionally unstable under moisture exposure
Cost factor	Low cost	Added surface treatment cost	Increase in demand leading to competitive prices	High manufacturing cost
Mechanical parameters	High Strength - Weight ratio	Low load carrying capacity and brittle failure	Limited Shrinkage during curing and transfer stresses	Susceptible to mechanical damage
Visual appearance	Pleasant aesthetic	Surface defects such as splits and knots	Clear liquid	May require mechanical faster
Categories	EWPs		FRPs	
	Positive features	Negative features	Positive features	Negative Features
Environmental factor	Low embodied energy	Degrades	Durable	Deteriorates under UV rays
Cost factor	Economic alternative to steel and concrete	High manufacturing cost	Strength and stiffness	Expensive
Mechanical parameters	Aseismic property	Brittle failure	High capacity	Premature debonding
Visual appearance	Pleasant aesthetic	Finger joint	Tidy installation	Painting needed

MOISTURE CONDITIONS

The success of the rehabilitation work depends largely on the integrity of the timber-FRP interface. The review of past scholarly articles indicates moisture as the most important parameter affecting the performance of the timber-FRP interface. Hence, a critical understanding of the effect of continuous wet/dry cycles on the timber-FRP interface is essential to fabricate a durable joint. The following sections elaborately review the effect of moisture on the individual components of the timber-FRP system.

Effect of moisture on timber

Wood, being a natural material, is very much prone to environmental deterioration. Moisture is one of the most important factors impacting the strength as well as the dimensional stability of timber

element [18]. Continuous exposure to moisture cycles at varied temperature causes the development of hygrothermal stresses in the wood elements. These stresses affect the bond between dissimilar materials and are detrimental to the timber-FRP interface. There were many experiments that recorded and demonstrated the effect of moisture in timber structures. One of such experiments was highlighted by Björngrim, Hagman & Wang in the year 2016 where sensors were used to assess the health of timber bridge subjected to aggressive moisture attacks. The purpose of setting up sensors was to check the moisture levels at various sections of the bridge. It was found that if the moisture content was above 20%, the wood section was at high risk of rotting. Further, frequent inspections of moisture levels helped to identify locations of high moisture content and hence, reducing the risk of biological degradation leading to failure of the bridge elements [25]. Nonetheless, researchers are still trying to develop efficient and effective methods to protect and rehabilitate timber members from moisture attacks.

Effect of moisture on FRP

It is important to study the effects of moisture on the FRPs where they are used as externally bonded materials. The externally bonded FRPs are the first point of contact for the environmental stresses and the knowledge of their behaviour under moisture attacks would provide valuable insights on the durability of the timber-FRP interface. It is now established that moisture plays an important role in affecting the long-term performance of FRPs. It is the epoxy matrix in FRP that might get affected due to diffusion of water through the various layers of FRPs. In general, there is no definite relationship between moisture content and the durability of FRP. However, it has been found that glass fibres are more prone to moisture degradation than carbon fibres. The surface microcracks give way for the ingress of water molecules in glass fibres leading to crack propagation and deterioration [23]. FRPs are generally immune to moisture attacks. But, researchers provide evidence of cases where wet and dry cycles over an extended period of time have led to a reduction of strength in FRPs [20].

Effect of moisture on epoxy adhesives

In 2003, Charles R. Frihart, one of the pioneer scholars in the field of Timber-FRP analysis, indicated that the failure of adhesive to transfer stress effectively across timber substrate to the FRP was responsible for the debonding of timber-FRP under moisture conditions. In the subsequent years, researchers were able to establish the fact that the decrease of bond strength of timber-FRP composites was witnessed due to exposure to wet cycles over an extended period [24]. Hence, moisture is an important factor to consider while fabricating a bonded system using adhesive.

An epoxy adhesive is a structural adhesive used in the timber-FRP interface for its many benefits. Although the production cost of epoxy adhesive is high, it does not cause stress concentration, unlike mechanical fasteners. Moreover, there are certain epoxies that could be used to fabricate a stronger timber-FRP interface. Hence, suitable selection and application of adhesives could lead to durable bonded systems [22]. Epoxy adhesive has gap-filling properties which can treat micro-cracks in the timber substrate producing durable bond. However, application of epoxy adhesives in moisture conditions resulted in loss of nearly 50% of the bond strength [18]. Vulnerability of epoxy adhesives to moisture attack is due to their molecular affinity to water molecules [20]. Although researchers have established significant theories around the role of adhesives in debonding under moisture conditions yet, there is a scope of further research and development of adhesive suitable for durable timber-FRP composites to be used in rehabilitated timber structures.

Effect of moisture on Timber-FRP interface

The application process of adhesive while fabricating the timber-FRP bond should be done extremely cautiously. Any development of air bubbles will lead to failure of the bond [27]. In a significant research work published in 2015, Zhou, Tam, Yu and Lau explained their experiments which were intended to understand the correlation of moisture development and failure behaviour of the timber-FRP joint. They found that development of air bubbles may lead to premature failure of the timber-FRP interface if the moisture content is more than 20%. Conversely, under low moisture condition (moisture content < 15%), the timber-FRP composite may also fail. However, the failure under low moisture conditions would be brittle. This implies that the presence of a failure plane within the timber substrate of the timber-FRP system in case of brittle failure. With the increase in moisture content from less than 15% to more than 20% over 8 weeks' time, the debonding failure plane demonstrated movement from within the timber substrate to the timber-FRP interface. The failure under moisture conditions (moisture content > 20%) was progressive in nature as compared to sudden failure in low moisture conditions (moisture content <15%). It was found that the timber-FRP interface failed prematurely at higher moisture content. The experiment also revealed the failure behaviour of seasoned timber in normal environmental conditions. Seasoned timber at normal room conditions has a moisture content less than 15% [21]. However, in case of marine wooden structures in the context of Australian coastal regions, seasoned timber used for structural purposes may also experience high moisture content and could lead to premature debonding failure. Interestingly, another recent development in concrete-FRP composites suggested that the failure plane shifted from within the concrete substrate towards the timber-FRP interface when exposed to moisture [20]. This study reinstated the outcomes of the aforesaid experiment which indicated the movement of failure plane from within the timber section to the timber-FRP joint when subjected to moisture content greater than 20%. Such similarities and patterns in concrete-FRP composites and timber-FRP composites can help researchers to draw more conclusions from the already established earlier system to consolidate durability studies for the latter one.

Hence, it is evident from the studies that the failure plane moves from within the timber towards the interface under moisture exposure and fails prematurely [8,20,21,22]. Figure 2 gives a representation of the load versus deflection graph depicting the premature failure of the timber-FRP interface under different moisture conditions.

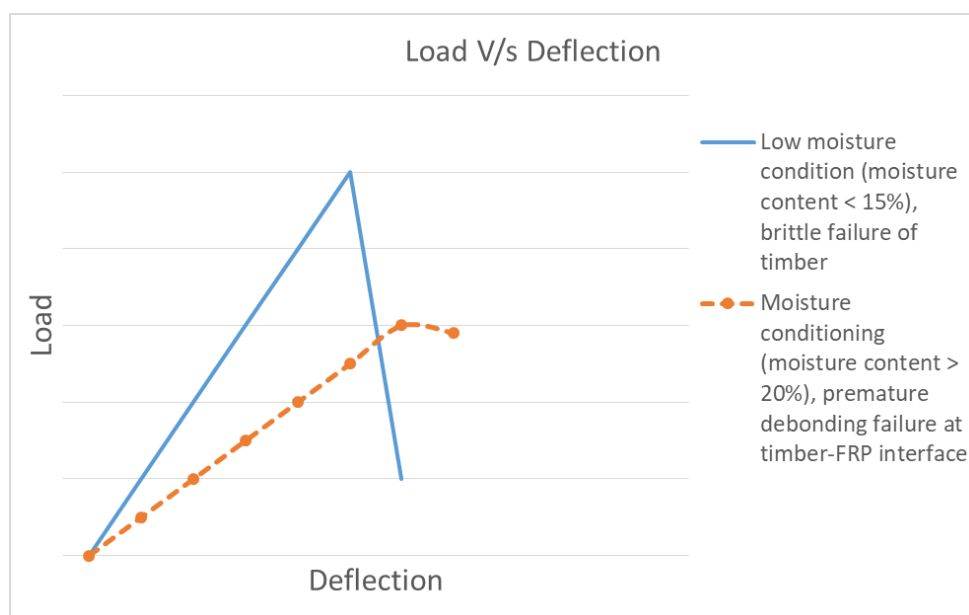


Fig. 2 – Illustration of premature failure of Timber-FRP interface under the effect of moisture

CONCLUSION

The paper encourages engineers and building practitioners in Australia to take into account the effect of moisture on bond durability of timber-FRP interface. Consideration of moisture variations is crucial while strengthening the timber elements (eg. timber decks of bridges) using externally bonded FRPs. The paper also highlighted the application of adhesion promoter in enhancing the performance of the timber-FRP interface. Adhesion promoters, or commonly known as coupling agents, are brush-applied materials used as a priming coat to increase the adhesive strength of a substance to bind two dissimilar materials. Among the many variants of coupling agents in the market, authors recommend silane-based coupling agents for epoxy adhesives because of their unique characteristic of transferring stresses from resin-based substance (epoxy adhesive) to the substrate (timber composite). In addition, it is important to note that the effectiveness of the adhesion promoter, and subsequently the durability of the timber-FRP interface depends on the surface preparation of the timber substrate. This preparation is necessary to avoid any air bubble formation as well as the inclusion of dust and contamination during the application of the adhesive.

Such a reconstruction procedure is of great consequence to the construction industry of Australia because it has a number of timber structures that are approaching the end of their life and are in need of immediate rehabilitation works, especially heritage bridges close to a marine region like the Hampden Bridge built during the 1890s in Kangaroo Valley. Many of these structures are in the coastal belt which makes it difficult for the engineers to carry out long-lasting repair and rehabilitation works.

In conclusion, the paper establishes the fact that timber composites, as well as epoxy adhesives, are prone to detrimental changes due to variations in moisture level over the service period of a structure. It is the view of the authors that thicker bondline may be more likely to result in increased porosity and micro-cracking resulting in low bond strength. Therefore, this paper attempts to provide modest guidance to the future scholars for developing a proper design guideline or a design handbook with definite specifications on the bond length and bond-line thickness for fabricating durable and economic timber-FRP interface. The paper also came up with a unique comprehensive table that summarizes the characteristics of different components of the timber-FRP interface under the effect of various factors. The summary table is very convenient for any engineer or academician to have a look and get initial views of the merits and demerits of different materials involved in the rehabilitation of timber structures. It is evident from the review work that among various service conditions, moisture plays a dominant role in affecting the durability of the timber-FRP composite system. High moisture content (greater than 20%) shifts the failure plane from within the timber substrate towards the interface of the timber-FRP bond causing pre-mature debonding and failure of the repaired section. This failure pattern is analogous to the failure model of concrete-FRP composites. As a result, the authors suggest proven and established theories of concrete-FRP composites should be used as a baseline reference for carrying future research in the field of timber-FRP composites. Finally, the authors support further work in this field to produce valuable insights not only in developing a durable timber-FRP interface, but also to have a sustainable balance between the construction of new structures and rehabilitation of old structures.

ACKNOWLEDGMENTS

This research work is carried out as a part of graduate project in the School of Civil and Environmental Engineering at the University of Technology Sydney. The author acknowledges Mr. Abbas Vahedian, Ph.D. Candidate, Faculty of Engineering and IT at the University of Technology Sydney for his endless support and guidance in making this work happen as well as the team of

42003: Engineering Project Preparation for their direct and indirect contribution to the completion of this dissertation.

REFERENCES

- [1]. Lokuge, W., Gamage, N. & Setunge, S. 2016, 'Fault tree analysis method for deterioration of timber bridges using an Australian case study', *Built Environment Project and Asset Management*, vol. 6, no. 3, pp. 332-44.
- [2]. Wei, P., Wang, B.J., Zhou, D., Dai, C., Wang, Q. & Huang, S. 2013, 'Mechanical properties of poplar laminated veneer lumber modified by carbon fiber reinforced polymer', *BioResources*, vol. 8, no. 4, pp. 4883-98.
- [3]. Wang, J., He, J., Yang, N. & Yang, Q. 2017, 'Study on Aseismic Characteristics of Tibetan Ancient Timber Structure', *Advances in Materials Science and Engineering*, vol. 2017.
- [4]. Calanter, P. 2018, 'EUROPEAN UNION STRATEGY ON COMBATING CLIMATE CHANGE AND PROMOTING ENERGY FROM RENEWABLE SOURCES', *Calitatea*, vol. 19, no. S1, pp. 130-4.
- [5]. Liew, K.C. & Grace, S. 2016, 'Engineered Wood Composite of Laminated Veneer Lumber: Physical and Mechanical Properties', *Materials Science Forum*, vol. 842, Trans Tech Publ, pp. 103-28.
- [6]. Stevens, G.R. & Kesner, K. 2016, 'Evolution of the ACI 562 Code—Part 1', *Concrete International*, vol. 38, no. 2, pp. 37-40.
- [7]. Stanila, O., Isopescu, D. & Hohan, R. 2010, 'Timber Elements: Traditional and Modern Strengthening Techniques', *Buletinul Institutului Politehnic din Iasi. Sectia Constructii, Arhitectura*, vol. 56, no. 3, p. 75.
- [8]. Vahedian, A., Shrestha, R. & Crews, K. 2017, 'Effective bond length and bond behaviour of FRP externally bonded to timber', *Construction and Building Materials*, vol. 151, pp. 742-54.
- [9]. Yang, Y.-l., Liu, J.-w. & Xiong, G.-j. 2013, 'Flexural behavior of wood beams strengthened with HFRP', *Construction and Building Materials*, vol. 43, pp. 118-24.
- [10]. Gilfillan, J., Gilbert, S. & Patrick, G. 2003, 'The use of FRP composites in enhancing the structural behavior of timber beams', *Journal of reinforced plastics and composites*, vol. 22, no. 15, pp. 1373-88.
- [11]. Svecova, D. & Eden, R. 2004, 'Flexural and shear strengthening of timber beams using glass fibre reinforced polymer bars—an experimental investigation', *Canadian Journal of Civil Engineering*, vol. 31, no. 1, pp. 45-55.
- [12]. Sen, R. 2015, 'Developments in the durability of FRP-concrete bond', *Construction and Building materials*, vol. 78, pp. 112-25.
- [13]. Sheikh, S. & Ahmad, Y. 2015, 'Flexural Strengthening of Structural Timber in the 21st Century: A State of the Art Review', *Applied Mechanics and Materials*, vol. 735, Trans Tech Publ, pp. 128-40.
- [14]. Vahedian, A., Shrestha, R. & Crews, K. 2018, 'Analysis of externally bonded Carbon Fibre Reinforced Polymers sheet to timber interface', *Composite Structures*, vol. 191, pp. 239-50.
- [15]. Zaman, A., Gutub, S.A. & Wafa, M.A. 2013, 'A review on FRP composites applications and durability concerns in the construction sector', *Journal of Reinforced Plastics and Composites*, vol. 32, no. 24, pp. 1966-88.
- [16]. Maxineasa, S.-G. & Taranu, N. 2013, 'Traditional building materials and fibre reinforced polymer composites. A sustainability approach in construction sector', *Buletinul Institutului Politehnic din Iasi. Sectia Constructii, Arhitectura*, vol. 59, no. 2, p. 55.
- [17]. Kinloch, A., Korenberg, C., Tan, K. & WATTS, J. 2004, 'The durability of structural adhesive joints', *Proc. 7th European Adhesion Conference, Freiburg, Germany*.
- [18]. Vanerek, J., Benesova, A., Rovnanik, P. & Drochytka, R. 2014, 'Evaluation of FRP/wood adhesively bonded epoxy joints on environmental exposures', *Journal of Adhesion Science and Technology*, vol. 28, no. 14-15, pp. 1405-17.
- [19]. Sousa, J.M., Correia, J.R. & Cabral-Fonseca, S. 2018, 'Durability of an epoxy adhesive used in civil structural applications', *Construction and Building Materials*, vol. 161, pp. 618-33.
- [20]. Cabral-Fonseca, S., Correia, J., Custódio, J., Silva, H., Machado, A. & Sousa, J. 2018, 'Durability of FRP-concrete bonded joints in structural rehabilitation: a review', *International Journal of Adhesion and Adhesives*.
- [21]. Zhou, A., Tam, L.-h., Yu, Z. & Lau, D. 2015, 'Effect of moisture on the mechanical properties of CFRP-wood composite: an experimental and atomistic investigation', *Composites Part B: Engineering*, vol. 71, pp. 63-73.

- [22]. Raftery, G.M., Harte, A.M. & Rodd, P.D. 2009, 'Bonding of FRP materials to wood using thin epoxy gluelines', *International Journal of Adhesion and Adhesives*, vol. 29, no. 5, pp. 580-8.
- [23]. Karbhari, V., Chin, J., Hunston, D., Benmokrane, B., Juska, T., Morgan, R., Lesko, J., Sorathia, U. & Reynaud 2003, 'Durability gap analysis for fiber-reinforced polymer composites in civil infrastructure', *Journal of composites for construction*, vol. 7, no. 3, pp. 238-47.
- [24]. Rowlands, R., Van Deweghe, R., Laufenberg, T.L. & Krueger, G. 2007, 'Fiber-reinforced wood composites', *Wood and fiber science*, vol. 18, no. 1, pp. 39-57.
- [25]. Björngrim, N., Hagman, O. & Wang, X.A. 2016, 'Moisture content monitoring of a timber footbridge', *BioResources*, vol. 11, no. 2, pp. 3904-13.
- [26]. Frihart, C.R. 2003, 'Durable wood bonding with epoxy adhesives', *Proceedings, 26th Annual Meeting, Adhesion Society, Inc*, pp. 23-6.
- [27]. Davalos, J.F., Qiao, P. & Trimble, B.S. 2000, 'Fiber-reinforced composite and wood bonded interfaces: Part 1. Durability and shear strength', *Journal of Composites, Technology and Research*, vol. 22, no. 4, pp. 224-31.

GEOMETRY CONSTRUCTION METHOD OF HEX-TRI RECIPROCAL FRAME

Lin Qi, Wenbo Zhang, Zifei Li, Ronglai Sun and Xin Huang

Civil Aviation University of China, Tianjin, China; qilin1208@vip.163.com, 1535218494@qq.com, 840259926@qq.com, 1070318660@qq.com, huangxin1395602@163.com

ABSTRACT

In this paper the geometrical characteristics and construction method of hex-tri reciprocal frame are studied. The naming rules of structural units, members and joints of hex-tri reciprocal frame are proposed. Based on the study of relationships between the structural geometrical parameters, the formulas for the joint coordinates of the structural unit are derived, and the calculating method for normalized direction vectors of the unit members is also developed. The geometry construction method of hex-tri reciprocal frame is established in this paper. By this method the whole structure is formed as an assembly of the units arranged in rings about the structural center. The influences of the diameter, the length and the binding length of the member on the rise of hex-tri reciprocal frame are analyzed by an example. If the rise of hex-tri reciprocal frame needs to be specified in the design, the values of the diameter, the length and the binding length of the structural member need to be coordinated to meet the design requirements.

KEYWORDS

Hex-tri reciprocal frame, Structural geometry, Geometrical characteristics, Structural unit, Construction method

INTRODUCTION

Reciprocal frame is a kind of self-balancing structure. The model is arranged in such a way as to form a closed circuit of mutually supporting elements [1]. The support points are different, and not all of them are located at the end points of the member. The windmill-liked roof shown in Figure 1 is a simple example of reciprocal frame.

Currently there is a clear trend towards prefabricated construction in building industry, and there is much application potential for reciprocal frame as an applicable structure type for this tendency. Compared with the traditional large-span space structure, joints of reciprocal frame are simple and unified. Generally, there is a large number of members and joints in traditional space structures, and many members are connected by the same joint in some cases. So the joints are complex in construction, and the assembly errors are likely to be caused. The reciprocal frame joint usually connects only two members, which avoids the possible multi-member intersection in traditional space structures [2,3]. Generally, there is only one type of joint with the uniform dimension in reciprocal frame. This makes it easy for mass manufacturing while avoiding drawbacks of the traditional space structures [4].

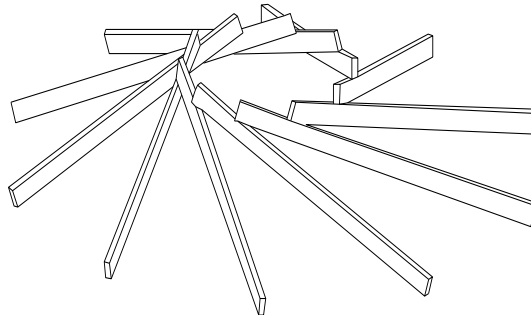


Fig. 1 – Windmill-like reciprocal frame

Although the early reciprocal frame emerged centuries ago, systematic research on this structure began in the 1990s. Graham Brown firstly proposed the concept of reciprocal frame [2]. Chilton and Choo carried out a series of studies on geometry, mechanical properties and structural construction of reciprocal frames [5,6]. Popovic published a monograph with regard to reciprocal frame [7]. While teaching in Hong Kong, Bertin developed a variety of reciprocal frame models based on the reciprocal principle [8]. Baverel proposed a shape forming method for reciprocal frame based on genetic algorithm and gradient algorithm [9]. Rizzuto studied the geometrical configuration of reciprocal frames using space analytic geometry method [10]. Parigi and Peng et al. proposed some methods to generate new types of reciprocal structure [11-13]. Rizzuto and Olga studied connection systems in reciprocal frames and mutually supported elements space structure [14]. Dario et al. analysed the static and dynamic properties of planar reciprocal components [15]. Some architects carried out some engineering practice based on the concept of reciprocal structure. For example, Brown built a Round House which is a reciprocal frame using metal material [7]. The external maintenance structure has been constructed at Mount Rokko-Shidare Observatory in Japan by using the reciprocal space structure [16]. Using aluminium alloy as the material, Gelez built a reciprocal frame in Bibracte, France, as the exhibition hall of cultural relics [17].

At present, systematic calculation and design method for reciprocal frame have not been established. So the reciprocal frame has not been used at a large scale. The completed structures of reciprocal frames are usually small in scale. Different from the traditional space structure, members of reciprocal structures are eccentrically connected. This leads to a quite different geometric construction of reciprocal structures from the traditional structure. It is necessary to propose the geometric construction method of reciprocal frame, which is the basic requirement for further analysis of structure mechanical behaviour. In this paper, the formulas for the joint coordinates of the structural units which compose the hex-tri reciprocal frame are derived, and the calculating method for normalized direction vectors of the unit members is also developed. The naming rules of structural units, members and joints of hex-tri reciprocal frame are proposed. The geometry construction method of hex-tri reciprocal frame is established in this paper by which the whole structure is formed as an assembly of the units arranged in rings about the structural center.

STRUCTURAL UNIT

The hex-tri reciprocal frame is shown in Figure 2. It is constituted of hexagonal and trilateral grids which are alternately distributed.

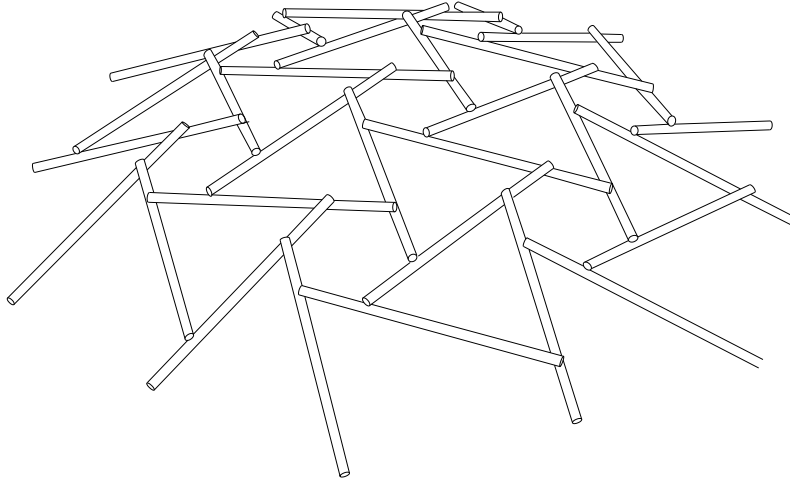


Fig. 2 – The hex-tri reciprocal frame

The hex-tri reciprocal frame is constituted of continuously arranged units which are shown in Figure 3. The unit consists of six members, and each member joint the adjacent one at an angle of 60° . Axes of the structure reciprocal members will never meet, so there is a space between the adjacent axes. This would cause the eccentricity. Members of the unit are numbered counter clockwise as $H_{01}^1, H_{01}^2, H_{01}^3, H_{01}^4, H_{01}^5$ and H_{01}^6 . Direction vectors of each member are numbered as $\overrightarrow{h_{01}^1}, \overrightarrow{h_{01}^2}, \overrightarrow{h_{01}^3}, \overrightarrow{h_{01}^4}, \overrightarrow{h_{01}^5}, \overrightarrow{h_{01}^6}$. When any geometrical parameter of a member equals to that of any other members of the unit, the six outside endpoints of the unit are in the same plane, so are the six inside endpoints and the six joints. As shown in Figure 3, a 3D rectangular coordinate system with XOY plane parallel to those of the six outside endpoints as well as the six inside endpoints of the unit is established. The reciprocal members overlap each other, so the axes are not intersected and the contact point does not locate on the axis. In this paper, the contact point is called reciprocal point and the corresponding points on its upper and lower axis are called axis joint. In the unit, axis joints of the supported members are $N_{01}^1, N_{01}^2, N_{01}^3, N_{01}^4, N_{01}^5$, and N_{01}^6 respectively. Axis joints of the supporting members are $\overline{N}_{01}^1, \overline{N}_{01}^2, \overline{N}_{01}^3, \overline{N}_{01}^4, \overline{N}_{01}^5$ and \overline{N}_{01}^6 respectively.

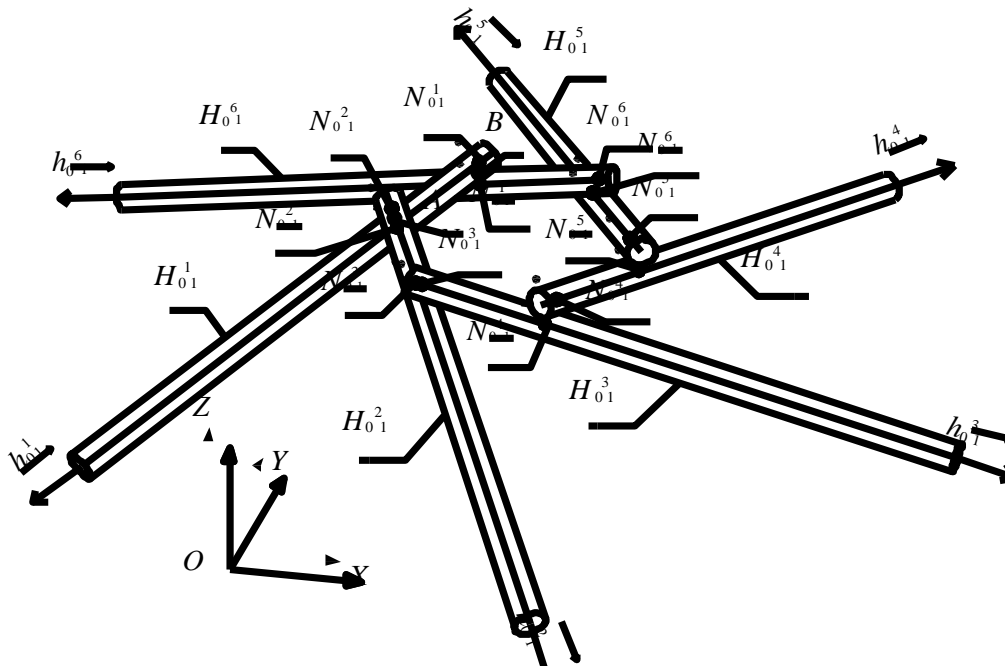


Fig. 3 – Numbers of the unit members and joints

The longitudinal section of member H_{01}^1 is shown in Figure 4. In Figure 4, L is the member length; L_e is the binding length; d is the diameter of the cross section; e is the distance between the two axes of the reciprocal members; s is the distance between the two axis joints; θ is the angle between the member and the horizontal plane;

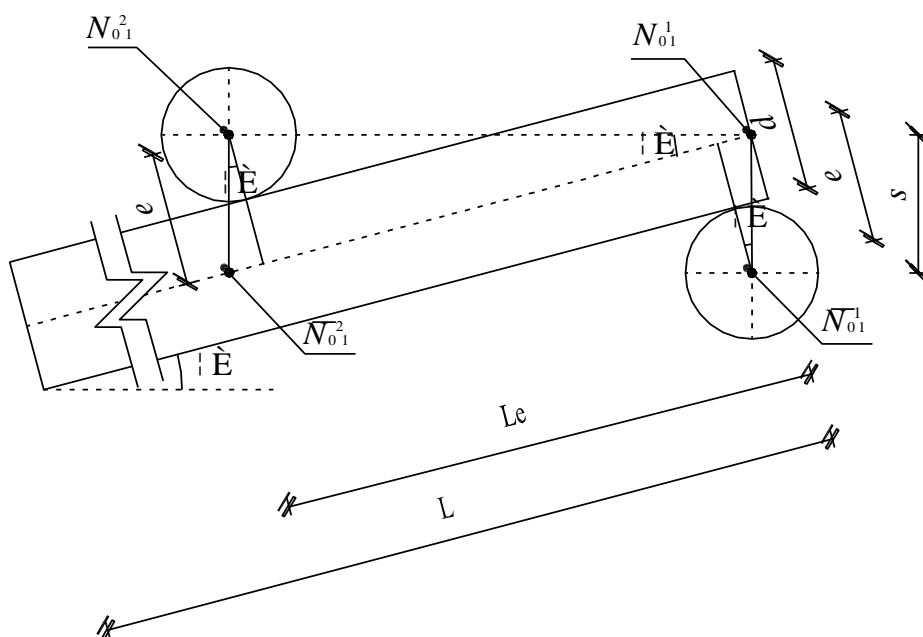


Fig. 4 – Longitudinal section of the member

As shown in Figure 4, when the structural member has the same cross section diameter,

$$e = d \quad (1)$$

Then the distance s between the two axis joints is given as follows:

$$s = \frac{e}{\cos \theta} = \frac{d}{\cos \theta} \quad (2)$$

Based on Figure 4, the relationship of L_e , θ and s can be derived as follows:

$$L_e \sin \theta = s \quad (3)$$

The following equation can be obtained by plugging Eq. (2) into Eq. (3).

$$L_e \sin \theta = \frac{d}{\cos \theta} \quad (4)$$

Let the coordinate of N_{01}^1 be (x_1, y_1, z_1) . The distance between N_{01}^1 and \bar{N}_{01}^1 can be obtained as $d / \cos \theta$ based on Eq. (2). So the coordinate of \bar{N}_{01}^1 can be given as follows:

$$\bar{N}_{01}^1 \left(x_1, y_1, z_1 - \frac{d}{\cos \theta} \right) \quad (5)$$

The coordinate of \bar{N}_{01}^1 can be obtained by plugging Eq. (4) into Eq. (5).

$$\bar{N}_{01}^1 (x_1, y_1, z_1 - L_e \sin \theta) \quad (6)$$

Let the coordinate of N_{01}^2 be (x_2, y_2, z_2) . The formula of this coordinate can be derived based on Figure 3.

$$x_2 = x_1 - \frac{L_e \cos \theta}{2} \quad (7a)$$

$$y_2 = y_1 - \frac{\sqrt{3}L_e}{2} \quad (7b)$$

$$z_2 = z_1 \quad (7c)$$

So the coordinate of N_{01}^2 is

$$N_{01}^2 \left(x_1 - \frac{L_e \cos \theta}{2}, y_1 - \frac{\sqrt{3}L_e \cos \theta}{2}, z_1 \right) \quad (8)$$

Likewise, the coordinate of \bar{N}_{01}^2 can be given as follows:

$$\bar{N}_{01}^2 \left(x_1 - \frac{L_e \cos \theta}{2}, y_1 - \frac{\sqrt{3}L_e \cos \theta}{2}, z_1 - L_e \sin \theta \right) \quad (9)$$

Similarly, coordinates of each axis joint in the unit can be derived as follows:

$$N_{01}^3(x_1, y_1 - \sqrt{3}L_e \cos \theta, z_1) \quad (10a)$$

$$\bar{N}_{01}^3(x_1, y_1 - \sqrt{3}L_e \cos \theta, z_1 - L_e \sin \theta) \quad (10b)$$

$$N_{01}^4(x_1 + L_e \cos \theta, y_1 - \sqrt{3}L_e \cos \theta, z_1) \quad (10c)$$

$$\bar{N}_{01}^4(x_1 + L_e \cos \theta, y_1 - \sqrt{3}L_e \cos \theta, z_1 - L_e \sin \theta) \quad (10d)$$

$$N_{01}^5\left(x_1 - \frac{3L_e \cos \theta}{2}, y_1 - \frac{\sqrt{3}L_e \cos \theta}{2}, z_1\right) \quad (10e)$$

$$\bar{N}_{01}^5\left(x_1 - \frac{3L_e \cos \theta}{2}, y_1 - \frac{\sqrt{3}L_e \cos \theta}{2}, z_1 - L_e \sin \theta\right) \quad (10f)$$

$$N_{01}^6(x_1 + L_e \cos \theta, y_1, z_1) \quad (10g)$$

$$\bar{N}_{01}^6(x_1 + L_e \cos \theta, y_1, z_1 - L_e \sin \theta) \quad (10h)$$

Based on the axis joint coordinates, the normalized direction vectors of the members can be obtained as follows:

$$\bar{h}_{01}^1 = \frac{\bar{ON}_{01}^2 - \bar{ON}_{01}^1}{L_e} = \left(-\frac{\cos \theta}{2}, -\frac{\sqrt{3} \cos \theta}{2}, -\sin \theta\right) \quad (11a)$$

$$\bar{h}_{01}^2 = \frac{\bar{ON}_{01}^3 - \bar{ON}_{01}^2}{L_e} = \left(\frac{\cos \theta}{2}, -\frac{\sqrt{3} \cos \theta}{2}, -\sin \theta\right) \quad (11b)$$

$$\bar{h}_{01}^3 = \frac{\bar{ON}_{01}^4 - \bar{ON}_{01}^3}{L_e} (\cos \theta, 0, -\sin \theta) \quad (11c)$$

$$\bar{h}_{01}^4 = \frac{\bar{ON}_{01}^5 - \bar{ON}_{01}^4}{L_e} = \left(\frac{\cos \theta}{2}, \frac{\sqrt{3} \cos \theta}{2}, -\sin \theta\right) \quad (11d)$$

$$\bar{h}_{01}^5 = \frac{\bar{ON}_{01}^6 - \bar{ON}_{01}^5}{L_e} = \left(-\frac{\cos \theta}{2}, \frac{\sqrt{3} \cos \theta}{2}, -\sin \theta\right) \quad (11e)$$

$$\bar{h}_{01}^6 = \frac{\bar{ON}_{01}^1 - \bar{ON}_{01}^6}{L_e} = (-\cos \theta, 0, -\sin \theta) \quad (11f)$$

GEOMETRICAL CONSTRUCTION OF THE STRUCTURE

The whole structure can be seen as a unit assembly in a regular manner. The hex-tri reciprocal frame is formed by the hex-tri units arranged in rings about the structural center. The structure geometry method explicates an example structure consisting of elements arranged in two rings, as shown in Figure 5. There is a central unit which locates at the structure center (Figure 5a). The hex-tri reciprocal frame is constructed by arranging the units in the first ring (Figure 5b) and then in the second ring (Figure 5c).

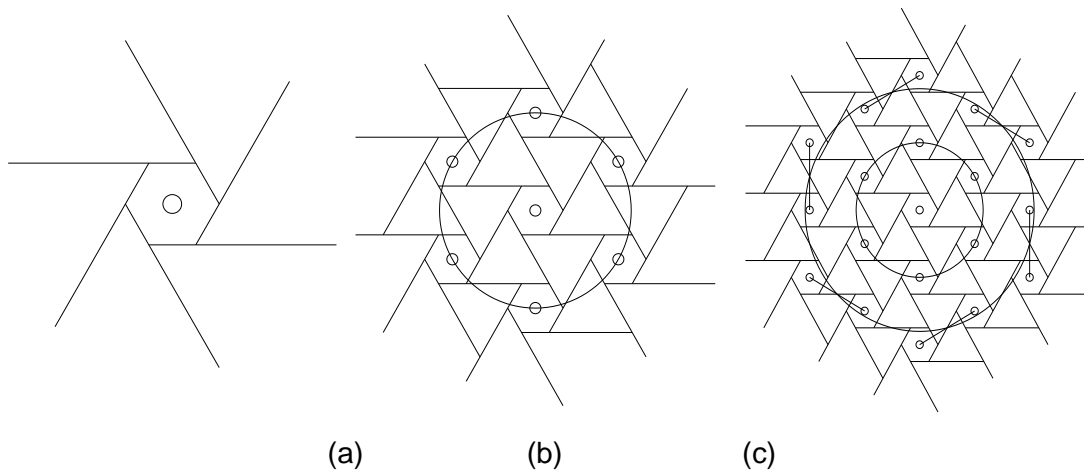


Fig. 5 – An example hex-tri reciprocal structure

The numbers of the members in the central unit are as same as those illustrated in Figure 3. The structural member is represented by H_{ij}^k , where i indicates that the member locates in the i^{th} ring of the structure; j indicates that the member locates in the j^{th} unit; k indicates that this is the k^{th} member of the unit. The unit is represented by U_{ij} , where i indicates that the unit locates in the i^{th} ring of the structure; j indicates that this is the j^{th} unit in the ring. In the hex-tri reciprocal frame, one member is shared by two units arranged in two rings. If the 1st member of 1st unit in the i^{th} ring is shared by a unit in the $i+1^{\text{th}}$ ring, this unit is defined as the 1st unit in the $i+1^{\text{th}}$ ring. The other units are numbered counter clockwise. As shown in Figure 6, the unit in the 1st ring that shares H_{01}^1 of the central unit is defined as U_{11} . The other units in the 1st ring are defined as U_{12} , U_{13} , U_{14} , U_{15} and U_{16} counter clockwise. The numbering order of members in each unit is as same as that of the central unit. The shared member has different number when it is used by different unit. Some numbers of unit, member and joint are shown in Figure 6.

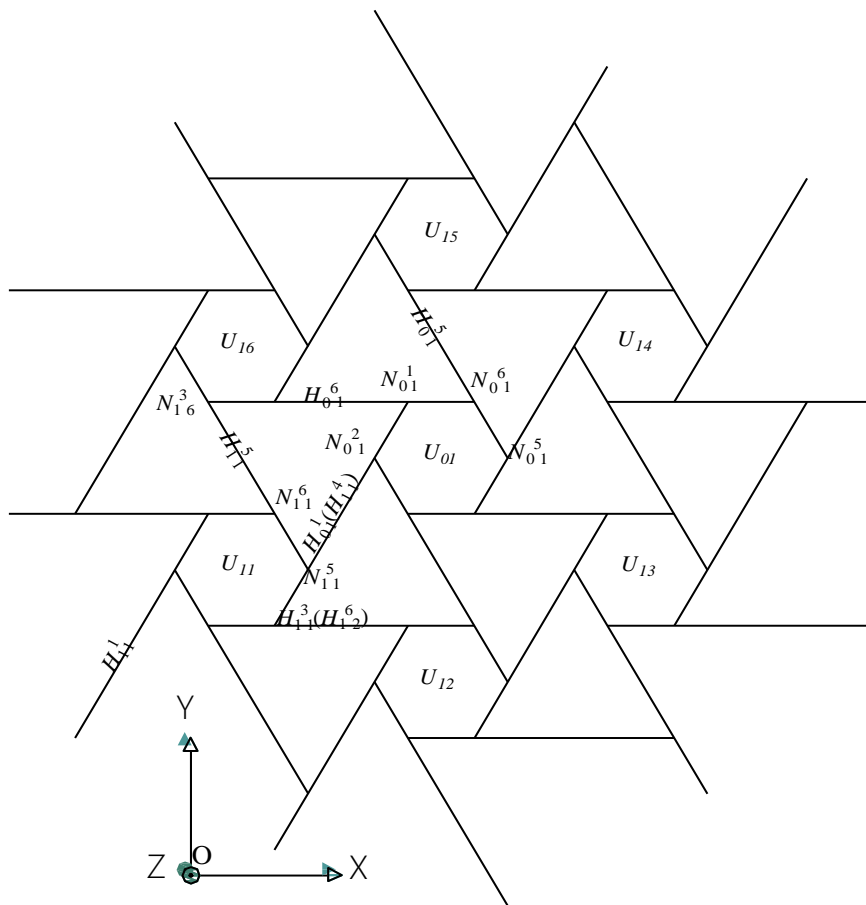


Fig. 6 – Some numbers of unit, member and joint

The coordinate of $N_{01}^1(x_1, y_1, z_1)$ needs to be determined firstly. Coordinates of the axis joints of the central unit can be obtained based on Eq. (6), Eq. (8), Eq. (9) and Eq. (10). Normalized direction vectors of the central unit members can be obtained based on Eq. (11).

Since N_{16}^3 is on the member H_{01}^6 where both \bar{N}_{01}^1 and N_{01}^6 locate, its coordinate can be derived based on the coordinates of these two joints.

$$N_{16}^3(x_1 - (L - L_e)\cos\theta, y_1, z_1 - L\sin\theta) \tag{12}$$

Likewise, since \bar{N}_{11}^5 is on the member H_{01}^1 where both N_{01}^1 and \bar{N}_{01}^2 locate, its coordinate can be derived based on the coordinates of these two joints.

$$\bar{N}_{11}^5(x_1 - (L - L_e)\cos\theta\cos 60^\circ, y_1 - (L - L_e)\cos\theta\sin 60^\circ, z_1 - (L - L_e)\sin\theta) \tag{13}$$

Based on Eq.(3) and Eq.(12), the coordinate of axis joint \bar{N}_{16}^3 can be obtained as follows:

$$\bar{N}_{16}^3(x_1 - (L - L_e)\cos\theta, y_1, z_1 - L\sin\theta - L_e\sin\theta) \tag{14}$$

Based on Eq.(3) and Eq.(13), the coordinate of axis joint N_{11}^5 can be obtained as follows:

$$N_{11}^5 \left(x_1 - \frac{(L-L_e)\cos\theta}{2}, y_1 - \frac{\sqrt{3}(L-L_e)\cos\theta}{2}, z_1 - L\sin\theta + 2L_e\sin\theta \right) \quad (15)$$

The direction vector of member H_{11}^5 can be derived based on Eq. (14) and Eq. (15):

$$\overline{h_{11}^5} = \frac{\overline{ON_{16}^3} - \overline{ON_{11}^5}}{L-L_e} = \left(-\frac{\cos\theta}{2}, \frac{\sqrt{3}\cos\theta}{2}, -\frac{3L_e\sin\theta}{L-L_e} \right) \quad (16)$$

$$\text{Let } \overline{h_{11}^5} = \overline{h_{01}^5}[T] \quad (17)$$

When Eq.(11e) and Eq. (16) is plugged into Eq. (17), the following Equation is obtained:

$$[T] = \begin{bmatrix} 1 & 0 & 0 \\ 0 & 1 & 0 \\ 0 & 0 & \frac{3L_e}{L-L_e} \end{bmatrix} \quad (18)$$

Structural unit $U_{12} \sim U_{16}$ is constructed in a manner similar to that of U_{11} . H_{1j}^m of unit U_{1j} in the first ring and H_{01}^j of the central unit U_{01} are one and the same member. The relationship between the direction vectors $\overline{h_{1j}^n}$ and $\overline{h_{01}^n}$ is given as follows:

$$\overline{h_{1j}^n} = \overline{h_{01}^n} \begin{bmatrix} 1 & 0 & 0 \\ 0 & 1 & 0 \\ 0 & 0 & \frac{3L_e}{L-L_e} \end{bmatrix} \quad (19)$$

Where m and n are integers range from 1 to 6, and $|m-j|=3$; $|n-j|=4$. Based on the constitution method of unit U_{01} in the center and unit U_{11} in the first ring, the rest units are formed, and so on the whole structure can be formed then. The modelling process of hex-tri reciprocal frame is illustrated in Figure 7.

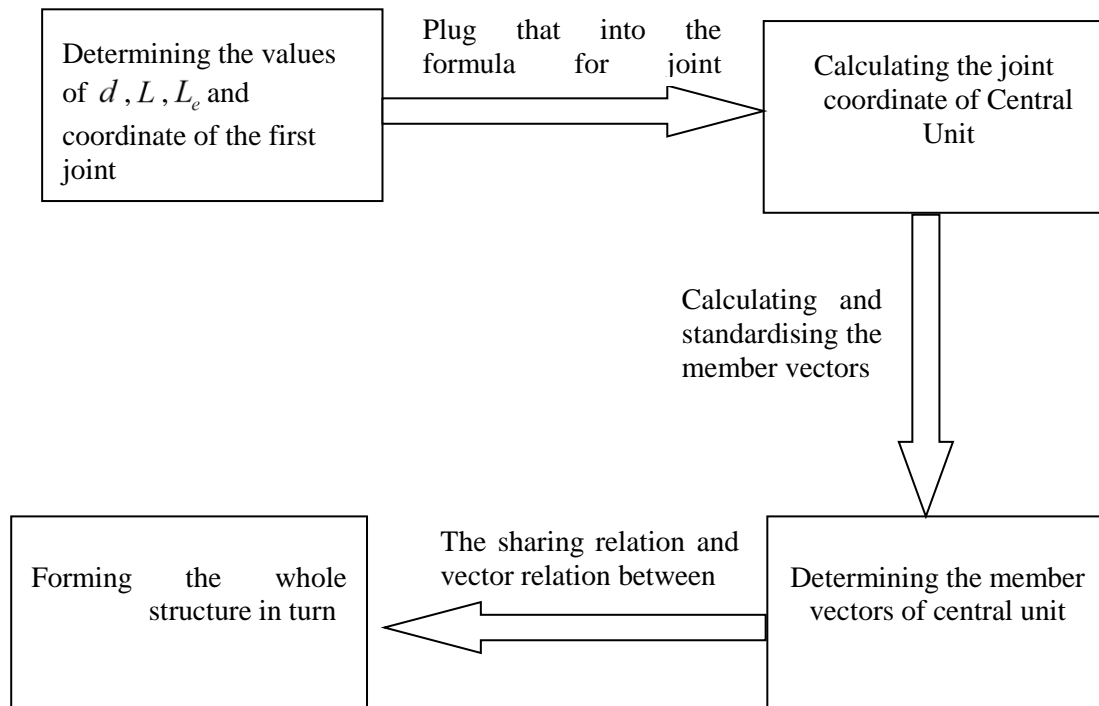


Fig. 7 – Modelling process of hex-tri reciprocal frame

EXAMPLE

When the values of the ring number n , the member cross section diameter d , the member length L and the binding length L_e are specified, the hex- tri reciprocal frame is constructed based on the structural geometry construction method proposed in this paper. The rise of hex-tri reciprocal frame varies with the change of the values of d , L and L_e . The influences of the geometrical parameters d , L , and L_e on the structural rise are examined based on a hex-tri frame composed of the central unit.

The influence of d on the structural rise h is examined by changing the value of d while fixing the values of L and L_e . The result is shown in Table 1.

Tab. 1 - The influence of d on the structural rise h

No.	1	2	3	4	5
L/m	4.00	4.00	4.00	4.00	4.00
L_e /m	1.00	1.00	1.00	1.00	1.00
d/mm	50.00	150.00	250.00	350.00	450.00
h/mm	200.00	600.00	1000.00	1400.00	1800.00
Structure sketch					

It can be seen from Table 1 that the structural rise gets bigger linearly with the increment of the member cross section diameter d . The influence of L on the structural rise h is examined by changing the value of L while fixing the values of d and L_e . The result is shown in Table 2.

Tab. 2 - The influence of L on the structural rise h

No.	1	2	3	4	5
d/mm	250.00	250.00	250.00	250.00	250.00
L_e/m	1.00	1.00	1.00	1.00	1.00
L/m	3.00	3.50	4.00	4.50	5.00
h/mm	750.00	875.00	1000.00	1125.00	1250.00
Structure sketch					

It can be seen from Table 2 that the structural rise gets bigger linearly with the increment of the member cross section diameter L . The influence of L_e on the structural rise h is examined by changing the value of L_e while fixing the values of d and L . The result is shown in Table 3.

Tab. 3 - The influence of L_e on the structural rise h

No.	1	2	3	4	5
d/mm	250.00	250.00	250.00	250.00	250.00
L/m	4.00	4.00	4.00	4.00	4.00
L_e/m	0.50	0.75	1.00	1.25	1.50
h/mm	666.67	800.00	1000.00	1333.33	2000.00
Structure sketch					

It can be seen from Table 3 that the structural rise gets smaller with the increment of the member cross section diameter L_e .

In the design of the traditional space structure, the rise can be specified independently. Differing from the traditional space structure, the rise of the hex-tri reciprocal frame depends on d , L and L_e . If the rise of hex-tri reciprocal frame needs to be specified in the design, the values of the diameter, the length and the binding length of the structural member need to be coordinated to meet the design requirements.

CONCLUSIONS

- (1) The geometrical characteristics and construction method of hex-tri reciprocal frame are studied. The naming rules of structural units, members and joints of hex-tri reciprocal frame are proposed.
- (2) Based on the study of relationships between the structural geometrical parameters, the formulas for the joint coordinates of the structural unit are derived, and the calculating method for normalized direction vectors of the unit members is also developed.
- (3) The geometry construction method of hex-tri reciprocal frame is established in this paper. By this method the whole structure is formed as an assembly of the units arranged in rings about the structural center.
- (4) The influences of the diameter, the length and the binding length of the member on the rise of hex-tri reciprocal frame are analyzed by an example. If the rise of hex-tri reciprocal frame needs to be specified in the design, the values of the diameter, the length and the binding length of the structural member need to be coordinated to meet the design requirements.

ACKNOWLEDGEMENTS

Financial supports from Natural Science Foundation of Tianjin (18JCTPJC66200), Fundamental Research Funds for Central Universities (3122016C008) and Scientific Research Program of Tianjin Education Commission (2018KJ244) are gratefully acknowledged.

REFERENCES

- [1] B. Di Carlo, 2008. The wooden roofs of Leonardo and new structural research. *Nexus Network Journal*, vol. 10: 27-38.
- [2] R.L. Zhou, T. Z.Y., G.H. Ji, A preliminary study on the parameterization of three dimensional reciprocal structure.
- [3] Y. Wu, Y. Su, G. Qiao, 2018. A form-finding method for reciprocal spatial grid structure. *Journal of Building Structures*, vol. 7.
- [4] D. Zou, N. Xiao, 2016. Research on configuration generation optimization of reciprocal structure. *Spatial structure*, vol. 9: 17-26.
- [5] J. Chilton, B. Choo, Reciprocal frame long span structures. In *Innovative Large Span Structures*, Toronto: Toronto, 1992, 100-109.
- [6] J. Chilton, B. Choo, P. Coulliette, Retractable roofs using the reciprocal frame. In *IABSE Report: International Association for Bridge and Structural Engineering*, IABSE Report: International Association for Bridge and Structural Engineering, 1994, 49-54.
- [7] P.L. Olga, Reciprocal Frame Architecture.
- [8] B.L. Vito, One principle, many forms.
- [9] O. Baverel, H. Nooshin, Y. Kuroiwa, 2004. Configuration processing of nexorades using genetic algorithms. *Journal of the International Association for Shell and Spatial Structures*, vol. 45: 99-108.
- [10] J. Rizzuto, 2007. Rotated mutually supported elements in truncated icosahedric domes. *Journal of the International Association for Shell and Spatial Structures*, vol. 48: 3-17.
- [11] D. Parigi, Kinematics of Reciprocal Frames: Toward Adaptable Structures for Architectural Heritage. Torino: Politecnico di Torino, 2011.
- [12] P. Song, C.-W. Fu, P. Goswami, et al., 2014. An interactive computational design tool for large reciprocal frame structures. *Nexus Network Journal*, vol. 16: 109-118.
- [13] S. Peng, Reciprocal Frame Structures Made Easy. Singapore: Nanyang Technological University, 2014.
- [14] J. Rizzuto, O.P. Larsen, 2010. Connection systems in reciprocal frames and mutually supported elements space structure networks. *International Journal of Space Structures*, vol. 25: 243-256.
- [15] D. Parigi, M. Sassone, P.H. Kirkegaard, et al., 2014. Static and kinematic formulation of planar reciprocal assemblies. *Nexus Network Journal*, vol. 16: 37-59.

- [16] O.P. Larsen, 2014. Reciprocal frame (RF) structures: real and exploratory. Nexus Network Journal, vol. 16: 119-134.
- [17] S. Gelez, S. Aubry, B. Vaudeville, 2011. Nexorade or reciprocal frame system applied to the design and construction of a 850 m² archaeological shelter. International Journal of Space Structures, vol. 26: 303-311.

SELECTED POSSIBILITIES OF DATA EXCERPTION FROM THE DATABASE OF HISTORICAL ATLASES

Petra Jílková and Tomáš Janata

CTU in Prague, Faculty of Civil Engineering, Department of Geomatics, Prague, Thákurova 7, Czech Republic; petra.jilkova@fsv.cvut.cz, tomas.janata@fsv.cvut.cz

ABSTRACT

A large database of more than 400 existing historical atlases released after 1950 was created as a result of an extensive analytic research within the preparation of cartographic works on the Czech Historical Atlas. The database was published in the form of a web application that allows the user to reveal and analyse associated information about historical atlases across interactive dashboards. To improve the information value of the database, the authors decided to arrange further possibilities of data excerption with the use of specialized data visualization methods that may reveal additional information and new phenomena which are not clearly visible from the database itself. The performed analyses supplement the paper in the form of diagrams and charts and present the data from various perspectives with the focus on similarities and differences between the cartographic and the thematic content of the historical atlases in the publishing countries, the changes in the thematic focus of the atlases or changes in the use of methods of thematic cartography in atlas works over time. The authors also deal with relations between the thematic focus of the atlas and the applied methods of thematic cartography. All analyses are performed on the sample of 88 atlas works.

KEYWORDS

Historical atlas, Database, Web Application, Data visualization, Czech Historical Atlas

INTRODUCTION

During an extensive analytic research within the preparation of cartographic works on the Czech Historical Atlas, a comprehensive database of historical atlases was created. Information about more than 400 atlases was collected within the research. In addition to the standard bibliographic description, the researchers fed the database with detailed information on the content of the atlases that are not available in any library catalogue. Even though the database does not cover the whole world production of historical atlases after 1950 (and it was not intended to do so), the team believes that more than 400 items comprise a sufficient and representative sample of the overall production. Thus, it was decided to make the database available to a broad public and publish it as a complementary web application to the Czech Historical Atlas web portal that is currently being worked on [1] [2]. Although the database in the form of a web application allows users to reveal and analyse associated information about historical atlases across an interactive dashboard, the authors decided to further improve the information value of the database and arrange potential excerpts of data analysis with the use of specialized data visualization methods that might provide a possibility to look at the data from different perspectives and thus reveal hidden relations between the collected items of information about the historical atlases stored in the database.

DATABASE OF HISTORICAL ATLASES

Historical atlases and their characteristics were selected according to the methodology concept devised by Bláha and Močíčková [3]. On the basis of two criteria defining the time and geographical delimitation of historical atlases for the study, two students of the Czech Technical University in Prague collected information about selected Czech (Czechoslovak) and foreign historical atlases released after 1950. During the first phase, the students searched for the standard bibliographic description (title, author, publisher, country of origin, language, etc.) of more than 400 atlases in electronic catalogues of Czech and foreign libraries. In addition, each item was provided with information on the focus category of the atlas (e.g. politics, demography, military issues) and with a list of libraries in which the atlas is physically stored. Due to the geographical delimitation of the studied atlas works, the database consists mainly of the atlases of Czech (106) and German production (97), followed by the atlases from France (65) and the United Kingdom (47), which account for more than three quarters of the database.

In the second phase of the research, the atlases, that were physically available to the researchers in the collections of Czech libraries or obtained through the international interlibrary loans from foreign library collections, were further examined in detail and partially digitized. The detailed examination of 88 selected atlases (out of 409) involved searching for detailed information on the content of the atlas (e.g. the chronological and geographical determination of maps) and evaluation of the map categories and applied methods of thematic cartography according to specialized literature, e.g. [4] [5]. Subsequently, the database was filled with digitized images of the cover, the front page, the content and the map excerpts from all selected atlases. To complete the database, digitized images of the covers of the remaining atlases were found using the web.

WEB APPLICATION

The web application is based on the existing database application for publication created with Keshif, a Javascript library providing an automated web-based interface for tabular data exploration that can be integrated or used as a web service [6]. The source code of the sample application was customized for the purpose of the database of historical atlases with basic web development technologies (JavaScript, HTML, CSS) with the use of selected JavaScript libraries, such as the D3 library, jQuery library, JSAPI.js or Moment.js. The mentioned libraries ensure the desired functionality of the application – they enable the transformation of data tables into visual graphics (D3.js) or the manipulation with date and time attributes (Moment.js). jQuery.js simplifies the manipulation of animations and AJAX, enabling dynamical changes of the content without the need for reloading the web page.

The layout of the application is divided into 10 interactive dashboards as shown in Figure 1. The main dashboard panel contains a list of all 409 historical atlases, which are sorted by the year of publication in descending order. Along the main dashboard, there are 9 additional panels showing specific information about the atlas and the distribution of data in each category. In the main panel, the user can expand each record to show detailed information including the preview of the cover of the atlas. Some records also include links to the digitised images of the front page, the content or the map excerpts. The application allows the user to search an individual atlas by its name or any other keyword, or to select or filter the atlases by predefined attributes directly in side panels. All panels are fully synchronised and responsive and update their content according to the user's activity. The application also enables to dynamically highlight associated information across all panels only by a mouse-over, and thus simply reveal all information about the atlases [7].

Database of Historical Atlases Since 2nd Half of the 20th Century



Fig. 1 – The layout of the web application

METHODS

The main aim of this study is to present potential data excerpts that will further improve the information value of the database. The data excerpts are derived from the analysis of the records in the database of historical atlases acquired during the second phase of the analytic research (see above). The study focuses on the analyses of information about the thematic and cartographic content of the atlases. The analyses are performed from various perspectives with the aim to reveal the similarities and differences between the cartographic and the thematic content of the historical atlases in the publishing countries, or the changes in the thematic focus of the atlases or in the use of methods of thematic cartography in atlas works over time. Besides that, the authors also study the relations between the thematic focus of the atlas and the applied methods of thematic cartography and analyse which cartographic methods and their combinations are mostly used in historical atlases. All analyses are performed on the sample of 88 atlas works that were analysed in detail in the second phase of the research during the creation of the database.

Data processing

For the purpose of the study, it was necessary to generalize the original classification of selected attributes.

Publishing country

The original 9 classes representing the publishing countries of 88 atlases were grouped into four classes on the basis of the political and historical context. The generalized classification follows on from the second selection criterion of geographical determination that determined the countries whose cartographic production of the atlases would be examined [3]. The first group “Central Europe” is comprised of the member states of the Visegrad Group (Czechia, Poland, Slovakia and Hungary). The two other groups represent Western European countries that were divided according to the language of the atlases they have published – German (Austria, Germany) and English and French (Belgium, France, the United Kingdom). The last group consists of the atlases published in the USA.

Methods of thematic cartography

The initial classification that consisted of 16 methods of thematic cartography identified in the content of 88 atlases was generalized into 9 classes representing the basic groups of methods of thematic cartography – area-class maps “Ar”, isoline maps “Iz”, diagram maps “KDall”, choropleth maps “K”, figural symbols “Lb2”, line symbols “LI2”, specific methods “Sp”, dot (density) maps “Te” and time methods “čas”. The coding and the classification of the methods (as well as the coding and classification of the map categories) follow on from [3].

Data analysis and visualization

To present potential data excerpts, various visualization methods were applied according to the character of data. Some of the visualizations were made with the Google Charts API enabling the creation (and further customization) of various interactive chart types over structured data and their integration directly into the website. In addition, using the HTML5 and SVG technology for rendering charts, the chosen solution is cross-browser compatible and cross-platform portable, thus it is not so necessary to consider the end-user’s device.

Because of the time demands, the remaining analyses and the subsequent visualization were performed using the combination of GIS and graphic software (see below). All presented outputs serve only as examples of potential data excerpts and are planned to be further processed and customized to be embedded in an existing web application in the form of interactive charts that will enable the user to gain insights into the data in an effective and comprehensible way. The respective analyses and the applied visualization solutions are described below:

Cartographic content by publishing country / by thematic focus of the atlas

- For the purpose of this analysis, only individual occurrences of a feature (cartographic method / map category) were considered, not their combinations. Even if a feature occurred in more than one combination, it was taken as a single occurrence of that feature.
- As the best solution to visualize the similarities and differences in using cartographic methods (or map categories) in the atlas works in the publishing countries we opted for the Google Charts interactive Sankey diagram, that is suitable to show many-to-many relations between two or more sets of values. In the diagram, the relation is symbolised by a line whose width is proportional to the represented quantity.
- There were two main aims of this visualization – to show the similarities or differences between cartographic productions of the politically distant parts of the latter-20th-century Europe and, in addition, to try to evaluate the hypothesis whether the atlas production of Austria is more related to the overall Western-Europe cartographic production or whether there is a remainder of the relation to the pre-20th-century Austro-Hungarian cartographic school, which might relate Austrian atlases closer to the Czech(o)Slovak or Hungarian production.

Change in thematic focus / cartographic content over time

- As the time series of the year of publication was not continuous (some years were missing or some years occurred in the list more than once), we have decided to create time intervals that will continuously cover all years of publication preserving approximately similar numbers of titles within the particular intervals. The number and the range of the intervals were selected in order to cover similar numbers of titles.
- To visualize changes in the thematic focus of the atlas or in the use of methods of thematic cartography, the use of the Google Charts interactive area chart was chosen, showing a change in a trend over time.

Thematic focus of the atlas by publishing country

- The third example of the output stands for a simple diagram map with pie charts showing the relative proportion of particular thematic groups within the main areas of European historical cartographic production (see above). A separate diagram rendering the situation of the US cartographic production is attached for comparison.
- In compare to previous outputs, this example presents a statistical information over map background, using the spatial information of data. For this purpose, the original data were enhanced with the spatial information representing the geolocation of the publishing countries.

Combination of cartographic methods

- The set of analysed atlases may also be assessed from several purely cartographic perspectives. One of the most interesting is the evaluation of cartographic methods of expression (and their combinations) in one overall chart as brought in Figure 2.
- The nine aforementioned general classes were used in this rendition. For the purpose of this study, the time methods were not considered as a separate method of expression but as an attribute of other appropriate methods. For each method or combination of methods used, a single unit is found in the chart, which may be slightly confusing as this approach assigns different “weights” to particular atlases. In a global perspective, it enables to assess the database as a whole, though.

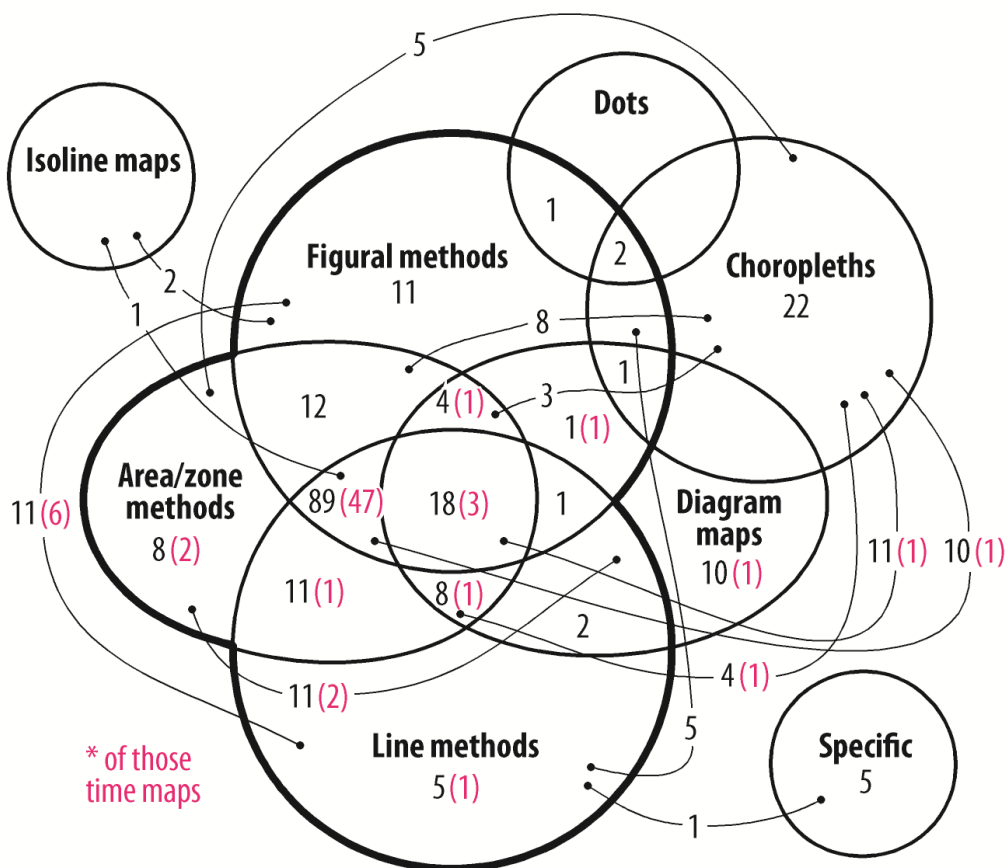


Fig. 2 – Combination of methods

DATA EXCERPTS

There exist only slight differences in map categories used in the historical atlases between the European and the US cartographic production (see Figure 3). Historical atlases published in Europe consist mainly of political/administrative maps or of maps depicting the location of point objects and the chronological sequence. The relative proportion of map categories that appear in the historical atlases closely corresponds to the relative proportion of cartographic methods used in them (Figure 4a).

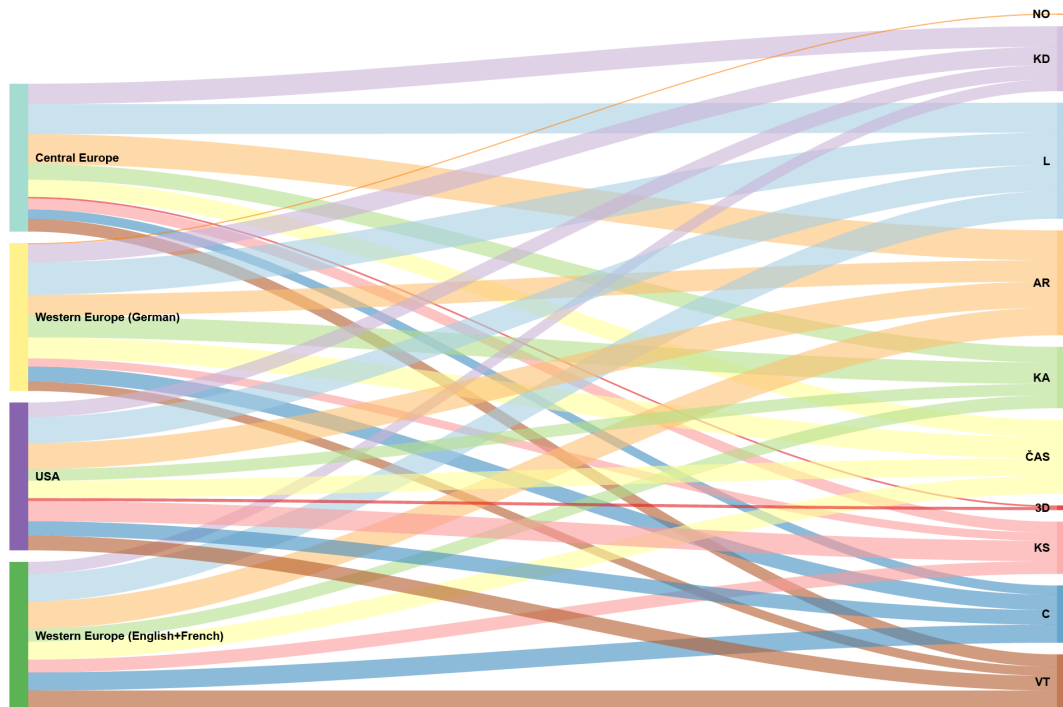


Fig. 3 – Map categories in the historical atlases by publishing country

Comparing Figure 4a and 4b, more could be said about the aforementioned correctness of the decision where to incorporate the atlases published in Austria. The character of the Austrian atlas production after 1950 ranks this country in the same group with German atlases rather than in the Central-European group of countries with whom Austria, due to its historical development, shared a great part of its history during the time of the Austro-Hungarian Empire. This may be explained by quite a long period elapsed since the moment when the Austro-Hungarian cartographic school dissolved into the successor states' productions. The size of the nodes on the right implies which of the cartographic method (or map category) is used the most.

All presented outputs together form a more complex picture of the historical atlases from a cartographic perspective. The users can better understand which states preferred using certain cartographic methods or map categories to others and how the use of cartographic methods varied over time (Figure 6). Although there is a very slight change in the use of cartographic methods over last 70 years of the cartographic production, the thematic focus of the atlases varies over time. Since 1990, more historical atlases with a special thematic focus has started to be published. Until then, mainly general focused historical atlases had been published. By the comparison of Figure 3 and Figure 7, the readers may understand whether countries that published an atlas of certain thematic focus more than others did also prefer the use of certain map categories over the other ones. In the USA only monothematic atlases were published with the prevalence of atlases focusing on military issues. On the contrary, in Europe and especially in Central European countries, there is a tradition

of atlases combining various topics. The relation between the thematic focus of the atlas and the map categories can be identified from Figure 5.

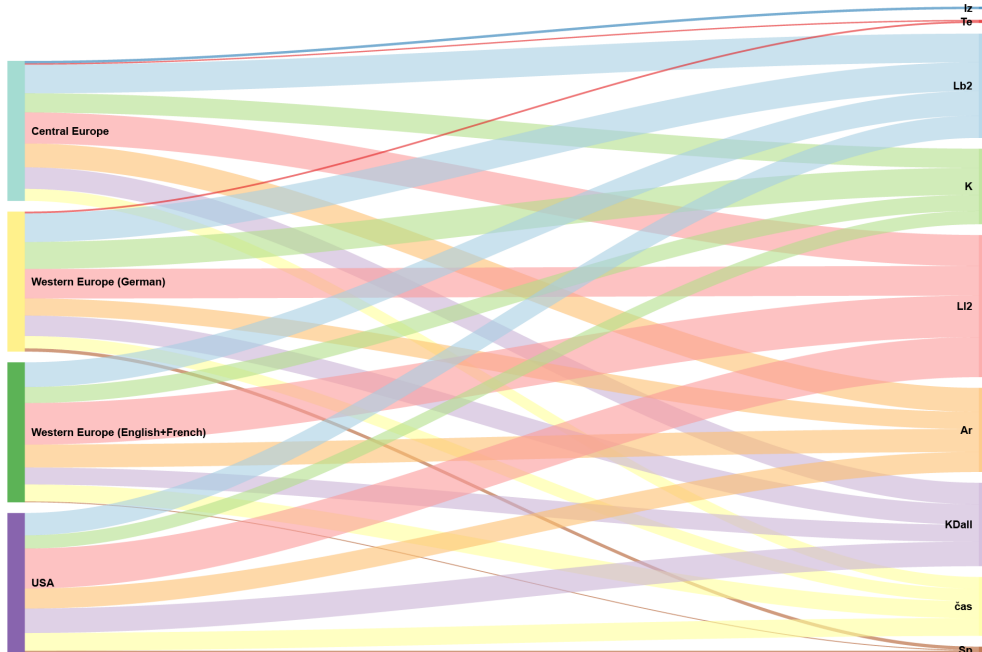


Fig. 4a – Methods of thematic cartography used in the historical atlases by publishing country

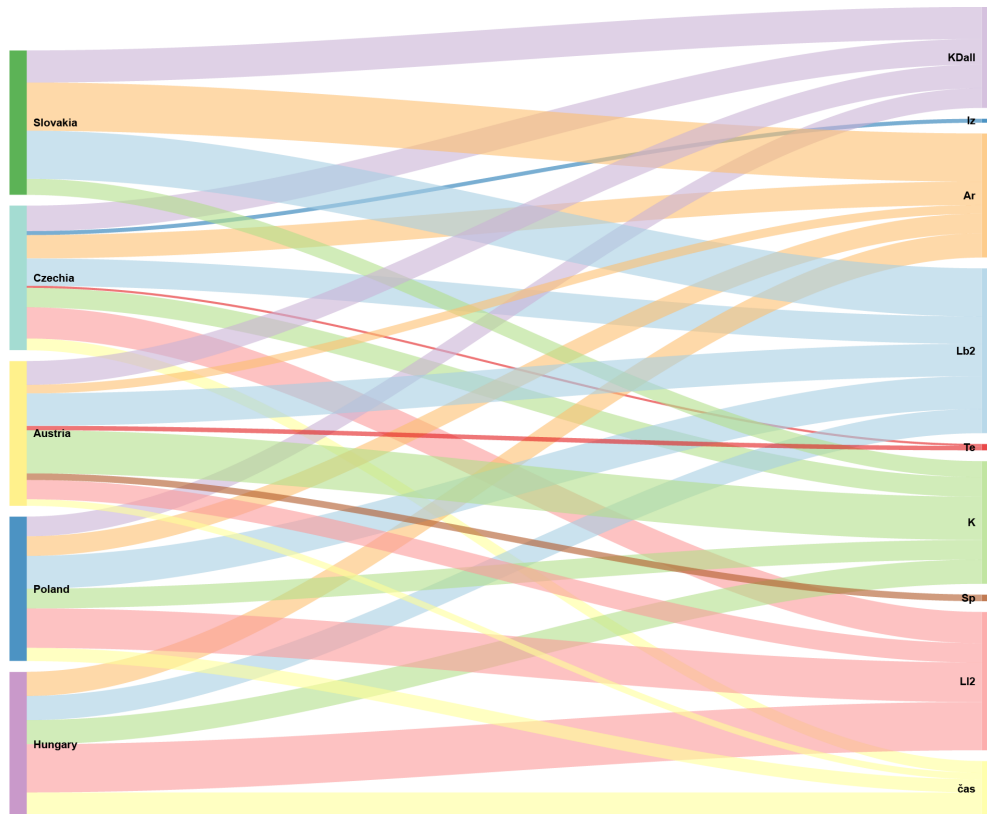


Fig. 4b – Methods of thematic cartography used in the historical atlases by publishing country (Central European states vs. Austria)

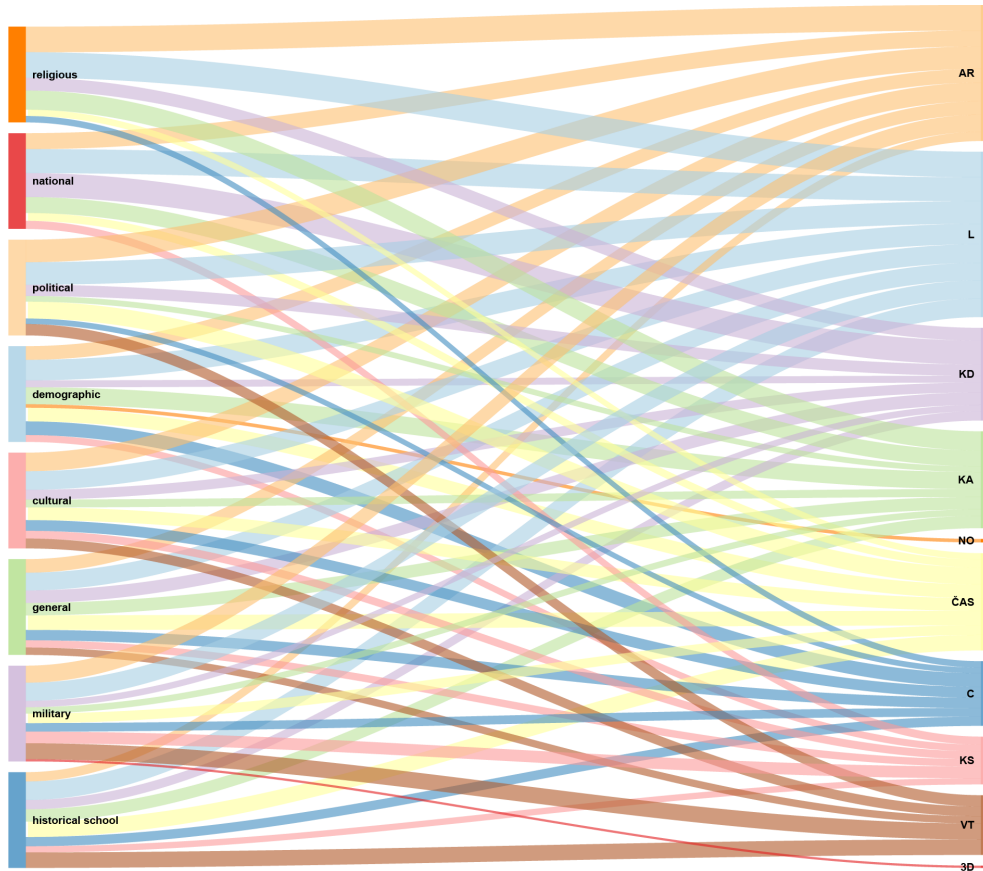


Fig. 5 – Map categories according to the thematic focus of the atlas

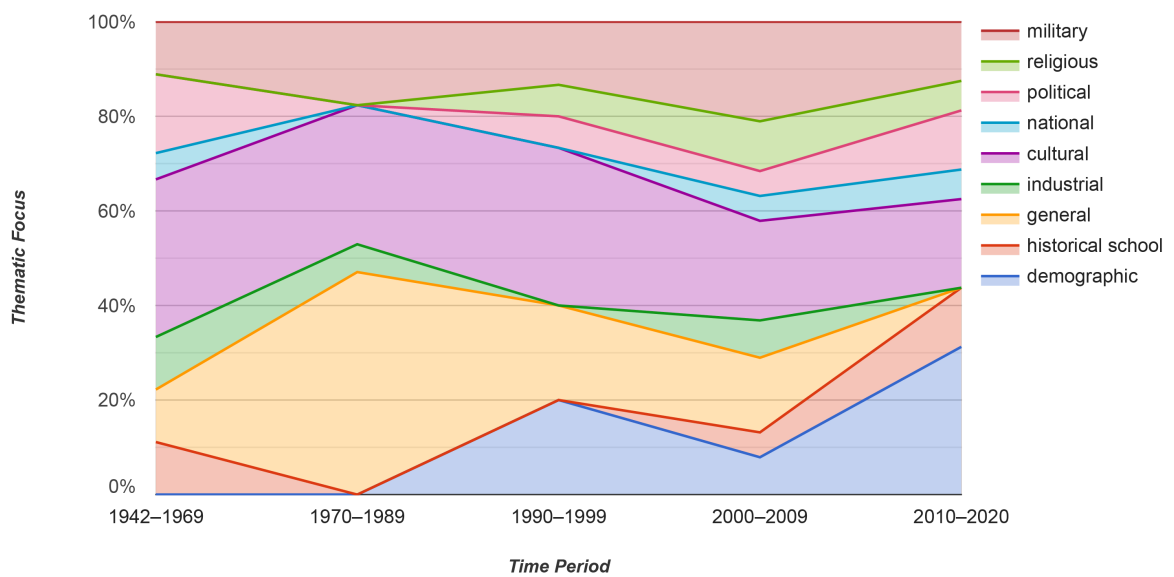


Fig. 6 – Change of the thematic focus of the historical atlases over time

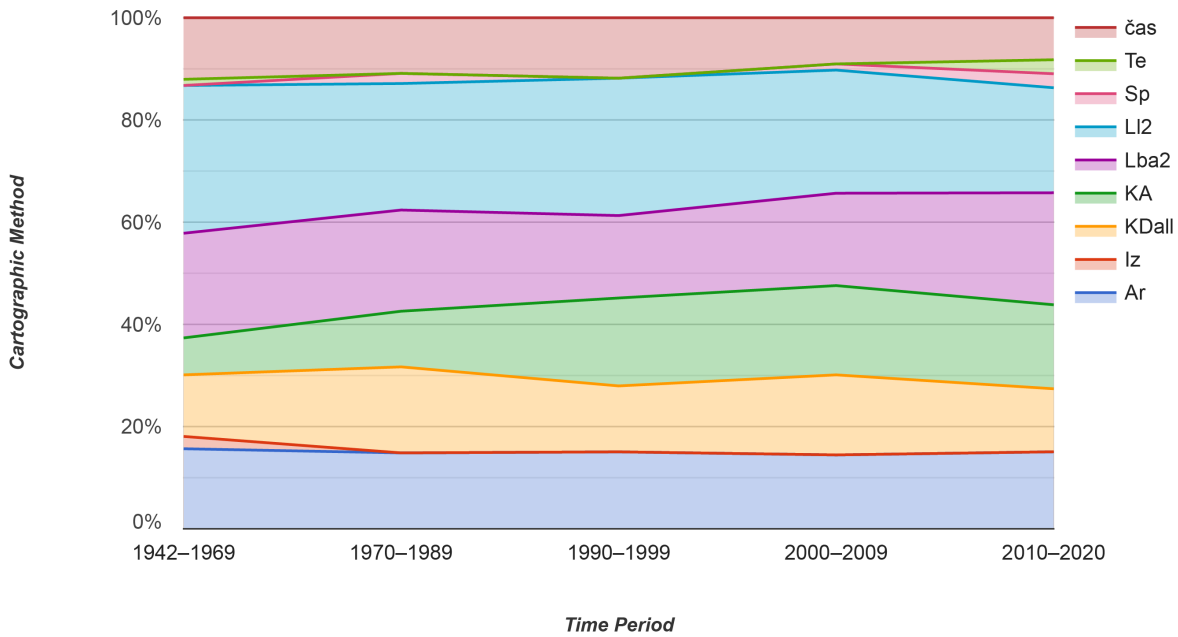


Fig. 7 – Change in the use of the cartographic methods in the historical atlases over time

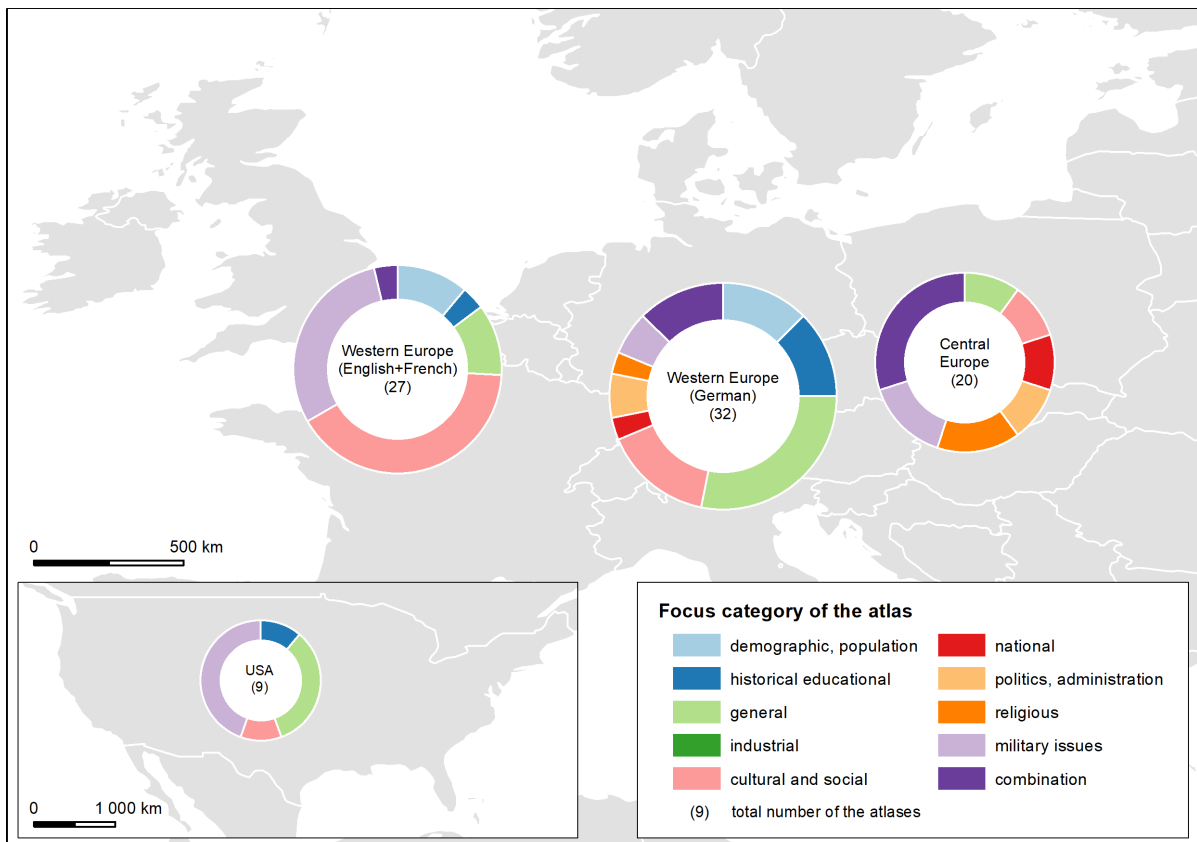


Fig. 8 – Thematic focus of the atlas works in different parts of the Europe and in the USA

CONCLUSION

One of the aims of the paper was to reveal new phenomena which are not clearly visible from the data or the database itself.

The presented charts appear more intuitive, easily understandable for the readers than an austere table view. They may show the relations between selected features in one chart not forcing the users to look for related information across many dashboards, thus they may place lower demands on the cognitive effort of the users.

It may enable the users to easily come to realize the differences or similarities in the content of historical atlases across Europe and compare them to atlases from the USA whose production was influenced by different historical factors and whose cartographic tradition has been developing entirely differently.

Nevertheless, the authors are aware of the fact that the sample of 88 atlases analysed in detail in the second phase of the research is very limited and cannot represent the world-wide production of historical atlases as a whole. But with regards to the aim of this study to only present potential data excerpts from the database and not to analyse and describe the world-wide production of historical atlases, the authors do not consider this as a significant obstacle.

The authors believe that the presented outputs as a whole will form a complex picture of the historiographic atlas production of the latter part of the 20th century; at least of the Anglo-Saxon approach.

ACKNOWLEDGEMENTS

This work was supported by the Ministry of Culture of the Czech Republic from the NAKI programme, DG16P02H010 project "Czech Historical Atlas".

REFERENCES

- [1] HIÚ AV ČR, ČVUT, 2017. Database of Historical Atlases. <http://cha.fsv.cvut.cz/web/atlasses>.
- [2] HIÚ AV ČR, ČVUT, 2019. Czech Historical Atlas. <http://cha.fsv.cvut.cz/web/>.
- [3] Bláha, J. D., Močíčková, J., 2018. The Research-Analytic Part of Preparation of a Cartographic Work: A Case Study of an Analysis of Historical Atlases as the Basis for Creating the Czech Historical Atlas. *AUC Geographica*, 53(1): 58-69. <https://doi.org/10.14712/23361980.2018.6>
- [4] Slocum, T. A., McMaster, R. B., Kessler, F. C., Howard, H. H., 2008. *Thematic Cartography and Geographic Visualization* (Pearson/Prentice Hall) 528 pp.
- [5] Voženílek, V., Kaňok, J. et al., 2011. *Methods of Thematic Cartography: Visualization of Spatial Features* (in Czech: *Metody tematické kartografie: Vizualizace prostorových jevů*) (Vydavatelství Univerzity Palackého, Olomouc) 216 pp.
- [6] Yalcin, M., Elmqvist, N., Bederson, B., 2017. Keshif: Rapid and Expressive Tabular Data Exploration for Novices. *IEEE Transactions on Visualization and Computer Graphics*. vol. 24(8): 2339-2352. <https://doi.org/10.1109/TVCG.2017.2723393>
- [7] Jílková, P., Cajthaml, J., 2019. Database of Historical Atlases: An Interactive Web Application. In: *Proceedings of the International Cartographic Association*, edited by H.Fujita eISSN 2570-2092.

MECHANISM OF EFFICIENCY OF SELECTED NANOSYSTEMS INTENDED FOR CONSOLIDATION OF POROUS MATERIALS

Klára Kroftová¹ and David Škoda²

1. *Czech Technical University of Prague, Faculty of Civil Engineering, Department of Architecture, Prague, Thákurova 7, Czech Republic; Klara.Kroftova@fsv.cvut.cz*
2. *Centre of Polymer Systems, Tomas Bata University in Zlin, Tr. Tomase Bati 5678, Zlin, CZ-76001, Czech Republic; dskoda@utb.cz*

ABSTRACT

Over the past 20 years, the possible usage of disperse and colloid systems of organic consolidation agents as well as mineral systems with particle size in nanodimensions in the context of cultural heritage care has been examined. Nanomaterials, with particle size of up to 1 μ m whose properties are at a certain intersection between properties at the level of molecules and mass are the subject-matter of extensive scientific research for their positive physical and mechanical properties such as high chemical efficiency, excellent plastic, consolidation and diffusion properties, low sintering temperature, cleaning capabilities and others. Nanomaterials whose consolidation efficiency has been tested by experimental research, include, in particular, hydroxide nanodispersions. The article summarises basic conditions for application and principles of efficiency of selected nanosystems for consolidation of historic lime-based porous materials, i.e. in particular lime-based plasters that form integral part of historic buildings

KEYWORDS

Nanomaterials, Calcium Hydroxide, Consolidation, Plaster, Cultural Heritage

INTRODUCTION

Consolidation – improving physical and mechanical properties and stabilising or, alternatively, slowing down or completely stopping degradation – is one of the fundamental objectives of restoration of historic plasters. The plaster consolidation principle is based on returning the binding material into their structure, filling up any cavities that arise and joining up cracks or increasing the adhesion of the plaster to the base and reducing salt content in the plaster porous system. Plaster layers can be strengthened and stabilised by a sequence of individual interventions and the specific procedure and scope of care cannot be universal and generally applicable. It is always an *ad hoc* process, affected by a number of factors, different for different buildings, conditions and properties of preserved historic materials. The general requirement is that renovation of historic buildings and cultural heritage should not damage the original preserved surface finishes and the original method and that the selected material for renovation should respect the preserved condition and follow the original composition of the plaster. After a conservation intervention is completed, the appearance, colour as well as structure of the new supplements and renovated parts should be as close to the original material as possible.

In recent decades, nanotechnologies have started to appear in restoration of surface finishes of historic buildings; these technologies introduce new ways of protection of building structures using specific, functionalised properties of materials caused by increasing the proportion of the area of the surface of the particles to the volume of the particles in nanomaterials. Nanomaterials, when compared to macro-materials, excel in extremely high “performance” in

contrast to a very low consumption of material. By achieving sufficient depth of penetration into the porous system and preserving the original mass, nanomaterials can facilitate the cleaning of surfaces degraded by vandalism (graffiti), they can provide temporary strengthening of the surface to be plastered, increase protection of material against UV radiation, provide biocide protection, and so on. Application of nanomaterials has been documented, inter alia, for deacidification of movable artworks (paper, textile or, for example, leather) [1] - [4], cleaning of surfaces of historic monuments (for example, using nanosuspension from titanium hydroxide, nanoemulsion of organic solvents in water, etc.) [5] - [7] or in consolidation of frescoes or mural paintings [8] - [9]. Preparations for protection and sterilisation of wood and walls against harmful and degrading agents are a specific area of application of materials doped with nanoparticles, for example. In certain justified cases, nanosuspensions can be applied to the surface of historic material independently or as carriers of nanoparticles (for example, silver or diamond) that lend them the capability to, for example, strengthen locally the damaged historic materials, to provide resistance against harmful effects of aggressive exterior environment, etc.

Probably the most widespread application of nanomaterials in care for historic buildings is the use of nanosuspensions based on calcium hydroxide, in particular to strengthen lime construction materials (plasters, limestones, etc.) [10] - [12]. The lime nanosuspension consists of nanoparticles of calcium hydroxide dispersed in alcohol, with individual types displaying different concentrations and type of alcohol. In terms of stabilisation and conservation of these materials, the main advantage is the chemical composition of the resulting product, i.e. calcium carbonate that forms the main binding element in lime materials. The calcium carbonate is deposited in the damaged material; hence, the ligations are strengthened again and the material is hardened. At the same time, calcium carbonate is highly compatible with the original lime-based material and it does not bring irreversible deposits into the consolidated material [13]. The size of nanoparticles usually ranges between 150 to 300 nm for lime nanosuspensions (for example, in the commercially available CaLoSiL® nanosuspension, the size of a particle of calcium hydroxide ranges between 50 and 200 nm) and this does not create any major limitations in relation to the size of pores of the treated material. The suspension contains also larger particles which, however, are produced most frequently by undesired agglomeration of primary particles during manufacture or subsequent storage [14]. The viscosity and colour of the suspension differs depending on its concentration – a more concentrated compound displays higher viscosity and is usually whiter (or it can have a light ochre or grey colour, depending on the source material and the production method used).

An undeniable advantage of consolidation of plasters using calcium hydroxide nanosuspension is a dramatic reduction of the number of impregnation cycles – already several applications of $\text{Ca}(\text{OH})_2$ nanosuspension will result in strengthening in the case of corrupt finishes; if limewater is used, such strengthening is achieved only after dozens of cycles (for example, 100 to 120 application cycles are required on average for strengthening with limewater while 5 to 10 applications are sufficient to achieve equivalent strengthening if lime nanosuspensions are applied). Dispersion of active agents in alcohols is also beneficial from technological perspective; first, no repeated wetting of surfaces by water, development of migration and re-crystallisation of salts occurs; second, their applicability in relation to the risk of freezing is not restricted. The success of the consolidation process using nanomaterials is affected by mineralogical and chemical composition of the treated material, properties of the porous system, surface structure, extent of erosion and degradation of material before treatment, properties of the active agent in the strengthening product (size of ions and particles, chemical composition, concentration, speed of drying and hardening, etc.) and, last but not least, temperature and moisture conditions upon application. If the lime nanosuspension displays sufficiently low surface tension, optimal wetting is safeguarded and this is responsible for deep penetration of dispersions in the porous plaster structure.

METHODS

In the NAKI research project, extensive research focusing on possible usage of nanomaterials in restoration of historic materials (in particular, plaster and stone) has been conducted. The research is carried out in co-operation with the Faculty of Civil Engineering of the Czech Technical University in Prague and the Centre of Polymer Systems of the Tomáš Baťa University in Zlín.

Consolidation materials and their properties

After the basic steps in restoration of lime-based surfaces of historic buildings are carried out (i.e. mainly cleaning, removing the causes of damping and reduction of salt content), the surface can be consolidated. The strengthening product should penetrate through the entire degraded layer, recover its structure and adhesion to the "healthy" base and not to create surface crust. The important properties of the consolidation product include:

- stability (against moisture, alkaloids and acids, light, air and microbiological attack);
- UV radiation resistance;
- display high penetration capability;
- it should not affect the appearance of the treated material (lustre, colour, surface structure, etc.);
- the coefficient of thermal expansion close to the coefficient of expansion of the original material;
- health-related fitness, easy application and affordability.

At the same time, the consolidation agent must be compatible with the original material, i.e. it must not change or affect materially the physical properties of original materials, e.g. porosity, vapour-permeability, thermal or moisture expansion, elasticity (modulus of elasticity). High durability and resistance against aging of the strengthening product and the consolidated material is also very important. The requirement of removability (reversibility) is among basically unrealizable requirements for products and procedures used in treatment of historic materials; it is tempered by the requirement of possible retreatability so as not to prevent subsequent care in later years. From this perspective, materials on inorganic basis, compatible with the treated material and, at the same time, stable with high efficiency following application, seem as most suitable consolidation products.

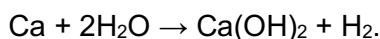
Great focus is placed primarily on penetration capabilities of the consolidation agent; the material is strengthened only when it penetrates into sufficient depth from the surface and spreads evenly in the mass of the substance to be strengthened (a sharp transition between non-strengthened and heavily strengthened material leads to development of tension between layers and subsequent mutual separation). The rate of penetration of the consolidation agent depends mainly on the properties of the strengthened material (in particular, its porosity, moisture and pH value), properties of the solution (size of solved molecules, viscosity) and the consolidation method. The higher surface tension, the lower viscosity, density and contact angle at the interface between a solid and a liquid the consolidation liquid displays, the better its penetration. When disperse consolidation products are used, the size of particles and possibility of their penetration into the porous system is important.

Possibilities of production of nanosuspensions

Until recently, nanoparticles of calcium hydroxide have been obtained either through hydrolysis of calcium hydride (CaH_2) under specific experimental conditions or through reaction of calcium oxide or calcium hydride CaH_2 with water in organic environment in the presence of surfactants [15].

A more modern possibility of synthesising crystallised nanoparticles of calcium hydroxide is the reaction of sodium hydroxide (NaOH) and calcium chloride (CaCl₂) that is added (drop by drop) into water solution at 90 °C and the reaction produces calcium hydroxide Ca(OH)₂ and sodium chloride (NaCl) that is removed from the suspension subsequently. In the last stage of production, the lime particles are broken in a ball mill to particles of several μm to nm in size; the resulting clusters of particles are subsequently separated using ultrasound [16].

Another known production method involves the reaction of metallic calcium with water in alcohol medium [17] to [18]. The reaction occurs pursuant to this equation:



Yet another alternative is a method based on ion exchange between resin (anion) and water solution of calcium chloride at 20 to 25°C. Clean suspension containing nanoparticles of Ca(OH)₂ can be obtained quickly after separation of the resin from the suspension without any need for cleaning. Exhausted resins can be regenerated and re-used for repeated production of nanolime [19].

When manufacturing nanosuspension, it is relatively difficult to create accurately the required concentration; different concentrations are achieved by evaporating the solvent during manufacture. Stability of suspension is proportionate to the particle size – the smaller the particle, the lower stability. Kinetically stable dispersions can be obtained with short-chain aliphatic alcohols. The benefit of these alcohols is that they evaporate fast (the cycles can be repeated quickly) and, when compared to other solvents, they have low toxicity.

Verifying the efficiency of selected nanosuspensions

In the NAKI research project, lime nanosuspensions were designed and manufactured by the most frequent procedure of synthesis of Ca(OH)₂; these nanosuspensions were subsequently modified and enriched by other components that had been assumed to display positive potential for use in cultural heritage care. The nanosuspensions have been manufactured in close co-operation with the Centre of Polymer Systems of the Tomáš Baťa University in Zlín. Based on the results of preceding research, 3 various lime nanosuspensions have been prepared and tested [20] - [21]:

Ca4: Ca(OMe)₂ dispersed in isopropyl alcohol;

Ca4O: calcium oxide dispersed in ethanol;

CaMg1: Ca and Mg pre-cursors have been dissolved in distilled water; subsequently, NaOH solution was added.

(Each nanosuspension was prepared in concentration of 5 g / l.)

In order to determine the crystalline structure of products, XRD powder analysis on the Rigaku MiniFlex 600 diffractometer was used. Each diffractogram was compared to the JCPDS Ca(OH)₂ (JCPDS 01-076-0571) (Figure 1) card.

The basic parameters in assessment of potential success of strengthening include the capability of the plaster to absorb the consolidation agent and the depth of its penetration associated therewith. The average values of the depth of penetration of consolidation products range between several millimetres and several centimetres, depending on the size and character of the porous system and the size of particles of the strengthening agent. The laboratory research verified the depth of penetration of the tested nanosuspensions on plaster beams using phenolphthalein (Figure 2). The research demonstrated sufficient depth of penetration and equal distribution of the consolidation product.

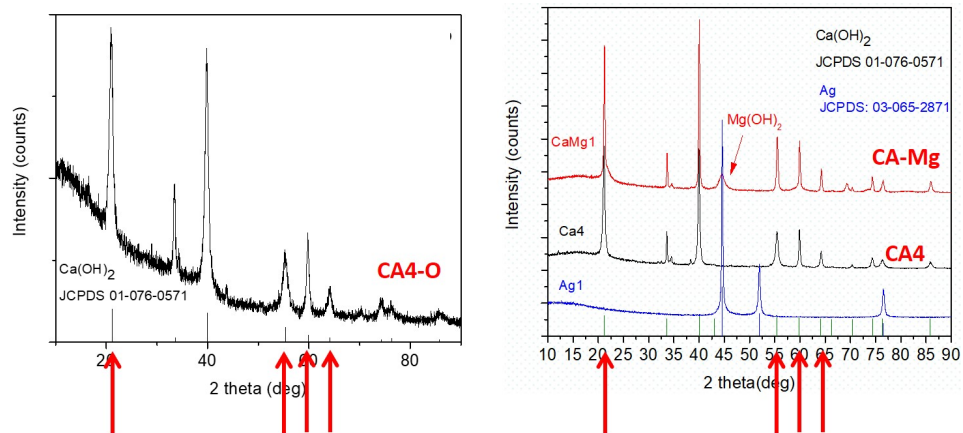


Fig. 1 - The XRD powder diffraction patterns of prepared products (Ca4-O, Ca4 and Ca-Mg) showing the peaks corresponding with the library diffractogram of Ca(OH)₂



Fig. 2 - Verifying the rate of penetration of selected nanosuspensions: a) Ca4-O; b) Ca4; c) Ca-Mg. The photographs of sections of historic plaster samples showing the depth of penetration of consolidation product using colouring caused by application of phenolphthalein indicator (the yellow dotted line shows the border of 25 mm)

Another important characteristic is provided by assessment of sub-surface cohesion of the plaster (cohesion, ultimate tensile strength) that represents the condition of the historic material before and after consolidation, in terms of efficiency and quality of consolidation intervention to the degraded plaster surface. The efficiency of consolidation products can be verified in the case of plaster-coated surfaces using, for example, the “Scotch tape test” that can be accompanied by scanning electron microscopic examination. This will provide information about the deposit of the strengthening agents (i.e. lime) in the porous system of the degraded plaster. The scratch “Scotch Tape” test provides a reliable estimate of surface and shallow sub-surface strengthening after application of consolidation products and it provides a clear presentation of the differences between individual types of treatment or agents. However, the measuring of the cohesion is without any link to correlations to solidity characteristics; the result of the test is a “strengthened – not strengthened” statement (Figure 3).

RESULTS

Nanosuspensions of calcium hydroxide in alcohols represent an alternative of almost water-free restoration of lime-based historic surface finishes. Clear advantages of lime nanosuspensions prepared in alcohol include their material compatibility with the original structural binding agent (i.e. lime), small size of lime particles (this should have positive impact upon the depth of penetration),

low number of application cycles which does not support mobilisation of water-soluble salts in the material.

The success of the strengthening process is influenced by a number of factors. The basic properties and parameters that need to be taken into consideration when designing the strengthening technology include: chemical and mineralogical composition of the material to be strengthened, hardness of the material before strengthening, size and shape of open pores, porosity, size of ions, molecules or particles of the active strengthening agent in the strengthening product, chemical composition and concentration of the active agent, speed of drying and hardening of the active agent in the strengthened substrate at specific temperature and moisture conditions of material and ambient air. The knowledge of the above parameters is a good basis when designing the strengthening technology - the type of the strengthening product, concentration of the active agent, method of application of the consolidation agents, number of repeated applications within one consolidation cycle, method of verification of substrate after impregnation.

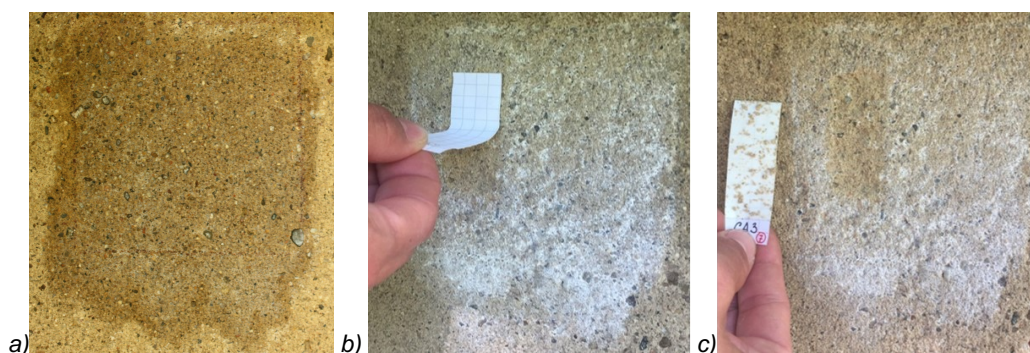


Fig. 3 - The Scotch tape test carried out in situ on the plaster of the historic building of the Voršilky Monastery: a) Test field after application of nanosuspension Ca4; b) after 28 days: pressing down of an adhesion tape during the Scotch tape test (third measuring out of ten); c) after the test tape was torn away.

CONCLUSION

At the moment, nanomaterials are applied in historic and cultural heritage structures in the Czech Republic occasionally and sufficient know-how and experience for their reliable and permanent application are not available. However, if these new materials should be applied, e.g., to surfaces or to below-surface layers of materials, verified know-how about long-term behaviour of these materials (i.e. verifying the stability in light of attack of outside environment, influence of radiation, interaction with the ambient environment, transparency, diffuse transmittance, resilience against chemical and biochemical degradation, etc.) would be required so as to avoid gradual and irrecoverable damage of valuable historic structures such as paintings, plaster, wooden, stone elements, etc. The tested nanosuspensions comply with the assumptions of their future use to consolidate porous lime-based materials.

ACKNOWLEDGEMENTS

This article was written as part of the NAKI DG16P02M055 research project “Development and Research of Materials, Methods and Technologies for the Restoration, Preservation and Strengthening of Historic Masonry Constructions and Surfaces and Systems of Preventive Conservation of Cultural Heritage Buildings Threatened by Anthropogenic and Natural Hazards”.

REFERENCES

- [1] Baglioni, P. et al Nano-Materials for the Conservation and Preservation of Movable and Immovable Artworks, Progress in Cultural Heritage Preservation – EUROMED 2012, dostupné online: https://www.researchgate.net/publication/270365605_Nano-Materials_for_the_Conservation_and_Preservation_of_Movable_and_Immovable_Artworks
- [2] Poggi, G. et al Hydroxide Nanoparticles for Deacidification and Concomitant Inhibition of Iron-Gall Ink Corrosion of Paper, *Langmuir*, 2010, 26 (24), pp 19084–19090
- [3] Kwitkowska, A. et al Paper deacidification with the use of magnesium oxide nanoparticles, *Forestry and Wood Technology* № 85, 2014: 144-148, dostupné online: http://agro.icm.edu.pl/agro/element/bwmeta1.element.agro-4b9d7961-05a7-43ed-9339-708f4ba9365a/c/144_Annals85.pdf
- [4] Giorgi, R. et al Nanotechnologies for Conservation of Cultural Heritage: Paper and Canvas Deacidification, *Langmuir*, 2002, 18 (21), pp 8198–8203
- [5] Graziani, L. et al Durability of self-cleaning TiO₂ coatings on fired clay brick facades: Effect of UV exposure and wet & dry cycles, *Building and Environment*, 2014, Vol.71, p.193-203
- [6] Quagliarini, E. et al Smart surfaces for architectural heritage: Preliminary results about the application of TiO₂ based coating on travertine, *Journal of Cultural Heritage*, 2012, Vol.13, p.204-209
- [7] Quagliarini, E. et al Self-cleaning materials on Architectural Heritage: Kompatibility of photo-induced hydrophobicity of TiO₂ coatingy on stone surfaces, *Journal of Cultural Heritage*, 2013, Vol.14, p.1-7
- [8] Baglioni, P., GIORGI, R. Soft and hard nanomaterials for restoration and conservation of cultural heritage, *Soft Matter*, 2006, Vol. 2, p.293-303
- [9] Grassi, S. et al The conservation of the Vecchietta's wall paintings in the Old Sacristy of Santa Maria della Scala in Siena: The use of nanotechnological cleaning agents, *Journal of Cultural Heritage*, 2007, Vol.8, p.119-125
- [10] Dei, L., Salvadori, B., Nanotechnology in cultural heritage conservation: nanometric slaked lime saves architectonic and artistic surfaces from decay, *Journal of Cultural Heritage*, Volume 7, Issue 2, April–June 2006, pp. 110–115, ISSN: 1296-2074, 2006
- [11] Macháčko, L., Consolidation of historic plaster layers on second OS of the arcaded walk of a former Rosa Coeli Monastery in Dolni Kounice by means of CaLoSiL lime nanosuspension, *Zpravy památkové péče*, Vol.72/2012, pp.122-128, 2012
- [12] Anoudi, P.N. et al Superhydrophobic films for the protection of outdoor cultural heritage assets, *Applied Physics A*, 2009
- [13] Baglioni, P. et al Nanotechnologies in the Conservation of Cultural Heritage – A compendium of materials and techniques, Springer Science+Business Media, Dordrecht 2015,
- [14] Drdácký M., Slížková Z. Nanomateriály v péči o památky, 2012, dostupné online: <http://abicko.avcr.cz/2012/10/06/>
- [15] Kociánová, I., Restaurování centrálního výjevu na klenbě kaple sv. Isidora v Křenově, Litomyšl, 2013. Diplomová práce. s. 22, Univerzita Pardubice, Fakulta restaurování, Obor Restaurování a konzervace děl nástěnné malby, sochařských děl a povrchů architektury Vedoucí práce Vojtěchovský, J.
- [16] Dei, L., Giorgi, R., Ambrosi, M., Neto, Ch., Baglioni, P. Colloidal Particles of ca(OH)₂: Properties and Applications to Restoration of Frescoes, Department of Chemistry and CSGI, University of Florence, via, Gino Capponi, 9, 50121 Florence, Italy, 2001.
- [17] Vojtěchovský J., Slouková, L. Konsolidační účinky vápenných nanosuspenzí a jejich směsí s estery kyseliny křemičité při zpevňování nástěnné malby, Zpráva k projektu realizovaného v rámci SGS Univerzity Pardubice, Fakulta restaurování, Litomyšl, 2015
- [18] Dunajská, J., Tests on sustainability of consolidation treatments with CaLoSiL® nanosuspensions on plaster reference samples, Fakulta restaurování, Univerzita Pardubice, Litomyšl, 2012, Diplomová práce
- [19] Taglieri, G., Daniela, V., Del Re, G. et al A New and Original Method to Produce Ca(OH)₂ Nanoparticles by Using an Anion Exchange Resin Advances in Nanoparticles, 2015, 4, 17-24, 2015
- [20] Kroftová, K., Kuřitka, I., Škoda, D., Šmidtová, M., Masař, M. Synthesis nanolime suspension and their potential use in cultural heritage preservation In. EASEC 15 – The Fifteenth East Asia – Pacific Conference on Structural Engineering and Construction, 2017
- [21] Kroftová, K., Šmidtová, M., Škoda, D., Kuřitka, I., Witzany, J. Comparison of the degree of consolidation of historic plaster layers by means of lime hydrate nanosuspensions In. 11th International Conference on Structural Analysis of Historical Constructions, 2018

FINITE ELEMENT ANALYSIS OF THE SEISMIC BEHAVIOR OF THE ASSEMBLED LIGHT STEEL FRAME- LIGHT WALL STRUCTURES

Liu Wenchao^{1,2*}, *Chen Zheng*³, *Wang Cheng*¹, *Dong Hongying*³, *Wang Ruwei*³

1. *Technology Research and Development Center, CCCC Fourth Highway Engineering CO.,LTD., Beijing 100022, China; liuwenchaoann@foxmail.com*
2. *Office of Postdoctoral Research, Beijing University of Technology, Beijing 100124, China; liuwenchao@bjut.edu.cn*
3. *Key Laboratory of Urban Security and Disaster Engineering, Beijing University of Technology, Beijing 100124, China; chenzhengbjut@foxmail.com*

ABSTRACT

In order to meet the needs of the development of low-rise assembly structure in rural areas, a fabricated light-weight steel frame-composite light wall structure is proposed in this paper. The light-weight steel frames are used to bear the vertical loads. The single-row-reinforced recycled concrete wall-boards are used as lateral members to resist most of the horizontal earthquake loads. The wall-board, EPS (Expanded Polystyrene) insulation modules, and fly ash blocks form the thermally insulated wall. Four fabricated lightweight steel frame-composite light wall structures and one light-weight steel frame (FRA) structure were tested under the low cyclic loads. The influence of wall reinforcement spacing and structural form (be it fly ash block or not) on the seismic performance of this new structure was analysed and the damage process of the specimen was simulated using the ABAQUS[®] software. The results show that the light steel frames and the single-row-reinforced recycled concrete wall-board can work well together. Furthermore, the structure has two clear seismic lines. Due to the use of EPS insulation modules and fly ash blocks, the structure has good anti-seismic and thermal insulation abilities. Reducing the spacing of bars or compositing fly ash blocks can significantly improve the seismic performance of the structure. The finite element method (FEM) calculations agreed well with the experimental results, which validates the proposed model.

KEYWORDS

Pre-fabricated construction, Rural residence, Fabricated light-weight steel frame- composite light wall structure, Seismic performance, Experimental study

INTRODUCTION

Due to rapid growth in the sector of construction and low production costs, pre-fabricated construction has attracted the attention of many scholars in the early 20th century. By the 1960s, pre-fabricated construction had preliminarily been established in developed countries, such as Great Britain, France and the former Soviet Union. China began to vigorously develop pre-fabricated construction in 2015, and introduced a series of related measures. In November 2015, the Ministry of Housing and Urban-rural Development issued the "Outline for the modernization and development of the construction industry", and in February 2016, the state council issued the "Guidelines on the vigorous development of prefabricated construction", both of which clearly pointed out the development of pre-fabricated construction. According to some statistics, at present, the construction of villages and towns accounts for more than 50% of the total buildings in China. There is only a handful of research on the structural technology suitable for pre-fabricated construction in villages and towns. Villages and towns are in urgent need of developing new assembly-type structural systems.

Domestic and foreign scholars have conducted a lot of research on the assembled residential systems. Serrette et al. studied the thin-walled light steel structure, and carried out a series of tests and theoretical analyses on the lateral resistance of light steel keel composite wall [1-4]. Based on the frame of the concrete light wall structure, Tsinghua University developed SW structure [5]. Hao et al. (2010) developed the CL building system based on the welded steel grid technology [6]. Beijing University of Civil Engineering and Architecture developed the LI+T composite concrete building system (2007), in which the connection between different types of wall-boards is unified, whereas the number of structural nodes is also reduced [7]. Xi'an University of Architecture and Technology and Beijing Jiaotong University jointly developed the energy saving system having multi-ribbed composite plate and light frame structure (2010), which is suitable for high-rise earthquake-resistant structures consisting of pre-fabricated components and integral pouring of external frames [8].

Mochizuki tested the seismic performance of vertical joints of pre-cast concrete shear wall, and found that the ultimate bearing capacity of the wall was related to the constraint conditions of horizontal joints (including pin action). Chen et al. (2012) carried out low-cycle repeated load test on the one-half reduced scale four-storey space model of the full-prefabricated shear wall structure, and showed that the yield load is much higher than the seismic shear force, whereas the test piece maintained elasticity under medium earthquake and therefore, can meet the fortification target of large earthquakes [10]. Cao et al. (2017) carried out an experimental study on the seismic performance of semi-assembled low-rise recycled concrete shear wall, and the results showed that, under horizontal load, horizontal crack and a small slip appear in the joint connection between the pre-cast shear wall and the foundation wall, whereas the structure had good seismic performance [11].

Many studies have been conducted on the seismic performance and connection performance of light steel shear wall. Most of them have focused on industrial and high-rise

buildings. However, research on the seismic performance of pre-fabricated light steel frame-composite light wall structure, suitable for rural residential buildings, has not been reported in literature. To this end, the low-cycle cyclic load tests of four assembled light-weight steel-light wall structure and one light-steel hollow frame were designed. This paper studies the influence of construction measures (be it the composite fly ash block layer or not) and spacing of distributed bars on the bearing capacity, hysteretic characteristics, ductility, stiffness and failure mode of the wall structure, and provides a reference for the design of assembled structure of rural buildings.

EXPERIMENTAL

Material Properties

The specimen was made of 42.5 grade ordinary Portland cement, in which the replacement of recycled coarse aggregate(RCA) was 100% (particle size of 5-10 mm). The recycled coarse aggregate was made up of crushed concrete of a demolished building in Beijing, China. Fine aggregate used natural sand (aggregate size 0-5 mm). All aggregates were mixed with tap water. The mixing ratio and cubic compressive strength (f_{cu}) of recycled aggregate concrete is presented in Table 1.

The measured concrete strength is presented in Table 1. The mechanical properties of the steel used in the test piece are given in Table 2. The EPS modules were used as the insulation layer. The compressive strength of fly ash blocks, used in the specimen, was 2.35 MPa. The M10 mixed mortar (The strength representative value is 11.5MPa~16.0MPa) was used for building the specimen.

Tab. 1 - Mixing proportion and cubic compressive strength of the specimen (kg/m^3)

RCA/%	Cement	Fly ash	Mineral powder	Sand	Recycled pebble	Water reducer	Water	f_{cu}/MPa
100	369	78	78	841	841	3.5	181	43.6

Tab. 2 - Mechanical properties of steel bar and steel tube

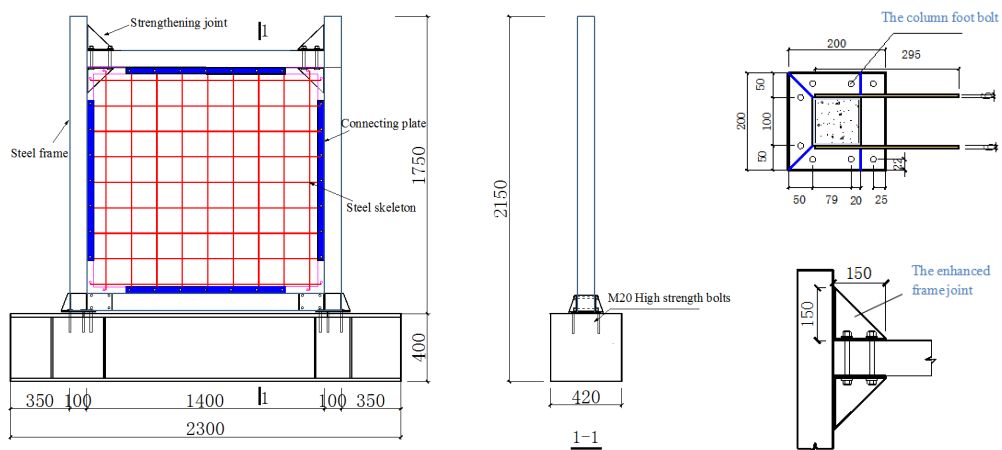
Steel type	Steel size /mm	Yield strength f_y /MPa	Ultimate strength f_u /MPa	Elongation δ %	Modulus of elasticity E /MPa	Thickness /mm
Steel bar	D5	680	786	5.5	2.09×10^5	—
Steel plate	—	309	467	25.27	2.11×10^5	4
Steel tube	100×100	375	477	23.23	2.18×10^5	4

Details of the Test Specimens

Four fabricated light-weight steel frame-composite light wall structures and one light-weight steel frame structure were designed. The main parameters of the specimens are presented in Table 3. The light-weight steel frames were constructed of square steel tubes having the thickness of 4 mm and which were filled with recycled concrete. In order to facilitate the bolt connection with the single-row-reinforced recycled concrete wall-boards, steel plate with the thickness of 4 mm was welded. The frame joint was enhanced, and the column foot was provided with 8 bolt holes to facilitate the connection with the I-foundation. The column foot bolt adopted M20 high-strength bolt. The recycled concrete wallboard was composed of frame steel plate with the thickness of 4 mm and distributed reinforcement with a diameter of 5 mm. The connecting bolt of the wall-board was M10. The single-row distributed reinforcement of wall-board was placed in two directions. The reinforcement ratio of the distributed rebar was 0.33%~0.49%. The size and reinforcement details of the specimens are shown in Figure 1.

Tab. 3 - Main parameters of the specimens

Serial No.	Wallboard thickness/mm	Reinforcement spacing/mm	EPS module thickness /mm	Fly ash block thickness /mm
PFS40-S1-1	40	100	70	-
PFS40-S1-2	40	100	70	60
PFS40-S2-1	40	150	70	-
PFS40-S2-2	40	150	70	60
FRA	-	-	-	-



(a) Details of the specimen



(b) Construction of the specimen

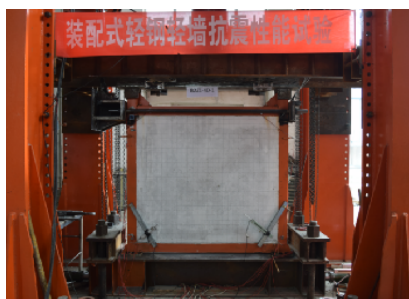
Fig. 1 - Size and reinforcement details of specimens

Test Set-Up and Loading Programme

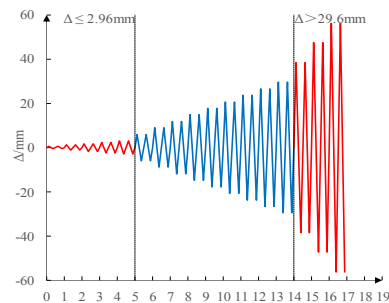
In this work, low cyclic load method was adopted for the tests. In this regard, 600 kN vertical load was applied at the top center of the distribution beam, which remained constant during the loading process. The loading field is shown in Figure 2(a). The horizontal load was applied at the center of the frame beam. The loading point was 1480 mm from the top of the foundation, and the axial compression ratio was 0.35. In order to prevent the out-of-plane instability of specimens during loading, lateral restraint braces were set in the vertical direction of horizontal loading. The column base of the specimen was fixed to the steel beam of the foundation using high-strength bolts, and the steel beam of the foundation was fixed to the ground using ground anchor bolts.

The measured horizontal displacement of the loading point was used as the control displacement. When the displacement angle was less than $1/500$, the displacement loading increment was $1/2500$. When the displacement angle was less than $1/50$, the displacement loading increment was $1/500$. When the displacement angle was greater than $1/50$, the displacement loading increment became $3/500$, which was twice per stage. During the whole testing process, the displacement loading rate was consistent. It is stipulated that the force was positive when the horizontal jack was pushed out. The magnitude of the displacement loading is shown in Figure 2(b).

Force sensors are arranged at the ends of vertical and horizontal jacks. At the loading height, the horizontal displacement meter is arranged at the end of the loading beam.



(a) Loading field



(b) Loading history

Fig. 2 - Loading device and the loading history

RESULTS AND DISCUSSION

Failure Characteristics

The obvious shear failure took place in the wall, which indicated that the wall undertook a lot of horizontal shear force. With the wall cracked, the light steel frame became the main force-bearing member at the later stage of loading. It finally underwent bending failure, while no obvious damage was found in the joint. The structure had two clear seismic lines. In the later stage, the

connecting members between the wall and the frame were not obviously damaged, which indicated that the two components worked well together. With the increase of reinforcement ratio, the width of diagonal crack in the wall obviously decreased. The damage of the wall with fly ash layer was not obvious, which indicated that fly ash block could effectively withstand the horizontal force of the wall. Figures 3(a) - 3(h) show the ultimate failure models and crack distribution of specimens.



(a) Broken of the bar

(b) Steel plate tearing

(c) Separation of EPS

(d) Bulging of steel tube



(e) PFS40-S1-1

(f) PFS40-S2-1

(g) PFS40-S1-2

(h) PFS40-S2-2

Fig. 3 - Failure models and crack distribution of specimens

Load-Displacement Response

The measured characteristic results of specimens on the skeleton curve are presented in Table 4. In Table 4, F_y is the yield load, F_u is the peak load, and F_d is the failure load. Furthermore, Δ_c , Δ_y , Δ_u and Δ_d are the displacement values corresponding to F_c , F_y , F_u and F_d , respectively. Additionally, θ_c , θ_y , θ_u and θ_d are the corresponding interlayer displacement angles. The yield load is determined by energy equivalence method. The failure load is the corresponding load value when the peak load drops to 85%. The skeleton curves of specimens are shown in Figure 4.

Tab. 4 - Measured characteristic results of the specimens

Serial No.	F_y /kN	Δ_y /mm	F_u /kN	Δ_u /mm	F_d /kN	Δ_d /mm	μ
PFS40-S1-1	784.10	7.35	920.63	10.12	800.95	13.63	1.85
PFS40-S1-2	966.71	7.18	1141.11	11.44	969.95	14.88	2.07
PFS40-S2-1	623.27	7.87	731.89	11.10	622.10	13.71	1.74
PFS40-S2-2	797.68	7.20	936.34	9.82	795.89	14.85	2.06
FRA	120.74	26.83	143.56	47.54	122.03	64.89	2.42

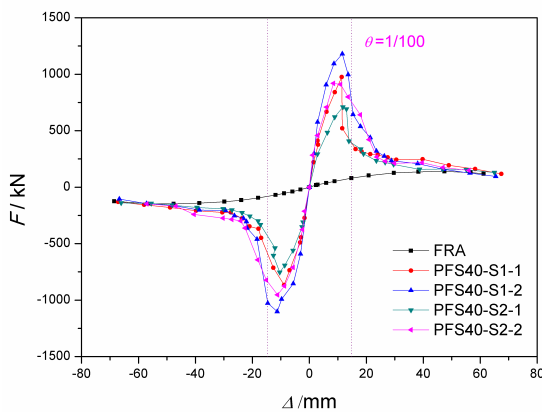


Fig. 4 - Skeleton curves of specimens

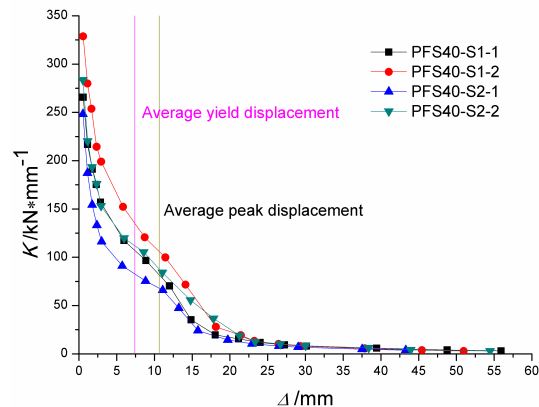


Fig. 5 - "Ki-Δ" curves of specimens

Compared with the specimens without filled fly ash block, the bearing capacity of the specimens filled with fly ash block was significantly increased. The yield loads of PFS40-S1-2 and PFS40-S2-2 increased by 18.9% and 21.9%, respectively, indicating that the bearing capacity of the structure significantly increased due to the filling by fly ash block. The wall reinforcement spacing had a relatively large impact on the bearing capacity of the structure. Compared with PFS40-S2-1 and PFS40-S2-2, the peak loads of PFS40-S1-1 and PFS40-S1-2 increased by 20.5% and 17.9%, respectively. The ultimate bearing capacity of light-weight steel frame was 139.61 kN. The ultimate bearing capacity of light-weight steel frame-composite light wall structures was 424.24% - 825.33% higher than that of light-weight steel frame.

The proposed structure meets the requirements of the Chinese Code for seismic design of buildings [12], which states that the elastic-plastic displacement angle of steel structure is limited to 1/50 and the failure displacement angle of specimen FRA is 1/23. The results show that the recycled concrete light-weight steel frame has good collapse resistance. Meanwhile, the elastic-plastic ultimate displacement angle of specimens PFS-S1-2 and PFS-S2-2 with fly ash filled layer meet the requirement, which states that the elastic-plastic displacement angle of reinforced concrete frame - seismic wall should not be higher than 1/100.

It is assumed that the weight of low-rise buildings is about 1.5T per square meter. For a 150 m² house, the total mass is about 225t. In the case of 8 degree seismic fortification intensity, the maximum value of the basic seismic acceleration is 0.3g, whereas the horizontal load is calculated

to be 675 kN. Furthermore, the average yield load of the wall specimen is 792.94 kN, while the overall structure is controlled within the elastic working range.

$$\mu = \frac{|\Delta_d| + |-\Delta_d|}{|\Delta_y| + |-\Delta_y|} \quad (1)$$

The displacement ductility coefficient μ is the ratio of Δ_d (failure displacement) to Δ_y (yield displacement). Since the hysteresis curve is not completely symmetrical, the displacement ductility coefficient is calculated according to Equation (1).

- 1) The recycled concrete light steel frame has good ductility, whereas the maximum failure displacement can reach the value of 64.89 mm. Compared with the light-weight steel frame, the ductility of the structure is reduced after the wall-board is assembled.
- 2) The specimens PFS40-S1-2 and PFS40-S2-2 filled with fly ash block have larger peak and failure displacements. Meanwhile, the ductility coefficient is also higher, which indicates that fly ash block can effectively improve the ductility of the structure.
- 3) Reducing the spacing of distributed reinforcement or increasing the reinforcement ratio of distributed reinforcement can effectively improve the ductility coefficient of the structure.

Stiffness and Degradation

The stiffness-displacement K_i - Δ curves of specimens as shown in Figure 5. In this study, K is the secant stiffness of peak points at different time intervals. As shown by the results presented in Table 5, K_0 , K_y , K_u and K_d represent the average values of secant stiffness of hysteresis curve in the initial stage, yield load, peak load and failure load, respectively. The K_i - Δ curves of specimens are obtained using Equation (2).

$$K_i = \frac{|+F_i| + |-F_i|}{|\Delta_i| + |-\Delta_i|} \quad (2)$$

where i is the number of cycles, K_i is the tangential stiffness of the i -th cycle, F_i is the peak load corresponding to the i -th cycle, and +, - represent the positive and negative directions of the horizontal force.

Tab. 5 - Experimental results of stiffness and degeneration coefficient

Serial No.	$K_0/(kN \cdot mm^{-1})$	$K_y/(kN \cdot mm^{-1})$	θ_y	$K_u/(kN \cdot mm^{-1})$	θ_u	$K_d/(kN \cdot mm^{-1})$	θ_d
PFS40-S1-1	265.48	106.68	1/201	90.97	1/146	58.76	1/108
PFS40-S1-2	304.88	134.73	1/206	99.75	1/129	65.18	1/99
PFS40-S2-1	248.24	79.20	1/188	65.97	1/133	45.38	1/107
PFS40-S2-2	283.41	110.87	1/206	95.35	1/151	53.60	1/100
FRA	15.88	4.50	1/55	3.02	1/31	1.88	1/23

The degradation of stiffness of light-weight steel frame-composite light wall structure can be divided into five stages, namely the Initial stage, the cracking stage, the yield stage, the limit stage, and the failure stage. The specimens have the character of higher initial stiffness, while the stiffness decreases rapidly with the cracking of the wall. When the wall is seriously damaged, the frame beam and the column are severely deformed. Then, the stiffness of the test piece continues to decrease, though the rate of decrease drops down significantly.

In the case of same reinforcement spacing, the structure with fly ash block layer had higher yielding stiffness, peak stiffness and failure stiffness. Compared with PFS40-S1-1 and PFS40-S2-1, the average initial lateral stiffness of PFS40-S1-2 and PFS40-S2-2 increased by 12.92% and 12.41%, respectively. In addition, the average yield stiffness increased by 20.82% and 28.56%, and the average peak stiffness increased by 8.75% and 30.81%, respectively. Fly ash block significantly delayed the structural damage during the process of loading.

In the case of same structural form, the spacing of distributed reinforcement bars has a great influence on the characteristic stiffness of the specimen. Smaller the spacing of reinforcement bars, higher was the characteristic stiffness of the specimen. The initial stiffness of the light steel frame structure was $15.88 \text{ kN} \cdot \text{mm}^{-1}$. Compared with the light-weight steel frame structure, the initial stiffness of the new structure increases by 1463.22 - 2002.20.

Energy Dissipation Capacity

The area of intersection of characteristic point load skeleton curve and coordinate axis is taken as the energy dissipation value. Furthermore, E_y is the yield energy dissipation, E_u is the peak energy dissipation and E_d is the destruction energy dissipation. Additionally, E_p is the cumulative total energy consumption, which is the cumulative area of the cyclic hysteresis loop when the specimen is destroyed. The experimental results of energy dissipation are presented in Table 6.

Tab. 6 - Experimental results of the energy dissipation

Serial No.	E_y	E_u	E_d	E_p
PFS40-S1-1	7.651	11.383	13.08566	153.465
PFS40-S1-2	9.586	17.261	20.855.92	214.786
PFS40-S2-1	6.912	10.101	12.85783	138.214
PFS40-S2-2	8.714	14.858	19.45049	198.689
FRA	4.510	9.388	13.12238	23.584

Compared with the light steel frame FRA, E_y , E_u and E_p increased by 112.55%, 58.93%, and 810.7%, respectively, indicating that the energy-dissipation capacity of the assembled wall-board can be significantly improved.

Compared with PFS40-S1-1 and PFS40-S2-1, the energy consumption of specimens PFS40-S1-2 and PFS40-S2-2 increased by 59.4% and 51.3%, indicating that the energy consumption of the structure can be significantly improved by filling fly ash blocks. Under the same structural form, the wall reinforcement spacing has little effect on the energy dissipation capacity of the specimens. As shown in Figure 6, comparing with PFS40-S2-1 and PFS40-S2-2, the damage energy consumption of PFS40-S1-1 and PFS40-S1-2 increased by only 2% and 7%, respectively.

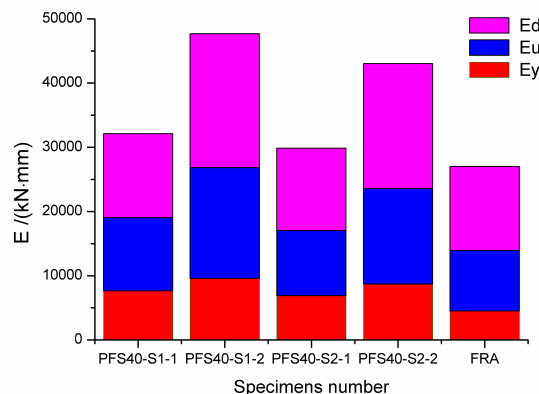


Fig. 6 - Energy dissipation histogram of specimens

FEM ANALYSIS

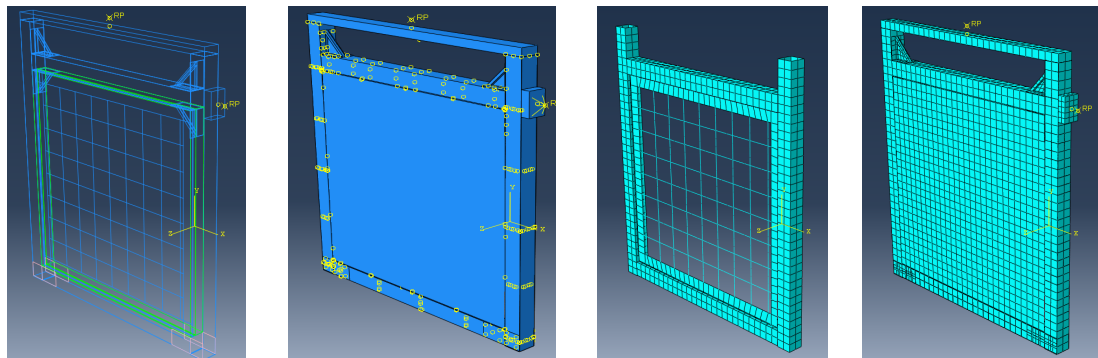
Finite Element Parameters

The damage-plasticity model of concrete is adopted in the calculations. The constitutive relation of the concrete in square steel tube is restrained by square steel tube as proposed by Cai [13], which is based on Mander [14] model. The compressive constitutive relationship of fly ash

block wall was adopted, as proposed by Wang [15]. The constitutive relation of steel adopted the double broken line model. The contribution of EPS module to shear capacity was ignored.

Finite Element Model

The solid element C3D8R was used to simulate the steel tube, concrete and fly ash. The truss element T3D2 was adopted for reinforcement of the wall-board, while the shell element S4R was adopted for the steel plate of the wall-board. The steel bars are modelled separately without considering the bond slip between the steel bars and the concrete. The model is divided using hexahedral structured mesh, and the shell element is divided using the tetrahedron-main unit free mesh, as shown in Figure 7.



(a) Constructional detail (b) Boundary condition (c) Steel skeleton (d) Wall structure

Fig.7 - Calculation models and meshing

Analysis of the Calculated Results - The Skeleton Curve

The comparison between the calculated and measured curves of force-displacement $F-\Delta$ is shown in Figure 8.

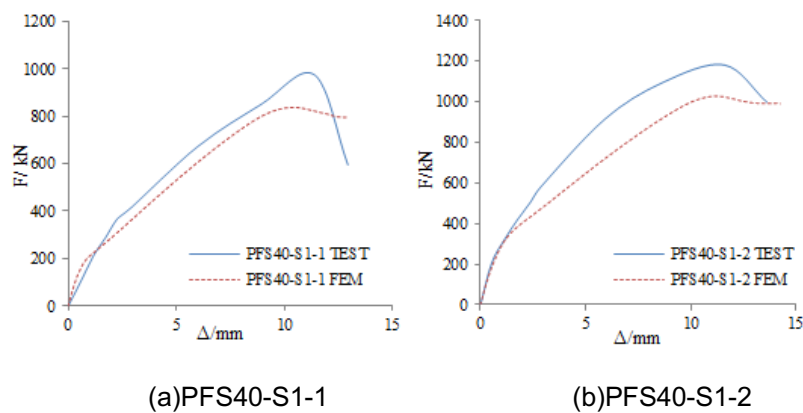


Fig. 8 - Comparison between the calculated and measured curves of $F-\Delta$

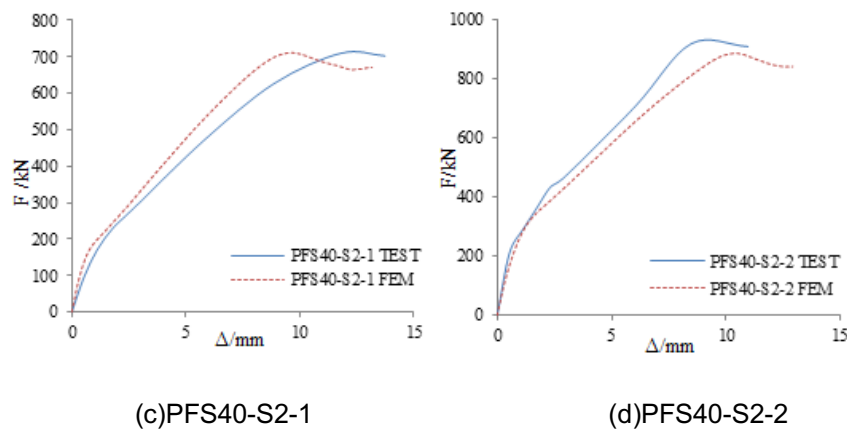


Fig. 8 - Comparison between the calculated and measured curves of $F-\Delta$

Figure 8 shows that, at the early stage of load, the calculated curve is in good agreement with the measured curve. While in the middle and late stages, the calculated results lie below the measured ones, whereas the error between the calculated and measured values of ultimate load is less than 15%.

CONCLUSIONS

- (1) The fabricated lightweight steel frame-composite light wall structure has two anti-seismic lines of composite light wall and light steel frame. The structure has good seismic performance. The EPS module and the fly ash filling layer can effectively slow down the structural damage process.
- (2) The structural form has a significant impact on the seismic performance of the structure. Filling the fly ash block can effectively improve the seismic performance of the structure. The spacing of reinforcing bars has a relatively small impact on the energy consumption performance. It is suggested that the reinforcement ratio of reinforcing bars, distributed on the wall-board, should be controlled within 0.25 - 0.33%.
- (3) The stiffness of FEM calculated curve is in good agreement with the measured curve at the early stage of loading. The calculated curve deviates from the measured curve during the middle and late stages. The calculated values are less than the measured ones. The error between the calculated and measured values is less than 15%.
- (4) According to the estimation, the structure is still in the elastic working range and has a high strength safety reserve under the circumstance of 8° seismic fortification intensity.

REFERENCES

- [1] Serrette R. L., José, Encalada, et al., 1997. Static racking behavior of plywood, OSB, gypsum, and fiber bond walls with metal framing. *Journal of Structural Engineering*, 123, 1079-1086.
- [2] Goggins J. M., Broderick B. M., Elghazouli A Y, et al., 2005. Experimental cyclic response of cold-formed hollow steel bracing members. *Engineering Structures*, 27, 977-989.
- [3] Landolfo R., Fiorino L., Corte G. D., 2006. Seismic behavior of sheathed cold-formed structures: numerical study. *Journal of Structural Engineering*, 132, 558-569.
- [4] Pourabdollah O., Farahbod F., Rofooei F. R., 2017. The seismic performance of K-braced cold-formed steel shear panels with improved connections. *Journal of Constructional Steel Research*, 135, 56-68.
- [5] Qian J. R., Song X. L., Feng B.C., et al., 2013. Experimental study and finite element analysis of seismic behavior of sprayed concrete sandwich shear walls. *Journal of Building Structures*, 34, 12-23. (in Chinese)
- [6] Hao Y. H., Mu L. H., WANG Y.Q., et al., 2013. Application study on CL building structure system in the construction of affordable housing. *Building Structure*, 43, 40-43. (in Chinese)
- [7] Zhou Q., 2006. The study of LIT composite concrete light-duty house system. Beijing University Of Civil Engineering And Architecture. (in Chinese)
- [8] Jia S, Cao W, Zhang Y., 2017. Damage index calibration of frame-supported concealed multi-ribbed wall panels with energy-efficient blocks. *Applied Sciences*, 7,453.
- [9] Mochizuki S., Kobayashi T., 1996. Experiment on slip strength of horizontal joint of precast concrete multi-story shear walls. *Journal of Structural & Construction Engineering*, 61, 63-73.
- [10] Chen J. S., Guo Z.X., 2012. Seismic Performance Study on Space Model of the New Precast Concrete Shear Wall Structure. *Construction Technology*, 41,87-89. (in Chinese)
- [11] Liu C.W., Cao W.L, Dong H.Y., et al., 2017. Test on seismic behavior of semi-assembled low-rise recycled concrete shear walls. *Journal of Harbin Institute of Technology*, 49,35-39. (in Chinese)
- [12] China Standards Publication, GB50011-2010, 2010. Code for seismic of design buildings; Standard Press of China: Beijing: China (in Chinese)
- [13] Cai J., Sun G., 2008. Constitutive relationship of concrete core confined by square steel tube. *Journal of South China University of Technology*, 36, 105-109.
- [14] Mander J. B., Priestley M. J. N., Park R, 1988 . Theoretical stress-strain model for confined concrete. *Journal of Structural Engineering*, 114,1804-1826.
- [15] Wang X., Li G., Shen Q.Z, 2005. Finite element analysis of the fly ash block walls strengthened by glass fiber reinforced plastics. *Industrial Construction*, 35, 96-98.

PARAMETRIC MODELLING FOR HBIM: DESIGN OF WINDOW LIBRARY FOR RURAL BUILDING

Zdeněk Poloprutský

CTU in Prague, Faculty of Civil Engineering, Department of Geomatics, Prague,
Thákurova 7/2077 166 29 Prague 6 Dejvice, Czech Republic;
zdenek.poloprutsky@fsv.cvut.cz

ABSTRACT

This article deals with parametric modelling of three types of windows from the 19th and 20th century. All three types of windows are fitted in the same set of buildings – a coaching inn. The article describes the design and creation process of library for Historic Building Information Modelling (HBIM). The design and development of the window-library are based on the analyses of available metric survey documentation - photo documentation, point cloud, drawings of ground plan. The characteristics of the final Building Information Model (BIModel) are derived from the nature of the case study, respectively type of historical building, Level of Details (LoD) of surveys, purpose of modelling and required Level of Development (LOD). Based on these specifications, it is possible to realize three different types of BIModel - simplified, detailed and shape-faithful. The aim of this modelling was to design a library usable for detailed BIModel.

KEYWORDS

19th and 20th century, Cultural heritage, Historic Building Information Modelling (HBIM), Metric survey documentation, Parametric modelling, Rural architecture

INTRODUCTION

The concept of Building Information Modelling (BIM) began to develop in the 1970s. In current sense of BIM, the term “*Building Model*” first appeared in scholarly articles in late 1980s. The term “*Building Information Model*” first appeared in a scholarly article in 1992, see [1]. However, the terms “*Building Model*” and “*Building Information Model*”, including BIM abbreviations, have been widely used since 2002. Currently, Building Information Modelling (BIM) can be defined as “*a set of technologies, processes and policies enabling multiple stakeholders to collaboratively design, construct and operate a Facility in virtual space. As a term, BIM has grown tremendously over the years and is now the 'current expression of digital innovation' across the construction industry*” [2]. Building Information Modelling thus allows building the Building Information Model (BIModel), which is the object-based, data-rich, 3D digital model generated by using a BIM Software Tool [2]. BIModel can represent two basic types of buildings:

1. New – BIModel is a part of the project of construction, especially in the field of AEC industry.
2. Existing – BIModel is created on the basis of metric survey documentation and surveys of buildings of interest, especially in the field of cultural heritage term HBIM is used.

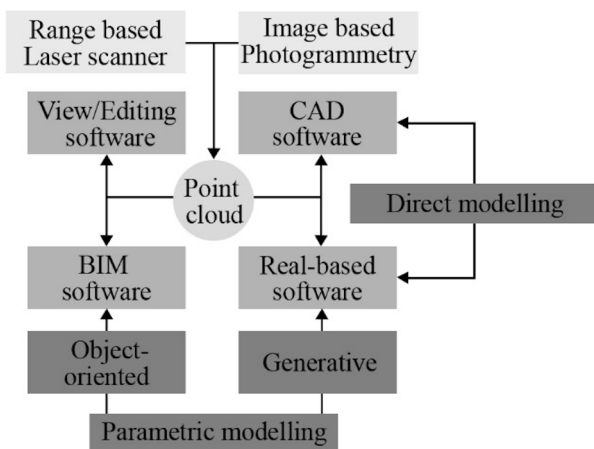


Fig. 1 –Point cloud management workflow: from dense survey data to various processing of 3D modelling [3]

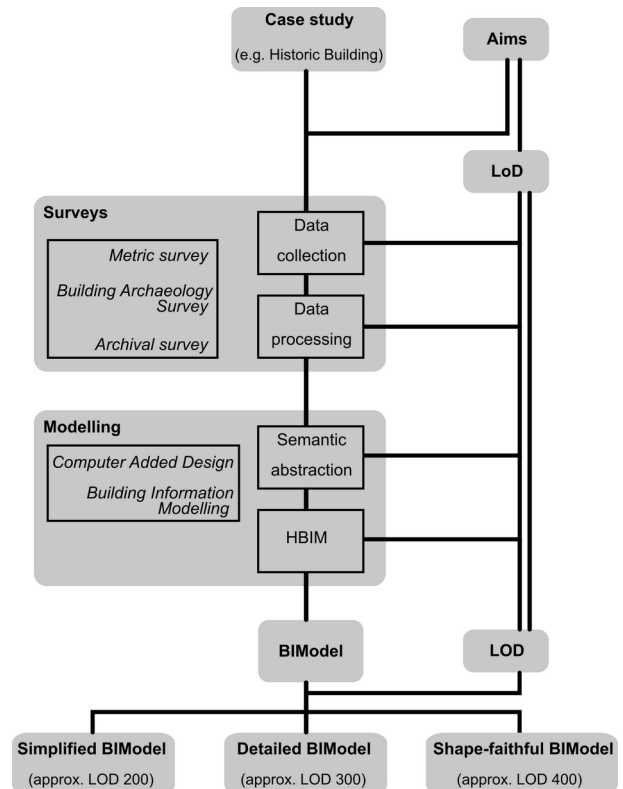


Fig. 2 – Proposed HBIM framework for architectural heritage, according to [4–6]

The concept of HBIM, i.e. Historic Building Information Modelling, was born in Dublin Institute of Technology [7–9]. Currently, this concept is being developed at various scientific workplaces in the world. In the context of HBIM, it is quite common to find the phrase “From point cloud to HBIM” [3, 4, 10] and the term *parametric modeling* [3, 4, 8] in the literature. Their relationship is illustrated in Figure 1.

HBIM-based workflows and methodologies are undergoing gradual development. In recent years, several professional publications have been published dealing with the use of BIM in the field of cultural heritage management, e.g. [3–6, 10–12], etc. The summary and synthesis of these aims are illustrated in Figure 2.

Currently, surveying technologies are popular for data collection if allow to create spatial point clouds. Therefore, terrestrial laser scanning (TLS) or close range photogrammetry, using Image Based Modelling and Rendering (IBMR) technology, are often used for detailed metric surveys, e.g. [3–6, 10–12]. On-site, detailed surveys should be complemented by observations of GNSS and total stations [10].

Building Archaeology Survey examines building objects and their structural elements, their mutual position and orientation in space, their development during the existence of the object and collects further descriptive information about the object, e.g. about used materials, technical condition of structures etc. [13]

A detailed analysis of modelling techniques used in the field of cultural heritage is described in [3]. It seems the best to use parametric object-oriented modelling to exploit the potential of HBIM. This technique is based on the use of pre-designed libraries of basic architectural and structural elements, so-called “smart objects” [6]. Whereas the BIM approach is made to design new buildings, its application to architectural cultural heritage is complicated. Most often, it is the

absence of relevant libraries. In recent years, several professional publications have been published dealing with the creation of libraries for HBIM. They describe several possible approaches:

1. Analyses of archival sources
2. Analyses of metric survey documentation
3. Combination of archival sources and metric survey documentation

The first approach involves outputs based on the analyses of historical literature that is well known or found in archival research. Subsequently, literary sources, most often architectural samplers, serve as a basis for the design and creation of libraries of parametric objects [8, 14].

The second approach involves outputs based on analyses of metric survey documentation – drawings, point clouds, orthophoto, etc. This approach creates ad-hoc architectural samplers. Subsequently, these serve as a basis for designing and building parametric object libraries. In recent years, several specialized publications have been published describing library modelling for vaulting systems [4–6, 15–18] – irregular walls, vaults, atriums, columns and pillars; a particular type of architectural element – Falconatura [3], Roshan [12, 19], portals from the Etnean region [20]; architectural style [12, 21, 22] etc.

The third approach combines the two previous ones, i.e. libraries are created in both approaches that complement each other [11].

In the context of metric survey documentation, several terms are needed that relate to the definition of detail – *Level of Detail (LoD)*, *Level of Development (LOD)* and *reference scale*. *Level of Detail* is a parameter that gives geometric detail and accuracy according to the current CityGML standard [23]. *Level of Development* is a parameter typically used in connection with BIM. The LOD is described not only in terms of detail of geometry, but also in terms of detail, accuracy and scope of information about individual objects [24]. Both parameters are primarily intended for applications in current construction, which works mostly with regular geometric shapes, therefore they are not entirely suitable for models of historical buildings. A historical building consists of a complex of structural elements, mostly of irregular shape, e.g. statues and elevated structures, which have to be modelled too. Therefore, it is necessary to appropriately adapt the application of LOD to models of historical buildings, for examples see [5, 25]. For metric drawings, a reference scale of 1 : 50 is used by default [3, 26, 27].

The characteristics of BIModel are derived from the nature of the case study, respectively type of historical building, details of surveys, i.e. LoD, purpose of modelling and required LOD, see Figure 2. Following these specifications, according to [24, 27], three different types of BIModel [5] can be implemented:

1. *Simplified BIModel*, approx. LOD 200 – simplified building model with low geometric detail and minimal information.
2. *Detailed BIModel*, approx. LOD 300 – detailed building model where the quantity, size, shape, location and orientation of the designed element can be measured directly from BIModel; modelling is done by creating parametrized and simplified families to obtain the model.
3. *Shape-faithful BIModel*, approx. LOD 400 – elements are modelled with sufficient detail and precision to produce the represented component, their quantity, size, shape, location and orientation can be measured directly from BIModel. BIModel copies as much as possible the geometric irregularities of the building and is enriched with the maximum amount of information.

This article describes the process of parametric modelling of three types of windows from the 19th and 20th century. All three types of windows are fitted in the same set of buildings – a coaching inn in Kostelec nad Vltavou (Písek District, Czech Republic). This building has been the subject of Artistic and Historical Research over the past few years [28]. The article describes the process of creating a library for HBIM, which is based on the analysis of available metric survey documentation. The aim of the modelling was to design a library usable for a detailed BIModel.

METHODS

In relation to Figure 1 and [6], the HBIM library creation process can be divided into several stages:

1. Data collection
 - a. Terrestrial laser scanning
 - b. Close range photogrammetry
 - c. Detailed survey
2. Data processing
 - a. Registration and georeferencing of point clouds
 - b. Filtration and decimation of point clouds
 - c. Elaboration of drawings – edge identification
3. Semantic abstraction
 - a. Typological identification of building structures in metric survey documentation
 - b. Selection and classification of building structures in metric survey documentation
 - c. Abstraction of building components
4. Historic Building Information Modelling (HBIM)
 - a. Geometric modelling – main BIModel and HBIM libraries
 - b. Data enrichment of IFC metadata – main BIModel and HBIM libraries
 - c. Application of smart objects into main BIModel

Surveys – data collection and data processing

Metric survey, i.e. data collection and subsequent data processing, was carried out in the form and scope according to [28]. The final outputs of the metric survey documentation, that are used for creation of the HBIM library, are:

- Photo documentation, see Figure 3 – Figure 5
- Point cloud, see Figure 6 – Figure 8
- Drawings of ground plan at the reference scale of 1 : 50, see Figure 9 – Figure 11



Fig. 3 – Example of the first window type - section from the photo



Fig. 4 – Example of the second window type - section from the photo



Fig. 5 – Example of the third window type - section from the photo



Fig. 6 – Example of the first window type - section from the point cloud



Fig. 7 – Example of the second window type - section from point cloud



Fig. 8 – Example of third window type - section from point cloud

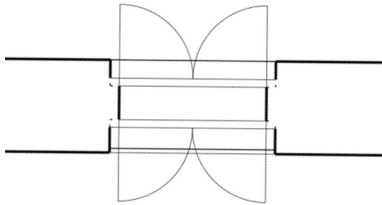


Fig. 9 – Example of the first window type - section from ground plan

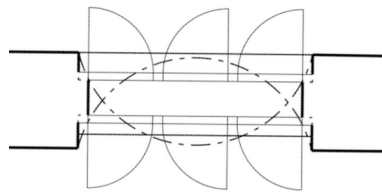


Fig. 10 – Example of the second window type - section from ground plan

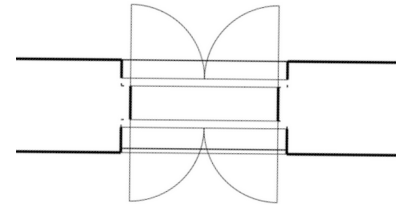


Fig. 11 – Example of third window type - section from ground plan

Modelling – Semantic abstraction and HBIM

Based on the analysis of existing metric survey documentation, it is possible to identify, select and typify building structures that are represented in the mass of a historical building. For HBIM, it is advantageous that the metric survey documentation enables the implementation of a digital 3D reconstruction of the building construction. Furthermore, it is advantageous that is possible to extend the created 3D model with additional descriptive information based on other surveys. Typologies of historical building structures can be divided as follows [29]:

- | | |
|-------------------------|---|
| 1. Masonry | 9. Roof trusses |
| 2. Wooden walls | 10. Roofing |
| 3. Clay and cardboard | 11. Heating |
| 4. Ceilings | 12. Ventilation, water regime and waste |
| 5. Vaults | 13. Doors and gates |
| 6. Floors and paving | 14. Windows |
| 7. Stairs | 15. Surface treatment |
| 8. Railings and grilles | |

Autodesk Revit software [30] was used for HBIM. According to the terminology of this software, these structures can be divided into families of the same name. Different elements belonging to a family, called components, may have different values for some or all of the parameters, but their names and meanings are the same. Revit software uses two types of parameters:

1. *Type* – it defines parameters that are common to components of the given type. For example, you can change the "Height" parameter for all components in the window family.
2. *Instance* – it defines the component-specific parameters. For example, you can change the "Height of sill" parameter for every component in a window family.

The parameterization of architectural and structural elements must also be a part of HBIM. Unlike BIM, freely available libraries of building components are not commonplace. Therefore, they usually need to be modelled according to the available background and the purpose they are intended to serve. During parameterization and subsequent modelling of this library, it was found that the parameters can be divided into several basic groups:

1. *Basic parameters* – Length, Width, Height – form the basic dimensions, so-called "bounding box", of a parametric object. For nested objects, typically doors and windows, some of the parameters can be labelled like Depth.
2. *Location parameters* – facilitate placement in BIModel. For example, for nested objects, it is useful to define the offset from the face of wall (horizontal plane) and floor (vertical plane).

3. *Architectural parameters* – define the architectural morphology of a parametric object. These are sets of architectural rules and shape grammars [6, 8, 9, 11, 15, 25] that characterize a modelled building element.
4. *Additional parameters* – extend the variability of a parametric object, e.g. in the fields of graphic representation, material composition and surface finishes, descriptive information, etc.

To ensure the interoperability between parameters of a component, such as dimensions, graphic representation or material composition, it is necessary to design logical links with its components. Revit software allows importing existing components in the design of new components. To ensure interoperability between sub-elements within a component, the new component must take over the parameters of the imported component. The interoperability of components is affected by the choice of types of parameters – *type* or *instance*. Very often, it is advantageous to define *localization parameters* and *extended parameters* as *instances*. The localization of individual components can be variable in BIModel. In the case of composite components, that contain imported components, the material compositions and surface finishes of the sub-components may vary, for example, for double windows - exterior vs. window colors, types and treatment of glass panes etc. The design and subsequent testing of component interoperability is an iterative process that can be time consuming in some cases.

RESULTS

The final results of parametric library modelling and examples of their application in BIModel are presented in Figure 12 – Figure 17. An example of parametric object variability is presented in Figure 18.

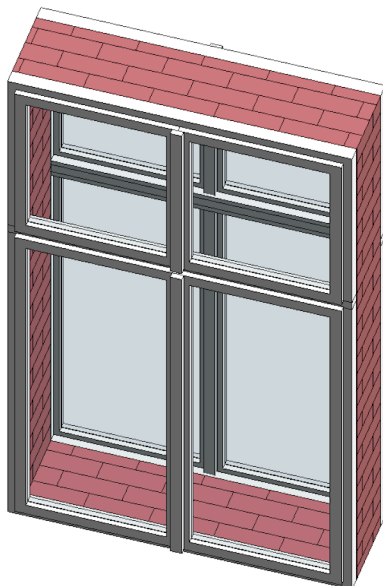


Fig. 12 – Example of the component of the first window type

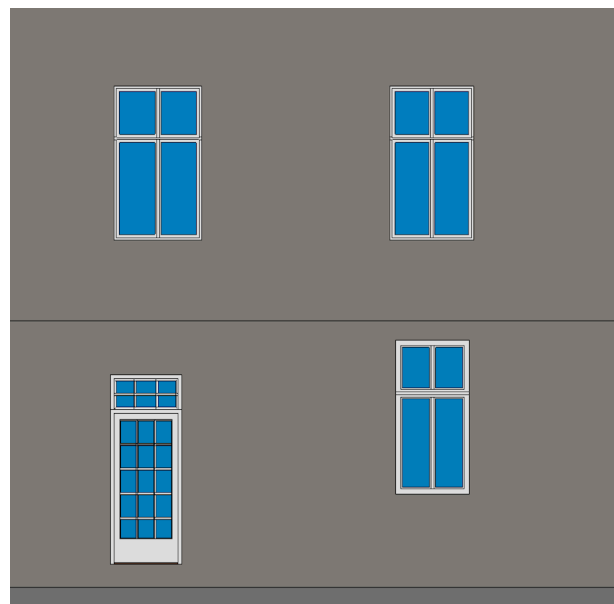


Fig. 13 – Example of the use of the first window type in BIModel – the location of the perimeter wall



Fig. 14 – Example of the component of the second window type

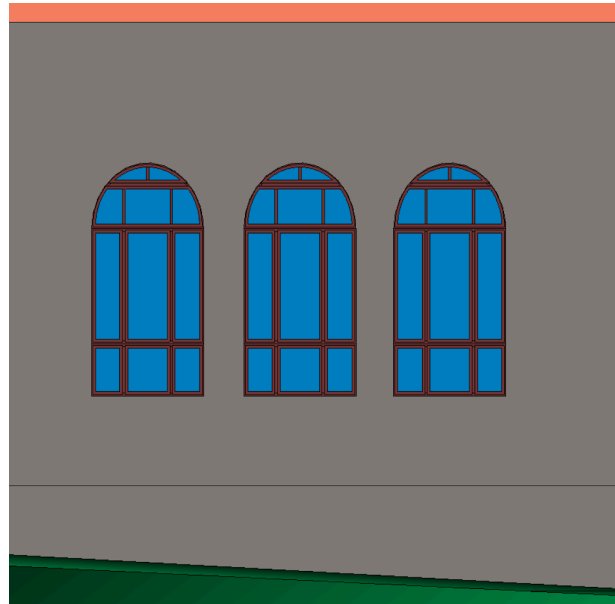


Fig. 15 – Example of the use of the second window type in BIModel – the location of the perimeter wall

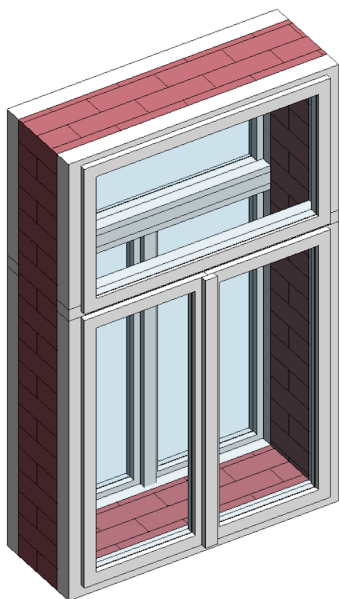


Fig. 16 – Example of the component of the third window type

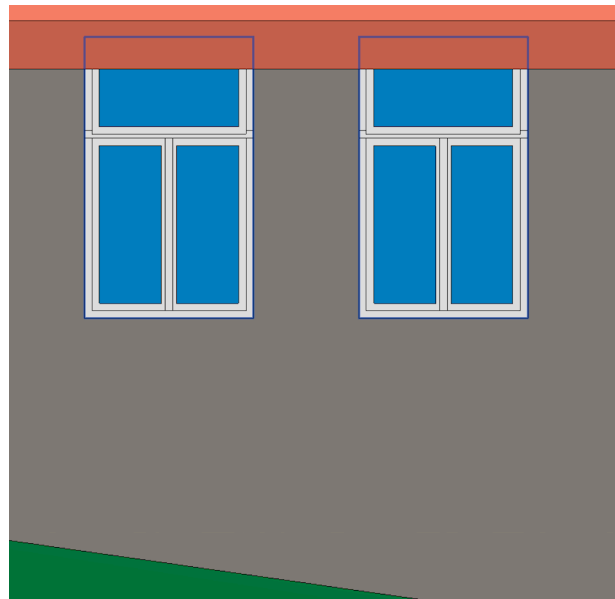


Fig. 17 – Example of the use of the third window type in BIModel – the location of the perimeter wall

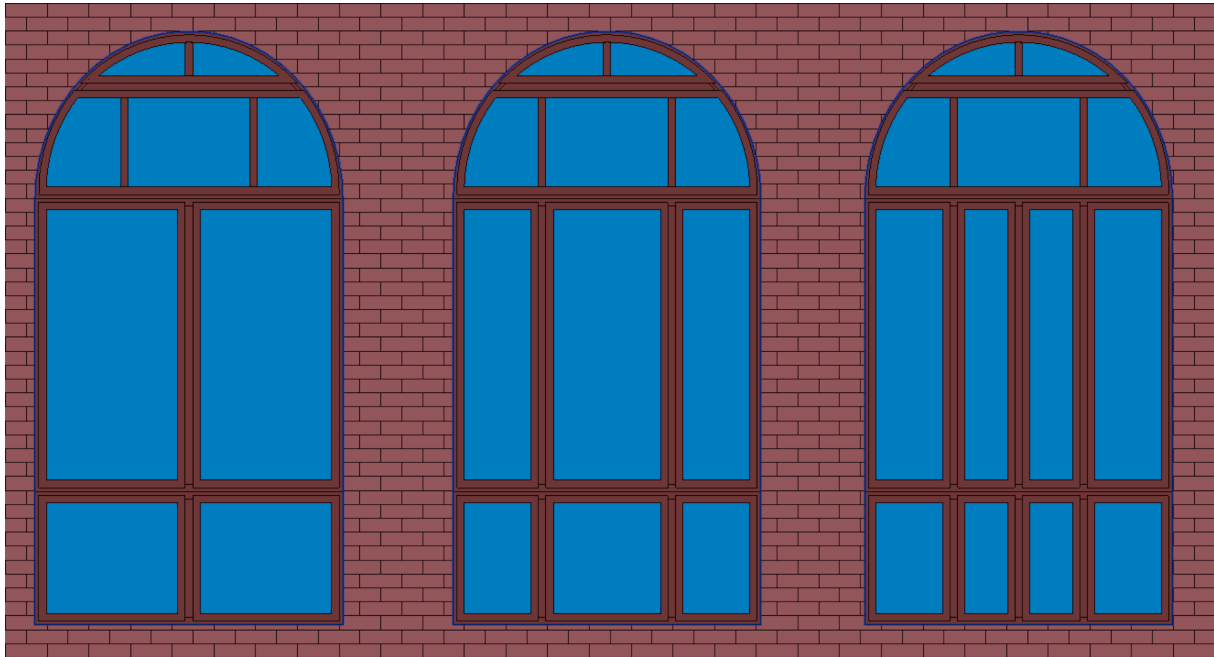


Fig. 18 – Example of the variability of component of the second window type – count of centre columns

CONCLUSION

This article deals with parametric modelling of three types of windows from the 19th and 20th century. All three types of windows are fitted in the same set of buildings – a coaching inn. This building has been the subject of Artistic and Historical Research over the past few years [28].

The article describes design and creation of library for HBIM. These processes were preceded by the study of the current state-of-art in this field. The results of the literature review are presented in the Introduction. Furthermore, the design and creation of the window library are based on the analysis of available metric survey documentation, which consists of photo documentation, point cloud, ground plan drawing, see Figure 3 – Figure 11. Based on the analysis of existing metric survey documentation, three types of window constructions were identified, selected and typified, which are represented in the historical building. These constructions were parameterized to sub-structural elements, from which new components were subsequently modelled, see Figure 12 – Figure 18. Generally, the characteristics of the final BIModel are derived from the nature of the case study, respectively historical building type, Level of Details of surveys, modelling purpose and required LOD, see Figure 2. The result of this modelling is the component library usable for a detailed BIModel.

ACKNOWLEDGEMENTS

This work was supported by the Ministry of Culture of the Czech Republic from the Program for the Support of Applied Research and Development of National and Cultural Identity for the years 2016 to 2022 (NAKI II), grant project "The Transformation of Rural Architecture with Emphasis on the Development of the 19th and 20th Centuries", No. DG16P02H023. For more information about this project, visit the project website <http://venkov.fsv.cvut.cz/projekt>.

REFERENCES

- [1] VAN NEDERVEEN, G.A. a F.P. TOLMAN. Modelling multiple views on buildings. *Automation in Construction* [online]. 1992, 1(3), 215–224. ISSN 09265805. DOI:10.1016/0926-5805(92)90014-B
- [2] BIME INITIATIVE. *BIM Dictionary* [online]. 2019 [2019-10-14]. URL: <https://bimdictionary.com/>
- [3] TOMMASI, C., C. ACHILLE a F. FASSI. FROM POINT CLOUD TO BIM: A MODELLING CHALLENGE IN THE CULTURAL HERITAGE FIELD. *ISPRS - International Archives of the Photogrammetry, Remote Sensing and Spatial Information Sciences* [online]. 2016, **XLI-B5**, 429–436. ISSN 2194-9034. DOI:10.5194/isprs-archives-XLI-B5-429-2016
- [4] CHIABRANDO, F., G. SAMMARTANO a A. SPANÒ. HISTORICAL BUILDINGS MODELS AND THEIR HANDLING VIA 3D SURVEY: FROM POINTS CLOUDS TO USER-ORIENTED HBIM. *ISPRS - International Archives of the Photogrammetry, Remote Sensing and Spatial Information Sciences* [online]. 2016, **XLI-B5**, 633–640. ISSN 2194-9034. DOI:10.5194/isprs-archives-XLI-B5-633-2016
- [5] BRUSAPORCI, S., P. MAIEZZA a A. TATA. A FRAMEWORK FOR ARCHITECTURAL HERITAGE HBIM SEMANTIZATION AND DEVELOPMENT. *ISPRS - International Archives of the Photogrammetry, Remote Sensing and Spatial Information Sciences* [online]. 2018, **XLII-2**, 179–184. ISSN 2194-9034. DOI:10.5194/isprs-archives-XLII-2-179-2018
- [6] GARAGNANI, Simone. Building Information Modeling and real world knowledge: A methodological approach to accurate semantic documentation for the built environment. In: *2013 Digital Heritage International Congress (Digital Heritage): 2013 Digital Heritage International Congress (Digital Heritage)* [online]. Marseille, France: IEEE, 2013, 489–496. ISBN 978-1-4799-3170-5. DOI:10.1109/DigitalHeritage.2013.6743788
- [7] MURPHY, Maurice, Eugene MCGOVERN a Sara PAVIA. Historic building information modelling (HBIM). *Structural Survey* [online]. 2009, **27(4)**, 311–327. ISSN 0263-080X. DOI:10.1108/02630800910985108
- [8] MURPHY, Maurice, Eugene MCGOVERN a Sara PAVIA. Historic Building Information Modelling – Adding intelligence to laser and image based surveys of European classical architecture. *ISPRS Journal of Photogrammetry and Remote Sensing* [online]. 2013, **76**, 89–102. ISSN 09242716. DOI:10.1016/j.isprsjprs.2012.11.006
- [9] MURPHY, M., A. CORNS, J. CAHILL, K. ELIASHVILI, A. CHENAU, C. PYBUS, R. SHAW, G. DEVLIN, A. DEEVY a L. TRUONG-HONG. DEVELOPING HISTORIC BUILDING INFORMATION MODELLING GUIDELINES AND PROCEDURES FOR ARCHITECTURAL HERITAGE IN IRELAND. *ISPRS - International Archives of the Photogrammetry, Remote Sensing and Spatial Information Sciences* [online]. 2017, **XLII-2/W5**, 539–546. ISSN 2194-9034. DOI:10.5194/isprs-archives-XLII-2-W5-539-2017
- [10] BAIK, A. FROM POINT CLOUD TO EXISTING BIM FOR MODELLING AND SIMULATION PURPOSES. *ISPRS - International Archives of the Photogrammetry, Remote Sensing and Spatial Information Sciences* [online]. 2019, **XLII-5/W2**, 15–19. ISSN 2194-9034. DOI:10.5194/isprs-archives-XLII-5-W2-15-2019
- [11] DORE, C., M. MURPHY, S. MCCARTHY, F. BRECHIN, C. CASIDY a E. DIRIX. Structural Simulations and Conservation Analysis - Historic Building Information Model (HBIM). *ISPRS - International Archives of the Photogrammetry, Remote Sensing and Spatial Information Sciences* [online]. 2015, **XL-5/W4**, 351–357. ISSN 2194-9034. DOI:10.5194/isprsarchives-XL-5-W4-351-2015
- [12] BAIK, A. a J. BOEHM. HIJAZI ARCHITECTURAL OBJECT LIBRARY (HAOL). *ISPRS - International Archives of the Photogrammetry, Remote Sensing and Spatial Information Sciences* [online]. 2017, **XLII-2/W3**, 55–62. ISSN 2194-9034. DOI:10.5194/isprs-archives-XLII-2-W3-55-2017
- [13] BERÁNEK, Jan a Petr MACEK, ed. *Building Archaeology Survey: A Methodology*. Prague: National Heritage Institute, 2015. ISBN 978-80-7480-037-5.
- [14] PRIZEMAN, Oriël Elizabeth Clare. HBIM and matching techniques: considerations for late nineteenth- and early twentieth-century buildings. *Journal of Architectural Conservation* [online]. 2015, **21(3)**, 145–159. ISSN 1355-6207, 2326-6384. DOI:10.1080/13556207.2016.1139852
- [15] ORENI, D., R. BRUMANA, A. GEORGOPOULOS a B. CUCA. HBIM FOR CONSERVATION AND MANAGEMENT OF BUILT HERITAGE: TOWARDS A LIBRARY OF VAULTS AND WOODEN BEAN FLOORS. *ISPRS Annals of Photogrammetry, Remote Sensing and Spatial Information Sciences* [online]. 2013, **II-5/W1**, 215–221. ISSN 2194-9050. DOI:10.5194/isprsannals-II-5-W1-215-2013
- [16] JOSÉ LÓPEZ, Facundo, Pedro MARTIN LERONES, José LLAMAS, Jaime GÓMEZ-GARCÍA-BERMEJO a Eduardo ZALAMA. Semi-automatic generation of bim models for cultural heritage.

- International Journal of Heritage Architecture: Studies, Repairs and Maintenance* [online]. 2017, 2(2), 293–302. ISSN 2058-833X, 2058-8321. DOI:10.2495/HA-V2-N2-293-302
- [17] BRUMANA, Raffaella, Paola CONDOLEO, Alberto GRIMOLDI, Fabrizio BANFI, Angelo Giuseppe LANDI a Mattia PREVITALI. HR LOD based HBIM to detect influences on geometry and shape by stereotomic construction techniques of brick vaults. *Applied Geomatics* [online]. 2018, 10(4), 529–543. ISSN 1866-9298, 1866-928X. DOI:10.1007/s12518-018-0209-3
- [18] STÖBER, Dina, Roko ŽARNIĆ, Davorin PENAVA, Margareta TURKALJ PODMANICKI a Romana VIRGEJ-ĐURAŠEVIĆ. Application of HBIM as a Research Tool for Historical Building Assessment. *Civil Engineering Journal* [online]. 2018, 4(7), 1565. ISSN 2476-3055. DOI: doi:10.28991/cej-0309195
- [19] BAIK, A., A. ALITANY, J. BOEHM a S. ROBSON. Jeddah Historical Building Information Modelling „JHBIM” - Object Library. *ISPRS Annals of Photogrammetry, Remote Sensing and Spatial Information Sciences* [online]. 2014, II-5, 41–47. ISSN 2194-9050. DOI:10.5194/isprsannals-II-5-41-2014
- [20] SANTAGATI, C., M. LO TURCO a G. D'AGOSTINO. POPULATING A LIBRARY OF REUSABLE H-BOMS: ASSESSMENT OF A FEASIBLE IMAGE BASED MODELING WORKFLOW. *ISPRS - International Archives of the Photogrammetry, Remote Sensing and Spatial Information Sciences* [online]. 2017, XLII-2/W5, 627–634. ISSN 2194-9034. DOI:10.5194/isprs-archives-XLII-2-W5-627-2017
- [21] LU, Y. C., T. Y. SHIH a Y. N. YEN. RESEARCH ON HISTORIC BIM OF BUILT HERITAGE IN TAIWAN - A CASE STUDY OF HUANGXI ACADEMY. *ISPRS - International Archives of the Photogrammetry, Remote Sensing and Spatial Information Sciences* [online]. 2018, XLII-2, 615–622. ISSN 2194-9034. DOI:10.5194/isprs-archives-XLII-2-615-2018
- [22] SOONWALD, E. S., A. E. WOJNAROWSKI, S. G. TIKHONOV, O. V. ARTEMEVA a S. V. TYURIN. BUILDING INFORMATION MODELING APPLIED TO THE INDUSTRIAL ARCHITECTURAL MONUMENTS CASE STUDY OF SAINT PETERSBURG. *ISPRS - International Archives of the Photogrammetry, Remote Sensing and Spatial Information Sciences* [online]. 2019, XLII-5/W2, 59–63. ISSN 2194-9034. DOI:10.5194/isprs-archives-XLII-5-W2-59-2019
- [23] GRÖGER, Gerhard, Thomas H. KOLBE, Claus NAGEL a Karl-Heinz HÄFELE, ed. *OGC City Geography Markup Language (CityGML) Encoding Standard* [online]. 2012 [2019-10-18]. URL: <http://www.opengis.net/spec/citygml/2.0>
- [24] BIM FORUM. *Level of Development (LoD) Specification Part I & Commentary: For Building Information Models and Data* [online]. 2019 [2019-10-18]. URL: www.bimforum.org/loD
- [25] YANG, X., M. KOEHL, P. GRUSSENMEYER a H. MACHER. COMPLEMENTARITY OF HISTORIC BUILDING INFORMATION MODELLING AND GEOGRAPHIC INFORMATION SYSTEMS. *ISPRS - International Archives of the Photogrammetry, Remote Sensing and Spatial Information Sciences* [online]. 2016, XLI-B5, 437–443. ISSN 2194-9034. DOI:10.5194/isprs-archives-XLI-B5-437-2016
- [26] CHIABRANDO, F., M. LO TURCO a F. RINAUDO. MODELING THE DECAY IN AN HBIM STARTING FROM 3D POINT CLOUDS. A FOLLOWED APPROACH FOR CULTURAL HERITAGE KNOWLEDGE. *ISPRS - International Archives of the Photogrammetry, Remote Sensing and Spatial Information Sciences* [online]. 2017, XLII-2/W5, 605–612. ISSN 2194-9034. DOI:10.5194/isprs-archives-XLII-2-W5-605-2017
- [27] VESELÝ, Jan. *Metric survey documentation of historic buildings for use in heritage management*. Prague: National Heritage Institute, 2014. ISBN 978-80-86516-79-0.
- [28] POLOPRUTSKÝ, Zdeněk. METRIC SURVEY DOCUMENTATION AS A BASIS FOR UNDERSTANDING THE DEVELOPMENT OF RURAL ARCHITECTURE. *Stavební obzor - The Civil Engineering Journal* [online]. 2018, 27(1), 48–59. ISSN 1805-2576. DOI:10.14311/CEJ.2018.01.0005
- [29] ŠKABRADA, Jiří. *Konstrukce historických staveb*. Praha: Argo, 2003. ISBN 978-80-7203-548-7.
- [30] AUTODESK. *Autodesk Knowledge Network* [online]. 2019 [2019-10-14]. URL: <https://knowledge.autodesk.com/>

A COMPARISON OF THE EFFECTIVENESS OF GROUTING METHODS, PENETRATION AND SURFACE APPLICATION OF GELS IN INCREASING THE STRENGTH OF HISTORIC MASONRY

Tomáš Čejka, Jiří Karas and Jan Kubát

CTU in Prague, Faculty of Civil Engineering, Department of Building Structures, Prague, Thákurova 7, Czech Republic; cejka@fsv.cvut.cz, jan.kubat.2@fsv.cvut.cz

ABSTRACT

This article focuses on the verification of the effect of selected grouting agents on historic brick masonry with different degrees of weathering using different techniques of grouting application. The effectiveness of grouting was verified by changes in the masonry strength. Experimental research also verified the effectiveness of the penetration of grouting agents as bonding primers on the surface of selected materials often found in historic buildings.

KEYWORDS

Masonry, Grouting, Brick, Mortar, Experimental research

INTRODUCTION

The grouting of historic masonry with degraded binders is a method frequently applied in the rehabilitation of historic masonry. Historic masonry is most often treated with grouting agents based on minerals, mostly lime or its modifications, or with admixtures. In the case of the requirement for a significant improvement of mechanical characteristics, resin-based substances are used in justified cases.

The experimental and theoretical research into the effect of grouting on the physical and mechanical characteristics of historic masonry carried out within the NAKI II research project (DG16P02M055 project "Research and development of materials, processes and techniques for restoration, preservation and strengthening of historic masonry structures and surfaces and systems for preventive protection of historic and listed buildings threatened by anthropogenic and natural risks") [1] includes the verification of the effect of the grouting method (pressure and pressureless grouting), the type of grouting agent (grouts based on minerals, resins and silicates) on the major physical (pore system) and mechanical (strength, deformation characteristics) properties of masonry [2, 3]. The objective of Phase I and Phase II of the research also covered the investigation of the effect of grouting on degraded masonry.

OBJECTIVE AND SUBJECT OF RESEARCH

The objective of experimental research was to verify the strengthening of degraded masonry or surface and near-surface layers of masonry, with selected grouting agents and techniques.

Selected historic brick masonry with a lime binder, or a lime binder with a 2.5% admixture of cement, was the subject of monitoring the strengthening effect of grouting on historic masonry for different types of grouts and different grouting techniques. The application of different types of

mortar in the brick masonry allowed the verification of the effect of brick masonry strengthening by grouting in relation to the degradation rate of the masonry, primarily mortar.

METHODOLOGY OF EXPERIMENTAL VERIFICATION

Experimental research into the verification of the effect of grouting agents and techniques was conducted on brick masonry segments made up of solid burnt bricks on different types of lime mortar, or lime mortar with a 2.5% admixture of cement. Individual types of mortar differed in the amounts of binder and filler – ratios of 1:3, 1:5 and 1:7 were used. In this way, the degradation of the binder – masonry was simulated.

The subject of the research focusing on the verification of the effectiveness of grouting on the major mechanical characteristics was to identify the strength (load-bearing capacity) of masonry test pieces treated by pressure and pressureless grouting. The results were analysed on a limited number of masonry test pieces, which did not allow statistical evaluation. With a view to this fact and considering the dispersion of the physical and mechanical properties of the masonry, the results of the analysis must be interpreted with sensitivity.

The brick pillars for the experimental research were made up of CP 20 bricks on lime mortar with the binder: filler ratio of 1:3 or 1:5. The binder was five-year-old aged slaked lime, and the filler sand with a grains size of 0-4 mm. A part of the pillars with the above types of mortar was fitted with artificially made voids in the bed joints. Another part of the experimental pieces were brick pillars from CP20 bricks on lime mortar with a 5% admixture of MV 1 cement mixed in a 1:1 ratio with sand 0-2 mm with a resulting strength corresponding to the 1:7 ratio. The walling was executed under stabilized conditions of a testing laboratory – with the air temperature ranging from 15 to 20°C, and the relative humidity of ca. 30 to 40%.

The grouting agents selected for the experimental research were based on lime (V1, V3), on a mixture of hydraulic lime and lime nanoparticles (V5), on silicates (K1, for the penetration test) and on epoxy resin (P2). The V5 grouting agent based on hydraulic lime and lime nanoparticles had been developed within the NAKI II DG16P02M055 research project, in which the research workplace cooperated with the Centre of Polymer Systems (Tomas Bata University in Zlín).

The characteristics of masonry units, mortar and grouting agents are presented in Table 1.

The dimensions of the brick masonry test pieces were 300 x 450 x 420 to 450 mm, or 300 x 600 x 420 to 450 mm. After walling, the pillars were left for 28 days to mature, and, afterwards, grout holes Ø18 mm, at an angle of inclination of 30° were made in all pillars ca. 90 mm below the pillar upper edge, terminated ca. 50 mm from the opposite masonry face. The next step was the mounting of grout packers and low-pressure (3 to 10 bars using a low-pressure screw pump for suspension grouting) or pressureless (hydrostatic pressure) grouting. After grouting, the grout holes were filled with a low-shrinkage mix (Oxal VP TK2). The length of the technological break depended on the grouting agent used – for grouting agents based on minerals or organosilicates, the technological break necessary for hardening was 28 days, and for epoxy-based substances from several hours to several (three) days. Individual sets of test pieces contained a so-called reference pillar, in which all preparatory phases had been performed identically to the grouted pillars. The tests of the grouted pillars and the reference pillar were carried out ca. 3 to 4 weeks after the grouting and filling in the grout holes (Figure 1).

Tab. 1 - Characteristics of masonry units, mortar, grouting agents – compressive and tensile strength

Label	Mortar - ratio	Mortar – $f_{compr,m}/f_{tension,m}$	Brick - $f_{compr,b}$	Grouting mixture	Grouting mixture – $f_{compr}/f_{tension}$
	-	MPa	MPa	-	MPa
CP01-1:7-P2	1:7	0,50/0,21	22,01	P2	64,6/43,3
CP02-1:7-P2	1:7				
CP03-1:3-P2	1:3	1,03/0,59	22,23		
CP04-1:3-P2	1:3				
CP05-1:5-P2	1:5	0,67/0,28	21,11		
CP06-1:3-V5	1:3	0,96/0,59	22,23	V5	0,88/0,53
CP07-1:3-V5	1:3				
CP08-1:5-V5	1:5	0,67/0,25	21,11		
CP09-1:5-V5	1:5				
CP10-1:7-V3	1:7	0,50/0,21	22,01	V3	1,26/0,11
CP11-1:7-V3	1:7				
CP12-1:3-V3	1:3	0,96/0,59	22,23		
CP13-1:3-V3	1:3				
CP14-1:5-V3	1:5	0,67/0,25	21,11		
CP15-1:5-V3	1:5				
CP16-1:7-V1	1:7	0,48/0,16	22,01	V1	2,500/-
CP17-1:7-V1	1:7				
CP18-1:3-V1	1:3	1,03/0,59	22,23		
CP19-1:3-V1	1:3				
CP20-1:5-V1	1:5	0,67/0,28	21,11		
CP21-1:5-V1	1:5				

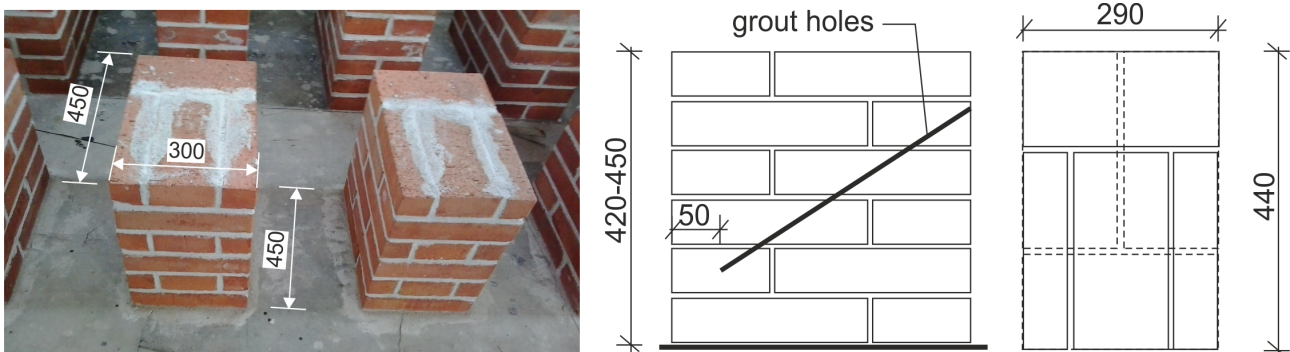


Fig. 1 - Photo and diagram of the test pieces

Considering the attributes of the grouting mixes, the propagation of the grouting agent through the masonry units and the binder was first verified on the brick pillars by pressure and pressureless grouting. Based on the experimentally obtained results and information, the grouting agents to be used as the bonding primer were selected and applied.

The grouting technique was chosen with a view to the attributes of the grouting agents and the brickwork pillars to avoid any damage to the experimental pieces during grouting. The epoxy-based substance was applied by a pressureless technique, while the substances based on lime or a mixture of lime and lime nanoparticles were applied by low-pressure grouting.

Verification of grouting effectiveness

Load tests under concentric compression until failure were performed in an actuator with a digital data logger for reading compression manufactured by the German MFL Company – (range of 0 to 10 000 kN, operational accuracy of ± 0.1 kN). The deformations in the vertical and horizontal directions were measured by LVDT strain gauges (6 pieces). The monotonously rising loading of the pillars under concentric compression was exerted by steps of 50 to 75 kN, i.e. ca. 10 to 15 % of the theoretically identified ultimate loading of pillar masonry under ČSN EN 1996 (EC6).



Fig. 2 - a) Test piece during the load test with mounted strain gauges, b) Test piece after the completed load test

Verification of penetration effectiveness

The penetration abilities of selected grouting agents were verified by the depth of their penetration into selected materials after the application of repeated coatings on the vertical surface (the number of repetitions differed for individual substances due to their characteristics). All grouting agents were applied as the bonding primer, and epoxy-based substances were successively only used for a second coating, while the other grouting agents were applied for another 11 coatings following the bonding primer. The grouting agents were coloured to allow the visual observation of the penetration depth and to avoid changes in the properties of the grouts. The grout coatings were gradually applied on the surface of bricks, sandy marlstone, sandstone and limestone, see Figure 3.

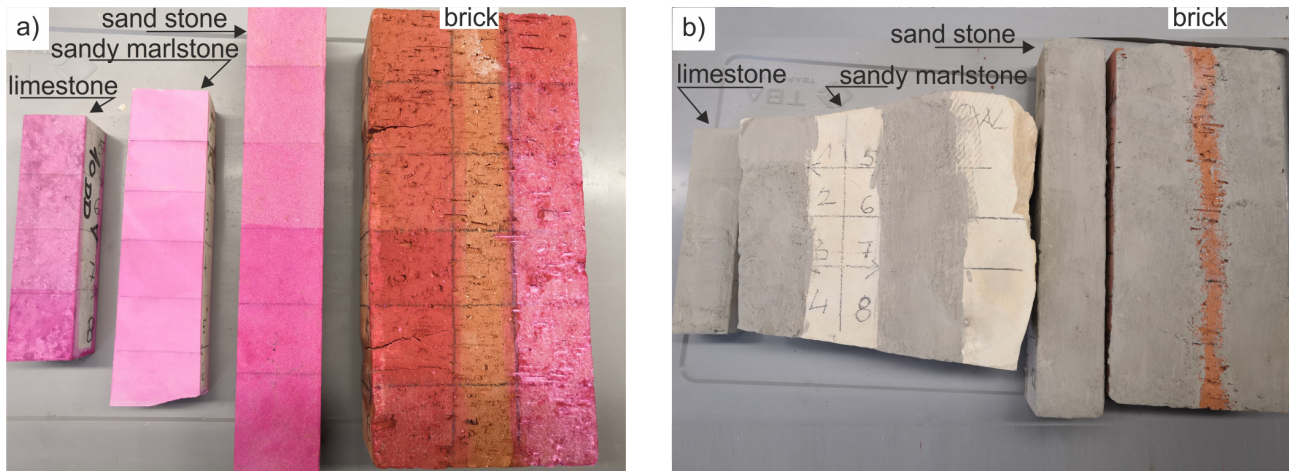


Fig. 3 - Example of test pieces with a bonding primer a) using V5, b) using V3

EVALUATION OF PARTIAL RESULTS OF EXPERIMENTAL VERIFICATION OF METHODS

Evaluation of grouting

The results of the load tests of masonry pillars under concentric compression – strength in concentric compression, the values of experimentally identified vertical and horizontal deformations, modulus of elasticity, or the ratio of vertical and horizontal strain, were processed graphically and in tables for successive analysis for individual sets of test pieces after the grout application. Due to large amounts of obtained data, the sections below present partial results of this analysis aimed at the evaluation of the grouting effectiveness measured by the strength of the grouted masonry in compression, the effect of the grouting technique, the effect of the pore system and the grouting agent's particle size, and potential changes in the pore system of the grouted material as compared to ungrouted material.

Partial results of the experimentally identified parameters of the masonry of test pieces are presented in Table 2.

Based on the comparison of the experimentally identified ultimate strength in concentric compression of brick masonry, including both pillars with voids and reference pillars (mortar 1:3 and 1:5) and pillars without voids with reference pillars (mortar 1:7), we may draw the following conclusions (ungrouted masonry $f_{exp} = 100\%$):

In pressureless grouting applying the P2 epoxy-based agent, the ultimate strength of the pillars in compression $f_{exp,epox} = 217\%$ for the mortar of the pillars with a mixing ratio of 1:3, and 197% for the mortar of the pillars with a mixing ratio of 1:5. The P2 epoxy-based grout applied on the pillars with mortar with a mixing ratio of 1:7 increased strength on average to 116% of the reference pillars.

Note: The ultimate strength of masonry was averaged for the whole pillar area. Due to high strength of the grouted masonry zone, the differences in average strength are small for both types of mortar.

In low-pressure grouting applying the V1 lime-based grouting agent, the ultimate strength of the pillars in compression $f_{exp,epox} = 196\%$ for the mortar of the pillars with a mixing ratio of 1:3, and 165% for the mortar of the pillars with a mixing ratio of 1:5. In low-pressure grouting applying the V1 lime-based grouting agent on the pillars with mortar with a mixing ratio of 1:7, the compressive strength of the masonry ranged from 96 to 107% of the reference pillars.

Tab. 2 - Experimentally identified parameters of test piece masonry

Label	Compressive strength	Modulus of elasticity	Hor. def. δ_x at 50% N_{um}	Vert. def. δ_y at 50% N_{um}	Hor. def. δ_x at 500 kN	Vert. def. δ_y at 500 kN	Ratio ϵ_x / ϵ_y at 50% N_{um}	Ratio ϵ_x / ϵ_y at 500 kN
	MPa	GPa	mm	mm	mm	mm	(-)	(-)
CP01-1:7-P2	6,00	0,26	0,51	-4,14	1,06	-5,21	0,15	0,25
CP02-1:7-P2	5,62	0,36	0,52	-2,60	0,52	-2,60	0,24	0,24
CP03-1:3-P2	7,46	0,87	0,38	-1,63	0,38	-1,63	0,30	0,30
CP04-1:3-P2	6,67	0,76	0,10	-1,70	0,16	-1,89	0,08	0,11
CP05-1:5-P2	3,61	0,52	-0,07	-1,26	X	X	-0,07	X
CP06-1:3-V5	6,59	1,21	0,00	-0,90	0,01	-1,19	0,00	0,01
CP07-1:3-V5	6,28	1,41	0,15	-0,70	0,29	-1,02	0,27	0,36
CP08-1:5-V5	4,87	0,44	0,02	-1,98	0,39	-3,04	0,01	0,16
CP09-1:5-V5	5,84	0,83	0,05	-1,17	0,44	-1,83	0,05	0,31
CP10-1:7-V3	4,79	0,22	0,94	-3,42	4,56	-6,345	0,33	0,87
CP11-1:7-V3	5,44	0,28	1,45	-3,385	1,45	-3,385	0,52	0,52
CP12-1:3-V3	6,27	0,74	0,21	-1,55	0,43	-1,895	0,17	0,29
CP13-1:3-V3	6,66	1,22	0,12	-0,96	0,17	-1,14	0,16	0,19
CP14-1:5-V3	4,40	0,50	2	-2,895	2	-2,895	0,88	0,88
CP15-1:5-V3	5,82	0,67	0,01	-1,45	0,31	-2,195	0,01	0,18
CP16-1:7-V1	4,70	0,25	X	-2,9	X	-6,1	X	X
CP17-1:7-V1	5,53	0,75	X	-1,04	X	-1,04	X	X
CP18-1:3-V1	7,46	0,87	0,38	-1,625	0,38	-1,625	0,30	0,30
CP19-1:3-V1	6,67	0,76	0,1	-1,695	0,16	-1,89	0,08	0,11
CP21-1:5-V1	5,42	0,47	0,24	-2,165	1,08	-2,715	0,14	0,51

Note: X - values not measured

In low-pressure grouting applying the V3 lime-based grouting agent, the ultimate strength of the pillars in compression $f_{exp,epox} = 179\%$ for the mortar of the pillars with a mixing ratio of 1:3, and 141% for the mortar of the pillars with a mixing ratio of 1:5. In low-pressure grouting applying the V3 lime-based grouting agent on the pillars with mortar with a mixing ratio of 1:7, the compressive strength of the masonry ranged from 94 to 111% of the reference pillars.

In low-pressure grouting applying the V5 grouting agent based on a mixture of hydraulic lime and lime nanoparticles, the ultimate strength of the pillars in compression $f_{exp,epox} = 178\%$ for the mortar of the pillars with a mixing ratio of 1:3, and 148% for the mortar of the pillars with a mixing ratio of 1:5.

Figure 4 shows the relationship of the strength of brick masonry pillars on mortar with mixing ratios of 1:3, 1:5 and 1:7 to the used grouting agent, and the comparison with the strength values theoretically identified under ČSN EN 1996-1-1.

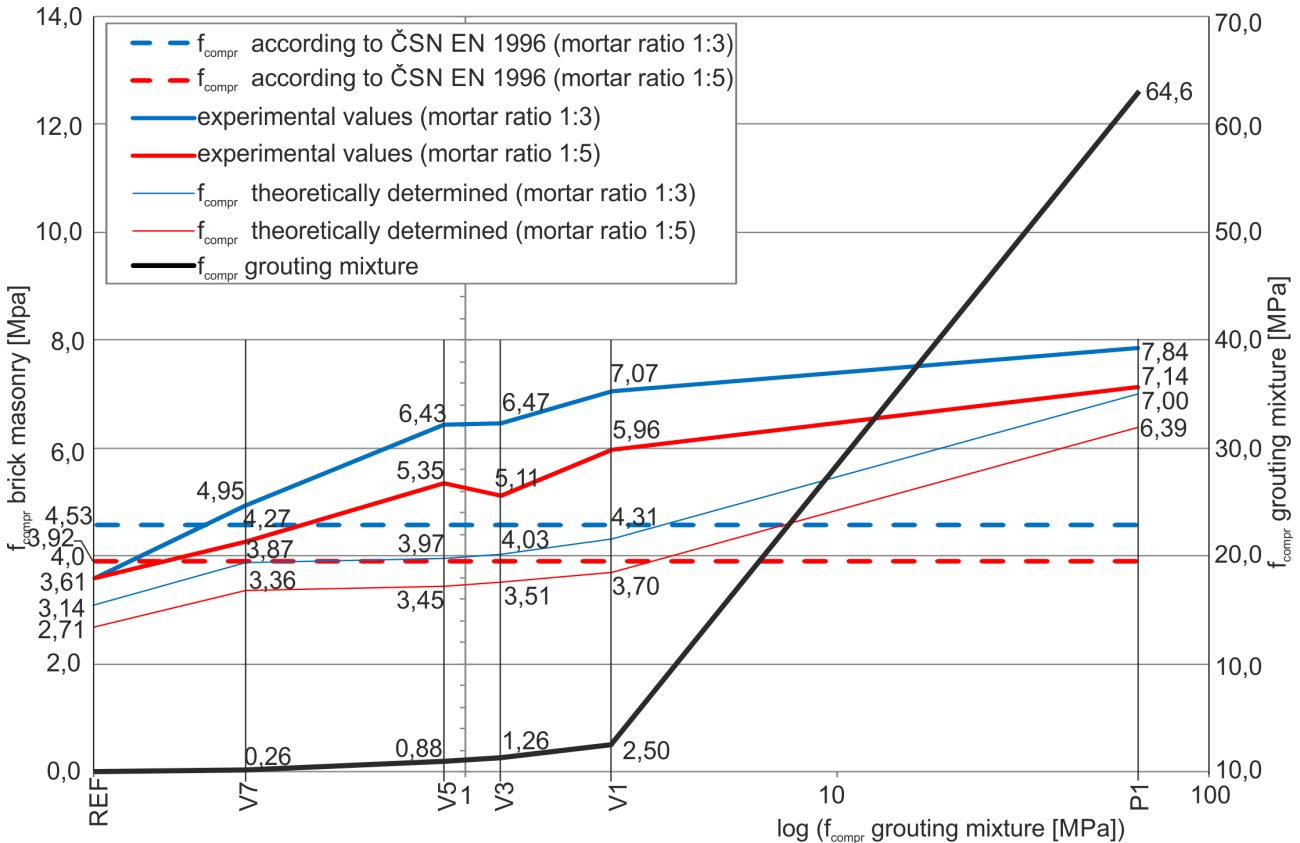


Fig. 4 - Relationship of the strength of brick masonry pillars on mortar 1:3, 1:5 to grouting agents used

Summary of grouting results

The experimentally identified compressive strength values indicate that the ultimate strength of the masonry in compression grew in the verified cases of brick masonry pillars with mortar with a mixing ratio of 1:3 and 1:5 after grouting with the above agents. The increase in strength ranged from 41% to 117% of the strength of ungrouted masonry. In the pillars with mortar with a mixing ratio of 1:7, the identified strength values ranged from only 94 to 111% of the strength of ungrouted masonry.

The load tests of masonry pillars have manifested the relationship of the strength of grouted brick pillar masonry to the strength of the grouting agents filling in the voids and penetrating into the masonry around the voids and the borehole. The effect of grouting on the masonry strength is gradually falling with the decreasing strength and penetration abilities of the grouting agent, or due to imperfect filling of the voids and cavities with the grout.

The experimentally identified strength values of grouted masonry for mortar with a mixing ratio of 1:3 and 1:5 are mutually roughly affine, and the comparison of experimental values for both types of mortar with the values calculated for the respective material characteristics under ČSN EN 1996-1-1 has brought similar results, too (see Figure 4).

The experimental verification did not prove a greater effect of low-pressure grouting in terms of compressive strength as compared to pressureless grouting.

Evaluation of penetration

As the number of coatings with the “grouting” substances increased, they penetrated into the near-surface layers. The penetration depth differed for different materials and grouting agents (Table 3).

Tab. 3 - Penetration depth of “grouting” substances

Label - Penetration substance	Penetrated material	Penetration depth [mm]	Note
P2	Brick CP 20	≤ 1	Only 3 coats, then epoxy sealed the surface forming glass-like film
	Sandy marlstone	max 0.1 mm	
	Sandstone	up to 1 mm	
	Limestone	up to 0.05 mm	
V3	Brick CP 20	up to 0.05 mm	Filled uneven surface spots, on the surface
	Sandy marlstone	---	Only on the surface
	Sandstone	up to 0.1 mm	Filled uneven surface spots, on the surface
	Limestone	---	Only on the surface
V5	Brick CP 20	up to 0.1 mm	From 8 th coating white lime film on the surface
	Sandy marlstone	up to 0.05 mm	
	Sandstone	0,1 to 0.5 mm	Up to 5 th coating - depth of ca. 0.1 mm, 6 th to 12 th coating – depth of 0.1 to 0.5 mm
	Limestone	---	In places of microcracks up to 0.01 mm, only on the surface
K1	Brick CP 20	up to 0.15 mm	Up to 6 th coating 0.1 mm, 7 th – 12 th coating up to 0.15 mm, from 9 th coating shiny sealed surface
	Sandy marlstone	up to 0.01 mm	
	Sandstone	up to 0.1 mm	From 7 th coating shiny sealed surface
	Limestone	---	In places of microcracks up to 0.01 mm, only on the surface

Summary of penetration results

In limestone samples, all the grouting agents remained only on the surface. The best results (greatest penetration depths) were reached with the P2 epoxy-based agent, whose three coatings penetrated to a depth of ca. 1 mm in the case of bricks and sandstone, and to a depth of 0.1 mm in sandy marlstone. The V3 lime-based agent remained only on the surface in limestone and sandy marlstone samples, and in the case of sandstone and bricks it penetrated to a depth of ca. 0.1 mm. The K1 silicate-based grouting agent penetrated to a depth of ca. 0.2 mm in bricks, to 0.1 mm in sandstone and 0.02 mm in sandy marlstone. The V5 agent based on hydraulic lime and nanolime penetrated to a depth of ca. 0.1 to 0.5 mm in bricks and sandstone, and to 0.05 mm in sandy marlstone.

Regardless of the base of the grouting agents applied on the surface, the greatest penetration depth was reached in sandstone and bricks, while, on the contrary, all grouting agents

applied on limestone remained only on the surface. Partial results of the experimental research manifested low penetration abilities of the verified grouting agents and excessive dependence of the penetration on the pore system of penetrated materials.

CONCLUSION

Due to the dispersion of the monitored parameters of grouted and ungrouted brick masonry and a limited number of samples, statistical data analysis allowing the formulation of unambiguous conclusions is impossible. The presented evaluation was made on the basis of the results of experimental research into the effect of grouting on major physical and mechanical characteristics of undamaged and compact brick masonry (Phase I) and brick masonry damaged by an artificial cavity (Phase II).

Partial results of experimental research into the effect of grouting on the strength of degraded brick masonry have manifested a positive effect of grouting on increasing the masonry strength. The effect of selected grouting agents on the strength of masonry with mortar with a mixing ratio of 1:3 and 1:5 was analogous. The partial experimental results obtained do not allow an unambiguous manifestation of a higher effectiveness of the pressure or pressureless grouting technique.

Partial results of experimental research into the penetration of selected grouting agents applied on the surface of materials often found in historic buildings have pointed out a possibility of using this technology for the strengthening and improving the adhesion of mainly the surface and near-surface layers of masonry structures of historic buildings.

ACKNOWLEDGEMENTS

The article was written with support from the NAKI DG16P02M055 project "Development and Research into Materials, Procedures and Technologies for Restoration, Conservation and Strengthening of Historic Masonry Structures and Surfaces and Systems of Preventive Care of Historic and Heritage Buildings Threatened by Anthropogenic and Natural Risks".

REFERENCES

- [1] NAKI DG16P02M055 Development and Research into Materials, Procedures and Technologies for Restoration, Conservation and Strengthening of Historic Masonry Structures and Surfaces and Systems of Preventive Care of Historic and Heritage Buildings Threatened by Anthropogenic and Natural Risks, 2015-2020, lead researcher prof. Ing. Jiří Witzany. DrSc.
- [2] Witzany, J.; Zigler, R.; Čejka, T.; Pospíšil, P.; Holický, M.; Kubát, J.; Maroušková, A.; Kroftová, K., Physical and Mechanical Characteristics of Building Materials of Historic Buildings, The Civil Engineering Journal. 2017,(4), 343-360. ISSN 1805-2576.
- [3] Witzany, J.; Zigler, R.; Kroftová, K.; Čejka, T.; Kubát, J.; Holický, M.; Karas, J., The Effect of Pore Distribution in Historic Masonry on the Grouting Method and Grouting Mix Selection, The Civil Engineering Journal. 2018, 3(10), 307-329. ISSN 1805-2576.

STUDY ON THE INFLUENCE OF SAFETY EDUCATION ON THE WILLINGNESS OF CONSTRUCTION WORKERS TO HABITUAL SAFETY BEHAVIOUR

Mei Shang and Wei Zhang

Xi'an University of Science & Technology, School of Management, Xi'an 710055, China, 940615683@qq.com (Shang), 1791522257@qq.com (Zhang)

ABSTRACT

In order to explore the impact of safety education on the willingness of construction workers to habitual safety behaviours, the relevant literatures are analysed, relevant research hypotheses are proposed, and the theoretical model of habitual safety behaviour willingness influencing factors is established, and the verification and analysis are carried out by means of inter-group experiments. The results show that different types of safety education have different influences on the willingness of construction workers to habitual safety behaviours under the mediating role of time scale adjustment and perceptual behaviour control.

KEYWORDS

Safety education, Willingness to act, Perceptual behaviour control, Time scale

INTRODUCTION

The construction industry plays a very important role in China's economic development and it is a pillar industry of China's national economy. However, construction safety accidents occur frequently, causing heavy losses in casualties. The Heinrich accident survey pointed out that the direct cause of a security incident is human unsafe behaviour. The unsafe behaviour of human beings is the result of the combined effects of various factors. Most of the construction workers have not received safety education, lack basic safety knowledge and construction skills, and are vulnerable to safety accidents [1]. Therefore, the implementation of safety behaviour of construction workers depends to a large extent on safety education.

The concept of willingness first came from the field of psychology research, and Fishbein (1975) defined willingness as the subjective probability that individuals engage in specific behaviours [2]. Ajzen (1991) defines the willingness to act as the degree to which an individual voluntarily performs a particular act and the level of effort that is intended to be done [3]. At present, there are few related studies on the impact of behavioural willingness and safety education. The root cause of unsafe behaviour of construction workers is their lack of safety awareness and lack of relevant safety knowledge [4]. Safety awareness must be gradually established through long-term, long-lasting and effective safety education [5], while workers have Safety knowledge affects their cognitive attitudes [6], and cognitive attitudes have a certain impact on behavioral willingness [7]. Therefore, it is of great significance to study the relationship between safety education and behavioural willingness and improve the quality of safety education, which is to improve the safety management effect of construction enterprises and reduce the accident rate of construction work.

THEORY AND ASSUMPTIONS

Safety education is an important measure to prevent unsafe behaviour of construction workers. The so-called safety is not to eliminate all potential accidents, but to make the system not exceed the allowable range [8]. Navidian pointed out that safety education plays a positive role in strengthening the knowledge and attitudes of workers, especially the implementation of safe behaviour [9]. Sun Jun pointed out that the safety awareness of workers has a direct and significant positive impact on construction safety behaviour [10]. The habitual safety behaviour of this paper refers to the daily repetitive construction behaviour, which needs to adjust the construction method and daily habit construction behaviour. The habitual safety behaviour will refer to the psychological tendency and behaviour motive of the individual before engaging in the habitual safety behaviour. Yang Gaosheng pointed out that the development of safe behaviour habits requires knowledge learning and experience accumulation^[11]. Different types of safety education methods have different effects on the willingness to act. Starting from Maslow's "demand level theory", according to the most basic physiological needs, security needs, belonging and love needs, respect for needs, As well as self-fulfilling needs, the way of education is corresponding to economic education, social education influenced by others, social education and safety education that affect others. Yang Zhenhong pointed out that the influence degree of influencing factors of unsafe behaviour from large to small is individual susceptibility, safety atmosphere, communication behaviour characteristics, reward or punishment, and rewards safety modellers or members who punish unsafe behaviour, can suppress insecurity to some extent. The spread of behaviour [12]. Based on the above analysis, the following assumptions are made:

H1: Safety education has a significant positive impact on the willingness to habitual safety behaviour. Non-economic education is more likely to promote habitual safety behaviour than economic education. That is, the positive impact of economic education, social education influenced by others, social education and safety education affecting others on the willingness to habitual safety behaviours has increased in turn.

American scholar Ajzen (1985) first proposed the theory of planned behaviour, introducing the concept of perceptual behaviour control into the theory, and believed that perceptual behaviour control is an important factor affecting behavioural will [13]. Klöckner used a structural equation model to compare 56 data sets and found that perceptual behavioural control can predict behavioural will [14]. Xu Lizhong pointed out that people's knowledge base and understanding of things significantly affect the control of perceived behaviour [15]. Yuan Hongping [16] based on the theory of planned behaviour, found that the perceptual behaviour control has a significant impact on the willingness of architectural behaviour. Based on the above analysis, the following assumptions are made:

H2: Safety education has a positive impact on perceived behavioural control.

H3: Perceptual behavioural control has a positive impact on the willingness to habitual safety behaviour, and together with hypothesis H2, perceptual behavioural control plays a mediating role in the impact of safety education on the willingness to habitual safety behaviour.

Time scales are widely used in geography, atmospheric science, biological oceanography, physics, fractal geometry, and ecology. In the field of building safety education, there has not been any in-depth study on the regulation of time scales. However, in the field of propaganda, the propaganda content of different time scales has already appeared, such as "1 yuan per day, one year for broadband" and "broadband package". 350 yuan a year." The results show that people's perceptions of different units of measurement are different, and the information demands of

different units of measurement may have different effects. This paper argues that different time scales will regulate the process of safety education affecting the willingness of habitual safety behaviour, and divide the time scale into small scale (one day) and large scale (one year). Combined with the hypothesis H2 of the impact of safety education on perceived behavioural control, the following hypotheses are proposed:

H4: Time scales regulate the impact of safety education on the willingness to habitual safety behaviour.

H5: The time scale regulates the impact of safety education on perceived behavioural control, which in turn affects the willingness to habitual safety behaviour.

Based on the above analysis, the following research framework is established:

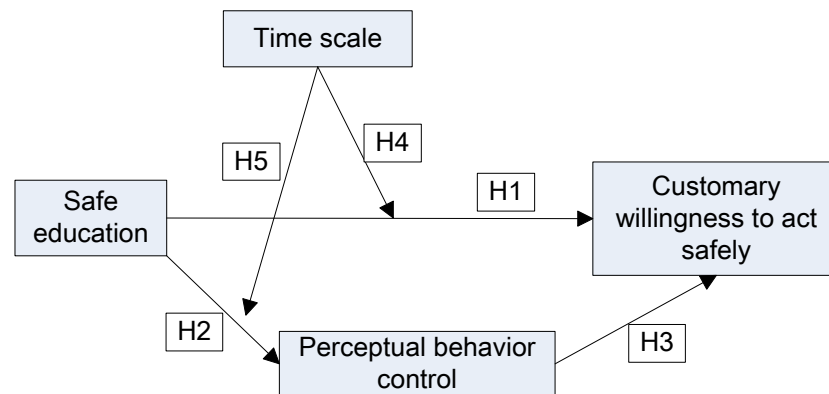


Fig.1 - Theoretical model of the influencing factors of habitual safety behaviour

RESERCH ESIGN AND EXPERIMENTAL ANALYSIS

Experimental design

The experimental method adopts 4 (safety education: economic education VS social education influenced by others VS social education affecting others VS safe education) × 2 (time scale: small scale VS large scale) inter-group factor design. Among them, Perceptual Behaviour Control Measurement Scale draws on the research results of Perujini [17], Taylor [18], etc., and divides perceptual behaviour control into control degree and difficulty level, and develops into willingness for habitual safety behaviour. Perceived Behaviour Control Scale. The research results of Shirley [19] and János [20], which are based on the habitual safety behaviour willingness measurement scale, are developed into a habitual safety behaviour willingness measurement scale by combining forward question and reverse question. A total of 216 valid data was collected from the experiment. The construction workers were randomly divided into 8 groups, and the number of participants in each experimental group was 27.

Experimental results and analysis

The reliability and validity of the scale are tested accordingly. In the reliability, the Cronbach's α value of the Perceived Behaviour Control Scale is 0.711, and the Cronbach's α value of the Habitual Safety Behaviour Scale is 0.762, both exceeding the standard of 0.7. In terms of validity, the confirmatory factor analysis showed that the factor load of the variable exceeded 0.5, the average variance of the variable (AVE) was close to 0.5, and the variable convergence efficiency was good, indicating the reliability and validity of the scale used in the study better.

Firstly, it analyzes the direct impact of safety education on the willingness of construction workers to conduct safe behavior. Using one-way analysis of variance, the results show that the average value of economic education, social education influenced by others, social education and safety education affecting others' habitual safety behaviors are 5.086, 5.107, 5.132, 5.141, indicating that the positive effects of the four educations on the willingness to habitual safety behavior increased in turn, but the analysis of variance showed that the four did not have statistically significant differences ($p > 0.05$), indicating that the safety education is willing to the habit of customary safety behaviors. The effect is not significant, so assume that H1 is not verified.

Two-factor ANOVA is used to analyze the main effects of safety education and time scale and the interaction between them. The output results are shown in Table 1.

Tab. 1 - Regulatory effects of time scales on the impact of safety education on habitual safety behaviors

Category	Type III square sum SS	Degree of freedom df	Mean square MS	Statistic F	Significance P
Safe education	0.221	3, 317	0.067	0.208	0.743
Time Scale	0.201	1, 317	0.201	0.507	0.299
Safety education × time scale	9.038	3, 317	3.006	8.485	0.000

The results showed that the interaction between safety education and time scale was significant ($F(3,317)=8.485, p < 0.05$), indicating how one factor works and is affected by another. Therefore, after the interaction is significant, a simple effect test should be carried out to explore how the time scale affects the role of safety education in the willingness to habitual safety behavior. The results of the MANOVA simple effect test for safety education are shown in Table 2.

Tab. 2 - Simple effects of safety education

	Type III square sum SS	Degree of freedom df	Mean square MS	Statistic F	Significance P
Safety education (small scale)	6.01	3	2.01	5.62	0.001
Safety education (large scale)	3.31	3	1.04	3.17	0.022

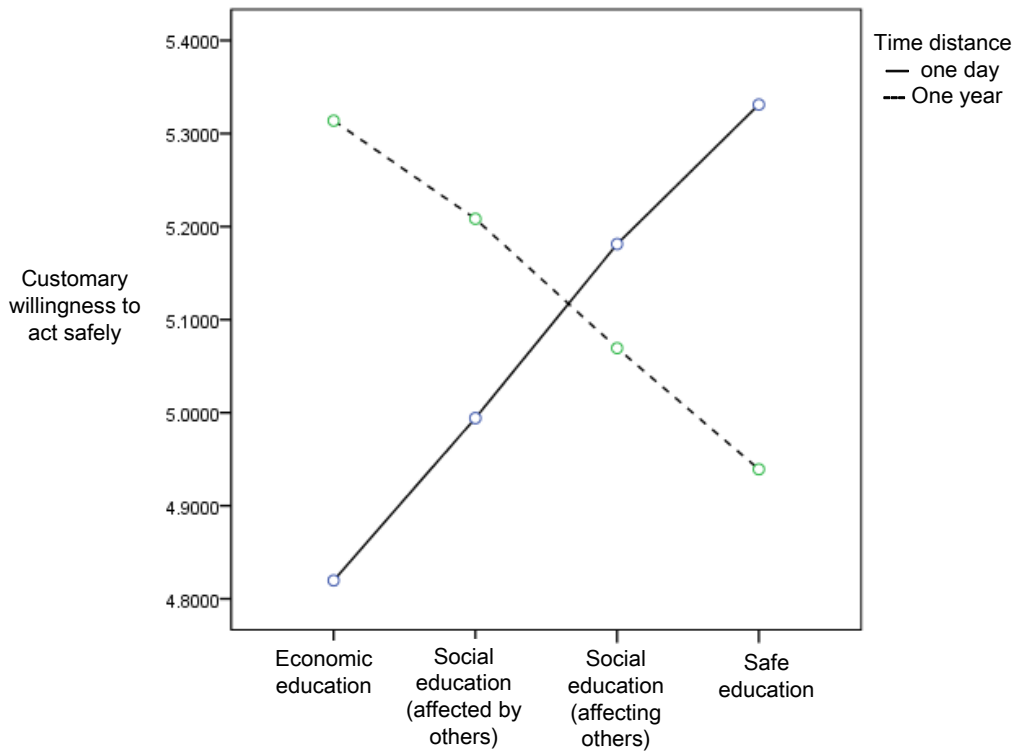


Fig. 2 - Simple effect of safety education

The simple effect results showed that there were significant differences in safety education at small scales ($F=5.62, p=0.001<0.05$) and large scales ($F=3.17, p=0.022<0.05$) (as shown in Figure 2). At a small time scale (one day), the willingness of the habitual safety behaviors of the four educations increased in turn; on the large time scale (one year), the willingness of the four types of education to habitually safe behavior decreased in turn. Among them, the safety information has a good matching effect with the small scale, and the economic information has a good matching effect with the large scale. The mean value of the habitual safety behavior will be 5.322 and 5.305 respectively. Assume that H4 is supported. When using small-scale safety education, safety education can promote the willingness of construction workers to generate habitual safety behaviors compared with economic education (see Figure 2); when using large-scale safety education, economic education is more important than safety education. It can

promote the willingness of construction workers to generate habitual safety behaviors (see Figure 2), assuming that H1 does not hold.

Using the mediation effect test procedure proposed by Zhao [21], based on the adjusted mediation analysis model proposed by Hayes [22], Bootstrap test is used to mediate the perceptual behavior control, with perceptual behavior control as the mediator variable and time scale as the regulatory variable. To test the mediating effect of the independent variable safety education on the perceptual behavioral control of the dependent variable habitual safety behavior and the time-scale adjustment effect (Table 3). The sample size is chosen to be 5000, in the 95% confidence interval.

Tab. 3 - Mediating effect of perceived behavioral control on the willingness of safety education to influence habitual safety behaviors

Input variable	Output variable	95% confidence interval					
		Effect size coeff	Standard error SE	Statistic T	Significant P	Lower limit LLCI	Upper limit ULCI
safe education	Perceptual behavior control	0.2848	0.1148	2.4865	0.0134	0.0587	0.5109
Time Scale	Perceptual behavior control	0.5435	0.1923	2.8300	0.0049	0.1650	0.9220
Safety education × time scale	Perceptual behavior control	-0.2052	0.0722	-2.8508	0.0046	-0.3476	-0.0629
safe education	Customary willingness to act safely	0.3433	0.0785	4.3813	0.0000	0.1887	0.4979
Time Scale	Customary willingness to act safely	0.5549	0.1318	4.2139	0.0000	0.2953	0.8144
Perceptual behavior control	Customary willingness to act safely	0.4411	0.0377	11.6947	0.0000	1.7181	2.7048
Safety education × time scale	Customary willingness to act safely	-0.2061	0.0495	-4.1735	0.0000	-0.3030	-0.1085

Safety education has a positive impact on perceived behavioral control (LLCI=0.0587, ULCI=0.5109, coeff =0.2848), and this interval does not contain 0, assuming H2 is established. Perceptual behavior control has a significant positive impact on habitual behavioral willingness (LLCI=1.7181, ULCI=2.7048, coeff=0.4411), which does not include 0, assuming H3 is established.

The influence of time scale on the willingness of habitual safety behavior (LLCI=0.2953, ULCI=0.8144), the interval does not contain 0, and the interaction between safety education and time scale has a significant impact on the willingness of habitual safety behavior (LLCI=-0.3030, ULCI = -0.1085), assuming H4 is established, that is, the time scale adjusts the impact of safety education on the willingness to habitual safety behavior. The influence of time scale on perceptual behavior control (LLCI=0.1650, ULCI=0.9220), the interval does not contain 0, and the cross-terms of safety education and time scale have significant influence on perceptual behavior control (LLCI=-0.3476, ULCI=-0.0629), assuming that H5 is established, that is, the time scale regulates the impact of safety education on perceived behavioral control. In summary, safety education has a mediating effect on the willingness to habitual safety behavior.

Tab. 4 - Mediating effect of perceptual behavior control on the influence of safety education on habitual safety behavioral behavior at different time scales

Regulating variable state	Mediation effect type	Effect size coeff	95% confidence interval				
			Standard error SE	Statistic T	Significant P	Lower limit LLCI	Upper limit ULCI
Small scale	Direct effect	0.1362	0.0350	3.9156	0.0001	0.0673	0.2052
	Mediation effect	0.0342	0.0266*	—	Contains 0	-0.0148	0.0883
Large scale	Direct effect	-0.0688	0.0347	-2.0121	0.0450	-0.1371	-0.0006
	Mediation effect	-0.0550	0.0231*	—	Does not contain 0	-0.1004	-0.0107
Interaction	Mediation effect	-0.0902	0.0365*	—	Does not contain 0	-0.1671	-0.0220

Table 4 analyzes the mediating effects of safety education on the behavioral control of habitual safety behaviors in different time scales. The mediating effect of perceptual behavioral control on the willingness of safety education and time-scale interactions to influence habitual safety behaviors is negative (LLCI=-0.1671, ULCI=-0.0220, coeff=-0.0902). The impact of safety education on the willingness to habitual safety behavior on a time scale of one day (LLCI = 0.0673, ULCI = 0.2052), this interval does not include 0; the impact of safety education on the willingness to habitual safety behavior on a time scale of one year (LLCI=-0.1371, ULCI=-0.0006), this interval does not contain 0, that is, safety education has a significant impact on the willingness to habitual safety behavior. When the time scale is one day, the influence coefficient of safety education is 0.1362>0, that is, the higher the level of demand corresponding to the content of safety education, the better the influence on the willingness of habitual safety behavior, the willingness of perceptual behavior control to influence the habitual safety behavior of safety education. There is a mediating effect (LLCI=-0.0148, ULCI=0.0883); when the time scale is one year, the impact coefficient of safety education is -0.0688<0, that is, the higher the level of demand corresponding to the content of safety education, the lower the willingness to habitual safety behavior. Perceptual behavior

control has a negative mediating effect on the willingness of safety education to influence habitual safety behavior (LLCI=-0.1004, ULCI=-0.0107, coeff=-0.0550).

CONCLUSION

(1) Different types of safety education have different degrees of influence on the willingness of construction workers to habitual safety behaviors under the adjustment of time scale. When the safety education method adopts a small scale, the higher the level of demand corresponding to the safety education method, the stronger the influence on the willingness of the habitual safety behavior; when the safety education method adopts the large scale, the lower the level of demand corresponding to the safety education method, the habit The stronger the will of sexual safety behavioral willingness. Safety education has a positive influence on the control of perceived behavior. Perceptual behavior control has a significant positive impact on the willingness of habitual safety behavior. The mediating effect of perceptual behavior control is significant, and the time scale affects the customary safety behavior of perceptual behavior control intermediary safety education. There is a regulatory role in willingness.

(2) Divide safety education into four ways, and explore the influence of different modes of safety education on the time-scale adjustment and the intermediary role of perceptual behavior control on the willingness of construction workers to habitual safety behaviors, and make enterprises more in-depth. It is learned that what kind of education method can enhance the willingness of construction workers to safely behave, improve the quality of safety education, and provide reference for construction enterprises to carry out safety education for construction workers.

(3) There are certain deficiencies in the research: 1. There is no in-depth study of the impact of the basic information of the experimental object on the research results. 2. There are many factors and mechanisms that affect the willingness of construction workers to habitual safety behaviors. This paper only studies the direct effects of safety education, the mediating effects of perceived behavioral control, and the adjustment effects of time scales. It is impossible to deeply understand all the influences of habitual safety behaviors.

REFERENCES

- [1] XIE Yong, JIANG Quanbao. Land arrangements for rural—urban migrant workers in China: findings from Jiangsu province [J]. Land Use Policy, 2016, 50: 262—267.
- [2] Fishbein, M, Ajzen I. Belief, Attitude, Intention and Behavior[M]. Mass, Addison-Wesley, 1975.
- [3] Ajzen I. The theory of planned behavior[J]. Organizational Behavior and Human Decision Processes, 1991, 50(2): 179-211.
- [4] Robson L. S. et al. A systematic review of the effective-ness of occupational health and safety training [J]. Scand J Work Environ Health, 2012, 38(3):193-208
- [5] Du Yi, Chen Dingjiang, Lin Zhanglin, et al. Construction and Practice of Chemical Safety Education System [J] Experimental Technology and Management, 2015, 32(11): 231-233 + 236.
- [6] Liu Jialun, Han Yu, Zhang Jingjie, et al. Differences in the results of dangerous cognition among construction workers of different working ages[J].Journal of Civil Engineering and Management,2018,35(02):175-180.
- [7] Meng Hu, Ma Ji, Yang Yixiong, et al. Influencing factors of water label clothing purchase attitude and willingness to consume behavior[J].Wofang Technology,2017,45(07):72-76.
- [8] Ma Ruhong. Human factors engineering [M]. Beijing: Peking University Press, 2011: 2-4.

- [9] Navidian A, Rostami Z, Rozbehani N. Effect of motivational group interviewing-based safety education on Workers' safety behaviors in glass manufacturing.[J]. *Bmc Public Health*, 2015, 15(1):1-7.
- [10] Sun Jun, Yan Sen, Du Chunyan. The Impact of Construction Enterprise Security Atmosphere on Employees' Safety Behaviors and Empirical Research[J]. *Journal of Safety and Environment*, 2014, 14(02):60-64.
- [11] Yang Gaosheng, Ju Jie, Xu Xin. Study on the Design of Safety Education and Training Program for Construction Enterprises[J]. *China Safety Production Science and Technology*, 2013, 9(03):176-183.
- [12] Yang Zhenhong, Ding Guangcan, Zhang Tao, et al. Study on the influencing factors of unsafe behavioral transmission of construction workers based on SEM[J]. *Journal of Safety and Environment*, 2018, 18(03):987-992.
- [13] Ajzen, I. From intentions to actions: a theory of planned behavior[J]. Springer Berlin Heidelberg, 1985, 20(8): 1-63.
- [14] Klöckner C.A. A comprehensive model of the psychology of environmental behavior-A meta-analysis[J]. *Global Environmental Change*, 2013, 23(5): 1028-1038.
- [15] Xu Lizhong, Chen Fang, Yang Jing, et al. Analysis of the motivation of public environmental protection payment willingness based on the theory of planned behavior[J]. *Journal of Fujian Normal University(Natural Science Edition)*, 2013, 29(05):87-93.
- [16] Yuan Hongping, Li Ancong. Study on the Reduction Behavior of Construction Workers' Waste—Based on the Theory of Planned Behavior[J]. *Journal of Huaqiao University(Philosophy and Social Sciences)*, 2018(01):36-44.
- [17] Perugini M., Bagozzi R. P. The role of desires and anticipated emotions in goal-directed behaviours: Broadening and deepening the theory of planned behaviour[J]. *British Journal of Social Psychology*, 2001, 40(1): 79-98.
- [18] Taylor S. D., Bagozzi R. P., Gaither C. A. Decision making and effort in the self-regulation of hypertension: Testing two competing theories[J]. *British Journal of Health Psychology*, 2005, 10(4): 505-530.
- [19] Shirley Taylor, Peter Todd. An integrated model of waste management behavior: a test of household recycling and composting intentions[J]. *Environment and Behavior*, 1995, 27(5): 603-630.
- [20] János, L Máté. Students energy saving behavior - case study of University of Coimbra. Portugal[D]. Coimbra: University of Coimbra, 2011.
- [21] Zhao X, Lynch J G, Chen Q. Reconsidering baron and kenny: myths and truths about mediation analysis[J]. *Journal of Consumer Research*, 2010, 37(2): 197-206.
- [22] Hayes A F. An introduction to mediation, moderation, and conditional process analysis: A regression based approach[M]. New York: Guilford Press, 2013.

VERTICAL WALL STRUCTURES IN TENEMENT HOUSES AT THE TURN OF 20TH CENTURY

Martin Ebel

*National Technical Museum, Museum of Architecture and Civil Engineering,
Kostelní 42, Prague 7, Czech Republic; martin.ebel@ntm.cz*

ABSTRACT

This article analyses the development of masonry, used extensively during the construction of tenement houses in Czech towns after the middle of the 19th century, peaking at the turn of the 20th century. The dimensions (wall thickness) were defined by architectural codes issued for Czech Crown Lands (i.e. Bohemia, Moravia & Silesia) in three waves – the first one taking place from 1833 till 1835, the second one from 1864 till 1884, and the third one from 1886 till 1894. Tenement houses belonged, without exception, to the so-called “below-threshold” buildings, where a wing was 6.32 m deep (later 6.5). These principles are presented in historical examples of selected works by students of the Prague Polytechnical Institute and architectural designs for Prague (Bubeneč and Nusle boroughs).

KEYWORDS

Tenement house, 19th century, Masonry, Architectural order, Building codes

INTRODUCTION

Tenement houses became a new phenomenon in the 19th century.¹ Tenement flats were, nonetheless, quite common in historic towns almost from the Middle Ages. But the situation was different in individual town categories.

Observing Prague at the beginning of the 19th century, we would see three-, or less commonly, even four-storey houses on the busiest streets. Two- or three-storey houses were typical on side streets; single-storey houses were exceptional. Houses had backyard wings; built space was often maximized. Aside from the landlord's flat, there were several other flats, sized from studios to multi-room flats; there were shops and quite often horse stables on the ground floor. Each flat had its own kitchen, at that time in the form of a scullery, with a hood and a crawl chimney. In adjacent rooms, Dutch stoves were fed from the kitchen.

METHODS

A different situation existed in other bigger towns, (e.g. in Pilsen) where three-storey houses were rare and only on main squares. More common were two-storied houses and one-storied on side streets. Houses within fortified walls (usually 220 – 250 of them) in former historic royal towns

¹ In terms of typology and, first of all, the layout of flats connected to practical features such as, daylighting, circulation, sanitary facilities, and other trends, Pavel Janák's excellent article A Hundred Years of Tenement House in Prague Styl, ed. XIII, Prague 1933-1934 page 15-18, 39-42, 55-65 dealing with tenement houses has still been absolutely valid.

were mostly single-storey. A two-storey house was an exception. At the same time, the smaller the town, the lower the number of tenement flats. The backyard wings of historic houses were an early step to later tenement houses; while the well-grounded foundation of a house with a vaulted ground floor was often preserved, even during a major rebuilding, entirely new backyards wings were connected to the old house by galleries.

Tenement houses differed from historical tenement building in several ways. The continuity of using the parcels of historic homes often dated back to the times of the town's origin. Some privileges were related to them - usually brewing rights and craft production. On the contrary, tenement houses were often new buildings. They were either built on the site of a demolished house where historic privileges had lost their meaning (were sold) and production was relocated, or built on different plots, ideally on the outskirts of the town.

The situation was specific in Prague, or more correctly, in close vicinity to the city. One urban agglomeration originated in Prague's historic suburbs – Karlín (1870), Smíchov (1838), Vyšehrad (1883) Holešovice-Bubny (1884), Libeň (1901), others enjoyed the status of an independent town: Vinohrady (1879), Žižkov (1881), Košíře (1896). And it was where the situation was favourable for building tenement houses. Outside Prague, the ideal area was established by tearing down the fortification walls and converting the reclaimed land into the parks or building plots.

The list presented above suggests that the 19th century brought an unusual construction boom that had to be regulated very soon. There were several reasons for it. Aside from the traditional worries about fires and thus, an understandable preference for the non-combustible structures, the loadbearing capacity of walls was critically important in multi-storey buildings.

Vertical structures were entirely linked to the height of buildings and their number of storeys. Although historically, as mentioned above, there were a few four-storey (Baroque) buildings in Prague, buildings were allowed to be only two-storey according to the 1815 Prague Building Code. Adding higher storeys had to be approved separately. To save space, the Building Code for the new Karlín suburb (1817), stipulated at least single-storey buildings; the Building Order for Brno from 1828 requested the same. Rooms or flats had to be at least 10 Lower Austrian feet high (3.16 m) in Prague; in its 1828 Building Order, Brno specified the height of the first and second storey as 10 feet (3.16 m) on the ground, and the third storey had to be at least 9 feet (2.84 m).²

Provincial building codes defined the design conditions since 1830s. They were published in three series; the code for Bohemia first and then the one for Moravia, circumstances in Silesia were more complicated (see below).

THE FIRST SERIES OF BUILDING CODES

The oldest building codes for Bohemia, Moravia & Silesia were issued between 1833-1835³; they stayed valid, only slightly modified, until 1864 in Bohemia, until 1869 in Moravia and even until 1883 in Silesia, which is deep into the second half of the 19th century. To save space, one- and two-storey buildings were built in both bigger and smaller towns. Higher buildings had to be approved by the gubernium later replaced by the office of the steward (Imperial-Royal Governorate of Bohemia); factories were exempted. Buildings had to be founded on raft foundations or even piles, if built on an unsuitably sandy or damp sub-base. The thickness of masonry was calculated from the number of storeys and was derived from the highest storey – it had to be 1 ½ feet thick on the topmost storey (47 cm); walls had to be by 3 to 6 inches (8-16 cm) thicker for lower storeys, foundation

² The Building Code for Prague dated 11 May, 1864. The Building Code for Czech Lands No. 20/1864. The Building Code for Moravia, the Code for the Margraviate of Moravia No. 1/1870 dated 20 December 1869. The Building Code for Silesia 1883, the Code for Upper and Lower Silesia dated 2 June, 1883.

³ The 1833 Building Code for Bohemia; the instructions of the Czech governorate, dated 17 May, 1833. The Building Code for Moravia and Silesia; the instructions of the Moravian governorate, dated 12 September, 1835. The 1845 Building Code for Bohemia; the instructions of the Czech governorate, dated 27 March, 1845.

masonry had to be at least 6 inches (16cm) thicker than on the ground floor. For fire-prevention purposes, adjacent houses had to be fitted with party walls extending high above the ridge. The norm for a firewall (party wall) was specified in Moravia as protruding 12 to 15 inches (32 – 39 cm) above the roof of the higher building.

In Bohemian towns, the floor had to be at least 6 inches (16 cm) above grade on the ground floor; the Moravian Code from 1835 specifies at least one foot (32 cm), the Building Code for towns from 1845 specifies 6 inches as a minimum or, better, double that (16 and 32 cm).

The ideal height of vaulted rooms was also specified – 10 feet (3.16 m); it had to be 10 feet in non-vaulted habitable rooms (3.16 m), at least 9 feet (2.84 m); rooms in village homes could be by as much as 6 inches lower (16 cm).

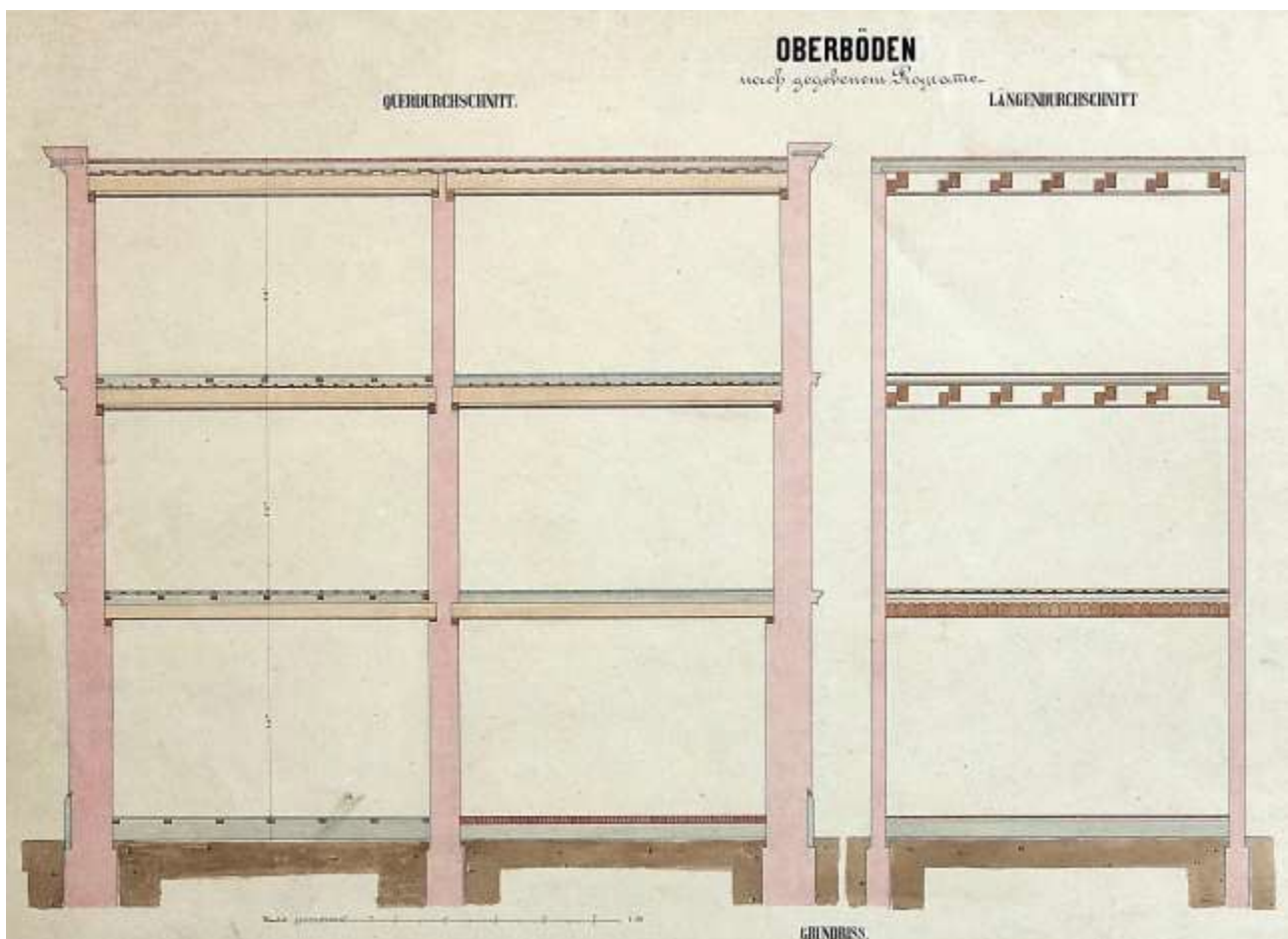


Fig. 1 – Student work by Quido Bělský from Prague Polytechnic; second half of the 19th century. The thickening of masonry is well demonstrated in this section. There is a side-by-side timber log floor above the ground floor (we call it “typlový” to distinguish it from round or half-round floors); on higher storeys, there are floors supported by joists with attached smaller secondary joists not transferring the movement into the plastered soffit below. [NTM, ANTM, D8/55, 357.]

THE SECOND SERIES OF BUILDING CODES

Another wave of Building Codes was based on those from the year 1864 for Bohemia, and in 1896 for Moravia.⁴ They introduced the approved number of storeys – a house could have a maximum of four storeys above the ground floor and one mezzanine; in Moravia, it was either three or four storeys, plus a mezzanine. The construction authority had the right to limit the number of storeys in both cases, if warranted. The maximum front height of new buildings was 12 fathoms (22.75 m) for Moravia. The 1883 Silesian Building Code allowed three storeys plus a ground floor.

The section regarding the wall thickness underwent major changes. Buildings started to be divided into less deep ones – wings with rooms up to 20 feet deep (6.32 m) – and deeper ones exceeding this limit. If the wing was within the limit, the main brick walls complied if 1 ½ foot thick (47 cm); stone walls conformed if 2 feet thick (63 cm). If the walls were deep beyond the limit, stone masonry had to be thicker, up to 2 feet 3 inches (71 cm in total); brick masonry had to be 2 feet thick (63 cm). Main walls had to be thicker by 3 inches (8 cm) on every lower floor and foundations 6 inches thicker than walls on the ground floor. The building authority could request even thicker masonry, if necessary.

Other details differ in municipal versions. The Czech version specifies that in case of side-by-side log (timber) floors, masonry must be thicker on every lower story by 6 inches. Middle pillars had to be rectangular prisms or preferably made of iron, rather than brick. In Bohemia and Moravia, rooms between two masonry walls had to be divided by a plastered wooden partition (timber or timber-framed); it was not allowed to place a stove next to the partition.

The Silesian Building Code following this trend was not published until 1883- thirteen years after the introduction of the metric system. Below-threshold houses with shallower wings were approximated to 6.3 metres in depth. Their main stone-masonry walls had to be 60 cm thick, brick walls 70 cm thick; above-threshold stone-masonry walls had to be 70 cm thick, brick walls 60 cm. Each lower storey had to have walls that were 15 cm thicker. If there were no floor structures bearing on these walls, they could be 60 cm thick (stonework), or 45 cm (brickwork). Foundations had to be 15 cm thicker than ground-floor masonry. The Silesian Building Code had sophisticated provisions allowing 70 cm thick (stone) or 60 cm (bricked) main (load-bearing) walls carrying ceiling joists or ceilings vaulted into I beams to be of the same thickness on two storeys when stacked. Central walls had to be 60 cm thick (stone) or 45 cm (brick) on the topmost floor; walls on each second floor below were required to be 15 cm thicker; walls supporting the so-called side-by-side timber log floor structures⁵ had to be by 15 cm thicker on each floor as they descended. The minimum thickness of partitions had to be 25 cm.

This series of Building Codes naturally also addressed fire gables with strengthened pillars. Czech Codes do not specify their exact parameters; Moravian Codes require them to protrude 9 inches (24 cm) above the roof, the Silesian ones request 25 cm. Moreover, there is a new element in the Silesian Code from 1883 – fire gable walls had to be installed every 30 meters within the house.

The Czech and Moravian Codes from the 1860's specified different requirements than the older ones, in the section regarding the height of the ground floor above grade. Flats in new buildings were allowed 12 or more inches (32 cm) above the ground in Bohemia; this height was allowed to be lower, only if the flats were perfectly dry, day lit and ventilated and in the event one side was at least 4 feet (1.26 m) above grade, if built into a slope. Basement workshops were allowed only if their ceiling was at least 2 feet (63 cm) above grade and sufficiently ventilated. The Moravian Code approved floors in a flat if installed lower, if it did not contradict health codes. If a building was built

⁴ The Building Code for Prague dated 11 May, 1864. The Building Code for Czech Lands No. 20/1864. The Building Code for Moravia, the Code for the Margraviate of Moravia No. 1/1870 dated 20 December 1869. The Building Code for Silesia 1883, the Code for Upper and Lower Silesia dated 2 June, 1883.

⁵ It means the so-called "typlový" (side-by-side log floor structure) according to the current terminology.

in a flood-prone area, floors of houses had to be 12 inches (32 cm) above the highest flood level. The requirements for basement workshops were the same. In Silesia, since 1883, floors had to be a minimum of 30 cm above grade, or above the highest flood level in a flood-zone; basement workshops had to have a ceiling at least 90 cm above grade. The clearance is slightly modified. In Bohemia, vaulted rooms had to be at least 10 feet (3.16 m) high, those with flat ceilings a minimum of 8 ½ feet (2.69); in Moravia, it was 9 feet (2.84.m), and in Bohemian and the Moravian countryside, the minimal clear height of living rooms was only 8 feet (2.53). The 1883 Silesian Building Code specified the lowest clearance of habitable rooms to be 2.8 m; all rural rooms and cattle sheds were 2.5 m high.

With respect to the increasing depth of new buildings, a passage was implemented [in codes] defining the form of a light shaft (their existence was prohibited before). A light shaft had to rest on solid walls reaching above the roof, with an iron frame; naturally, they had to be, fire-resistant and structurally separated from the attic.

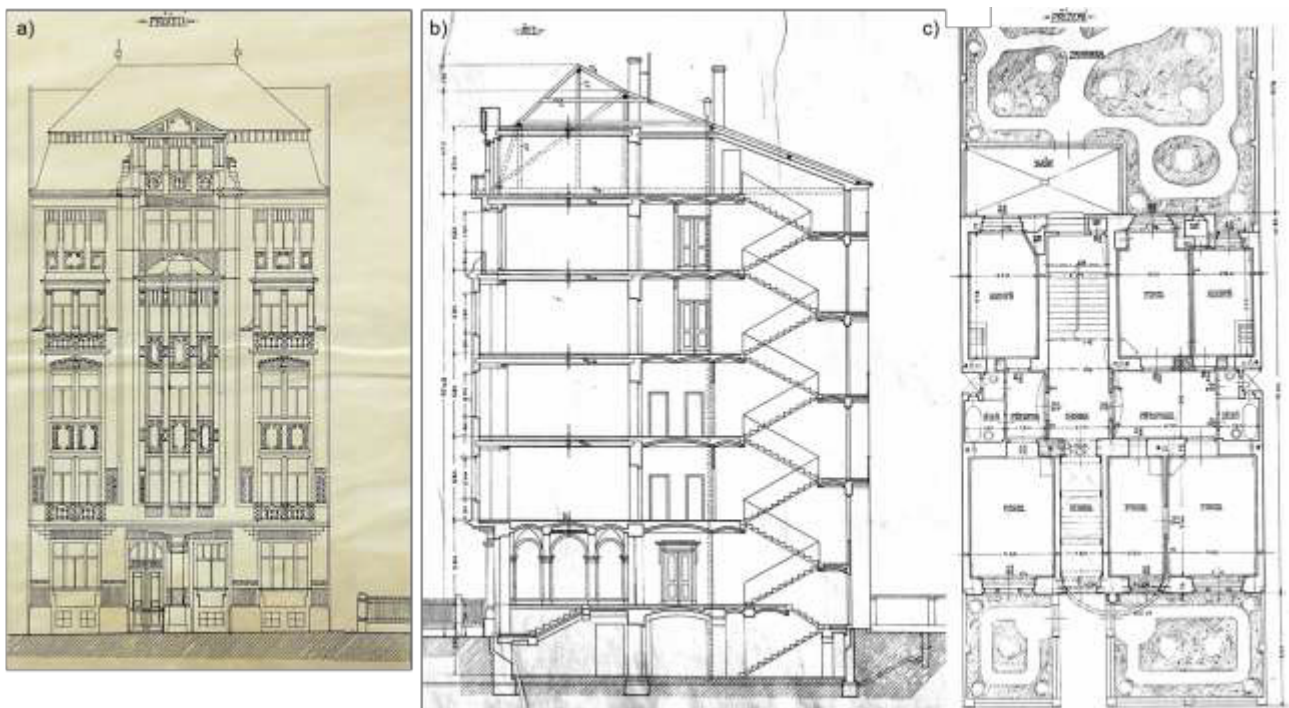


Fig. 2 – The undated proposal (from the early years of the 20th century) for a new building of a four-storey apartment building in Prague's Bubeneč by architect Václav Řezníček is one of the top productions of this type of house. In the entrance to the house there are alternating two-barrel vaults with segments with a flattened vault in the middle, in other roads there are relatively simple segmented vaults into traverses. On the first and second floor there is one five-room apartment, on the upper two floors of two-room apartment, all are equipped with bathrooms. [NTM, AA, Fund 197, 20090909/02]

NAVRH SCHODU.

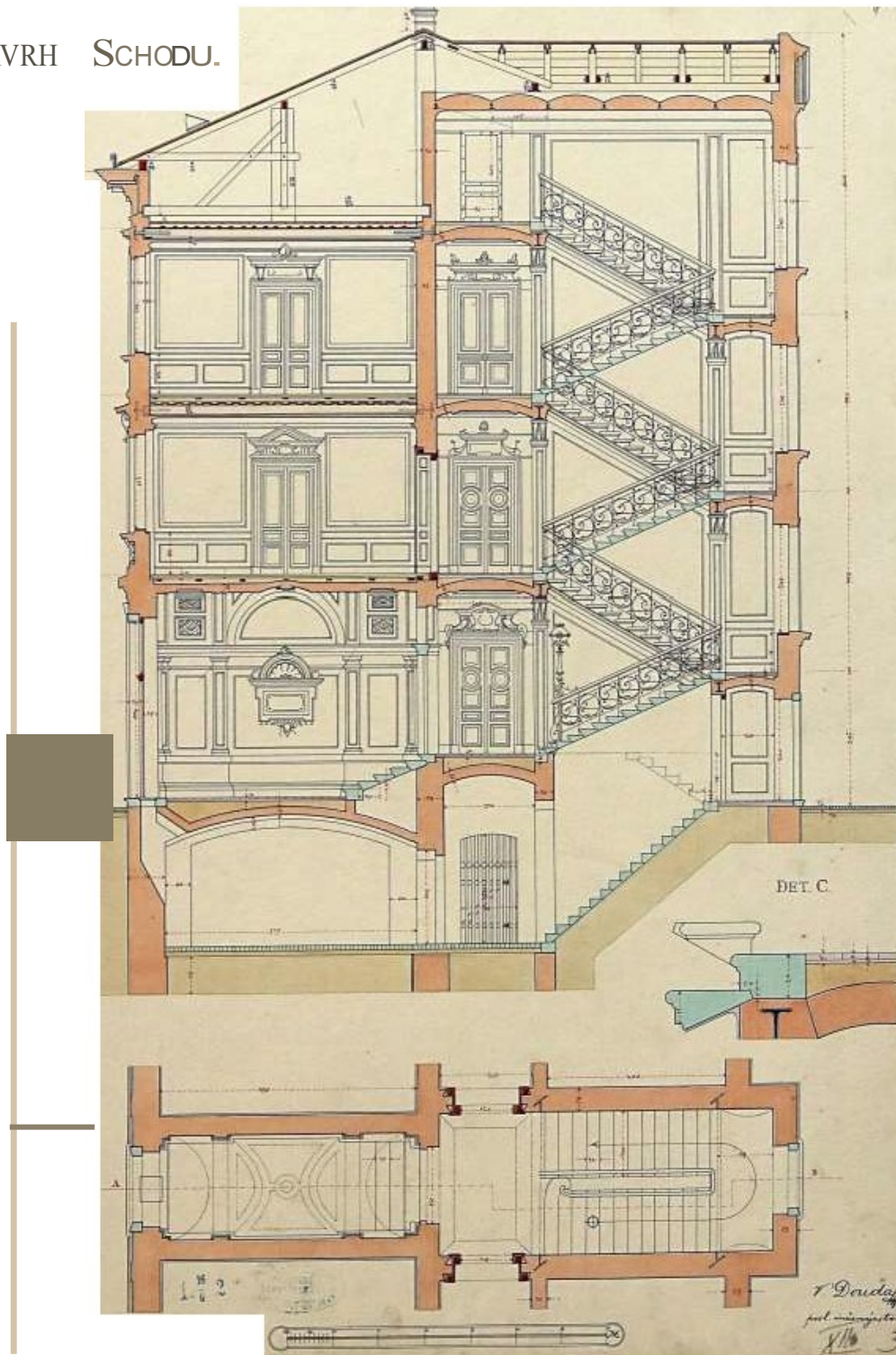


Fig. 3 – The design of the stairs, listener of engineering V. Douda, 1902. The drawing clearly shows the widening masonry in accordance with the building code from 1886. In the basement there are barrel segmented vaults, barrel vaults with sectors in the entrance, mirrored vaults corridors, barrel vaulted barrel, barrel vaulted bar above the staircase. Reed ceilings in the room (reed beams are not so well visible from this section). [NTM, ANTM, D6 / 55, 263]

THE THIRD SERIES OF BUILDING CODES

Newly reviewed Building Codes were issued between 1886 and 1894 for Bohemia and Moravia (this update did not include Silesia). In towns, the maximum allowed height of buildings was 25 meters, measured to the cornice; the top floor level could be maximum of 20 meters above the ground. Houses in large Czech towns could have a ground floor, plus four storeys above; outside these towns, only three storeys were allowed. Moravian towns were regulated differently – an overly high storey could be divided horizontally, but only if each storey still measured three meters.

This edition also recognized buildings with narrower and broader leaves – the borderline was 6.5 m. The wall thickness had to be pre-determined, based on structural calculation without the plaster. The topmost storey a maximum of 6.5 m deep had to have main walls 45 cm thick (brick) and 60 cm (stone); wings over this limit could have brick walls a minimum of 60 cm thick and quarry-stone walls 70 cm thick. The 1886 Czech Code for large towns required that the main wall is by at least 8 cm thicker on every lower floor, or by 15 cm every second lower floor. Codes from 1889 and 1894 for all of Moravia (and the Czech countryside) required walls on the second from last floor to be 15 cm thicker; two storeys below, the walls had to be thicker by 15 or more centimetres. Moravia specified thickening the walls as they descended by 15 cm on every lower floor, for the loose placement of side-by-side timber log floor structures. Generally, main walls not loaded by floor structures that would weaken them sufficed if 45 cm thick. Central walls in buildings up to two storeys had to be 45 cm thick; three-storey buildings had to be 60 cm thick on all floors. A four-storied Moravian houses had to have walls 75 cm thick on the ground floor and 60 cm above. Moreover, in the Czech countryside, middle walls in three-storied buildings carrying a floor on only one side and light shaft walls were only 45 cm thick. Middle walls in two-storey buildings and party walls next to adjacent buildings had to be only 30 cm thick. Partition walls were generally acceptable if built 15 cm thick (an exemption was partitioning in flats in Moravia, as local codes required 30 cm).

Each wall with chimneys or pipes always had to match the thickness of the brick. In Moravia, outer staircase walls complied if 30 cm thick in buildings up to two storey high; outer walls in higher buildings or buildings with suspended steps had to be at least 45 cm thick. Partition walls had to be a minimum of 15 cm thick and 30 cm between two flats. In the case of vaulted and timber floors on steel beams, load-bearing stone or iron columns or pillars, the wall dimensions were determined by structural calculations.

This series of Building Codes featured many substantial improvements. In selected big Czech towns and all of Moravia, a building had to have a special fire separation wall as high as the attic on the side facing the neighbour; this wall had to be solid without any opening and if rafters bore on these walls, 30 cm of solid masonry had to be left unloaded. Firewalls had to stretch at least 15 cm above the roof and be plastered. If a firewall was on a property line, it had to be built up to half of its height, according to the conditions for a wall on a property line; a wall above this limit could be 30 cm thick or 15 cm, if strengthened by 15 cm pilasters. Similar fire-separation walls at least 15 cm thick, with required reinforcement pillars and isolated from rafters, had to be built in buildings 25 m long in the Czech countryside and over 30 meters long in all of Moravia. Passages through these walls had to be fitted with iron doors in an iron or stone doorframe.

Floors in ground-floor flats had to be at least 45 cm above the street in large Czech towns and 30 cm above the highest flood level in flood-prone areas. The Czech Country Order and both

⁶ The 1886 Building Code for Prague, the Building Code for Czech Lands No. 40/1886 dated 10 April, 1886. The 1887 Building Code for Pilsen, the Building Code for the Czech Kingdom No. 16/1887 dated 22 February, 1887. The Code No. 71/1888 dated 26 December, 1887. The Building Code for České Budějovice, the Code for the Czech Kingdom No. 5/1889 dated 8 February, 1889. The 1893 Building Code for Bohemia (aside from the specified towns), the Code for the Czech Kingdom No. 5/1889 dated 8 February, 1889. The 1894 Building Code for Brno, the Code for the Margraviate of Moravia No. 63/1894 dated 1 June 1, 894. The Building Code for Moravia, the Code for the Margraviate of Moravia No. 64/1894 dated 16 June, 1894.

Moravian Orders stipulated that floors in ground-floor flats were at least 30 cm above grade and for churches at least 15 cm, and 30 cm above the highest recorded flood level in flood areas. It was legally possible, under certain circumstances, to establish flats and workshops below grade. Such flats had to be damp-proofed, their clear height was at least 3 meters; 2.75 m sufficed in the Czech rural areas. If a room was 4 m high, at least half of it had to be above grade; moreover, the size and dimensions of the outer space were complexly determined based on how and where the basement rooms received daylight. The lowest floor level below grade was 2 m in Bohemia and 1.5 m in Moravia. A second parallel cavity wall with a 30 cm wide gap was required in big Czech towns and

15 cm in rural locales to keep the rooms dry; the space between the walls had to be ventilated. Workshops in cellars had to be vaulted; half of the height had to be above grade, the floor had to be partly concrete, 15 cm thick. If the area was in a flood zone, installing partially basement flats and workshops was not allowed.

According to Building Codes from the end of the 19th century (starting with the Prague's from 1886), the minimum clear height of flats and workspaces was 3 meters; 2.9 m were enough in rural areas.

Building codes related to light wells were further developed. Light wells had to be installed only where necessary. According to all codes, their basic area had to be at least 12 m². This figure was valid for three-storey buildings in all of Moravia; for higher buildings, 1 m² had to be added per each meter of height within a light well. If a light well daylighted only corridors, 6 m² were enough. This figure was valid for two-storey buildings in all of Moravia; for higher buildings, a half square meter had to be added per each vertical meter of a light well. The minimum profile of vents for ventilating toilets had to be 1 m². This figure was valid for two-storied buildings for all of Moravia; for higher buildings, 0.1 m² had to be added per each vertical meter of a vent. Air had to be supplied to each light well and a vent on the ground floor level. If a light well daylighted a staircase, it had to have an iron frame bearing on masonry. A light well then had to terminate above the roof – at least 15 cm in large Moravian towns and 5 cm in the countryside. Rooms daylighted from above were not allowed to be connected to the attic. Ventilation openings had to be on the top below a glazed roof.

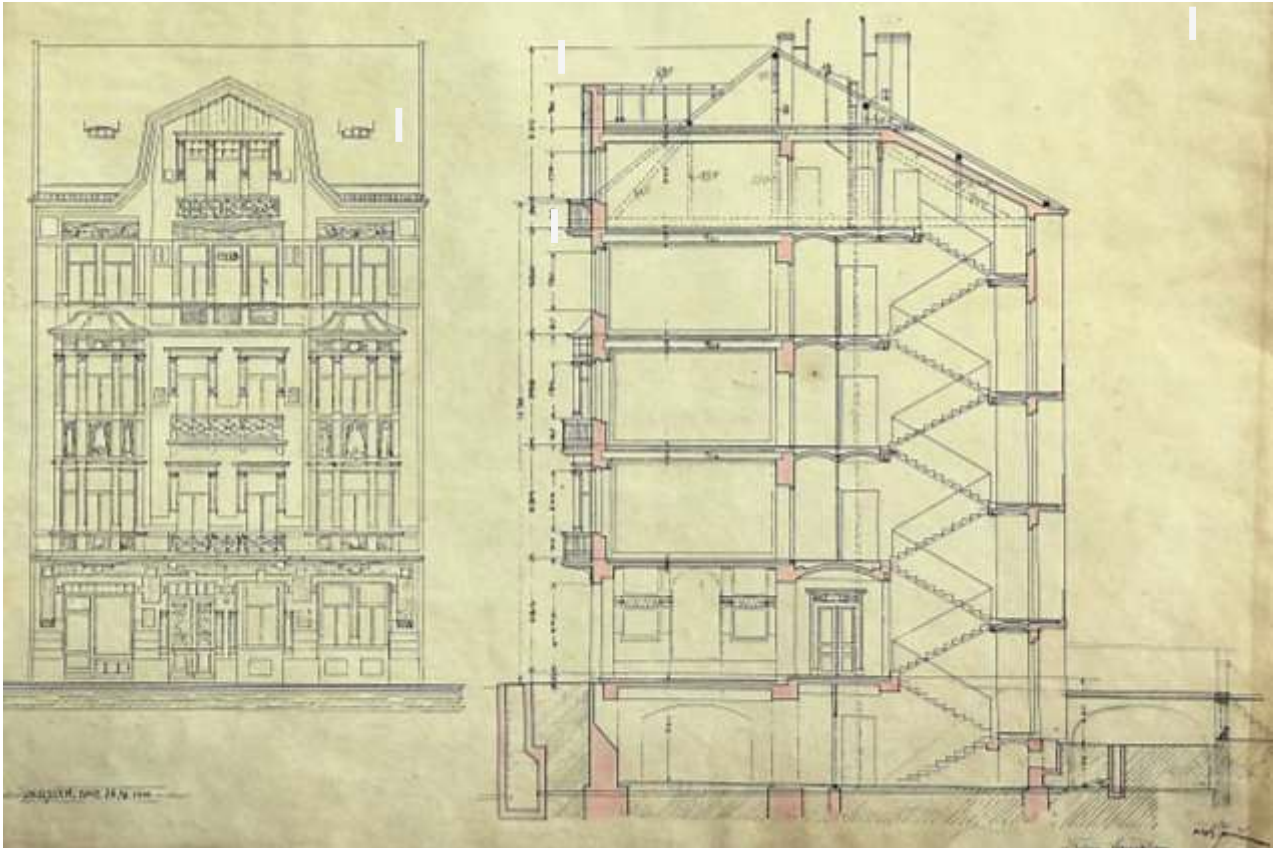


Fig. 4 – Design for a three-storey apartment building in Nusle by architect Václav Řezníček. The house in the style of geometric Art Nouveau from 1910, its concept corresponds to its time. Again, the masonry is increasing downwards. The house is in comparison with the previous lower category, most of the apartments are two-roomed and have a private bathroom, in one-room apartments is only a toilet. Cellars still have segmented vaults with passports (which is very archaic), on the ground and in the corridors these vaults are as usual into traverses, the ceiling construction is drawn rather without reed beams as a cheaper solution with reed ceiling and plaster directly on the ceiling. [NTM, AA, Fund 197, 20060808/03]

CONCLUSION

The article presents a summary of development of the construction of vertical walls of tenement houses from the mid-19th century to the beginning of the 20th century. The period was influenced by three gradually issued building codes, which reflect the building boom of this period. Raising of buildings forced the issuance of precise rules for variously tall and deep buildings of the observed period. Thanks to these regulations, which were based on long-term construction experience, practically no serious defects occurred in new buildings. The vertical constructions are closely related to the used ceiling constructions, both in the combustion and non-combustion variants.

ACKNOWLEDGEMENTS

This article was written as part of the NAKI DG 18P02 OVV 038 research project “Traditional City Building Engineering and Crafts in the Turn of 19th and 20th Centuries” (2018 – 2022, MK0/DG)“.

REFERENCES

- [1] EBEL, Martin. *Dějiny českého stavebního práva*. Praha: ABF - Arch, 2007. Stavební právo. ISBN 978-80-86905-21-1.
- [2] Joendl, Johann Paul: Poučení o stavitelství pozemním, Praha 1840.
- [3] Niklas, Josef - Šanda Fratišek: J. P. Jöndlovo Jöndl Poučení o stavitelství pozemním, Praha 1865.
- [4] Pacold, Jiří: konstrukce pozemního stavitelství, díl I., Praha 1890.
- [5] ŠKABRADA, Jiří. *Konstrukce historických staveb*. Praha: Argo, 2003. ISBN 80-7203-548-7.
- [6] Archiv architektury Národního technického muzea
fond 121, práce žáků. Archiv Národního technického muzea:
fond 55, Vysoká škola technická Praha, pozemní a vodní stavitelství;
fond 63, Státní průmyslová škola v Praze;
fond 64, Státní průmyslová škola v Praze – Novotný.